

Beam Dynamics and Limits for High Brightness,  
High Average Current  
Superconducting Radiofrequency  
(SRF) Photoinjectors

DISSERTATION  
zur Erlangung des akademischen Grades

doctor rerum naturalium

(Dr. rer. nat.)

im Fach: Physik  
Spezialisierung: Experimentalphysik

eingereicht an der  
Mathematisch-Naturwissenschaftlichen Fakultät  
der Humboldt-Universität zu Berlin

von  
M. Sc. Eva Panofski

Präsidentin der Humboldt-Universität zu Berlin:  
Prof. Dr.-Ing. Dr. Sabine Kunst

Dekan der Mathematisch-Naturwissenschaftlichen Fakultät:  
Prof. Dr. Elmar Kulke

- 
1. Gutachter: Prof. Dr. Andreas Jankowiak
  2. Gutachter: Prof. Dr. Ursula van Rienen
  3. Gutachter: Prof. Dr. Geoffrey Krafft

Tag der mündlichen Prüfung: 4. Februar 2019



# Abstract

An increasing number of future accelerator projects, light sources and user experiments require high brightness, high average current electron beams for operation. Superconducting radio-frequency (SRF) photoinjectors running in continuous-wave (cw) mode hold the potential to serve as an electron source that generates electron beams of high brightness.

Different operation and design parameters of the SRF photoinjector impact the beam dynamics and, thus, the beam brightness. Therefore, an in-depth understanding of the beam dynamics processes in an SRF photoinjector and the dependency of the beam dynamics on the photoinjector set parameters is crucial. Choosing suitable values for the photoinjector settings in order to run the facility in a high brightness mode, poses a significant challenge for the injector design and operation. A high brightness beam operation requires a global optimization of the SRF photoinjector that allows to find suitable photoinjector settings and to figure out and extend the physical performance limits of the investigated injector design. The dissertation at hand offers a detailed analysis of the beam dynamics in an SRF photoinjector regarding internal space charge effects. Furthermore, the impact of the photoinjector elements on the electron beam is discussed. The lessons learned from this theoretical view are implemented in the development of an optimization tool to achieve a high brightness performance. A universal multi-objective optimization program based on a generic algorithm was developed to extract stable, optimum gun parameter settings for a high brightness operation from Pareto-optimum solutions. This universal tool is able to optimize and find the physical performance limit of any (S)RF photoinjector independent from the individual application of the electron source (energy recovery linac, free electron laser, ultra-fast electron diffraction). This thesis thereby verifies and complements existing theoretical considerations regarding photoinjector-beam interactions. The global optimization strategy can be introduced to variable optimization objectives as well as it can be extended to an optimization of further parts of the accelerator facility.

The use of such powerful tools as numerical methods, artificial intelligence, machine learning, and neural networks in accelerator physics to predict target machine parameters and to solve optimization and data analysis issues will increase over the next years. The developed multi-objective optimization program represents a starting point for the numerical optimization in accelerator physics in the evolution towards these strategies.



# Zusammenfassung

Zukünftige Beschleunigerprojekte und Nutzerexperimente erfordern für ihren Betrieb einen hochbrillanten Elektronenstrahl mit hohem mittlerem Strom um neue Perspektiven, z.B. im Bereich der Materialwissenschaften, zu eröffnen. Eine Elektronenquelle mit dem Potential die Anforderungen bzgl. einer hohen Strahlbrillanz zu erfüllen, ist ein supraleitender Hochfrequenz (SHF) Photoinjektor im Dauerstrichbetrieb.

Die Strahldynamik eines solchen Photoinjektor Systems bestimmt die maximal zu erreichende Strahlbrillanz und wird ihrerseits von den Design- und Betriebsparametern des SHF Photoinjektors beeinflusst. Ziel ist immer die entscheidenden Design- und Betriebsparameter der Elektronenquelle hinsichtlich einer maximalen Strahlbrillanz zu wählen. Diese Aufgabe verlangt ein detailliertes Verständnis der Strahldynamik-Prozesse in einem SHF Photoinjektor. Ferner ist es notwendig, eine Optimierung des Photoinjektors als Ganzes, mit dem Ziel einer maximalen Strahlqualität bei hohem mittlerem Strom, vorzunehmen. Dieses ermöglicht auch, die physikalischen Grenzen eines gegebenen Designs zu ermitteln und im Betrieb vollständig auszunutzen.

Diese Doktorarbeit befasst sich mit Strahldynamik-Prozessen in einem SHF Photoinjektor, unter Berücksichtigung interner Raumladungseffekte. Die Erkenntnisse zur Strahldynamik werden für die Entwicklung eines Optimierungsprogramms verwendet, um die Leistung des Injektors hinsichtlich der Elektronenstrahl-Brillanz zu verbessern. Die entwickelte Methode basiert auf Pareto-Optimierung mehrerer Zielfunktionen (minimaler transversaler Phasenraum, kurze Bunchlänge), unter Verwendung eines generischen Algorithmus. Das zentrale Ergebnis dieser Arbeit umfasst ein universelles Optimierungsprogramm, das für SHF Photoinjektoren unabhängig von ihrem Design und Anwendungsgebiet (Energy Recovery Linac, ultraschnelle Elektronenbeugung) genutzt werden kann. Für den Betrieb mit hoher Strahlbrillanz ist es möglich aus den erhaltenen Pareto-optimalen Lösungen einen stabilen Satz an Einstellwerten für den Photoinjektor zu extrahieren. Darüber hinaus wird der Einfluss der Photoinjektor Parameter auf die Strahlqualität des Elektronenstrahls erfasst. Durch die allgemeine Optimierungsstrategie lässt sich das entwickelte Programm auch leicht für andere Beschleunigerabschnitte, oder die Optimierung einer ganzen Anlage mit erweiterter Zielsetzung anpassen.

Das Programm bildet einen wichtigen Ausgangspunkt für die numerische Optimierung in der Beschleunigerphysik, die in den nächsten Jahren zunehmend künstliche Intelligenz und selbständig lernende Neuronale Netzwerke einbinden wird.



# Contents

<b>1</b>	<b>Motivation</b>	<b>1</b>
<b>2</b>	<b>Application of a High Brightness Electron Beam - Diffraction Limited Light Sources and User Experiments</b>	<b>9</b>
2.1	Diffraction Limited Storage Rings . . . . .	9
2.2	Free Electron Laser (FEL) . . . . .	11
2.3	Energy Recovery Linac (ERL) . . . . .	13
2.4	bERLinPro . . . . .	16
2.5	Ultrafast Electron Diffraction . . . . .	18
<b>3</b>	<b>Electron Injectors</b>	<b>21</b>
3.1	Overview of Current Electron Injectors . . . . .	21
3.2	SRF Gun Cavities for Photoinjectors . . . . .	26
3.3	Photoinjectors . . . . .	28
3.4	GunLab . . . . .	30
<b>4</b>	<b>Theory of the Transverse and Longitudinal Beam Dynamics</b>	<b>43</b>
4.1	Characteristics of an Electron Beam . . . . .	43
4.2	Maximum Beam Brightness . . . . .	50
4.3	Beam Dynamics in an SRF Photoinjector . . . . .	51
4.3.1	Emission . . . . .	51
4.3.2	Acceleration . . . . .	56
4.3.3	Solenoid . . . . .	65
4.3.4	Space charge . . . . .	69
4.3.5	Complete beam dynamics in an SRF photoinjector . . . . .	73
4.3.6	Impact of the electron bunch parameters on the beam brightness	76
4.4	Beam Brightness Maximization in an SRF Photoinjector . . . . .	77
4.4.1	Bunch shape optimization . . . . .	77
4.4.2	Emittance minimization . . . . .	80
4.4.3	Bunch compression . . . . .	87
4.4.4	Summary of transverse and longitudinal bunch compression methods in SRF guns . . . . .	96

4.5	Emittance-Bunch Length Trade-off . . . . .	97
<b>5</b>	<b>Optimization of an SRF Photoinjector</b>	<b>101</b>
5.1	Particle Tracking . . . . .	102
5.2	Optimization Strategies . . . . .	105
5.2.1	Swarm optimization . . . . .	105
5.2.2	Single-objective optimization . . . . .	107
5.2.3	Multi-objective optimization . . . . .	108
5.3	Multi-Objective Optimization Program for an SRF Photoinjector . .	116
5.4	Applications of the Developed Optimization Tool . . . . .	124
<b>6</b>	<b>Multi-Objective Optimization Results</b>	<b>125</b>
6.1	SRF Photoinjector Optimization without Solenoid Field Correction . . . . .	125
6.1.1	Beam parameter evolution in the compromise region . . . . .	130
6.1.2	Beam parameter evolution in the low emittance regime . . . . .	132
6.1.3	Pareto-optimization with a variable optimization point . . . . .	134
6.1.4	Beam parameter evolution in the short bunch length regime . . . . .	135
6.1.5	Correction of the solenoid field . . . . .	137
6.2	SRF Photoinjector Optimization with Solenoid Field Correction . . .	139
6.2.1	Beam parameter evolution in the short bunch length mode . . . . .	141
6.2.2	Phase space evaluation in the short bunch length regime . . . . .	143
6.2.3	Beam parameter evolution in the compromise region . . . . .	145
6.2.4	Phase space evaluation in the compromise region . . . . .	147
6.2.5	Beam parameter evolution in the low emittance region . . . . .	148
6.2.6	Phase space evaluation in the low emittance regime . . . . .	150
6.2.7	Discussion of the phase spaces . . . . .	152
6.2.8	Impact of the beam and the photoinjector parameters on the Pareto-optimum curve . . . . .	153
6.3	Application-Specific SRF Photoinjector Optimization . . . . .	160
6.3.1	Optimization of an SRF photoinjector for ERL operation . . . . .	160
6.3.2	Optimization of an SRF photoinjector for ultra-short pulses . . . . .	173
6.3.3	Gun cavity design study based on Pareto-optimization . . . . .	184
6.4	SRF Gun at Helmholtz-Zentrum Dresden-Rossendorf . . . . .	189
<b>7</b>	<b>Summary and Outlook</b>	<b>193</b>
7.1	Conclusion . . . . .	193
7.2	Outlook . . . . .	198
	<b>Appendices</b>	<b>205</b>



---

<b>A</b>	<b>ASTRA Tracking Procedure</b>	<b>207</b>
<b>B</b>	<b>Settings and Numerical Studies for the Developed Multi-Objective Optimization Program</b>	<b>209</b>
B.1	Settings for the ASTRA Simulations . . . . .	209
B.2	Settings for the Optimization . . . . .	213
B.2.1	Variator probability . . . . .	213
B.2.2	Number of parameter settings per population and resolution of the Pareto-optimum curve . . . . .	214
B.3	Properties of the Pareto-Optimum Front . . . . .	215
B.3.1	Convergence of the optimum curve . . . . .	215
B.3.2	Reproducibility of the Pareto-optimum curve . . . . .	216
B.3.3	Error estimations for the transverse emittance and bunch length	218
B.3.4	Stability of the Pareto-optimum settings . . . . .	219
	<b>List of Figures</b>	<b>223</b>
	<b>List of Tables</b>	<b>229</b>
	<b>List of Symbols and Abbreviations</b>	<b>229</b>
	<b>Acknowledgements</b>	<b>244</b>



# Chapter 1

## Motivation

Over the last 50 years, particle beams from accelerators pushed research in the natural sciences to the next level. Numerous fields in science have used accelerated particle beams either directly or indirectly. Direct application is based on the particle beam itself whereas indirect application means the generation of photon radiation.

Accelerated particles radiate photons when they move on curved beam paths due to the acceleration caused by transverse deflection. Therefore, accelerator facilities operate as synchrotron radiation sources with wavelengths ranging from the infrared to hard X-ray regime (e.g., BESSY II at Helmholtz-Zentrum Berlin (HZB)[1]).

The particle beam itself is deployed in particle physics to discover new particles, such as the gluon (DESY Hamburg PETRA, 1979 [2]) or the Higgs boson (CERN LHC, 2011 [3, 4]) in particle colliders. In those processes, accelerators confirm theoretical predictions, and they help to investigate the fundamental properties of elementary particles. Furthermore, particle beams are applied in medicine for cancer therapy (e.g., HZB eye tumor therapy [5]). Material scientists use accelerated particle beams for diffraction and scattering experiments (e.g. DESY Hamburg REGAE [6]).

Independent of the exact application of a particle beam, each application has individual requirements regarding the beam properties. Therefore, the accelerator must be designed, optimized and configured for the specific task the facility is working for. The goal in the design, commissioning and operation phases of an accelerator is to fulfill the beam requirements, to explore the performance limit of the current setup, and to find new designs and settings to improve the achieved beam parameters. The process of meeting these goals bases on entirely theoretically understood beam dynamics in the accelerator.

The operation of light sources that generate synchrotron radiation is one of the fundamental pillars constituting the research at the Helmholtz-Zentrum Berlin (HZB). The storage ring BESSY II [operating since 1998] offers synchrotron radiation for more than 1500 users per year [7]. The planned upgrade BESSY VSR will provide photon pulses with different temporal lengths simultaneously [1]. Furthermore, the energy recovery linac project bERLinPro is currently under construction at HZB. bERLinPro is a research and development facility paving the way for future applications of high brightness, high average current electron beams [8].

Many experiments in material science are based on the investigation of samples with synchrotron light. In order to gain the wanted information about a particular material, a photon probe beam hits a respective user sample. The requirements for the photon probe beam when generated by a future light source, such as BESSY VSR and bERLinPro, are determined by the system under measurement. In particular, the generation of synchrotron light in the X-ray regime offers great perspectives in research.

The spatial resolution is given by the wavelengths of the photons. For an investigation of atoms in a sample with a size that lies in the range of  $10^{-10}$  m, X-ray probe beams with wavelengths ranging from 0.01 nm to 10 nm are needed. A high temporal resolution of the photon probe beam provides a solution to make fast phenomena visible, such as protein folding ( $10^{-4}$  s), the shock wave propagation by one atom ( $10^{-12}$  s) or the electron exchange in chemical reactions ( $10^{-16}$  s). Short X-ray pulses of photons can provide time resolutions within these time-scales [9]. Additionally, to observe the different energy levels of an atom the energy resolution of the probe beam demands a small energy spread. X-ray beams with nearly single-energy photon pulses are necessary. If a high number of photons per pulse hits the sample, measurements can be completed within an acceptable time-frame and the beam can reach a high coherence volume. Finally, pulse-resolved measurements require every photon pulse to have similar properties.

Accelerator driven light sources are able to provide high intensity photon beams, even in the X-ray regime with wavelengths down to  $10^{-10}$  m for a resolution on an atomic level. Synchrotron radiation sources are usually operated by high intensity electron beams since the emitted photon energy, and thus the synchrotron radiation power, decreases with the fourth power of the particle mass [10]. The performance and quality of a light source are characterized by the photon bright-

---

ness parameter [10]:

$$B_{\text{photon}} \propto \frac{N_{\text{ph}}}{\sigma_x \sigma_{x'} \sigma_y \sigma_{y'} \sigma_t \frac{\Delta E}{E}}. \quad (1.1)$$

The photon brightness is defined as the number of photons  $N_{\text{ph}}$  per unit area, per unit solid angle and per time in a narrow spectrum to the photon energy [10]. A high photon brightness enables faster experiments with an improved spatial, temporal and energy resolution as well as higher coherence. Equation (1.1) shows that a compact, well-focused photon pulse leads to higher photon brightness. Since the electron beam properties determine the quality of the emitted photon radiation, accelerator based light sources must be operated with a high brightness electron beam to increase the photon brightness of the radiated beam. Therefore, an improvement of the synchrotron light quality always requires the improvement of the electron beam quality.

A high intensity photon beam translates into a highly charged particle beam in which each electron bunch occupies a small phase space volume. Hence, the electron beam must be well-focused in the transverse plane with a small beam size and minimum transverse divergence. Additionally, the particle bunch should provide a short bunch length with mono-energetic particles at best. All these beam properties are summarized in the beam quality parameter “beam brightness” that is defined as follows [11]:

$$B_{\text{electron}} \propto \frac{N_e}{\sigma_x \sigma_{x'} \sigma_y \sigma_{y'} \sigma_z \sigma_E}. \quad (1.2)$$

Here  $\sigma_{x,y}$  describes the transverse beam size,  $\sigma_{x',y'}$  is the transverse beam divergence.  $\sigma_z$  represents the bunch length and  $\sigma_E$  gives the energy spread. Minimizing all these parameters in a high current beam, with  $N_e$  as the number of electrons, leads to a high brightness beam.

In an attempt to reach ultimate brightness values, the electron beam volume in the transverse and longitudinal phase space can become smaller than the phase space volume of the photon beam. In that case, only diffraction effects in the insertion device of the accelerator, where the synchrotron light is generated, limit the phase

space of the radiation. The facility is then called “diffraction limited” [12].

Diffraction limited light sources entail significant progress in current research as they take the achieved photon brightness of third generation light sources to the next level [see Fig. 1.1]. Alongside ultimate storage rings, the energy recovery linac (ERL) and the free electron laser (FEL) are two further examples of diffraction limited light sources.

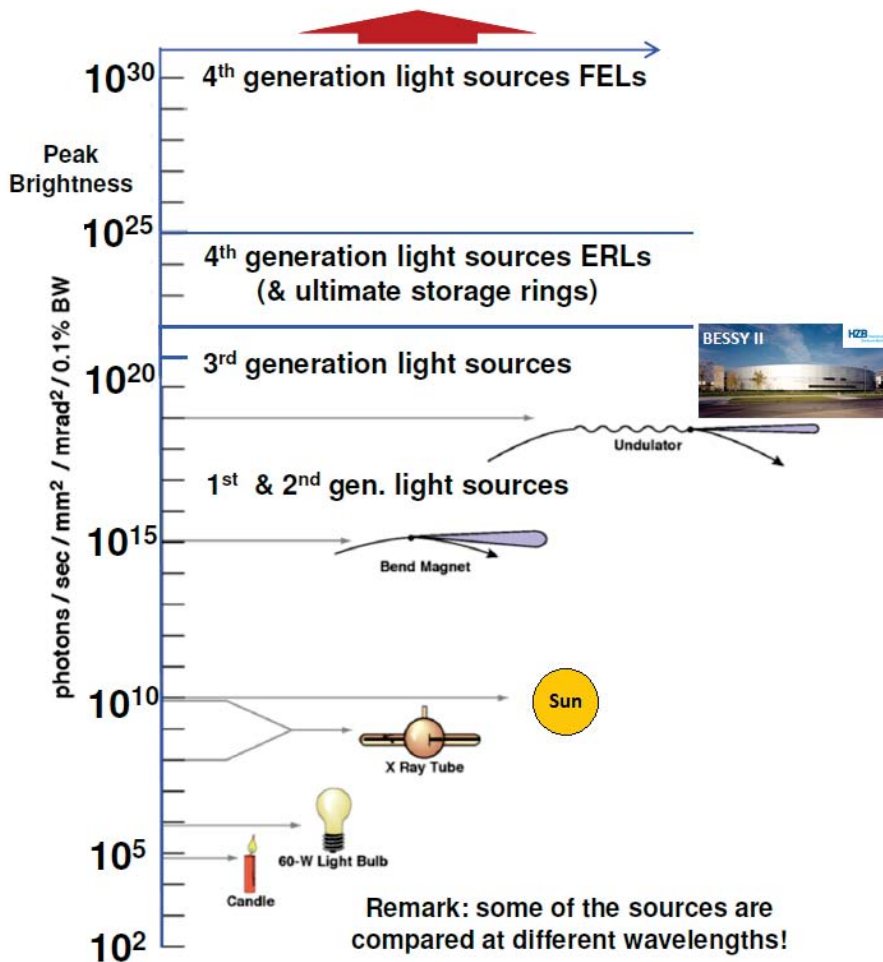


Figure 1.1: Beam brightness for different light sources [13].

The user demand for diffraction limited light sources requires a facility that is driven by a high brightness electron beam.

Even though the applications of high brightness electron beams are diverse, the requirements on the beam are always set by similar parameters that target the beam brightness: The bunch charge, the transverse and longitudinal phase space.

---

The high beam brightness in a diffraction limited storage ring is mainly achieved by a small transverse phase space, however, corresponding to rather long pulses and a large energy spread. A small transverse phase space is achieved by a lattice optimization in the ring. FELs and ERLs operate based on a linear accelerator (linac) that allows a small transverse phase space and a short bunch length simultaneously. In this case, the beam brightness is determined at the electron injector and must be preserved and controlled from the source through the accelerator. The beam brightness cannot be improved and high brightness cannot be achieved by beam manipulation downstream the source in the accelerator structure. As a consequence, the electron injector plays a prominent role in a high brightness, linac based accelerator facility. As the studies in this dissertation consider the ERL project bERLinPro at HZB, the focus lies on a high brightness electron source and its optimization.

It is crucial to understand the limitations of the electron injector to generate a high brightness beam, and to push the electron source performance to these limits and beyond. For that reason, it is equally essential to investigate the beam dynamics in the source and to keep them entirely under control. The most promising approach to fully explore the capability of the electron injector in an accelerator is a combination of simulation studies and experimental tests conducted in a research and development facility.

An analytical model referring to the calculation of relevant beam parameters, such as the transverse phase space volume or the bunch length, is a useful basis for theoretical studies. Nevertheless, the precision of this approach is limited since idealized assumptions are made (idealized field data, not all nonlinearities are considered). In contrast, particle tracking right from the electron emission process through all beam path elements permits the illustration of the transverse and longitudinal beam dynamics in the electron injector and the subsequent accelerator. Tracking can also include nonlinearities, for instance, space charge effects. Interactions and dependencies of the injector set parameters, and their impact on the beam dynamics in the injector can be figured out. Therefore, particle tracking provides a suitable and promising option to explore the beam dynamics and the evolution of the relevant beam parameters in an electron injector in detail.

Afterwards, the knowledge gained in beam dynamic simulations can be used to improve the injector performance. Further, it can help to exceed and extend the

(brightness) limits that are determined by design and the parameter settings of the injector. The photoinjector performance improvement can autonomously be done if the particle tracking is implemented in an optimization tool which follows user defined optimization criteria. The optimization program evaluates stable parameter settings to run the gun in a high brightness regime. Results from optimization strategies deepen the understanding of the electron injector, as they figure out the limits and challenges of the facility regarding its design and parameter settings.

In addition, measurements taken with beam diagnostic tools at an injector facility, work complementary to the theoretical studies. The results help to better understand the injector performance and to improve the injector model that can afterwards be implemented in the optimization procedure. Moreover, measurements render the verification of the beam dynamics simulations and the optimization results possible.

The dissertation at hand studies the beam dynamics and limits of one particular type of high brightness electron guns: the superconducting RF photoinjector. This photoinjector represents a promising electron source for future accelerators and accelerator applications, such as the mentioned ERL, FEL or ultrafast electron diffraction (UED), which have a crucial impact on the current research. The operation of an SRF photoinjector requires a fundamental theoretical understanding of the dependencies of beam parameters among themselves, the impact of the beam parameters on the beam brightness and the influence of photoinjector settings on the beam dynamics. As a consequence, this doctoral thesis mainly concentrates on theoretical studies of this highly complex system. Moreover, computer-based optimization plays an increasingly prominent role in accelerator research since the commissioning, operation, and verification of the accelerator model in measurements can be optimally prepared, facilitated and improved. Therefore, this work further emphasizes the investigation of optimization strategies in general, and the development of an optimization approach that mainly focuses on SRF photoinjectors in particular. In addition, measurements help to investigate the electron source, verify, and complement the theoretical model. Still, as the operation of an SRF photoinjector is part of the latest research, it poses hardware challenges (cathode transfer, high peak field operation of the superconducting cavity) limiting the contribution of beam dynamics measurements and underlining the particular importance of theoretical optimization studies. Especially the commissioning and first operation phases of an innovative, technically challenging injector facility require intense simulation and optimization studies. This is also the case when a new photoinjector design should be investigated. The phase spaces of the electron



---

beam are usually too complex to optimize them during the operation of the electron source. Furthermore, the beam diagnostic systems are often limited for high precision beam measurements. As a consequence, an optimization of the electron injector that provides stable injector settings for a high brightness operation and that offers knowledge about the beam dynamics, plays an outstanding role.

Hence, this thesis lays a clear focus on theoretical beam dynamic studies, while beam diagnostic measurements are just mentioned at the periphery of this work.

The beginning Chapter 2 of this dissertation introduces current and future applications of high brightness electron beams. The subsequent Chapter 3 provides an overview of current electron injectors and the superconducting RF photoinjector as the most suitable choice for high brightness electron beam production. Afterwards, Chapter 4 offers a detailed analysis of the beam dynamics in such an electron source. An optimization approach that optimizes an SRF photoinjector for a high brightness performance, constitutes the central part of this doctoral thesis. Chapter 5 gives a concise overview of particle tracking and possible optimization strategies. Previously, SRF photoinjector facilities were mainly optimized by particle tracking and swarm optimization. The developed program applies a multi-objective genetic algorithm (MOGA) to optimize an SRF gun towards high beam brightness, and to push the SRF photoinjector to its physical performance limits. A separate section [see Section 5.3] discusses the setup and working procedure of the developed program. The used method provides a global optimization of an SRF photoinjector considering all crucial operation and design parameters of the injector. Furthermore, the developed tool finds Pareto-optimum solutions fast and more efficient compared to previous approaches.

All optimization results are summarized in Chapter 6. In a first optimization run for a given SRF photoinjector design, the program provides stable, optimum photoinjector settings for a high brightness performance. These results can be used for the SRF photoinjector facility to facilitate a future commissioning in order to already start in a high brightness mode. Only slight fine-tuning is then required to achieve the desired electron beam properties.

Besides studies for the SRF gun test facility at HZB (see Chapter 6.2), optimization results for the SRF gun in an ERL mode supplemented with a booster section will follow [Chapter 6.3.1]. These optimization results successfully answer the question if the current electron source design is able to generate electron bunches that fulfill the specifications of the ERL prototype at HZB regarding the transverse and longitudi-

nal beam properties. Furthermore, it can be demonstrated how the beam dynamic processes in the booster improve the transverse and longitudinal phase space, and therefore, the beam brightness. The optimization results of the SRF photoinjector together with a 5-cavity booster section are successfully compared with optimum results of a DC injector at the Cornell University, as well.

Furthermore, the powerful tool can model and analyze beam dynamics of ps and fs long bunches of different bunch charges. It, therefore, allows the optimization for other SRF gun applications, such as an electron source for UED and FEL. Using the developed optimization tool, the application of the SRF gun as a stand-alone facility for ultrafast electron diffraction is simulated. The ability of an SRF photoinjector to generate fs long bunches for time-resolved diffraction experiments is demonstrated in the optimization results in Chapter 6.3.2. The successful optimization of another SRF photoinjector at Helmholtz-Zentrum Dresden-Rossendorf (Germany) in Section 6.4 shows the flexibility of the optimization code while introducing first optimization results of the SRF gun application in the high peak current FEL mode.

Finally, the optimization of the superconducting gun cavity for different field flatness values represents a first approach in the cavity design optimization based on the developed program [see Chapter 6.3.3]. For the first time, the impact of the cavity field flatness on the complete transverse and longitudinal electron beam dynamics in an SRF photoinjector is studied in detail.

Since the used multi-objective optimization procedure is universal, the optimization code can easily be adopted for other optimization objectives (i.e., lattice optimization), further accelerator parts (i.e., linac cavity design optimization), for the whole accelerator structure, and other accelerator types (i.e., storage ring, collider). Therefore, the electron beam parameters defining the performance of the corresponding facility and application, must be identified and afterwards, induced as objectives in the optimization procedure. All achieved optimization results underline that the developed optimization program represents a powerful tool in the SRF photoinjector research. Chapter 7 summarizes the results of this dissertation. A final outlook associates the presented optimization tool as an transition and important step towards future optimization strategies based on machine learning and artificial neural networks.

## Chapter 2

# Application of a High Brightness Electron Beam - Diffraction Limited Light Sources and User Experiments

This chapter gives an overview of current diffraction limited light sources and a user experiment utilizing a high brightness electron beam. Apart from the high brightness operation, each accelerator type and application focus on further beam parameters that must fulfill pre-defined defaults. An optimization of the facilities is essential to achieve the application goals and to improve the operation performance.

### 2.1 Diffraction Limited Storage Rings

Ultimate storage rings represent the upgrade of the current third generation storage rings. One examples in operation is the MAX IV accelerator [14]. The synchrotron radiation is generated in beam-guiding dipole magnets and, starting with the third generation light sources in the early 90's, in insertion devices (undulator or wiggler). An insertion device consists of a periodic structure of dipole magnets which force the electrons on an oscillating path, radiating parts of their energy in intense synchrotron light.

The beam dynamics in a storage ring is determined by two processes: The momentum loss of the particles due to synchrotron radiation leads to radiation damping while the consequent dispersion causes the excitation of betatron oscillations in the transverse direction [15].

The task in a storage ring is to provide a low emittance beam for synchrotron light generation. The transverse emittance defines the volume occupied by the bunch in

## 2. Application of a High Brightness Electron Beam - Diffraction Limited Light Sources and User Experiments

---

the transverse phase space. Third generation light sources work in the equilibrium where the radiation damping and the betatron oscillation excitation is balanced, in order to achieve a minimum emittance.

Ultimate storage rings significantly improve the beam brightness of the electron beam and the corresponding photon beam. The transverse emittance is minimized by controlling the dispersion induced during the synchrotron radiation generation. This technique suppresses the betatron oscillations and shifts the equilibrium. Additional magnetic structures consisting of dipoles, quadrupoles and sextupoles (multi-bend achromats) are inserted into the storage ring beam path to manage the dispersion, to damp the  $\beta$ -oscillations, and therefore, to minimize the beam emittance [10]. Fig. 2.1 depicts an example for the magnetic lattice of the diffraction limited storage ring MAX IV [14].

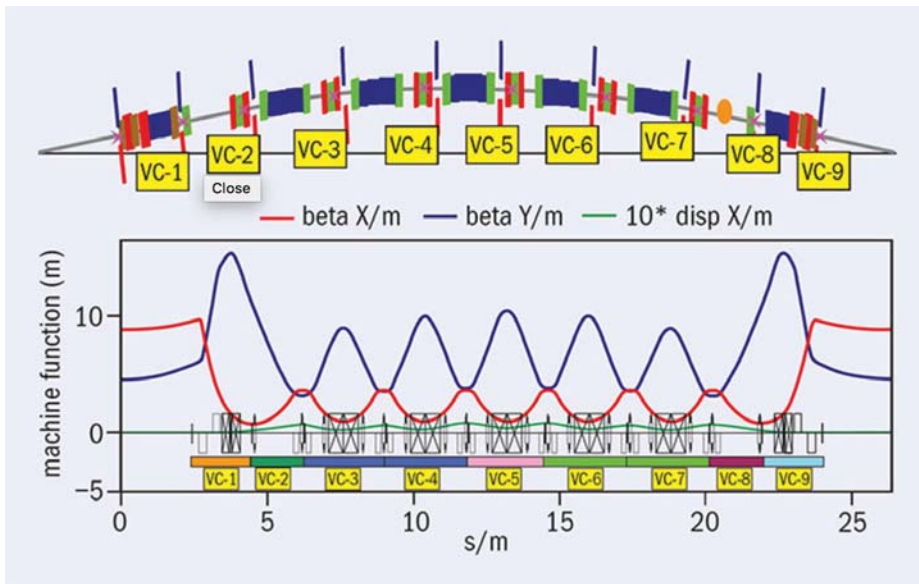


Figure 2.1: Magnetic lattice of one of the 20 multi-bend achromats at the MAX IV diffraction limited storage ring with dipoles (blue), quadrupoles (red), and sextupoles (green). The bottom graph shows the beam size evolution (betatron oscillations) and the dispersion evolution along the beam path. [16].

The accelerator design and operation are based on a lattice optimization including multi-bend achromats. However, a multi-bend achromat impacts and limits the dynamic aperture. The task is to optimize the lattice to improve the performance of a diffraction limited storage ring, and thus, to evaluate the trade-off between the transverse emittance and the dynamic aperture.

Even though ultimate storage rings are able to accelerate low transverse emittance beams, the achievable beam quality is limited by the rather long pulse lengths in order to reduce Touschek and intrabeam scattering. Linear accelerators offer a considerably higher peak quality in the beam by avoiding the equilibrium state of storage rings. The beam is discarded before establishing the equilibrium [17]. The synchrotron radiation is then generated behind the linac section in an undulator (insertion device). Such a setup represents a single-pass FEL.

## 2.2 Free Electron Laser (FEL)

In 1971, John Madey introduced the first free electron laser at Stanford University [18]. The objective of a FEL is to generate laser light using a relativistic electron beam as a lasing medium instead of a gas or a solid. As the electrons in an electron beam are not bound to atomic orbits, they are referred to as “free”. Compared to lasers that use a solid or gas as their optical medium, FELs offer a broad spectrum of wavelengths by tuning either the energy of the electrons or the magnetic field in the undulator. Wavelengths ranging from microwaves to X-rays are possible.

In order to generate a FEL photon beam, an accelerator is used to bring an electron beam to relativistic velocities. Afterwards, the beam is coupled to an undulator, an insertion device consisting of a periodic structure of dipole magnets. The radiation power of the generated light is proportional to the number of electrons. Thus, high peak currents are required. The magnetic field of the undulator magnets and the spatial period determine the amplitude of the electron oscillation, and thereby the energy band width of the generated radiation. The produced photons are monochromatic but incoherent since the electromagnetic waves from randomly distributed electrons interfere with time constructively and destructively [19].

In order to generate a coherent laser light from a FEL, the electron bunch must be modified. In the SASE principle of self-amplified spontaneous emission, the undulator is enlarged by several meters [9]. The generated incoherent photons are faster than the electrons on their wiggling path. The transverse electric field of the radiation interacts with the transverse deflected electron beam in the undulator. While some electrons are accelerated, some others slow down due to the ponderomotive force. This energy modulation leads to electron density modulations, and thus the

building of longitudinal sub-bunches. These so-called microbunches are separated by one optical wavelength. The electrons of one microbunch radiate in phase intense, high-power, coherent synchrotron light with an excellent beam quality. The SASE principle is illustrated in Fig. 2.2.

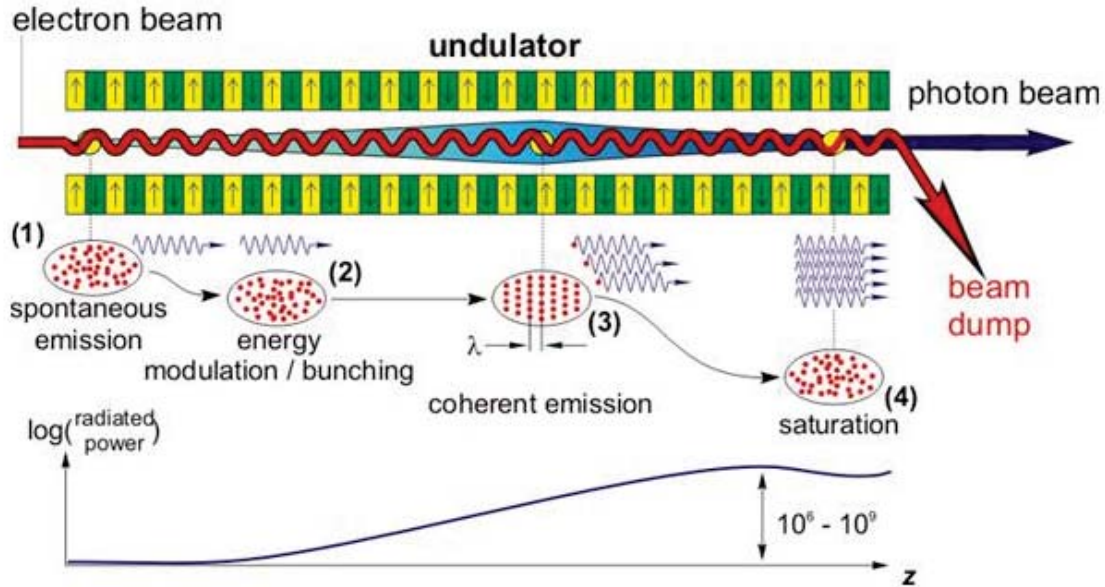


Figure 2.2: The SASE principle including an electron density modulation in a bunch due to electron photon interactions [20].

There are further solutions besides the SASE principle to generate the required photons for the microbunching process, such as seeding with an external optical laser or implementing an optical cavity system at the two ends of the undulator as a gain medium [19]. All current X-ray FEL facilities in operation are based on the SASE principle. However, Kwang-Je Kim suggested an X-ray FEL using an optical resonator in 2008 [21]. The setup is called XFELo (X-ray FEL oscillator).

The radiation production in a single-pass FEL requires an optimization of the accelerator in the design and commissioning phase with the focus on a low transverse beam emittance and a high peak current in the lasing slice. The transverse emittance is defined by the electron source. High peak currents call for short electron pulses which a bunch compressor can induce behind the injector. Therefore, the objective is to improve the electron gun design towards a low emittance performance to achieve

best FEL radiation for user experiments. Since the pulse length also contributes to the electron beam brightness, a high brightness electron beam optimization is necessary for an optimum FEL operation.

A well-known example of a facility based on the SASE principle is the single-pass European XFEL at DESY Hamburg [22, 23]. The electron beam which is accelerated in 97 superconducting cavity modules in a 10 Hz pulsed mode with 2700 bunches per pulse, generates extremely intense, ultra-short X-ray flashes in three undulators. Afterwards, the electron beam is dumped and the X-ray pulses are prepared to hit user samples that are to be studied. The facility, which began running in 2017, renders the analysis of structure on an atomic level (e.g., of viruses) possible. It offers researchers the chance to study the time resolution of ultra-fast phenomena (such as chemical reactions) or to examine unknown processes, like the ones occurring inside planets.

Furthermore, the availability of extreme ultraviolet (EUV) wavelengths below 20 nm, turn FELs into an interesting opportunity for next-generation lithography technologies, e.g., for integrated circuit manufacturing. However, a high brightness, high-power electron beam is required to drive an EUV FEL. A FEL driven by a linac cannot achieve the required high average power, whereas a high brightness electron injector in combination with an energy recovery linac is a promising alternative. The ERL allows for the acceleration of a high power electron beam [24].

## 2.3 Energy Recovery Linac (ERL)

An ERL combines the advantages of a storage ring (high average current, continuous wave beam) and the benefits of a linear accelerator (high beam brightness, short pulses), indicating the great potential of this accelerator type. Therefore, an ERL light source is expected to offer high average current beams with higher brilliance and shorter pulses in comparison to a current third generation storage ring for synchrotron radiation generation, especially in the X-ray regime.

The first time a structure that resembled an ERL accelerator, was mentioned was in 1965. Maury Tigner suggested a new concept of acceleration and deceleration in only one linac [25]. The first demonstration followed in Stanford 1987 (SCA/FEL) [26].

An energy recovery linac consists of an injection line, the main linac, two recirculation arcs and a dump [see Fig. 2.3]. The beam is generated in the electron source. A



booster section serves for further acceleration. Then, the beam is merged into the main ring. The electron bunch reaches its maximum energy in the linac. After one turn, the bunch enters the linac again but at a phase shift in the RF field of 180 deg. This leads to a deceleration of the electrons. The energy is recovered from the bunch and can be stored in the RF cavities of the linac nearly without losses. The bunch is then dumped at low energy.

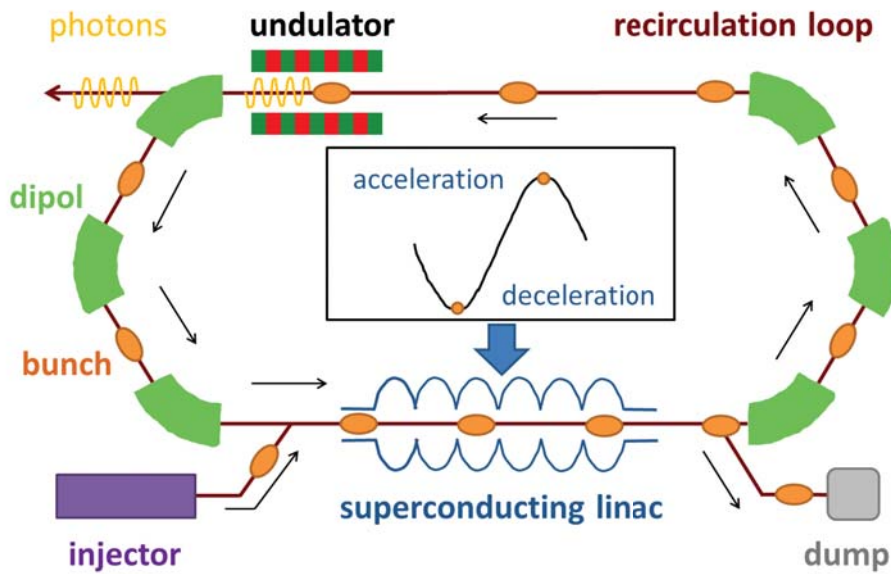


Figure 2.3: The setup of an energy recovery linac.

In order to drive a light source with an ERL, an undulator section can be placed on a straight section after the first arc. Compared to today's third generation storage rings, an ERL is able to generate synchrotron radiation with a brightness 1000 times greater than a third generation storage ring can [see Fig. 1.1].

High average current is enabled as an ERL takes advantage of superconducting RF technology for the linac cavities. Due to the reduced resistance in the superconducting cavity walls, high gradients in continuous wave (cw) mode can be reached in a superconducting (sc) cavity allowing for a compact ERL setup. The cw operation leads to a high average beam current. Due to the high quality factor of SRF cavities compared to normal-conducting (nc) RF cavities they are less affected by RF losses. Instead of the attempt to reduce these losses by adjusting the cavity design, the cavity shape can be optimized with regard to other properties. Then, a special



sc cavity design that aims for accelerating high average current beams with a high beam quality reduces beam-cavity interactions [27]. As a result, sc cavities facilitate a cavity design with wide beam tubes that damp higher order modes for high current operation.

The great advantage of an ERL is the recycling of the kinetic energy of the bunch instead of the particle beam itself that is dumped after one turn. Therefore, a small transverse emittance can be achieved. If an insertion device is used, the quality of the electron beam in the transverse plane decreases as a result of the radiation of synchrotron light [10]. As a new high brightness bunch is always used to radiate synchrotron light in an ERL, high beam brightness and high repetition rates can be maintained.

In order to adjust the ERL performance so that it fulfills the application requirements, the focus is on a low emittance, high brightness electron beam. A low emittance is mainly prepared in the electron gun. A short bunch length is mandatory to reach high peak currents and to allow the analysis of structural dynamics of user samples on a rapid time scale. Therefore, the electron injector design and operation, as well as the subsequent accelerator components, must be optimized for these purposes.

In general, an ERL represents an accelerator facility that is able to operate as a synchrotron source, a free electron laser, a collider, an electron cooler or a user facility for diffraction and scattering experiments. Figure 2.4 provides an overview of current and future ERL projects and their applications. Several facilities already demonstrate the ERL principle and serve as prototypes. Current and future energy recovery linac projects are the ERL at Jefferson National Laboratory (USA) [28], cBETA at Cornell University (USA) [29], eRHIC at Brookhaven National Laboratory [30], JAERI and the compact ERL (cERL) at KEK Laboratory (Japan) [31, 32], ALICE and 4GLS in Daresbury (UK) [33], LHeC at CERN (Switzerland)[34], MESA at the University Mainz (Germany) [35], bERLinPro at Helmholtz-Zentrum Berlin (Germany) [8] or the ERL at Budker INP in Novosibirsk (Russia) [36].

The ERL accelerators at Jefferson Laboratory, at KEK and the Budker Institute aim for ERL FEL applications while the accelerators in Daresbury are planned to operate as future light sources. cBETA and MESA will mainly be used for particle physics experiments. Regarding the research topic of electron cooling efforts are made, for example, by the future ERL RHIC at Brookhaven National Laboratory (USA), while

the LHeC proposed at CERN (Switzerland), for instance, attempts research in the area of hadron-electron-colliders.

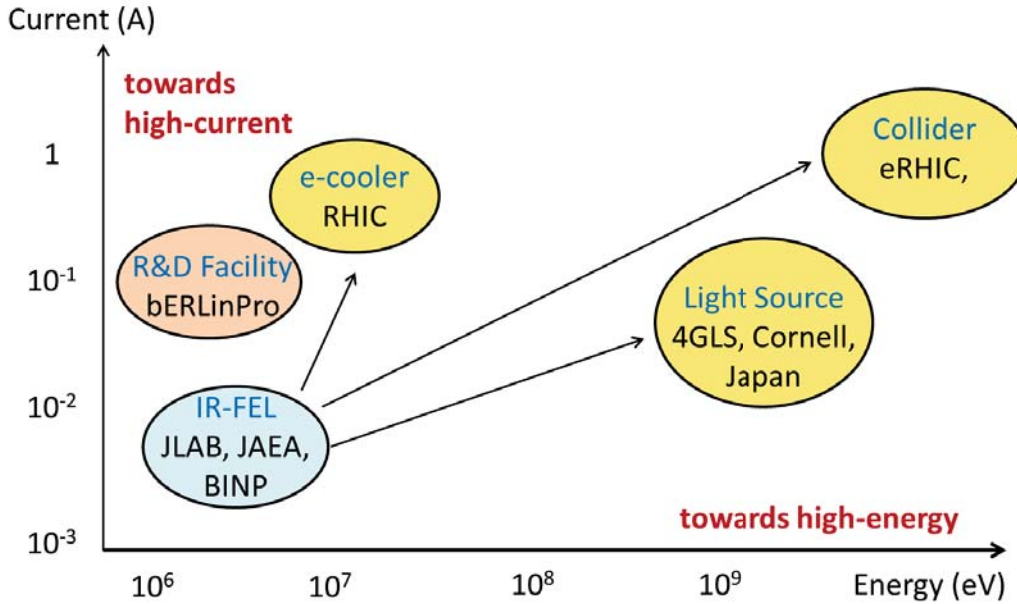


Figure 2.4: Current and future ERL projects [37].

bERLinPro including its electron beam injector which is currently built at Helmholtz-Zentrum Berlin, is the ERL accelerator facility that lies at the heart of the investigation in this thesis.

## 2.4 bERLinPro

bERLinPro (Berlin Energy Recovery Linac Project) at Helmholtz-Zentrum Berlin is currently under construction [8]. The facility will serve as a technology demonstrator for high brightness, high average current beam operations. Furthermore, the accelerator offers research and development opportunities. Following the target parameters, a subsequent application as a light source is feasible. Table 2.1 summarizes the bERLinPro target parameters.

The task for bERLinPro is to demonstrate a successful generation, acceleration, and energy recovery of a high brightness electron beam. Figure 2.5 illustrates the planned setup.

Table 2.1: Main bERLinPro parameters suitable for future X-ray light source applications

Parameter	Range	Unit
Beam energy	50	MeV
Maximum average current	100	mA
Bunch charge	77	pC
Repetition rate	1.3	GHz
Transverse normalized emittance	$\leq 1$	$\pi$ mm mrad
Bunch length ( <i>rms</i> )	$\leq 2$	ps
Maximum losses (relative)	$< 10^{-5}$	

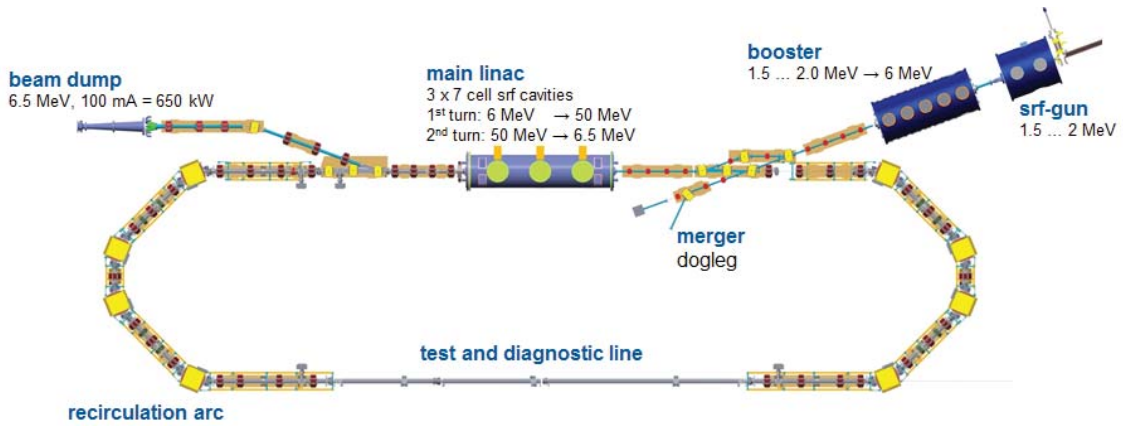


Figure 2.5: The setup of the energy recovery linac test facility bERLinPro at Helmholtz-Zentrum Berlin [Courtesy FG-IA, HZB.].

The electron bunches are generated in a superconducting RF photoinjector with a repetition rate of 1.3 GHz. Accelerated to 2.3 MeV in the electron source the beam is guided through a booster section of three 2-cell cavities. The booster offers further energy gain and bunch compression. The 6.5 MeV beam is then merged to the main ring. The 7-cell linac accelerates the electron beam to 50 MeV. The arcs in the racetrack structure consist of four dipoles per arc that lead to an 180 deg beam path turn per arc. Quadrupole sections in each arc are necessary to suppress dispersion and to adjust the Twiss parameters. Higher order multi-poles (sextupoles) counteract non-linear beam effects, like the impact of the space charge or the RF curvature. Opposite to the linac cavities behind the first arc, free space is kept open for future experiment setups like an undulator for radiation generation. After one turn the energy is recovered and the electron beam is dumped at 6.5 MeV. Crucial parameters of the high brightness beam are represented in the transverse emittance  $\varepsilon_{x,y}$ , the bunch

length  $\sigma_z$  and the average current  $I_{\text{avg}}$ . A high beam brightness requires a transverse emittance value lower than 1 mm mrad. The smallest bunch length of 2 ps is achieved after several bunch compression steps in the injection line (gun and booster) and the first arc in the ring. The objective is to reach an average current of 100 mA [38]. The commissioning of bERLinPro is scheduled for 2020.

If an ERL drives a FEL, the EUV and X-ray lithography technique renders the investigation of the deeper layers of a user sample possible. In order to analyze the surface structure or thin samples, a complementary method to the ERL operated FEL beam with adequate properties of the probe beam is the desired approach. Ultrafast electron diffraction (UED), based on an electron beam as a probe beam, offers a compact alternative with small penetration depths depending on the beam energy. UED enables time-resolved, high-resolution diffraction experiments. An electron beam with a moderate energy can operate UED experiments using parts of the ERL infrastructure, the electron gun and the injection line.

## 2.5 Ultrafast Electron Diffraction

In addition to operating future accelerators, high brightness electron beams can also be applied in user experiments in a low energy regime. In that case, the beam is generated in an electron gun, which equals the gun used for an ERL, and is manipulated to fit the user requirements. The beam is guided directly to the experiment. The beam energy determines the penetration depth to the sample. In order to analyze deeper layers, the electron gun is supplemented with a booster section of the ERL injection line for further beam acceleration. For these reasons, UED represents an innovative application of an SRF photoinjector and the ERL injection line that goes beyond their use for operating accelerators.

There is a growing interest in material sciences, biology and chemistry to analyze not only the static structure, but also the structural dynamics of different materials on an atomic level. Electron pulses are complementary to X-ray pulses as they provide larger scattering cross sections in the matter for comparable wavelengths. Another advantage of electrons over X-rays is that electrons deposit a lower energy into the user target [39].

The structure of a sample can be resolved with static electron diffraction. If an electron beam hits a sample, it is diffracted. The diffraction patterns detected by a high sensitivity camera resolve the structure of the sample in the regime of the transverse electron beam size. The diffraction studies enable the resolution of the structural dynamics and the static structure of a sample. UED is typically carried out as a pump-probe experiment [40]. The electron probe beam hits the sample after a fs laser pulse (pump beam) excited the latter. This process is illustrated in Figure 2.6. The diffraction patterns give information about the structure of the sample as a function of the pump-probe delay time. The beam quality at the sample defines the temporal and spatial resolution, and therefore the quality of the diffraction pattern.

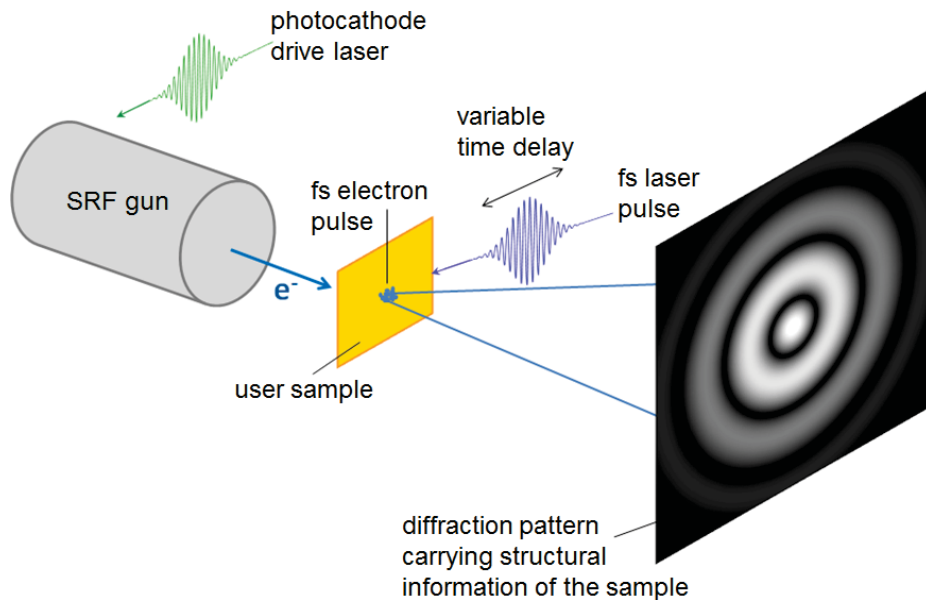


Figure 2.6: The setup of an ultrafast electron diffraction experiment [41].

There are challenging requirements for the beam that should hit the sample, including the electron bunches being relativistic, compact ( $\mu\text{m}$  spot size), and additionally ultra-short (fs regime) with high repetition rates (up to MHz) [42]. These requirements can be met with a high brightness electron beam and a strong focus on a short bunch length to receive a sufficient time resolution. Optimizing the electron gun and the injection line for high brightness operation is necessary to prepare and improve the beam properties for a UED experiment. Bunch compression techniques and their impact on the electron beam dynamics must be considered in the optimization procedure.

## 2. Application of a High Brightness Electron Beam - Diffraction Limited Light Sources and User Experiments

---

Several accelerator facilities and beam applications introduced in this chapter, are based on a linac structure (FEL, ERL, UED). In that case, the electron beam brightness is determined at the electron source which, therefore, plays an outstanding role in the whole setup. The following chapter provides an overview of current electron injectors and motivates the use of an SRF photoinjector as an appropriate choice to generate a high brightness electron beam.

# Chapter 3

## Electron Injectors

### 3.1 Overview of Current Electron Injectors

The particle injector represents one of the most important parts of an accelerator. The beam is generated in the electron source and accelerated to nearly relativistic energies in the gun. In contrast to storage rings, where the electron beam quality is the result of damping and excitation processes, and the properties of the magnetic lattice, the limits of the beam quality in linear accelerators are determined in the injector. Therefore, the injector plays an outstanding role in linear accelerators and ERLs. The output beam of the injector has to fulfill the requirements of the accelerator, defined by the beam application.

Different forms of injectors can be used for electron generation depending on the experiment for which the beam is generated. An electron injector always consists of four parts: a cathode that emits the electrons, an accelerating structure, an ultra-high vacuum and an element which focuses the generated beam for many different applications.

A cathode provides the electrons for the accelerator. There are different ways to force these electrons to overcome the potential barrier of the cathode material and to escape to the vacuum outside the cathode surface.

Electrons can be extracted from the cathode material adding extra energy to the conduction band electrons. Using the process of thermionic emission, the electrons receive additional energy by heating a filament with an electric current, while photoemission takes advantage of the photoelectric effect [see Fig. 3.1]. During the latter process, incoming photons provide their energy to the electrons in the conduction band.

As an alternative, electron emission can be triggered by manipulating the potential barrier. In the field emission process, a high electrostatic field ( $\approx 1 \text{ GV/m}$ ) is applied to a metallic cathode [43]. The external electric field reduces the potential barrier with the result that the electrons show a probability of presence outside the solid. The field emission process represents a quantum mechanical effect as the electrons are tunneling through the wall [see Fig. 3.1] [44].

The released electrons must rapidly be accelerated to higher velocities to control the acting space charge forces that are due to Coulomb repulsion. Furthermore, the immediate acceleration enables the emission of further bunches out of the cathode. DC or RF fields can be used for acceleration. Electron sources with DC accelerating gaps can provide a continuous or a pulsed beam with the possibility to modulate the amplitudes and frequencies of the accelerating voltage. The repetition rate is limited by the subsequent RF based acceleration section in the forward part of the facility.

In addition, an RF field coupled to a cavity can be used for first electron bunch acceleration [see Fig. 3.2]. Normal-conducting RF type guns operate in a pulsed mode with frequencies of hundreds of MHz to GHz regime, bunch repetition rates of Hz to 1 MHz, and high bunch charges up to nC [46]. The use of superconducting cavities further allows a cw mode, in which electron bunches fill every RF bucket. Frequencies of hundreds of MHz to GHz can be reached with a maximum bunch charge of hundreds of pC [47].

The operation of cavities requires ultra-high vacuum, and in case of superconducting acceleration elements, particle-freeness is mandatory. Then, electron-gas scattering in the gun and inside the following beam pipe is avoided. Some components, like the high-sensitivity photocathode or an RF cavity, require ultra-high vacuum with a pressure of  $10^{-9} \dots 10^{-11} \text{ mbar}$  [48].

Finally, focusing lenses need to be installed in each electron source to match the beam size to the subsequent acceleration section. A diverging electron bunch can be refocused with a radial field as from electrostatic or magnetic electron lenses.

The electron injector setup can in principle consist of a combination of all the possibilities each component has. The choice of a suitable particle source depends on the requirements for the electron beam. The primary beam properties for the two



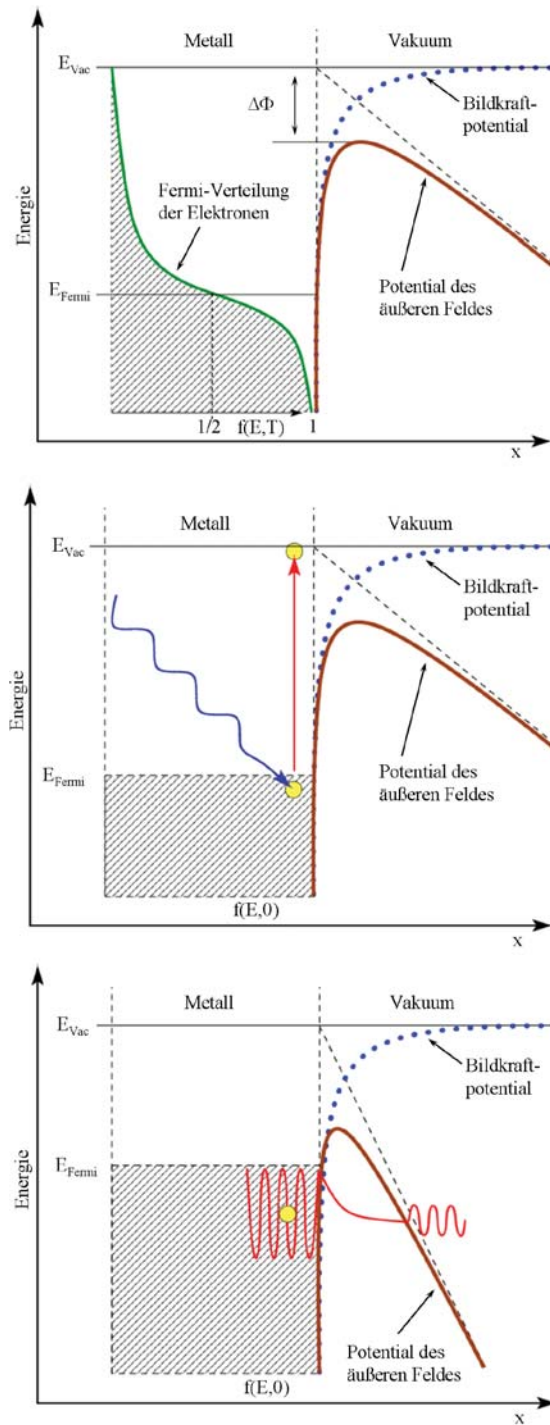


Figure 3.1: The illustration of thermionic, photo- and field emission of electrons. The Fermi-level is modulated by heating the filament in the process of thermionic emission (a). Photoemission is triggered by external photons (b). In the field emission process, the potential barrier is lowered by an external electric field that allows the electrons to tunnel through the wall (c) [45].

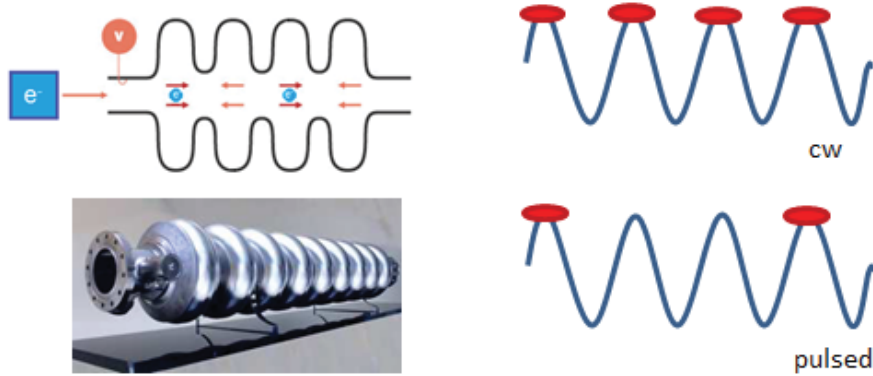


Figure 3.2: Accelerating structure using an RF field. The cavity can be operated in a pulsed and cw mode [Courtesy FG-ISRF, HZB.].

presented applications, FEL and UED, are summarized in Table 3.1.

Table 3.1: Electron beam properties for an FEL and a UED application

	FEL [22, 49]	UED [42]
Bunch charge	$\leq 1$ nC	$\leq 500$ fC
Transverse emittance	$\leq 1$ mm mrad	$\leq 500$ nm rad
Bunch length	$\leq 100$ fs	$\leq 100$ fs
Energy	several GeV	few MeV
Rel. energy spread	$10^{-4}$	$10^{-4}$

Both applications require a high-intensity beam, well-focused in the transverse plane and an ultra-short bunch length. For that reason, the electron injector must generate high brightness beams. An SRF photoinjector is able to fulfill the targeted properties. The decision to choose a photoemission high quantum efficiency cathode as the electron source together with an SRF cavity for acceleration and a transversely focusing solenoid magnet is reasoned as follows:

In order to maximize the beam brightness, small transverse emittance values must be achieved. Photoemission guns that are based on a high quantum efficiency photocathode are able to generate an electron beam with a transverse emittance smaller than 1 mm mrad. Figure 3.3 shows the strong trend towards low emittance photoinjectors that has occurred in the last years and their great advantage concerning the transverse, normalized emittance compared to thermionic guns [50]. Furthermore, an optical system drives the cathode in photoemission injectors. This laser system allows control over the transverse and longitudinal electron beam properties right after

emission by adjusting the laser parameters. Therefore, the laser settings represent a powerful control knob for the electron beam optimization. Lastly, the potential of photoinjectors to generate a polarized beam with a GaAs cathode is highly interesting for some accelerator users in the material sciences or in future projects, such as  $e^-e^+$ -colliders [51].

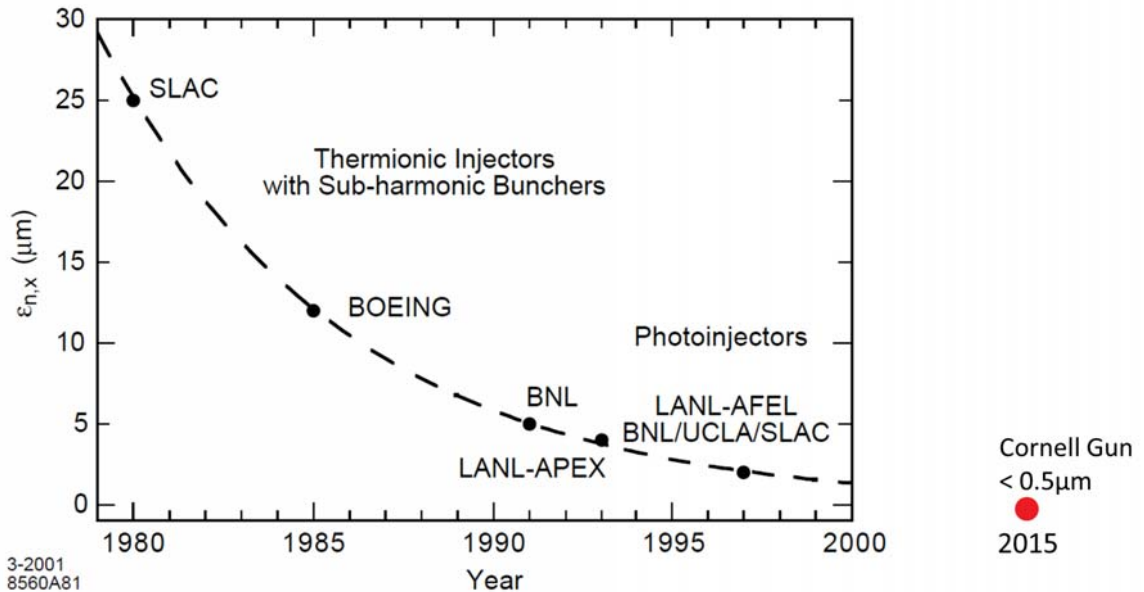


Figure 3.3: Trend from thermionic injectors to photoinjectors over the last 40 years with the goal to minimize the transverse emittance [50].

Using an SRF photoinjector, an RF cavity accelerates the electron beam. RF injectors provide high field gradients for beam acceleration while preserving the beam quality. Radial RF fields, as well as the momentum chirping during acceleration, can even be used to improve the transverse and longitudinal beam parameters. RF accelerating structures, however, pose new challenges, such as inserting high RF fields into the cavity (high klystron power requirements), higher order modes, unwanted field emission, and tuning/field flatness. Nevertheless, the significant advantage of implementing cavities that are made of a superconducting material, makes RF acceleration rather than DC acceleration interesting for the future, since SRF cavities allow a cw (continuous wave) operation with a 100% duty cycle. This mode enables the acceleration of the electron beam with highest fields aiming for lowest transverse emittance values. SRF cavities will be discussed in detail in Section 3.2.

The beam is focused electrostatically as well as magnetically. In the SRF gun, a solenoid is placed right at the cavity exit to suppress aberration effects as early as possible and to focus the beam within the transverse plane. Electrostatic focusing is used more indirectly through a cathode retreat in the RF cavity or by a particular cavity design that leads to a radial electric field at the cavity exit.

All these effects turn the (S)RF photoinjector into a promising electron source for operating an accelerator in a high brightness mode. The following section analyzes the advantages and challenges of SRF cavities for SRF photoinjectors.

## 3.2 SRF Gun Cavities for Photoinjectors

The first SRF gun concept was proposed by Heinz Chaloupka from the University of Wuppertal in 1989 [52]. Due to their low surface resistance, SRF cavities can reach high gradients (several tens of MV/m) in cw mode with 100% duty cycle. Fig. 3.4 presents measurements of the quality factor  $Q$  for the cavity over the gun gradient for an SRF cavity at DESY Hamburg [53]. The quality factor  $Q$  is indirectly proportional to the cavity surface resistance [54]. Acceleration peak fields of up to 60 MV/m could be achieved (blue curve in Fig. 3.4). There is still R & D work required to maintain this high level of performance. Multipacting, field emission, and the resulting dark currents must be controlled. Moreover, to insert a coated photocathode with high quantum efficiency in the cavity back-plane without contaminating the sc cavity, and thus impacting its performance, poses a challenge. The  $Q$ -value of the cavity in the DESY test stand decreased by a factor of 0.6 at low gun gradients after a lead-coated Nb cathode was set in the back-plane of the cavity (green and red curve in Fig. 3.4 compared to blue curve without plug). The performance of the superconducting cavity significantly declined at higher peak fields in the gun cavity. Nevertheless, stable operation at 30 MV/m with a sufficient  $Q$ -value of  $10^9$  could be realized in this first study.

The design including the cavity shape and the number of cells strongly impacts the SRF cavity performance and, therefore, the electron beam quality. Basic research regarding the design conditions of superconducting cavities was mainly conducted for the TESLA project [55]. The number of cavity cells defines the achieved active acceleration. The currently mounted cavities in photoinjectors consist of 1.4 cells (HZB) and 3.5 cells (HZDR) respectively and they are made of the superconducting material Niobium. The number of full cells in the gun cavity design is matched to

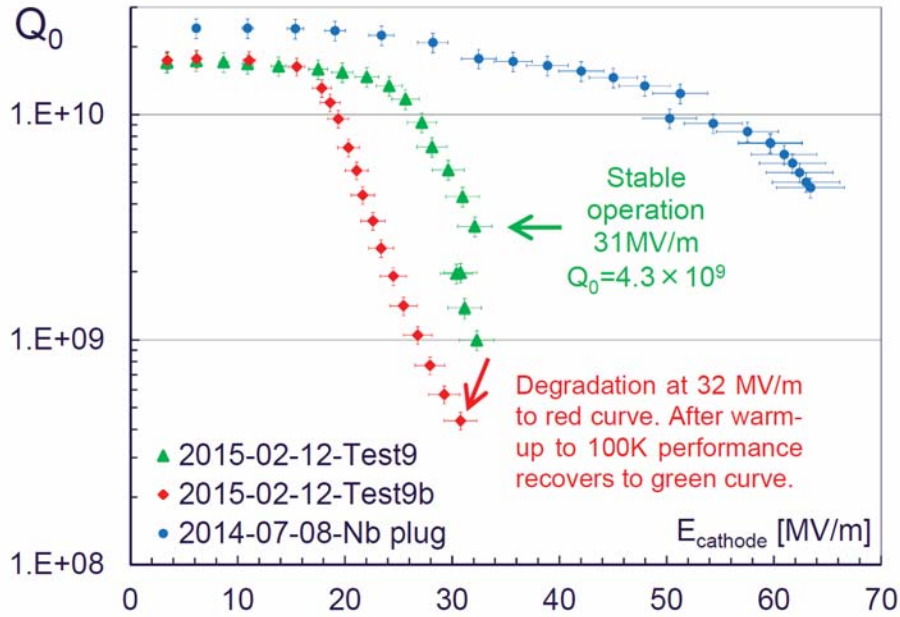


Figure 3.4: SRF gun cavity test in the cw mode at DESY Hamburg. The quality factor in the blue curve is measured with an uncoated Niobium plug. The green and red points represent a quality factor measurement with a lead-coated Niobium cathode plug [53].

the final energy that should be reached at the end of the photoinjector. Gun cavities with more than two full cells integrate a first booster section in the gun. The first cell has to be smaller than a full acceleration cell to achieve high field strengths on the cathode and to reach an optimum phase matching of the bunch. Beam dynamic studies indicate an improved beam quality if the half-cell is reduced from a length 0.5 to 0.4 [56].

The cell shape of the cavities is optimized to reduce such cavity effects as multipacting (spheric contour near the cavity equator) and wakefields (large iris radius). The expected particle velocity (depending on the implemented cavity gradient), the frequency and the required final energy define the cell length. The particle velocity and the time it takes to invert the field determine the iris length between the cells [57].

Since the SRF cavity design values impact each other and are linked with the number of cells in a complex way, an optimization that considers the cavity geometry parameters and the number of cells as decision variables can provide a significant influence on design choices and can help to improve the overall performance of the SRF photoinjector.

Superconducting gun cavities are part of the latest research. New superconducting materials beside Niobium that allowing a highly efficient cooling and a more economical operation, are under investigation at the moment. A significant progress to implement a stable cavity performance, to maximize the quality factor, and to overcome upcoming challenges is expected in the next years.

## 3.3 Photoinjectors

Figure 3.5 presents a sketch of an SRF photoinjector and its related subsystems. The particle source is based on the photoelectric effect.

The optical system of the drive laser generates the desired pulse structure. Afterwards, the generated laser beam illuminates a photocathode that emits electrons. The drive laser is mode-locked to the master oscillator, a timing and synchronization system, and therefore to the RF system which drives the gun cavity. The requirements on the drive laser include a stable operation, a low phase jitter, a well-synchronized frequency and a homogeneous intensity profile in the transverse plane. The transverse size and the pulse length of the laser, the transverse and longitudinal laser profile as well as the laser power constitute the main characterizing parameters of the laser pulse.

The photocathode is inserted in the back-plane of the first cavity cell. The cathode material and preparation quality determines the reliable operation and the amount of generated electrons. High-quality cathode preparation, transport, and operation pose a significant challenge in the photoinjector research. The ideal photocathode for a photoinjector that drives an accelerator offers a long-lasting life time with a nearly constant high efficiency in the injector. Moreover, a fast response is required when a laser pulse illuminates the photocathode and emits a desired uniform electron beam. The central photocathode parameters are the quantum efficiency of the cathode and its position in relation to the back-plane of the first cavity cell.

The SRF cavity is the central part of the gun. In order to accelerate an electron beam, an RF wave is required in the cavity. A klystron amplifies the RF signal. The RF power is then guided through a coaxial line or a waveguide to the cavity. Finally, an antenna couples the RF field into the cavity. The chosen electromagnetic field mode provides maximum acceleration by the electric field along the longitudinal

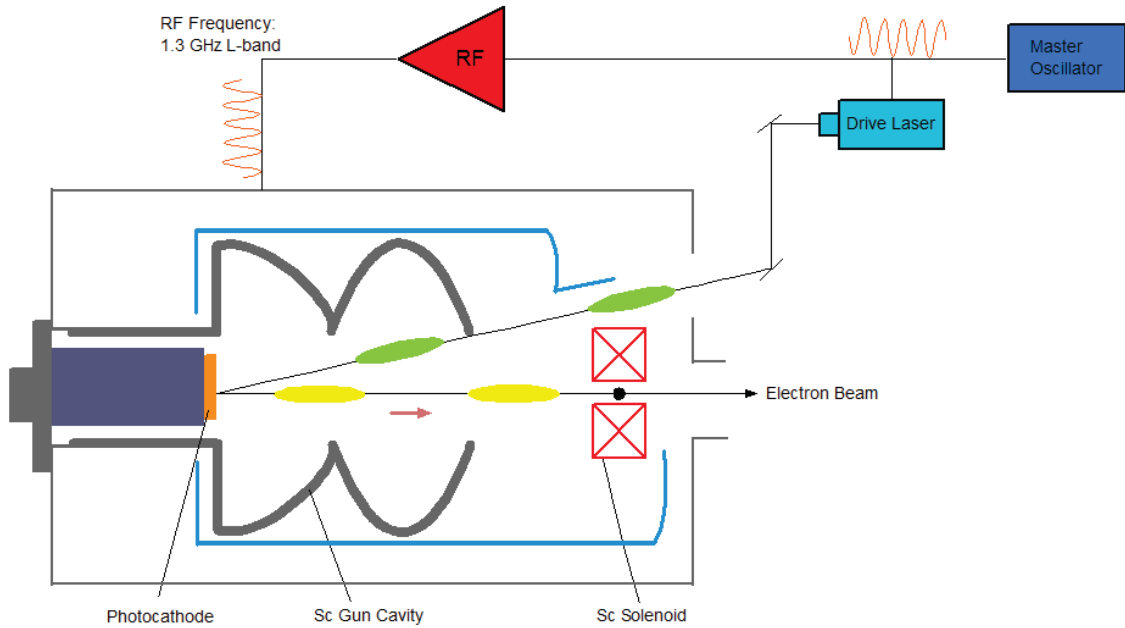


Figure 3.5: Sketch of an SRF photoinjector setup and its mode of operation based on the photoelectric effect.

cavity axis. The fundamental mode of the SRF cavities is set to 1.3 GHz to match the repetition rate of the following acceleration structures. 1.3 GHz represents a standard frequency in the SRF cavity operation. The reason using this particular frequency is that cost economics suggest a compact cavity design with corresponding high frequencies  $f$ . The frequency cannot be infinitely increased since the surface resistance grows with  $f^2$  and the wakefields are proportional to the second and third power of the frequency [57]. Consequently, the frequency is limited to 3 GHz. 1.5 GHz represents an optimum. The chosen frequency of 1.3 GHz can be explained with the commercial availability of high power klytrons. As summarized in Section 3.2, the cavity performance is mainly affected by the achievable peak field on axis, the phase relative to the field when the bunch is injected into the cavity, and the cavity shape design parameters.

The electron beam is defocused and transverse divergent at the gun exit due to space charge effects and high transverse RF fields in the gun cavity. In the case of normal-conducting cavities, a solenoid can be placed around the gun cavity to counteract these effects. However, placing the solenoid around the gun is impossible for SRF cavities since the superconductor shields the magnetic field once the sc cavity is



below its transition temperature (Meissner-effect) [58]. Therefore, a solenoid is placed behind the SRF gun to focus the beam and to further compensate the space charge emittance by slice alignment of the bunches. The position of the solenoid relative to the cavity exit as well as the magnetic field that defines the focusing strength of the solenoid, represent the central parameters of this beam path element.

A further beam focusing and an emittance minimization are caused by a recess of the cathode as well as a special cavity design that lead to transverse electric field components.

Emittance compensation and transverse focusing play an important role as soon as the beam is matched to a linac structure behind the gun. It is necessary to preserve the small emittance and beam size through further acceleration.

To summarize, many injector settings and design parameters dominate the performance of an SRF photoinjector. The resulting electron beam properties are the final product of these parameters and the complex interplay between all external and internal fields that act in the injector on the beam. As usual in physics, to understand the beam dynamics and the output beam, the SRF photoinjector is described by a model that needs adjusting and refinement. Such improvements can, on one hand, be based on a theoretical approach using simulation tools. On the other hand, improvements can result from measurements in an experimental setup using diagnostics. The motivation of this work is to verify and improve the understanding of SRF photoinjectors and to optimize the existing model which is presently mainly focused on simulation techniques. For that reason, a particle tracker and an optimizer are developed and implemented. The optimization program constitutes the central part of this dissertation. The results are discussed in detail in the Chapters 5 and 6. The following section introduces the SRF photoinjector test facility GunLab with its diagnostic line at HZB that serves to experimentally verify the model.

## 3.4 GunLab

GunLab is a test facility for the SRF photoinjector technology run by the HZB [59]. The developed and fully characterized injector will serve as the future electron source for the in-house energy recovery linac project bERLinPro [8].

The electron source development at HZB started in 2010 with Gun 0, a superconducting photoinjector. The second superconducting gun followed in 2017, Gun 1 [60, 61].



Figure 3.6 gives an overview of the current GunLab facility with Gun1. The cathode transfer system is mounted at the backside of the cryomodule. The transfer system is used to insert the normal-conducting photocathode into the back-plane of the gun cavity. All superconducting elements of the gun, the 1.4 cell accelerating cavity as well as the solenoid magnet, are mounted in the cryomodule which offers the complete cryo infrastructure including the insulation vacuum and liquid helium supply. The cryomodule also contains an input window for the laser beam that drives the photoemission process, a HOM absorber for damping the higher order modes in the gun cavity, as well as a steerer magnet for beam correction in the transverse plane. Since GunLab provides an SRF gun test facility, a diagnostic beamline is attached to the source analyzing the generated electron beam [62]. The results achieved by measurements in the diagnostic line are of great importance to understand and improve the photoinjector model.

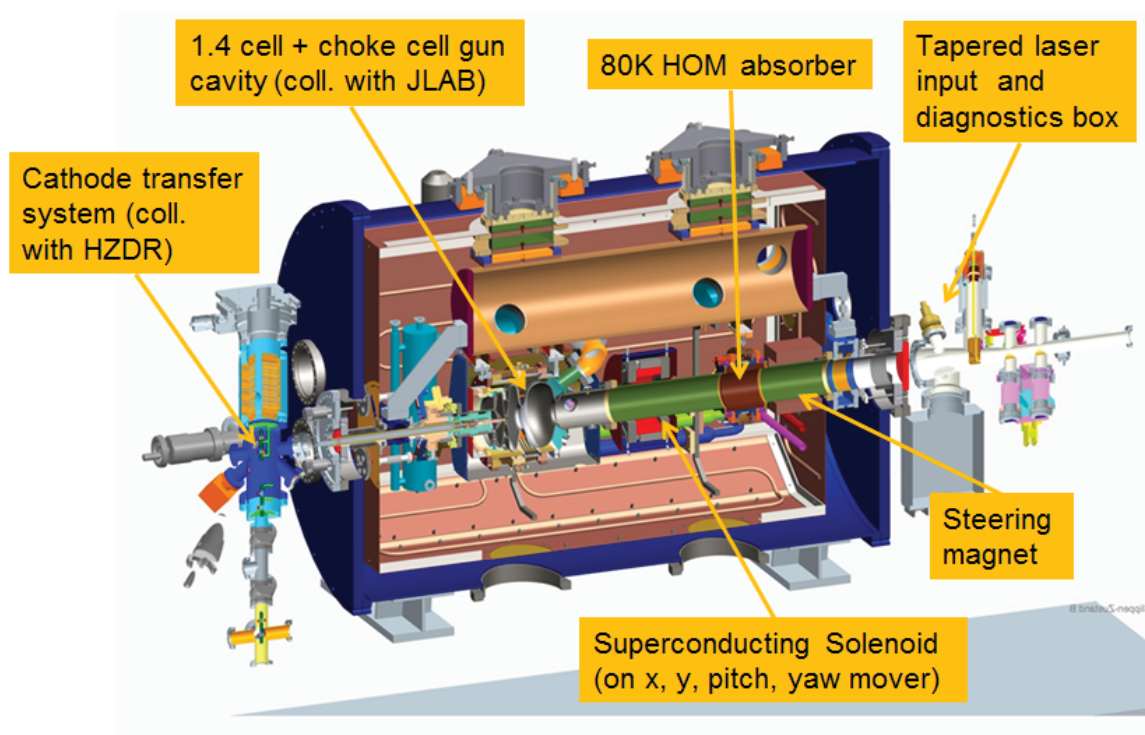


Figure 3.6: Setup of the current GunLab cryomodule including the 1.4 cell SRF cavity and the sc solenoid magnet. The transfer system is mounted outside to insert the photocathode to the cavity back-plane. The laser input window allows the laser beam to illuminate the photocathode in order to drive the photoelectric effect. A diagnostic beamline is attached at the cryomodule exit [see Fig. 3.11].

**Photocathode** research and development are among the leading research topics in the accelerator sector at HZB [48]. The work started with Gun0 in 2010 [63]. At that time, the photoinjector still had lead cathodes installed. The focus was to maximize the quantum efficiency QE as well as to study the impact of the cathode quality, such as the surface roughness has on the injector performance.

For the current GunLab run (Gun1) and the high average current mode of the bERLinPro project, the photocathode needs a quantum efficiency of at least 1%. Semiconductor cathodes provide the potential for achieving a high quantum efficiency and thus high bunch charges. Current research focuses on Molybdenum plugs coated with  $\text{CsK}_2\text{Sb}$  [64].

Meanwhile, a photocathode laboratory provides a preparation and analysis chamber [64]. Inside the preparation chamber, a substrate plug is coated with high QE material. Afterward the coating, the prepared cathodes are characterized in-situ in the analysis chamber due to their elemental composition, the initial transverse momentum of ejected test electrons, and their spectral response. The results of the last-mentioned measurement technique show a promising quantum efficiency of more than 10% for a  $\text{CsK}_2\text{Sb}$  cathode at green laser light (515 nm) prepared at HZB [see Fig. 3.7].

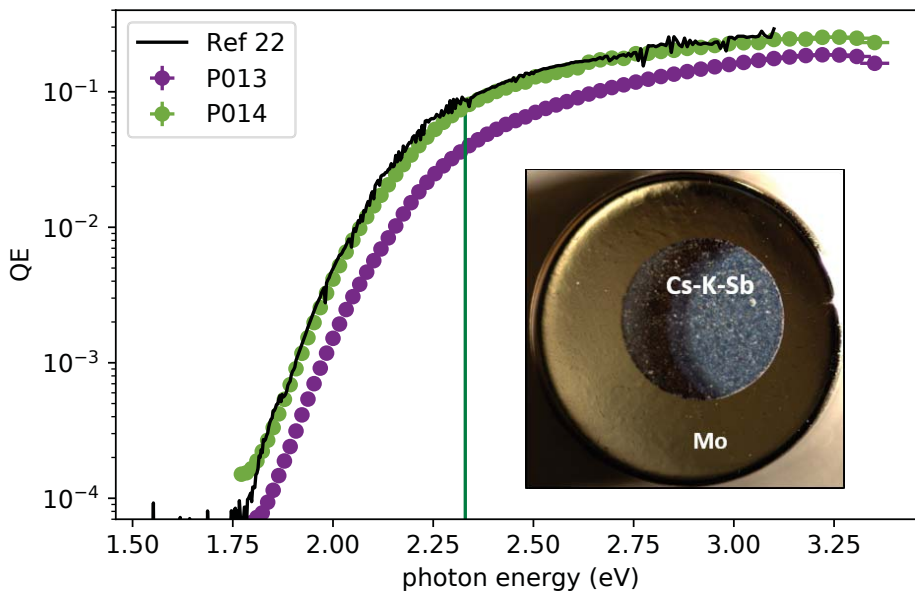


Figure 3.7: Spectral response measurements (green and magenta curves) of the photocathode coated in the in-house preparation chamber [Plot courtesy Martin Schmeisser, HZB]. The measurement data are compared with results from reference [65].

While the cathode quality as one of the characterizing parameters remains fixed during the preparation process and while it also must be preserved during transportation, the relative cathode position to the cavity back-plane is changeable. A manipulator helps to retreat the plug gradually in steps between 0 mm and 2.5 mm.

Figure 3.8 presents an overview of the Yb:YAG **drive laser** setup for the GunLab operation. The laser was designed and constructed in cooperation with the Max-Born-Institute in Berlin. The laser generates an IR laser beam. A wavelength converter enables the use of the 2nd and the 4th harmonic to drive either a semiconductor cathode (green laser light) or a metallic cathode (UV). Further, the pulse length can be continuously changed between 2 and 7 ps (*rms*) using a pulse stretcher (green). An imaging system along the beam path between laser hut and photocathode defines the final transverse size of the laser. The aperture enables spot sizes from 0.5 mm to 1.5 mm (*rms*) on the cathode. The current setup allows a gradual selection of the repetition rate between 120 Hz and 30 kHz, depending on the operation mode, which can be the commissioning, and the high average current mode in GunLab. The operation of bERLinPro at 1.3 GHz requires an adjustment of output power and repetition rate of the laser pulses that must always stay synchronized to the RF.

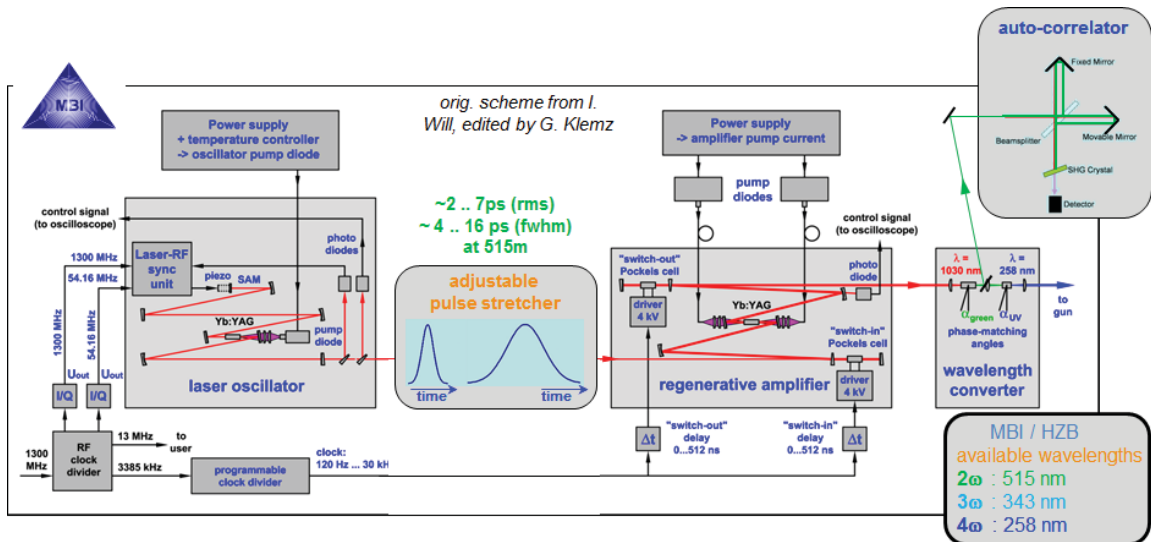


Figure 3.8: The setup scheme of the current photocathode drive laser for the GunLab operation [66].

A staged approach helped to improve the **cavity** design. Starting with a 1.6 cell cavity in a standard TESLA geometry for the first proof of principle in Gun 0 (2010) [60]. Afterwards, the design was optimized to a 1.4 cell Niobium cavity for an ERL mode in Gun 1. The commissioning of this second run in GunLab followed in winter 2017/2018 with the primary focus lying on the generation and acceleration of a high brightness electron beam from a high quantum efficiency cathode [61].

The maximum achievable peak field on the cavity axis represents an essential parameter in the optimization and improvement of the photoinjector model as the gun gradient impacts the beam dynamics significantly. Figure 3.9 shows the first test results in a horizontal test stand at HZB (Hobicat cryomodule) for the currently installed gun cavity. After several approaches, a peak field of up to 35 MV/m was achieved before the test run was terminated. The results exceed the bERLinPro specification point with a quality factor of  $5 \cdot 10^9$  and 2.5 MeV beam energy [61].

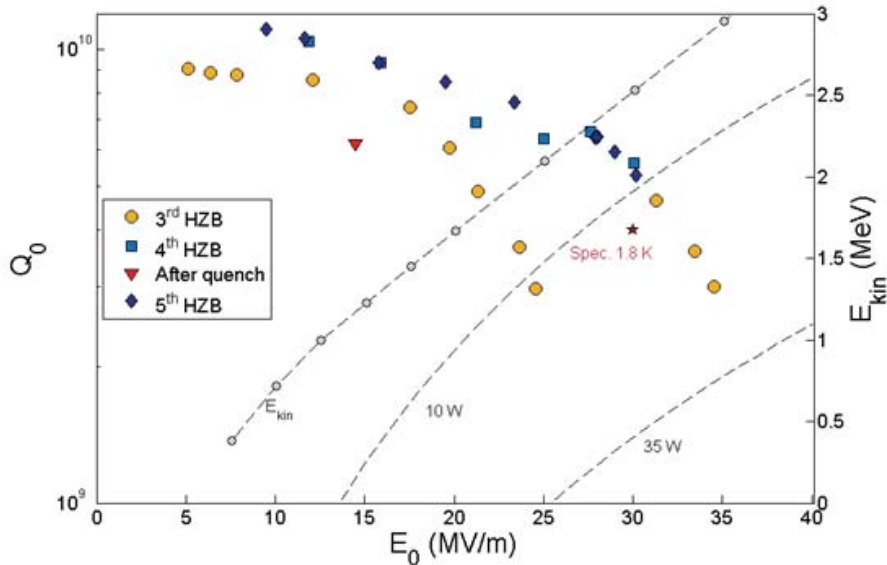


Figure 3.9: The cavity quality factor  $Q_0$  measured over the electric peak field which is coupled to the sc cavity. The accelerator requirements of 30 MV/m gun gradient and a dissipated power limit of 10 W result in the desired specification point for 1.8 K. In the third measurement run (yellow dots) a quality factor of nearly  $10^{10}$  was reached. At higher gradients, the  $Q_0$  factor drops due to field emission but can be improved after RF processing. High gradients without a decline due to field emission were observed in the next two runs (blue curves) [61].

Finally, a **solenoid** that focuses the beam in the transverse plane and compensates the transverse phase space, completes the photoinjector setup [62]. The magnet is made of a superconducting material in order to place the solenoid as close as possible to the cavity exit in the cryomodule. In order to align the solenoid axis to the beam axis, the solenoid is mounted on a motorized 3D moving frame [67]. After the first alignment for optimum bunch focusing, the transverse position remains fixed. During operation, small adjustments of the longitudinal solenoid position within the range of a few centimeters and its impact on the beam dynamics are of major interest. The current in the solenoid coils determines the magnetic strength that can be changed in a broad range from 0 mT to 500 mT. This magnetic field further represents an essential gun parameter with a substantial impact on the electron beam dynamics.

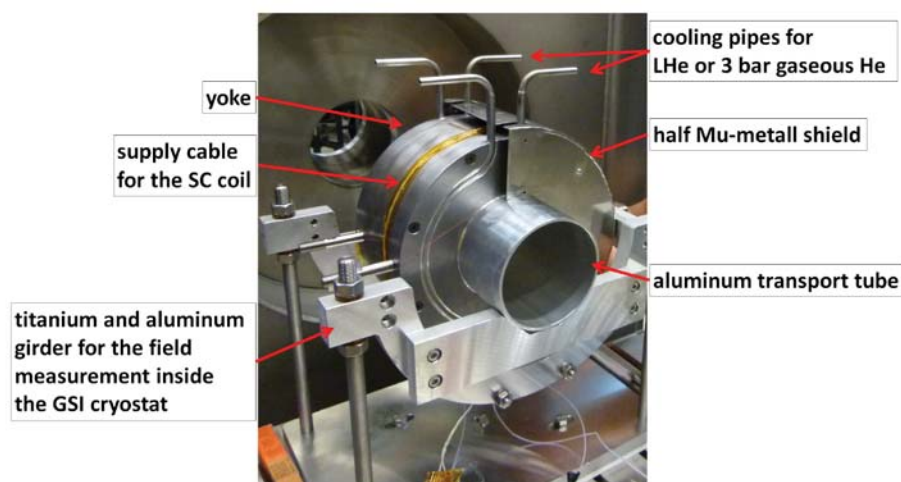


Figure 3.10: The GunLab solenoid prepared for field measurements at the GSI Darmstadt, Germany.

In order to experimentally understand the beam dynamics that act in the injector on the electron beam and to improve the SRF photoinjector model, the GunLab test facility is used for beam dynamic measurements. Therefore, a **diagnostic beamline** completes the beam path behind the cryomodule exit [see Fig. 3.11] [62]. The main beam parameters are evaluated at a reference point, that is 2.5 m downstream the cathode. GunLab represents the SRF photoinjector test facility for bERLinPro. The position of the reference point corresponds to a position right before the first bERLinPro booster cavity where the adherence of the beam specifications is unalterable for a high brightness operation of the following ERL facility. The reference point is also

used in the theoretical considerations of the SRF photoinjector model.

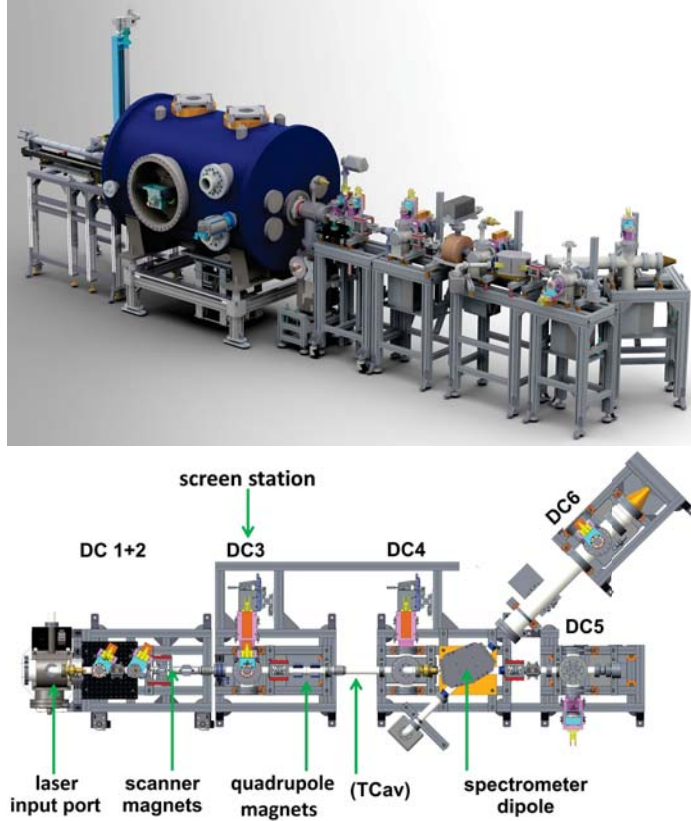


Figure 3.11: (a) top: The GunLab cryomodule with the attached diagnostic beam-line.

(b) bottom: The GunLab diagnostic beamline including a screen station with slit masks and a Faraday cup, free space for a transverse deflecting cavity and a spectrometer dipole [Courtesy FG-IA, HZB].

The beam parameters that must be controlled due to the requirements of the beam application, determine the diagnostic tools that are needed. Based on the desired high beam brightness as the primary goal for the electron beam properties at HZB, the transverse emittance and bunch length must be measured and controlled.

The slit-scan technique can reconstruct the transverse phase space [see setup illustrated in Fig. 3.12]. Therefore, two slit masks in horizontal and vertical direction are mounted on the screen station at the reference point. At this position, the measurement evaluates the two transverse emittances  $\epsilon_x$  and  $\epsilon_y$ . Two dipole magnets (or steerer magnets) in the diagnostic line move the beam over the selected slit. Only a small portion of the beam passes the slit while the rest is stopped by the tungsten



plate of the mask. The passing beamlet drifts to a viewscreen at a defined distance. Measuring the width and average position of the projected beamlet on the screen helps to reconstruct the transverse phase space at the reference point. At this position, the drift length between the slit mask and the viewscreen, the *rms* width and the position of the beamlet at the viewscreen define the initial transverse beam parameters of the beamlet (*rms* transverse width, divergence and correlation of these two parameters). The measurement procedure is repeated in a phase space scan that moves the beam over the slit mask for all beamlets  $i$  depending on their transverse offset  $x_i$ . The final transverse phase space distribution at the reference point is then reconstructed according to the projected widths and divergences of the beamlets at the viewscreen, the total number of beamlets, and their intensity.

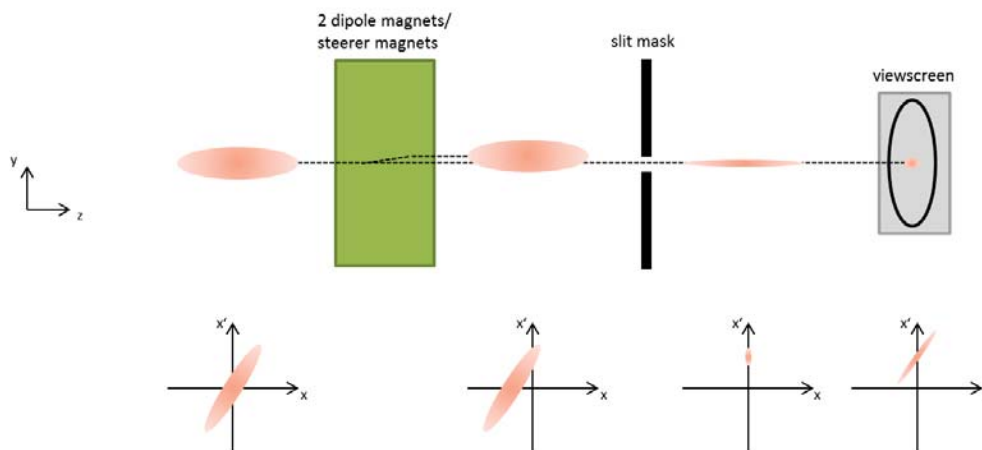


Figure 3.12: Setup of the transverse phase space scanner with steerer magnets, a slit mask at the screen station and a viewscreen. The evolution of the transverse phase space distribution along the  $z$ -axis is plotted below.

Moreover, several luminescence screens along the beam path, combined with a CCD camera as an optical readout, are mounted to display and control the transverse beam size at the different stages of beam propagation.

A transverse deflecting cavity (TCav) visualizes one part of the longitudinal phase space and allows for a measurement of the bunch length [68]. The setup and operation principle of the measurement station is displayed in Fig. 3.13. By shearing the bunch with a finite bunch length in the vertical direction, the initial longitudinal

bunch size is projected downstream the TCav on a screen as the vertical length of the imaged spot. The TCav works with a normal-conducting RF cavity. The RF field provides a repetition rate of 1.3 GHz. The transversely acting electric and magnetic field components of the selected  $TM_{110}$  dipole mode cause the bunch deflection. The RF field amplitude and RF phase define the vertical deflection angle of the beam. The RF phase is set to zero crossing, therefore, no deflection is induced to the bunch center. The sinusoidal field distribution of the RF signal deflects the head and the tail of the bunch in opposite directions. A viewscreen displays the vertically sheared bunch for an analysis of the longitudinal phase space. The beam size on the screen represents a convolution of the non-deflected beam size and the bunch length in front of the TCav. A TCav additionally enables slice emittance measurements and thereby significantly refines the beam diagnostics.

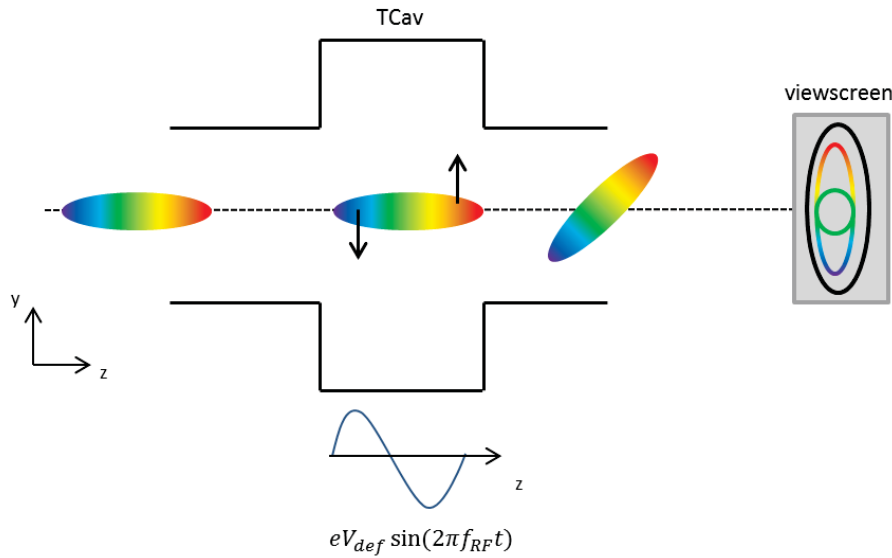


Figure 3.13: Operation principle of the transverse deflecting cavity (TCav). The longitudinal position in the bunch is sheared to a vertical position on the viewscreen due to a deflecting cavity field. The center of the bunch passes the TCav without deflection (zero crossing phase).

The beam brightness is also proportional to the beam current which is directly measurable through putting a Faraday cup in the beamline. The Faraday cup consists of a copper block with a bore and is placed on a screen station at 2.5m behind the cathode, which can vertically move into and out of the beam path. The incoming electrons are held inside the cup and the charge flows through an ampere-meter to



the ground. The ampere-meter measures the total current.

A Faraday cup also gives information about the unwanted dark current which still flows even when the photocathode drive laser is switched off. Dark currents affect beam dynamics, and therefore the sources of dark currents and their current strength are essential for the SRF photoinjector model.

The full characterization of the 6D phase space and the understanding of its evolution along the beam path greatly advances the beam dynamics studies. Therefore, momentum and momentum spread measurements are required using a spectrometer dipole that completely visualizes the longitudinal phase space together with the TCav [see spectrometer dipole and dispersive section in Fig. 3.11]. The spectrometer dipole was designed in collaboration with the Moscow State University [69]. The aim was to gain maximum kinetic electron energy of up to 10 MeV. For that reason, the primary focus of the dipole lies on reaching maximum sensitivity of the magnet on the electron momentum and on keeping the impact of the initial transverse emittance on the result as small as possible. The deflecting magnet bends the electrons into the dispersive section according to their momentum in the range of around 45 deg. The final width of the imaged spot on the viewscreen in the dispersive section is solely defined by the initial beam width and the bunch momentum spread. Together with the known transfer matrix elements (drift space, dipole edge, and bend magnet), the momentum spread can be calculated from the measured beam width at the reference point and the width on the viewscreen behind the spectrometer dipole.

For the momentum measurement, a control box calibrates the spectrometer field by measuring the field strength with a Hall probe. Afterwards, the momentum of a virtual electron is calculated based on the assumption that it crosses the magnet on an idealized path and hits the viewscreen center in the dispersive section.

Furthermore, additional beam diagnostic devices are required to ensure that the conditions for the electron beam in the real photoinjector are close to the assumed model. To verify that the electron beam propagates through the injector on the same beam path assumed in the model (on the  $z$ -axis without beam offset), a beam position monitor (BPM) together with beam-based alignment is implemented. Working as a non-destructive device, a BPM delivers the center-of-mass of the beam. The electromagnetic field of the beam induces a charge in an insulated metal plate [see Fig. 3.14]. For a bunched beam, an alternating current signal is detectable. This method is used to determine the beam position by cross-mounting four plates (pick-

ups) around the beam pipe. The center-of-mass position is then calculated from the difference in the signal strength [70].

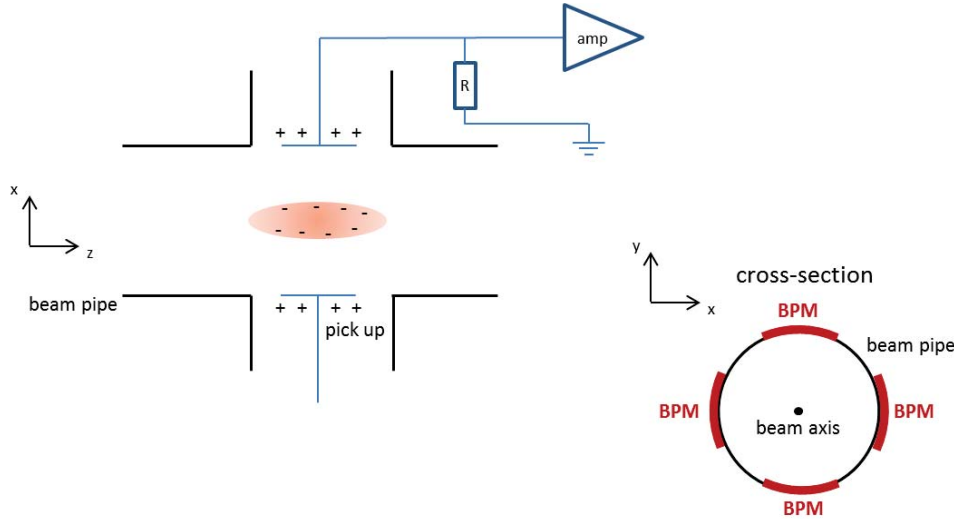


Figure 3.14: Beam position monitor (BPM) in the vertical direction. In order to determine the beam position, four pick ups are cross-mounted around the beam pipe.

To guarantee a beam propagation without a transverse offset, the magnetic center of the solenoid is correlated with the BPM. This procedure is called beam-based alignment [71]. If a perturbation of the magnetic current results in a shift of the beam path, it implies that the beam crosses the magnet with an initial offset. The BPM detects any shift of the beam. The beam is aligned through the solenoid of the SRF photoinjector and the following BPM in the diagnostic beamline by correcting the beam position with a steerer magnet until no beam shifts that are due to magnetic field changes can be observed.

All diagnostic and measurement systems are designed and optimized for the specifications of a high brightness mode with a high bunch charge up to 200 pC at repetition rates smaller than 10 kHz, with energies up to 3.5 MeV and electron bunch lengths smaller than 6 ps.

Apart from the GunLab test facility with its diagnostic beam line, a simulation and optimization technique is implemented at HZB to better understand and operate the SRF photoinjector. In order to operate and optimize an SRF photoinjector with maximum performance in a high brightness mode, the beam dynamics in the electron

injector must be fully understood at any step of the beam emission, first acceleration, and beam manipulation processes. In addition, the limits of the high brightness beam generation need to be found, as well as a strategy as to how these limits can be reached in any SRF gun. The following chapter discusses transverse and longitudinal beam dynamics in an SRF photoinjector considering space charge effects. A further section outlines the theoretical performance limits of an SRF gun. The crucial parameters that determine the performance limits of an SRF photoinjector are introduced, as well.



# Chapter 4

## Theory of the Transverse and Longitudinal Beam Dynamics

### 4.1 Characteristics of an Electron Beam

An SRF photoinjector provides complex beam dynamics as different components in the beam path, such as the cathode, the cavity, the solenoid magnet and space charge effects contribute to and act on the beam.

In order to analyze the beam dynamics and limits of an SRF photoinjector, some basic definitions and parameters in the accelerator phase space must be determined. This section presents different figures of merit which characterize an electron beam.

For theoretical considerations, it is assumed that the electron beam travels in the  $z$ -direction. The beam consists of many ensembles of particles so called bunches. In the context of beam dynamics, a bunch is usually described in accordance with the Cartesian system, with the coordinates  $x$ ,  $y$ ,  $z$  describing the space and the momenta  $p_x$ ,  $p_y$ ,  $p_z$  at a specific instant of time  $t$ . While  $x$  and  $y$  span the transverse phase space, the  $z$ -coordinate specifies the direction of the beam propagation. The ensemble of all bunches is defined as a beam if the longitudinal momentum component is much larger than the transverse momentum components ( $p_x \ll p_z$  and  $p_y \ll p_z$ ). A bunch, furthermore is characterized by the bunch charge  $q_b$  which is given by the number of electrons  $N_e$  in the ensemble together with the elementary electron charge  $e$ :

$$q_b = N_e \cdot e. \tag{4.1}$$

In addition, it is helpful to define one reference particle in the bunch. Starting at  $z=0$  at the cathode it has neither an initial transverse offset ( $x=0, y=0$ ) from the  $z$ -axis nor a transverse momentum ( $p_x=0, p_y=0$ ). The reference particle moves with the longitudinal momentum  $p_z$  in the  $z$ -direction. The position of all remaining electrons in the bunch is then set relative to the reference particle.

The parameters  $x, p_x, y, p_y, \zeta, \Delta p_z$  span the six-dimensional phase space, where  $x_j$  and  $y_j$  show the transverse offsets of any particle  $j$  from the  $z$ -axis which refers to the moving reference particle [see Fig. 4.1].  $p_{x_j}$  and  $p_{y_j}$  describe the transverse momenta of the particle  $j$ .  $\zeta_j$  displays the longitudinal distance to the reference particle at position  $z$  inside the bunch, while the absolute momentum difference to the longitudinal momentum of the reference particle, is given by  $\Delta p_{z_j}$ .

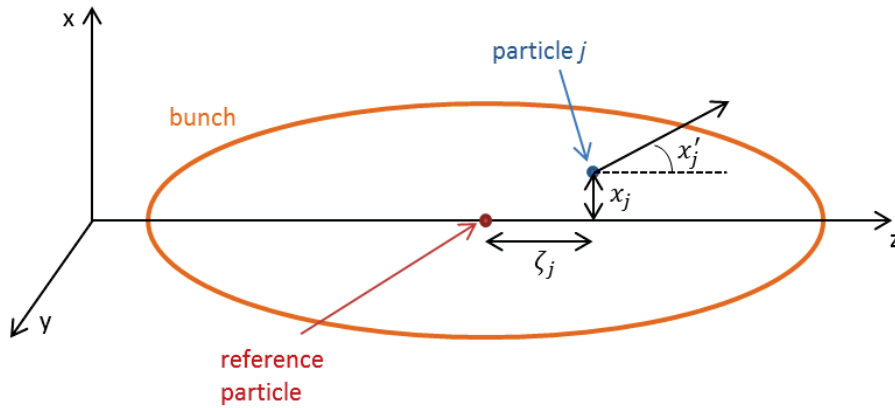


Figure 4.1: Bunch phase space with the reference particle at  $x_0=0, y_0=0, \zeta_0=0$ . Particle  $j$  in the bunch is defined by its transverse offset (displayed as the horizontal offset  $x_j$ ), its slope relative to the beam axis  $x'_j = dp_x/dp_z$  and its longitudinal distance to the reference particle  $\zeta_j$ .

The six-dimensional phase space is dividable into three subspaces in the horizontal ( $x$ ), vertical ( $y$ ) and longitudinal ( $z$ ) plane. In the following section, all subspaces are assumed to be uncorrelated with each other in order to discuss them separately.

With regard to the characterization of the transverse phase space of the bunch, the horizontal and vertical phase space are treated analogously. All beam parameters are given in *rms* quantities. The *rms* width of the bunch is then defined as

$$\sigma_x^2(z) = \langle x^2 \rangle - \langle x_0 \rangle^2 = \frac{1}{N_e} \sum_j (x_j - x_0)^2 \quad (4.2)$$

based on the second moment of the projected distribution [11]. The horizontal *rms* width  $\langle x^2 \rangle - \langle x_0 \rangle^2$  (with the average value given by the reference particle at  $x_0=0$ ) together with the vertical *rms* width  $\langle y^2 \rangle - \langle y_0 \rangle^2$  (with  $y_0=0$ ) characterize the transverse beam size.

The quantity  $x'_j = dp_x/dp_z$  describes the angle of the trajectory that is followed by particle  $j$  relative to the beam axis defined by the reference particle. The whole *rms* beam divergence is then represented in Equ. (4.3) [11]:

$$\sigma_{x'}^2(z) = \langle x'^2 \rangle - \langle x'_0 \rangle^2 = \frac{1}{N_e} \sum_j (x'_j - x'_0)^2. \quad (4.3)$$

Using these *rms* parameters with already subtracted average values given by the reference particle at the bunch center ( $x_0=0, x'_0=0, y_0=0, y'_0=0$ ), the phase space area in the horizontal plane of the whole particle ensemble can be determined. In general, the emittance represents the two-dimensional projected area of the six-dimensional phase space. This parameter can be used to evaluate the beam quality in the corresponding phase space. The transverse emittance is defined by the second moments of the particle distribution  $\langle x^2 \rangle, \langle x'^2 \rangle$  and  $\langle xx' \rangle$  [11]:

$$\varepsilon_{\text{norm.,x,y}} \equiv \beta\gamma \sqrt{\langle x^2 \rangle \langle x'^2 \rangle - \langle xx' \rangle^2} = \frac{1}{mc} \sqrt{\langle x^2 \rangle \langle p_x^2 \rangle - \langle xp_x \rangle^2} \quad (4.4)$$

If the transverse beam size of the bunch is small and its particles move nearly parallel to the  $z$ -axis with little transverse divergence and a low transverse momentum, the transverse emittance remains equally small. A small emittance, in turn, results in a good transverse beam quality. The last term  $\langle xx' \rangle$  represents the correlation between beam size and divergence which only equals zero at the waist of a uniform beam. A converging as well as a diverging bunch always contribute to the beam emittance.

The emittance is related to the elliptical area occupied by the particles in the  $x$ - $x'$ -space. It can be illustrated as the  $1$ - $\sigma$ -envelope of the projected particle distribution in the plane [see Fig. 4.2].

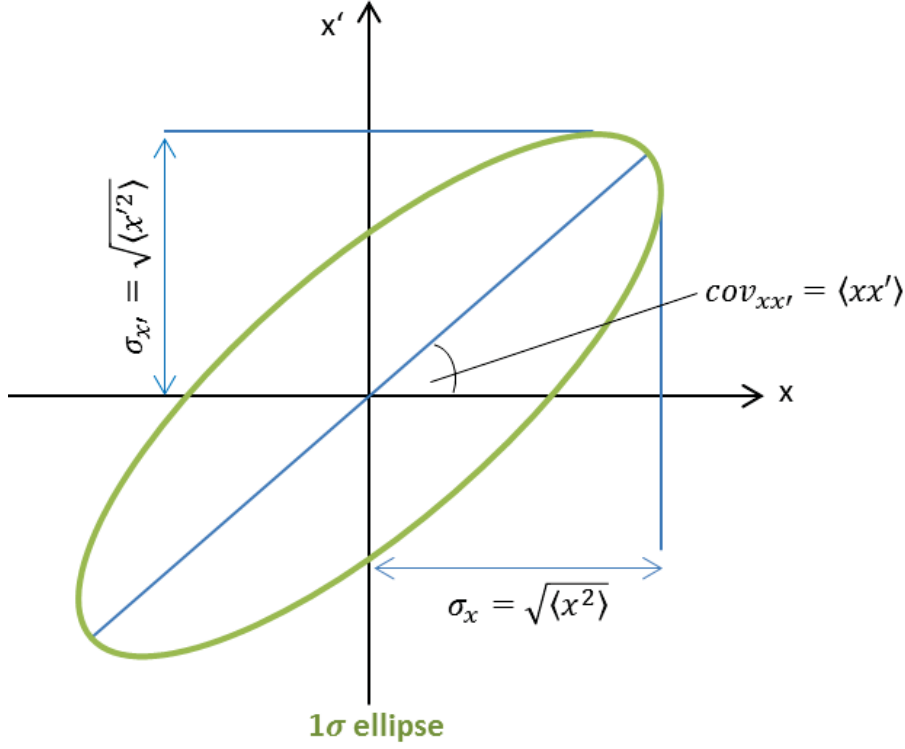


Figure 4.2: The  $1\text{-}\sigma$ -envelope of the transverse projected particle distribution. The *rms* beam size  $\sigma_x$ , the *rms* divergence  $\sigma_{x'}$  and the correlation between these two parameters  $cov_{x,x'}$  are illustrated.

The longitudinal phase space is characterized by the bunch length and the momentum spread. The second moment of the distances from the particles to the reference particle  $\zeta_j$  defines the *rms* bunch length

$$\sigma_z^2(z) = \langle \zeta^2 \rangle = \frac{1}{\beta c N_e} \sum_j \zeta_j^2. \quad (4.5)$$

The bunch momentum spread  $\Delta p_z$  is set by the momentum difference of the individual particles in the ensemble to the reference particle. The reference particle determines the kinetic energy of the bunch

$$E_{\text{kin}} = c \cdot p_z. \quad (4.6)$$

The bunch length  $\zeta$  and the absolute momentum spread  $\Delta p_z$  result in the longi-



itudinal emittance  $\varepsilon_z$  [11]. Analog to the transverse emittance, the two-dimensional projected area in the longitudinal phase space is given by

$$\varepsilon_z \equiv \beta\gamma\sqrt{\langle(\Delta p_z)^2\rangle\langle(\zeta)^2\rangle - \langle\Delta p_z\zeta\rangle^2}. \quad (4.7)$$

The parameter “normalized emittance” is introduced as an energy invariant to compare bunches of different energies along the accelerator beam line. The divergence  $\langle x' \rangle$  decreases during acceleration (adiabatic dumping) [72]. Consequently, the unnormalized (geometric) emittance varies along the beam path in the accelerator. Multiplying the geometric emittance value with the average longitudinal momentum  $\langle p_z \rangle$  leads to a constant normalized emittance during the beam acceleration when  $\langle p_z \rangle$  varies.

In order to discuss the beam dynamics in the following sections, the bunch slice model must also be introduced. The transverse emittance of a single bunch is normally shown as the projected emittance of the whole bunch [see Equ. (4.4)]. The projected emittance represents the maximum volume of the phase space that is occupied by the bunch since the emittance does not remain constant over the whole bunch length. According to the bunch slice model, the longitudinal phase space can be visualized as divided into several segments. These nearly independent longitudinal segments have a thickness of  $\delta\zeta$  and can be understood as micro-bunches. The relative slice charge is formulated in relation to the total bunch charge by  $g(\zeta) = q_{\text{slice}}/q_b$ . Additionally, the slice charge does not stay constant in all slices, but is defined by the charge distribution throughout the bunch. For a Gaussian distributed bunch, the slice charge diminishes towards the bunch ends. Each slice provides its own emittance value dependent on its phase space volume. The slice emittance can be mathematically expressed as the weighted sum resulting from the transverse emittances of all slices, which corresponds to the slice charge:

$$\varepsilon_{\text{slice}} = \sum_{\zeta} g(\zeta) \cdot \varepsilon(\zeta). \quad (4.8)$$

Consequently, the projected emittance is then defined as the projected phase space volume of the slices that are distributed along the entire bunch length. The slice emittance and the projected emittance values differ if the slices mismatch. This is the case if the slice ellipses are rotated in the transverse phase space with different

rotation angles and the emittance values of the individual slices are not similar [see Fig. 4.3]. The slice misalignment occurs if beam dynamic effects of the beam path elements or the space charge are functions of  $\zeta$ . A detailed discussion will follow in section 4.3.

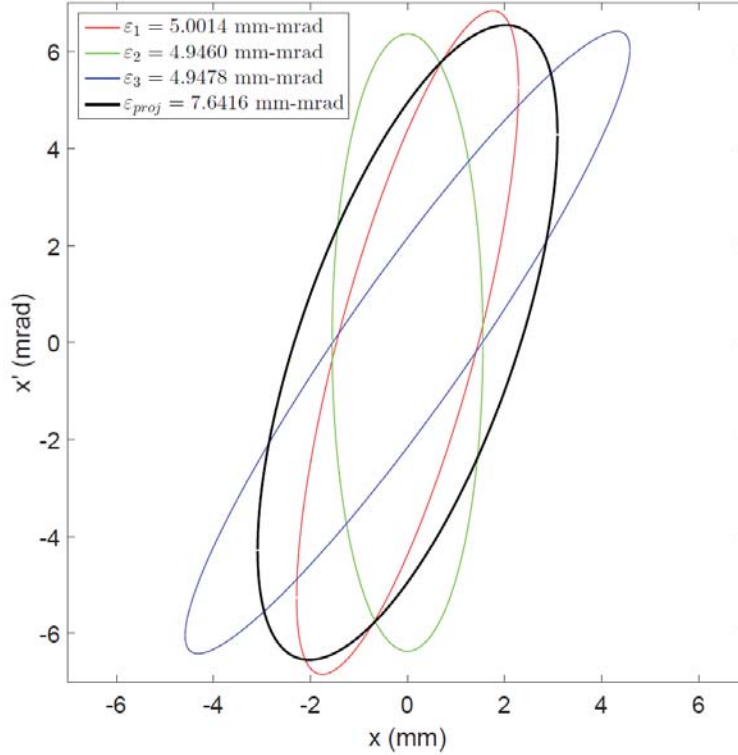


Figure 4.3: Three phase space distributions of three equally charged slices in one bunch are plotted (red, green and blue curve). The corresponding projected emittance (black curve) shows an increased emittance value compared to the slice emittances of nearly the same horizontal emittance [62].

If no correlation between the horizontal, vertical, and longitudinal coordinates exists, the six-dimensional phase space volume can be formulated as the product of the normalized emittances of the three planes:

$$V_{6D} = \varepsilon_{\text{norm.},x} \cdot \varepsilon_{\text{norm.},y} \cdot \varepsilon_{\text{norm.},z}. \quad (4.9)$$

According to the Liouville theorem, the six-dimensional phase space volume is preserved in time if only conservative forces are acting on the bunch [11].

The bunch is entirely characterized by its energy  $E$ , its bunch charge  $q_b$ , its six-dimensional phase space  $V_{6D}$  and thus it is defined by its transverse and longitudinal emittances  $\varepsilon_{\text{norm.},x,y,z}$ .

The bunch charge, the transverse emittance and longitudinal emittance can be summarized in the parameter “beam brightness”, a figure of merit for the beam quality of any electron source and any accelerator. The brightness is generally defined as the current density  $J$  per unit volume of a six-dimensional phase space with the unit area  $dS$  and the unit solid angle  $d\Omega$  [11]:

$$B = \frac{J}{dSd\Omega}. \quad (4.10)$$

Therefore, the brightness  $B$  is not constant over the whole bunch since the current density varies. An integration over the six-dimensional phase space volume sets the six-dimensional beam brightness as proportional to the beam intensity  $I$  which depends on the number of electrons in the beam  $N_e$ :

$$B_{6D} = \frac{N_e e}{V_{6D}}. \quad (4.11)$$

Therefore, the six-dimensional brightness is directly proportional to the horizontal, vertical, and longitudinal normalized emittances:

$$B_{6D} \propto \frac{N_e e}{\varepsilon_{\text{norm.},x} \varepsilon_{\text{norm.},y} \varepsilon_{\text{norm.},z}}. \quad (4.12)$$

The parameter “beam brightness” as it is defined in Equ. (4.10) was originally introduced by the inventors of the electron microscope Ernst Ruska and Bodo von Borries [73]. The so called “Richtstrahlwert” describes the quality of the microscope and thereby determines the achievable resolution. Moreover, it shows which types of experiments are possible. The relativistic analogue for accelerator electron sources corresponds to the five-dimensional beam brightness. If a hyperellipsoid bunch shape is assumed, the integration over the phase space volume leads to the 5D brightness expression:

$$B_{5D} = \frac{2I}{\varepsilon_{n,x}\varepsilon_{n,y}}. \quad (4.13)$$

The 5D brightness is mainly used to describe electron sources that drive FEL-based light sources since the peak current and thus the 5D beam brightness directly enters the FEL gain parameter [43].

In order to achieve a satisfying beam quality in an accelerator, the beam brightness must be maximized. The initial brightness of the beam is determined in the electron emission process. It cannot be further improved since the transverse phase space is conserved ideally (only conservative forces are acting) or the brightness lessens due to non-conservative and nonlinear beam influences after emission. The beam brightness must be as well preserved as possible in the subsequent accelerator stages where conservative and non-conservative forces are acting on the beam. The limits of the beam brightness of the electron injector will be discussed in a separate chapter as well as solutions for beam treatment in order to preserve maximum beam brightness best.

## 4.2 Maximum Beam Brightness

The theoretical limit of the electron beam brightness is given by the quantum limit. Due to the Pauli exclusion principle and Heisenberg uncertainty principle, an elementary quantum  $h^3$  unit can be filled with one spin-up and one spin-down electron [74], [75]. This leads to an absolute brightness limit with two electrons in a  $h^3$  volume

$$B_{\text{quantum}} = \frac{2e}{h^3}(mc)^3 \approx 10^{25} \frac{A}{m^2}. \quad (4.14)$$

This absolute brightness limit is far away from current photoinjector performances. An electron source that is able to provide the bERLinPro specification with a bunch charge of 77 pC, with a transverse normalized emittance of 1 mm mrad, and a bunch length of  $\sigma_t \leq 2$  ps can achieve a peak brightness of  $3.85 \cdot 10^{13}$  A/m<sup>2</sup>. Therefore, a brightness degradation of more than  $10^{-11}$  order of magnitudes already occurs at the electron source, which is triggered by the emission process as well as the electron bunch interaction with internal and external fields. In order to explain why the

achieved peak brightness differs from the absolute limit, the beam dynamics in the SRF photoinjector must be analyzed in detail. If the development of the electron beam and its crucial parameters in the longitudinal and transverse trace space is completely understood, the photoinjector can be optimized towards high brightness operation.

### 4.3 Beam Dynamics in an SRF Photoinjector

The whole bunch and, therefore, the central electron beam parameters, the **transverse** and **longitudinal emittance**, the **bunch charge** and the total **beam energy** are affected by the external forces that generate, accelerate, focus or deflect the beam during the transportation through the photoinjector. Additionally, internal forces due to the Coulomb repulsion of the electrons (space charge), influence the bunch. The electric and magnetic fields  $\vec{E}$  and  $\vec{B}$  of the different components act on the bunch, generating a force in the transverse and longitudinal direction. All inner (space charge) and outer (acceleration, focusing, deflection) fields are considered and summarized in the Lorentz force that is displayed in the following formula

$$\vec{F} = \gamma m \dot{\vec{v}} = \gamma q_b (\vec{E} + \vec{v} \times \vec{B}) \quad (4.15)$$

where  $q_b$  provides the bunch charge and  $\vec{v}$  is the bunch velocity in the  $z$ -direction [11].

For the discussion of the transverse and longitudinal beam dynamics in the SRF gun and for the derivation of the radial and longitudinal equation of motion, the contributions from the emission process at the cathode, the acceleration in the cavity, the solenoid focusing as well as space charge effects are each considered separately.

#### 4.3.1 Emission

The initial phase space volume of the bunch is defined by the emission process at the cathode of the photoinjector. For photoemission, the process is determined by the drive laser that triggers the electron emission from the cathode, and the cathode itself.

The relevant properties of the laser are given by the laser pulse energy  $E_{\text{laser}}$  and the laser beam size  $\sigma_{\text{laser},x}$  together with its pulse length  $\sigma_{\text{laser},t}$  defining the laser pulse

volume. Material (metal, semiconductor) and surface properties of the photocathode affect the emission process. In particular, the cathode material work function defines the required photon energy of the drive laser.

The emission process from metallic photocathodes can be described with a three step model introduced by Spicer [76] and illustrated in Fig. 4.4. First, the absorbed laser photons transmit their energy to the bound electrons in the cathode material. The energized electrons move to the cathode threshold, some of them lose their energy due to interactions with other electrons or with the lattice of the material. Finally, those excited electrons with sufficient energy to overcome the surface barrier of the material escape into the vacuum of the gun.

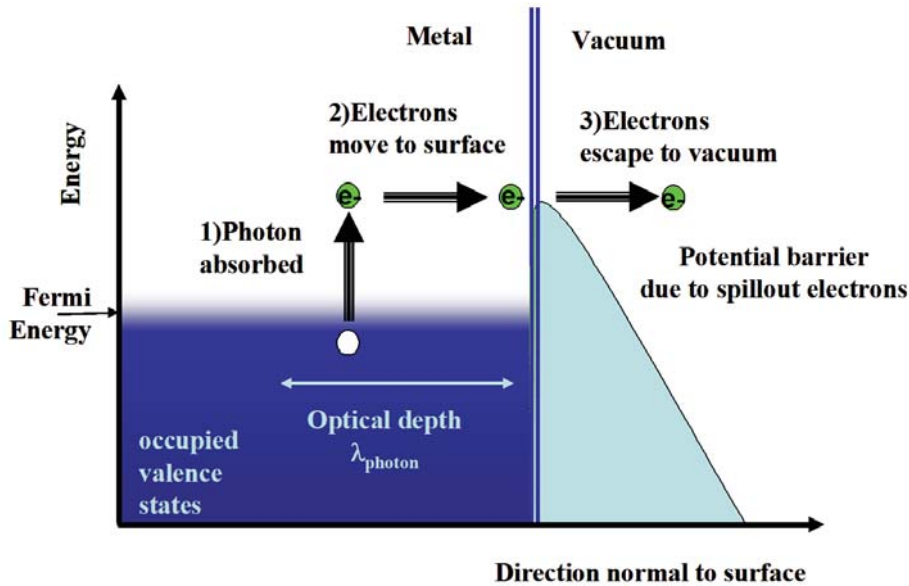


Figure 4.4: Photoelectric emission from a metallic cathode given by Spicer’s three step model. A photon is absorbed by an electron. In the second step, the energized electron moves to the surface. Finally, the electron escapes through the surface barrier to the vacuum [77].

The description of the three steps lead to a model for the quantum efficiency  $QE$  which defines the number of emitted electrons per incoming laser photon. The surface reflectivity (step 1), the electron-phonon and the electron-electron scattering probability (step2), as well as the energy spectrum of the excited electrons (step 3) determine the  $QE$ . Reference [78] gives a detailed overview.

The electrons excited by the laser beam, have to overcome the surface poten-

tial of the cathode material which is usually modeled by a step function [see Fig. 3.1(b)]. In case of an RF photoinjector, an external electric field lowers the surface potential [77]. This *Schottky* effect results in an enlarged number of excited electrons with sufficient energy to escape the cathode material and thus into a higher  $QE$ . The Schottky effect is also shown in the beam current measurement relative to the laser phase from the SRF photoinjector at HZDR [see Fig. 4.5]. Starting at a phase of -10 deg (without DC bias), first electrons are extracted from the cathode to vacuum. The bunch reaches its final length at 10 deg. Instead of a constant beam current at laser phases above 10 deg, an additional increase can be detected in Fig. 4.5 since further electrons escape from the photocathode due to the external RF field lowering the potential barrier.

However, a lowered surface barrier enables non-excited electrons to tunnel into the vacuum resulting in dark current.

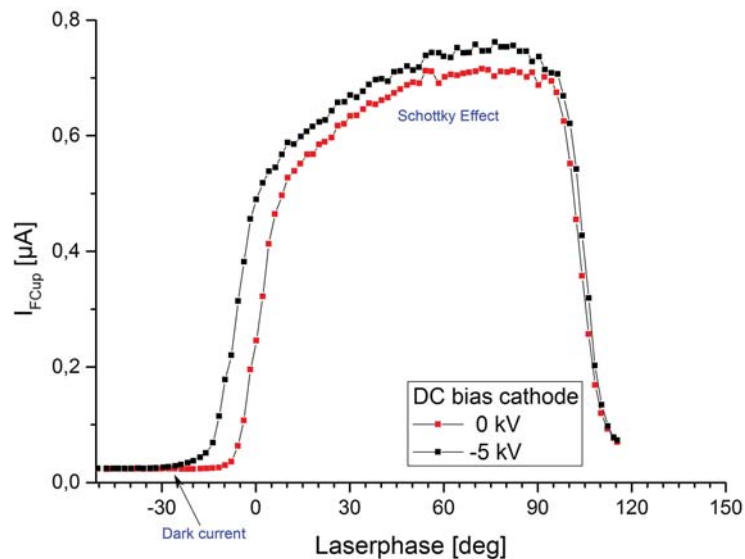


Figure 4.5: Measurement of the beam current relative to the laser phase in the SRF photoinjector at HZDR. The two curves represent measurements without (black curve) and with (red curve) a DC bias. An increased photocurrent due to the Schottky effect can be detected at phases above 10 deg.

The excess energy  $E_{\text{excess}}$  of the electrons depends on the laser photon energy  $\hbar\omega$  and the work function  $\phi_{\text{eff}}$  which represents the minimum energy that is needed to remove an electron from the cathode. The effective work function  $\phi_{\text{eff}}$  already considers a potential reduction that is due to the *Schottky* effect. The electron excess energy is proportional to the quantum efficiency [77].

$$E_{\text{excess}} = \hbar\omega - \phi_{\text{eff}} \quad (4.16)$$

The electron excess energy  $E_{\text{excess}}$  significantly impacts the four electron beam parameters that characterize the electron bunch. Using a simplistic model, a uniform and isotropic energy distribution is assumed in the emitted electron bunch ( $\langle E_x \rangle = \langle E_y \rangle = \langle E_z \rangle$ ). The initial **electron kinetic energy** simply equals 1/3 of the mean energy  $\langle E \rangle$  and thus 1/6 of the excess energy  $E_{\text{excess}}$ , since the mean energy  $\langle E \rangle$  corresponds to a half excess energy  $E_{\text{excess}}$  due to the uniform energy distribution between 0 and  $E_{\text{excess}}$  [79]. Hence, the larger proportion of the excess energy contributes to the mean transverse energy *MTE*:

$$MTE = \frac{2}{3}\langle E \rangle = \frac{1}{3}E_{\text{excess}}. \quad (4.17)$$

The *MTE* parameter also defines the initial transverse momentum  $\langle p_{x,y} \rangle$  at the cathode.

The **transverse phase space** of the bunch after the emission process is characterized by the transverse emittance contribution, called the intrinsic emittance. According to Formula (4.4) the beam size defines the transverse emittance together with the transverse momentum. Since the electron flow that just emerged from the photocathode is laminar the correlation between the beam size and the transverse momentum  $\langle xp_x \rangle$  ( $\langle yp_y \rangle$  respectively) can be neglected. The laser spot size on the cathode defines the initial beam size of the bunch  $\sigma_{x,\text{laser}}$ , while the momentum in x-direction  $p_x$  is determined by the derived *MTE* expression. With these relations in mind, the transverse, intrinsic emittance can be written as

$$\varepsilon_{\text{in},x} = \sigma_{x,\text{laser}} \sqrt{\frac{\hbar\omega - \phi_{\text{eff}}}{3mc^2}}. \quad (4.18)$$



The **longitudinal phase space distribution** of the bunch is given by the bunch length and the energy spread at the cathode.

The incoming laser pulse length  $\sigma_{z,\text{laser}}$  strongly dominates the initial bunch formation length. Furthermore, the response time of the cathode must be added, including the time needed for photon absorption and electron excitation, as well as the time the electron needs to travel to the cathode surface and allowing for potential scattering processes and electron escape. While a metallic cathode provides a fast response in the fs range, semiconductor cathodes can reach response times of several ps close to the laser pulse duration. Electron-electron scattering processes dominate in metals due to the high number of electrons and the resulting short mean free paths in the material [79]. The energy loss of the electrons due to the inelastic scattering prevents the electrons from escaping out of the metallic photocathode. Only electrons close to the surface with a lower scattering probability contribute to the emission. The response time of these cathodes is fast because the electrons have only a short distance to travel until they reach the surface.

Excited electrons in semiconductors scatter in a nearly elastic manner within the electron-phonon processes [79]. Due to the slight energy loss, electrons from deeper layers can be emitted. The traveling of the electrons to the photocathode surface and their several scattering processes enlarge the response time to several ps.

The longitudinal momentum spread of the electrons  $\Delta p_z$  is given by the number of excited states that occur in the cathode material. For a uniform energy distribution, the momentum spread is also considered in the model. Therefore, it also contributes to the *MTE* parameter and the kinetic energy. In general, the  $E_{\text{excess}}$  should intentionally be as small as possible. For that reason, the laser photon energy is set close to the work function of the cathode material by choosing an appropriate laser wavelength. In the course of this strategy only a limited number of atomic states is excited and the energy spread can be suppressed. Furthermore, the intrinsic transverse emittance is minimized.

Finally, the **bunch charge** is initialized at the cathode. The laser (the laser average power  $P_{\text{avg}}$ , the photon energy  $\hbar\omega$  and the pulse repetition rate  $f_{\text{rep}}$ ) and the cathode (quantum efficiency  $QE$ ) determine the amount of electrons extracted from the cathode. Following Equ. (4.1) the bunch charge can be derived as

$$q_b = \frac{eP_{\text{avg}}}{\hbar\omega f_{\text{rep}}} QE. \quad (4.19)$$

After the emission process has finished, an RF wave induced in the gun cavity accelerates the electrons away from the cathode. Now, the impact of the external RF field on the beam dynamics will be discussed in detail.

### 4.3.2 Acceleration

In order to accelerate the electron beam into the  $z$ -direction, a longitudinal electric field is needed which is achieved by coupling an electromagnetic field into the radio-frequency cavity of an SRF photoinjector. The field components can be examined analytically if one cavity cell in a pillbox shape is considered separately. Since the electric and magnetic field vectors always stand perpendicular to each other and forward acceleration requires a longitudinal electric field component along the pillbox axis, RF waves in the transverse magnetic field configuration, called  $\text{TM}_{mn}$  mode, can be used. The indices  $m$  and  $n$  describe the number of zero-crossings of the electromagnetic field in the azimuthal and radial direction. Equation (4.20) displays the accelerating electric field  $E_z$  of the  $\text{TM}_{mn}$  mode in a pillbox cavity based on the electric peak field  $E_0$ , the Bessel function  $J$ , as well as the RF phase  $\phi$ , the cavity cell length  $L_{\text{cell}}$  and the angular frequency of the RF wave  $\omega$  [54]:

$$E_z^{mn}(r, z) = E_0 J_m(k_{mn}r) \cos(m\phi) e^{i\omega t}. \quad (4.20)$$

Since a rotational symmetry of the bunch and the cavity shape is assumed, field and beam dynamic considerations are expressed in cylindrical coordinates  $(r, \phi, z)$ .

Usually, the  $\text{TM}_{01}$  mode is used in gun cavities with no zero crossings in the azimuthal direction and only one zero crossing in the radial plane. Therefore, the electric and magnetic fields have no angular dependency. The electric field responsible for acceleration is constant over  $z$ . The zero crossing in the transverse mode leads to a maximum acceleration on axis while, the cavity wall is free of an electric field ( $E=0$ ) without forward acceleration. This is a desired objective, since oscillating fields at the cavity walls drive those currents that lead to power losses. Even in cavities made of superconducting materials, power dissipation cannot be completely

suppressed. The azimuthal magnetic field vanishes on the beam axis [see Fig. 4.6].

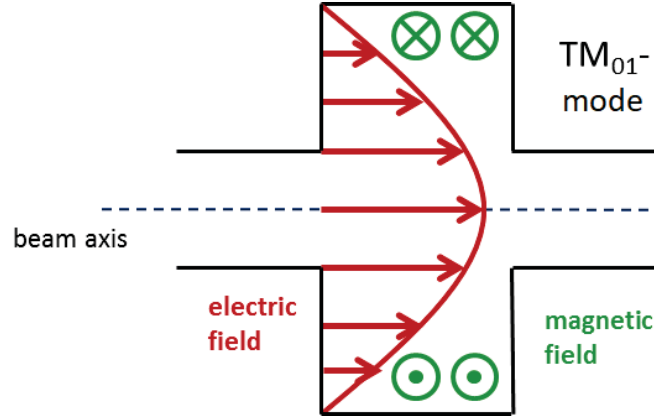


Figure 4.6:  $TM_{01}$  mode in a pillbox shaped cavity. The electric field is constant along the  $z$ -axis inside the cavity. The maximum field value is achieved on the beam axis while the cavity walls are free of an electric field. The azimuthal magnetic field vanishes on the beam axis [54].

Within photoinjectors, the acceleration takes place in a sequence of several cavity cells in order to reach the required beam energy. The cells work separately in the same TM mode. The phase shift between the cells can be defined. To always guarantee that the bunch is accelerated into the forward direction in each cell, the sign of the electric field must change when the bunch enters the iris between two cavity cells. SRF guns are normally based on a  $TM_{01-\pi}$  mode with a phase shift of 180 deg between the cells.

Moreover, the iris between the cells influences the longitudinal electric field component  $E_z$ . Although the electric field on the axis is no longer constant over  $z$  it can be approximated with a cos-function. Consequently, the longitudinal electric field in the  $TM_{01-\pi}$  mode can be expressed on the beam axis as [43]:

$$E_z = E_0 \cos(kz) \sin(\omega t + \phi_0). \quad (4.21)$$

where  $k = 2\pi/\lambda_{rf}$  is the wave number depending on the RF wavelength and where  $\phi_0$  is the phase in which the electron bunch is injected to the RF field.

As the electric field lines are always perpendicular to the cavity walls, a radial electric field component  $E_r$  but no azimuthal component  $E_\phi$  can be observed [see Fig. 4.7].

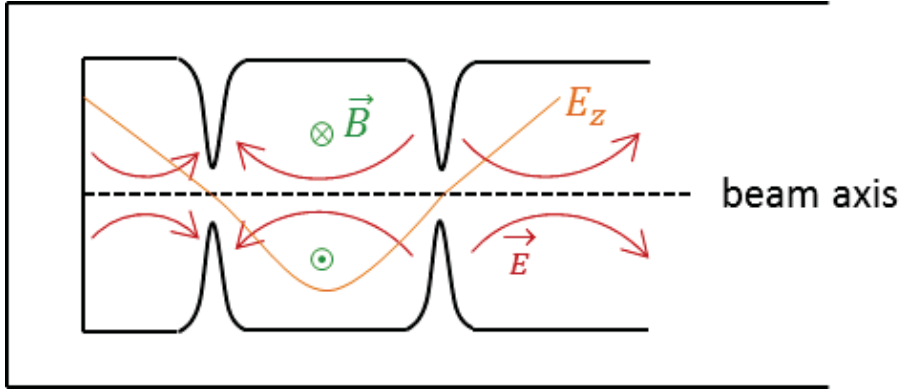


Figure 4.7: The  $TM_{01-\pi}$  mode in an RF cavity.

The radial electric field component can be derived from Gauss' law in a charge free region ( $\vec{\nabla} \cdot \vec{E} = 0$ ):

$$E_r = -\frac{r}{2} \frac{dE_z}{dz} = \frac{kr}{2} E_0 \sin(kz) \sin(\omega t + \phi_0). \quad (4.22)$$

Ampere's law provides the additional azimuthal magnetic field component

$$B_\phi = \frac{r}{2c} \frac{dE_z}{dt} = \frac{kr}{2} E_0 \cos(kz) \cos(\omega t + \phi_0). \quad (4.23)$$

In general, the described cavities can work in a standing wave or traveling wave mode. If the standing wave mode is used for acceleration, the wave is reflected nearly without losses at the end of the structure. A standing wave is caused by interference. In the traveling mode, the wave is decoupled at the end of the sequence before it is guided to an absorber. The gun cavity for the SRF photoinjector under consideration is based on the standing wave concept.

The impact of the derived external RF fields on the beam dynamics are investigated in the following section. For reasons of simplicity and in order to receive a compact theory overview, the following section approaches the beam dynamics in the longitudinal and transverse direction during the accelerating process separately.

### Longitudinal Beam Dynamics during Acceleration

With regard to the longitudinal direction, the Lorentz force states:

$$\frac{d}{dt}(\gamma m \dot{z}) = \dot{\gamma} m \dot{z} + \gamma m \ddot{z} = q(E_z + \dot{r} B_\phi - r \dot{\phi} B_r). \quad (4.24)$$

In the  $\text{TM}_{01-\pi}$  mode, the longitudinal electric field  $E_z$  contributes to the longitudinal beam dynamics. The azimuthal magnetic field  $B_\phi$  only impacts the longitudinal beam dynamics if the radial electric field  $E_r$  causes a radial movement ( $\dot{r} \neq 0$ ) in the cavity. No radial magnetic field component ( $B_r=0$ ) occurs. The accelerating force is proportional to the field gradient  $E_0$  and it depends on the gun injection phase  $\phi_0$  [see formula (4.21) and (4.23)].

In the non-relativistic regime close to the cathode, the term  $\gamma m \ddot{z}$  dominates the acceleration by the cavity field in the longitudinal direction. An ultra-relativistic term  $\dot{\gamma} m \dot{z}$  occurs for relativistic acceleration, therefore,  $\dot{\gamma} > 0$  must be fulfilled.

The longitudinal electric field component controls the longitudinal acceleration of the bunch in the gun cavity and therefore, the variation of  $E_z$  defines the **longitudinal phase space**.

Analytical expressions for the energy, gained during the acceleration in the gun cavity, as well as the bunch phase that affects the bunch length have been derived by Kim [80]. The lowest order approximation for the energy  $\tilde{\gamma}$  gained during the RF acceleration can be approximated next to the cathode ( $z \approx 0$ ) as

$$\tilde{\gamma}(z) = 1 + 2kz\alpha \sin(\phi_0). \quad (4.25)$$

$\tilde{\gamma}$  is used as an dimensionless relativistic beam energy that is normalized by the electron rest energy  $m_e c^2$ . In formula (4.25)  $\alpha$  describes the dimensionless RF field strength  $\alpha = \frac{eE_0}{2mc^2k}$ .

This equation follows Kim's approximation stating that the bunch phase is constant over  $z$  [80]. Nevertheless, this approximation is not suitable for a detailed study of the bunch phase anymore. When considered as a function of  $z$  and  $\tilde{\gamma}$ , the bunch slips back in phase. With this reasoning in mind, the phase can be expressed as

$$\tilde{\phi} = \omega t - kz + \phi_0 = \frac{1}{2\alpha \sin \phi_0} [\sqrt{\tilde{\gamma}^2 - 1} - (\tilde{\gamma} - 1)] + \phi_0. \quad (4.26)$$

This phase expression also leads to a better approximation for the energy  $\gamma$

$$\gamma = 1 + \alpha[kz \sin \tilde{\phi} + \frac{1}{2}(\cos \tilde{\phi} - \cos(\tilde{\phi} + 2kz))]. \quad (4.27)$$

Furthermore, equation (4.26) helps to estimate the final phase at the cavity exit

$$\phi_e \rightarrow \frac{1}{2\alpha \sin(\phi_0)} + \phi_0 \quad (4.28)$$

at relativistic energies  $\tilde{\gamma} \gg 1$ . A bunch compression occurs solely due to this phase slippage. It will be analyzed in section 4.4.3.

The defined beam exit energy  $\gamma$  and the beam phase  $\phi_e$  represent the average values of the whole bunch  $\langle \gamma \rangle_{\text{bunch}}$  and  $\langle \phi \rangle_{\text{bunch}}$ . Nevertheless, the initial phase spread and momentum spread that are caused by the emission process at the cavity entrance cannot be neglected.

Together with the bunch compression in the gun, the initial phase spread  $\Delta\phi_i$  after emission leads to the final phase spread  $\Delta\phi_e$  at the cavity exit. The spread in phase is equivalent to a spread in time and thus it defines the final bunch length  $\sigma_z$  at the cavity exit.

The initial phase spread also induces a momentum spread. At a constant RF peak field  $E_0$  in the gun cavity, the bunch longitudinal momentum depends on the phase. The phase-energy dependence is illustrated for a constant gun gradient of 30 MV/m in Fig. 4.8. Different phases at the bunch head and tail that are due to the finite bunch length lead to different momentum gains and thus produce a momentum spread.

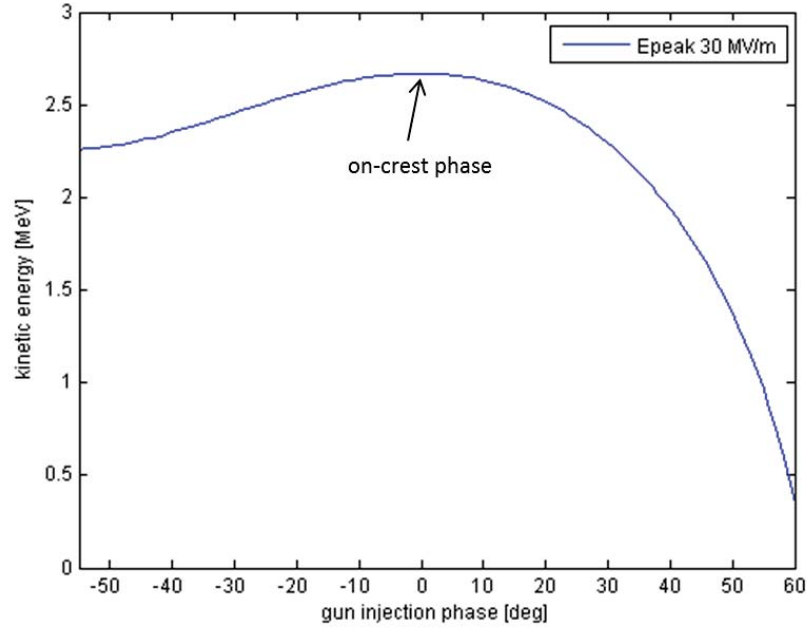


Figure 4.8: Dependency of the kinetic energy of the bunch on the gun phase illustrated for an acceleration gradient of 30 MV/m. The highest energy is achieved at the so-called on-crest phase. All phase values in the dissertation at hand are always indicated relative to the on-crest phase.

The phase and momentum spread impact the longitudinal emittance as shown in formula (4.7). The contribution of the longitudinal RF emittance can be written as follows:

$$\varepsilon_z = \frac{1}{k} \sqrt{\langle \Delta p_z^2 \rangle \langle \Delta \phi^2 \rangle - \langle \Delta p_z \Delta \phi \rangle^2} \quad (4.29)$$

After discussing the longitudinal dynamics that are caused by the RF field in the accelerating cavity, the RF contribution and changes to the transverse beam dynamics are now considered.

### Transverse Beam Dynamics during Acceleration

Formula (4.30) represents the beam dynamics in the transverse plane given by the Lorentz force.

$$\gamma m \ddot{r} = qE_r - q\dot{z}B_\phi - \gamma' m \dot{r} \dot{z}. \quad (4.30)$$

The third term  $\gamma' m \dot{r} \dot{z}$  results from the coupling of the transverse and longitudinal velocities  $\dot{r} \dot{z}$ . This expression leads to a focusing effect ( $\ddot{r} < 0$ ) if a divergent bunch ( $\dot{r} < 0$ ) moves along the z-axis. This force counteracts the defocusing of the radial electric field  $E_r$  and the azimuthal magnetic field  $B_\phi$  as well as other radial field components, e.g., components deriving from space charge.

Besides the coupling of the movement in the transverse and longitudinal direction, the optical properties of the SRF cavity also affect the transverse beam dynamics (First and second term of Equ. (4.30)). The radial electric field component of the RF cavity field in the  $\text{TM}_{01-\pi}$  mode is expressed by the z-derivative of the longitudinal field  $E_z$  given in formula (4.22). The azimuthal magnetic field is proportional to the time derivative of the  $E_z$  component [see Equ. (4.23)]. Both fields  $E_r$  and  $B_\phi$  leads to a radial force acting on the electron bunch.

In case a more general expression of the longitudinal electric field is assumed

$$E_z = E(z) \cos(kz) \sin(\omega t + \phi_0) \quad (4.31)$$

the radial force  $F_r$  that acts on the electron bunch can be formulated as follows:

$$F_r = qr \left[ -\frac{\partial}{\partial z} E_z - \frac{\dot{z}r}{c} \frac{\partial}{\partial t} E_z \right] \quad (4.32)$$

The radial momentum kick  $p_r$  can be derived by integrating the radial force with respect to time. It is assumed that the transverse deflection can be neglected and thus, the radial bunch offset  $r$  from the z-axis remains constant over time  $t$  [80].

If the  $E_z$  field is assumed to be constant over the gun cavity length, a radial force only impacts the bunch if the condition  $\frac{\partial E(z)}{\partial z} \neq 0$  is fulfilled. An effect based on the RF cavity field only occurs if the longitudinal electric field changes its size, as it is



the case at the exit of the cavity from  $E_0$  to zero [see illustration in Fig. 4.9].

Through using the derivative of the step function, a radial momentum kick  $\Delta p_r$  can be formulated as

$$p_r = \alpha k r \sin(\phi_e) \quad (4.33)$$

with  $\phi_e = kz_f - \omega t_f - \phi_0$  describing the exit phase of the bunch at the cavity end position  $z_f$  and the time  $t_f$  [80]. Expression (4.33) represents a defocusing kick when  $0 < \phi_e < \pi$  is fulfilled. The defocusing strength increases with high RF peak fields  $E_0$ . Therefore, it is important for SRF guns that aim for high field acceleration. This defocusing lens effect must be compensated by the focusing solenoid field. The defocusing forces decrease with the bunch acceleration by  $1/\gamma$  and are thus much slower than the forces in the longitudinal direction ( $\propto 1/\gamma^3$ ) [see Fig. 4.9].

The RF focusing is time dependent due to its direct proportionality to the phase  $\phi$ . Consequently, the electrons that are in a bunch with different positions  $\zeta$  are affected by different transverse momentum kicks  $p_r$ . In the bunch slice model, the slices show different slopes in the transverse phase space at the cavity exit [see. Fig. 4.3]. Therefore, the total trace space volume (envelope of the slice phase space volume) increases. This effect also corresponds to a total **transverse emittance** growth with the emittance contribution  $\varepsilon_{\text{rf},x}$ .

According to (4.4), the transverse momentum  $p_r$  together with the exit phase, written as  $\phi_e = \langle \phi_e \rangle + \Delta\phi$  with a Gaussian distributed phase deviation  $\Delta\phi$ , can be used to express the transverse RF emittance contribution as follows [80]:

$$\varepsilon_{\text{rf},x} = \alpha k \sigma_x^2 \left( \sigma_\phi |\cos \phi_e| + \frac{\sigma_\phi^2}{\sqrt{2}} |\sin \phi_e| \right). \quad (4.34)$$

Here,  $\sigma_{x,y}$  represents the transverse beam size and  $\sigma_\phi$  is the bunch length. All parameters are evaluated at the exit of the gun. Due to the sine- and cosine-dependence of the RF phase in the first and second order terms, there is always an RF contribution to the transverse emittance. The total emittance minimum is reached at an exit phase  $\phi_e$  of 90 deg. The nonlinear part of the RF emittance (proportional to  $\sigma_\phi^2$ )

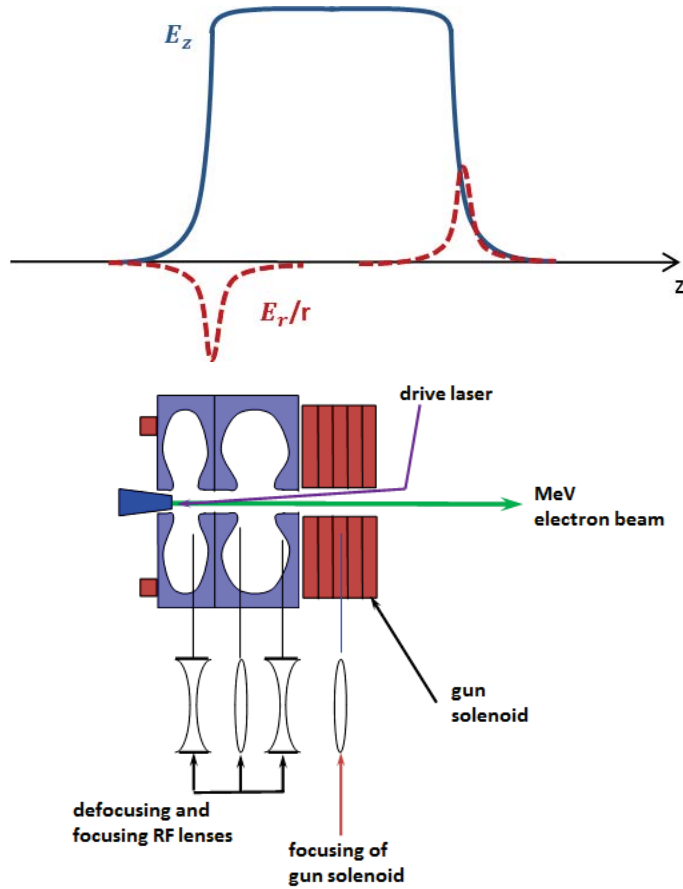


Figure 4.9: (a) Radial RF field contribution due to changes in the longitudinal electric field.

(b) Focusing and defocusing effects caused by cavity irises, the cavity exit and the solenoid [81].

follows from the RF curvature. The transverse RF emittance contribution is strongly affected by the bunch phase as well as the acceleration strength  $\alpha$  of the gun cavity.

It has to be mentioned that an additional radial focusing field can be achieved at the cavity backwall and the photocathode due to a special cavity design and photocathode insert system. A photocathode retraction and a backwall inclination lead to a high transverse field component that impacts the transverse beam properties during the emission process. Fig. 4.10 displays the radial RF component at a radial position of  $r=1\text{ mm}$  for five different cathode positions. In order to additionally focus the bunch in the radial direction, a retraction of the photocathode is always advisable. This is also confirmed in the results presented in this dissertation (see Chapter 6). However, a radial focusing right behind the cathode in the space charge dominated

regime forces unwanted space charge effects which must be controlled, e.g. by a moderate bunch length.

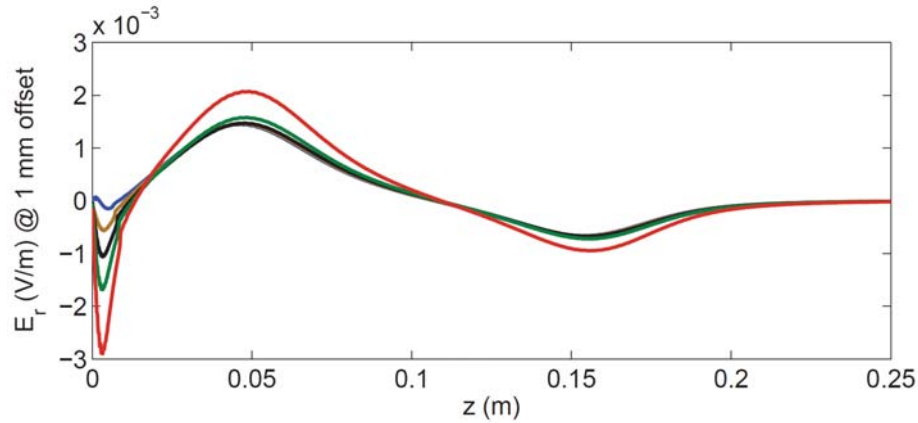


Figure 4.10: The radial electric field at the radial position  $r=1$  mm along the  $z$ -axis for five different cathode positions from 0 mm to a retreat of 2.3 mm [82].

Finally, the **bunch charge** is considered as the last crucial electron beam parameter that directly acts on the beam brightness. The bunch charge stays constant during the accelerating process as long as all electrons of the bunch gain enough momentum from the electric field to ensure that they do not slip back to decelerating phases.

### 4.3.3 Solenoid

The solenoid is one of the most important elements in the beam path. The task of this magnetic lens is to cancel the defocusing effect of the last RF cavity cell by focusing the beam in the transverse plane. Placed behind the cavity exit, the solenoid field slightly overlaps the cavity RF field, such as illustrated in Fig. 4.11.

Furthermore, the solenoid is able to minimize the total projected beam emittance using the effect of emittance compensation by slice alignment a process that will be described in section 4.4.2.

The solenoid induces a rotational symmetric field along the beam axis. The longitudinal field profile is illustrated in Fig. 4.12.

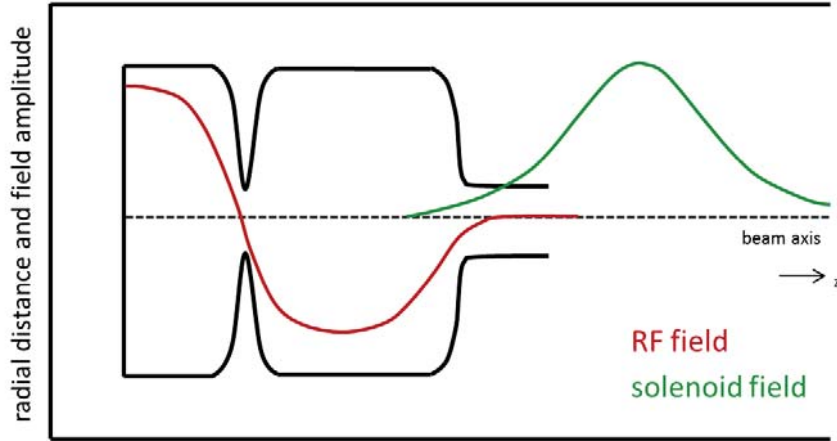


Figure 4.11: External fields of the RF wave and the solenoid acting on the electron bunch in the cavity and behind it [43].

The correlated radial and longitudinal field components  $B_r$  and  $B_z$  of the solenoid depend on the  $z$ -derivatives of the longitudinal field profile  $B(z)$  [11]. The radial magnetic field component acts on the particles in the bunch that moves along the  $z$ -axis. In addition an occurring force in azimuthal direction  $F_\phi$  causes a rotation around the  $z$ -axis. The subsequent azimuthal momentum  $p_\phi$  of the particles leads to an interaction with the longitudinal field component of the solenoid. The resulting radial force  $F_r$  focuses the beam towards the beam axis in the transverse plane. This process happens independent of the magnetic field orientation. As the focusing effect is rotationally symmetric, it minimizes the transverse offset of the electron bunch in the horizontal and vertical plane simultaneously with the same strength. In this case, a solenoid magnet differs from a quadrupole that focuses in one transverse direction only.

The focal length of the solenoid can be expressed as

$$\frac{1}{f_{\text{Sol}}} = K \sin(KL_{\text{eff}}). \quad (4.35)$$

The effective length  $L_{\text{eff}}$  of the solenoid is obtained by integrating the solenoid field along the  $z$ -axis [11]:

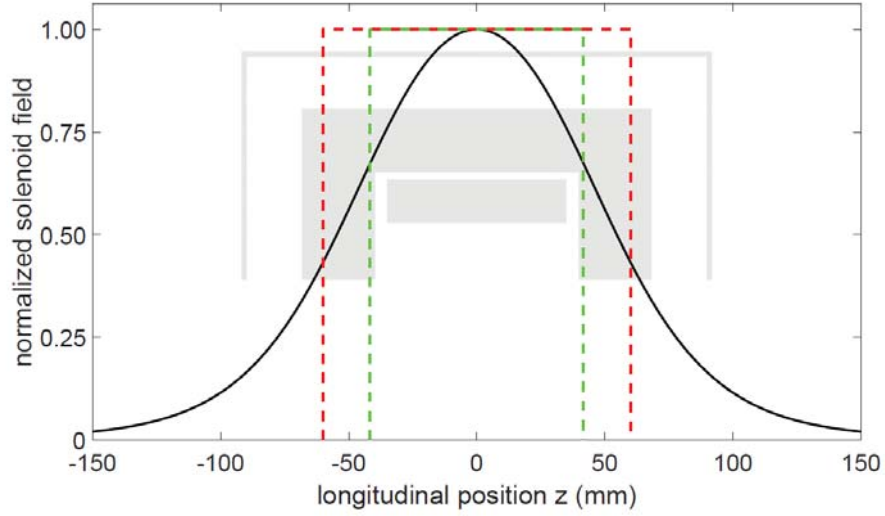


Figure 4.12: Field profile of the GunLab solenoid magnet (black). The solenoid cross section is shaded in gray and provides an geometric overview of the magnet. The focusing and rotational effective lengths are plotted with a green and a red dashed line [62].

$$L_{\text{eff}} = \frac{1}{B_0^2} \int_{-\infty}^{\infty} B^2(z) dz \quad (4.36)$$

where  $B_0$  is the peak magnetic field on axis. The parameter  $K$  in Equ. (4.35) represents the focusing strength of the solenoid

$$K = \frac{eB_0}{2p}. \quad (4.37)$$

Therefore, the transverse focusing of the solenoid depends on the maximum magnetic field  $B_0$  as well as on the beam momentum  $p$ .

### Transverse Beam Dynamics in the Solenoid Magnet

Since the solenoid acts like a lens in an optical beam path, aberration effects impact the **transverse phase space**. The momentum dependence of the focal length leads to a diverse focusing of an electron bunch with a finite momentum spread  $\sigma_p$ . Each particle is deflected due to its individual longitudinal momentum. Moreover, chromatic aberration effects occur.

The beam momentum dependence of the focal length does not only affect the transverse beam transformation through the solenoid, but also leads to an emittance growth that is caused by chromatic aberration [83]:

$$\varepsilon_{n,\text{chrom}} = \beta\gamma\sigma_x^2 \left| \frac{d}{dp} \left( \frac{1}{f_0} \right) \right| \sigma_p = \beta\gamma\sigma_x^2 K (\sin(KL) + KL \cos(KL)) \frac{\sigma_p}{p}. \quad (4.38)$$

In this formula  $\sigma_x$  describes the *rms* beam size inside the solenoid. The chromatic emittance contribution can reach several tenths of microns.

In order to receive a first estimation for GunLab, a bunch with a desired momentum of  $pc=3\text{ MeV}/c$  and a small momentum spread of 0.1% is assumed. The effective length of the currently installed solenoid in GunLab is given by 83.3 mm [62]. For a beam waist 2 m behind the cathode a magnetic field of around 100 mT is required. Based on these values a chromatic emittance contribution of  $\varepsilon_{n,\text{chrom}}=0.023 (\sigma_x[\text{mm}])^2$  mm mrad can be calculated depending on the *rms* beam size.

In addition to the chromatic aberration, each solenoid exhibits several nonlinear effects that impact the electron beam dynamics. One of the most dominant effects is the spheric aberration, a third order aberration that originates in fields at the ends of the solenoid. The spheric aberration emittance contribution is estimated with

$$\varepsilon_{n,\text{spheric}} \approx \sqrt{6}\gamma\beta \frac{|\tilde{C}_s|}{f} \sigma_x^4. \quad (4.39)$$

following Ref. [62]. The strength of the aberration  $|\tilde{C}_s|$  can be obtained by a particle tracking through the solenoid field. The current Gun 1 solenoid design in GunLab indicates a spheric emittance contribution of

$$\varepsilon_{n,\text{spheric}} = 0.0032(\sigma_{x,\text{Sol}}[\text{mm}])^4 [\text{mm mrad}]. \quad (4.40)$$

Because of the  $\sigma_x^4$  dependence of the geometric emittance on the transverse beam size, this contribution of the solenoid to the normalized transverse emittance cannot be neglected.

### Longitudinal Beam Dynamics in the Solenoid Magnet

In the following part, the development of the central parameters of the bunch in the longitudinal plane within the solenoid are considered. Even if the bunch momentum spread causes chromatic aberration effects that lead to a transverse emittance growth, the magnetic focusing keeps the **beam momentum**, and thus the **momentum spread** remains constant. Moreover, as the solenoid focuses in both transverse directions, it has no impact on the **longitudinal phase space** in the first order and, therefore, it does not contribute to the longitudinal emittance.

As the last crucial electron beam parameter, the **bunch charge** is also kept constant during the beam transformation through the solenoid magnet.

#### 4.3.4 Space charge

The Lorentz force in Equ. (4.15) is used to describe the impact of external electromagnetic and magnetic fields (RF cavity, solenoid) on the beam. These external fields do not depend on the beam current and the charge distribution in the bunch. Now, internal self-fields will be discussed.

Particles of the same charge are accumulated in a small bunch volume, whereby a Coulomb repulsion occurs in each bunch. In the following, these so called space charge effects are restricted to the collective regime. Therefore, only self-fields induced by the particle distribution, which only varies over large distances compared to the separation of the particles, are considered. Collisions between electrons and their neighbors in the bunch and the resulting effects are neglected.

Space charge (sc) effects influence the bunch directly from the emission process. At the photocathode, the bunch dimension is mainly affected and determined by the laser pulse volume. While the transverse electron beam size corresponds to the laser spot size on the cathode, the laser pulse length defines the initial bunch length. If the bunch is assumed as a homogeneous charged cylinder with a total charge  $q_b$ , a radius  $R$  and a length  $l$ , the sc electric field inside the cylinder at position  $s \leq R$  can be calculated with the Gaussian law:

$$\|\vec{E}\| = \frac{q_b s}{2\varepsilon_0 \pi R^2 l}. \quad (4.41)$$

If the space charge field  $\|\vec{E}\|$  should stay constant, the bunch length compression can only be achieved by blowing up the beam size. On the other hand, a minimization of the transverse phase space volume with transverse emittance compensation leads to an elongation of the bunch. The phase space volume is always preserved as well as the beam brightness. In this phenomenological description, the bunch is often compared to a waterbag that shows an expansion in one direction while it is compressed in the other one.

In accordance with Formula (4.41), the transverse *rms* beam size  $\sigma_x=R/2$  can then be expressed as

$$\sigma_x \propto \frac{1}{\sqrt{\sigma_z}}. \quad (4.42)$$

This equation gives a first hint to the trade-off between the transverse emittance and the bunch length that plays an important role in the injector optimization. The trade-off will be discussed in section 4.5 in detail.

In order to evaluate the impact of the space charge on the transverse and longitudinal beam dynamics, the self-force of the bunch is derived from the Lorentz force and the longitudinal and transverse space charge fields. For relativistic particles, the isotropic electrostatic field of the space charge in the rest frame is compressed to the transverse plane in the laboratory frame. This compression is due to Lorentz contraction. The relativistic effect is illustrated for the field lines of a charged particles with different velocities  $\vec{v}$  in Fig. 4.13. As a result, the longitudinal space charge component decreases fast for relativistic bunches ( $\gamma \gg 1$ ) and it can be neglected for that reason. The decision to consider the slices separately and without longitudinal interactions is based on that same reason, too. The space charge only affects the transverse phase space in the first approximation.

With a Lorentz transformation, the transverse sc Lorentz force on the bunch can then be expressed by

$$F_{sc,x} = e(E_x - v_z B_y)_{lab} = \frac{e}{\gamma} E_{x,rest}. \quad (4.43)$$

The change to the momenta in the transverse plane caused by the space charge can



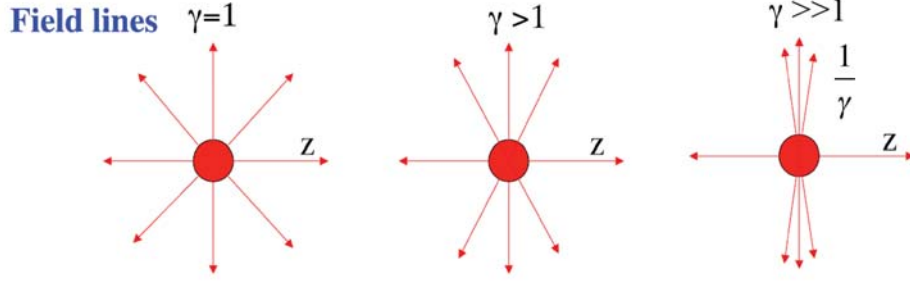


Figure 4.13: Lorentz contraction of the field lines of a charged particle at different energies [84].

be calculated through integrating the Lorentz force over time [see Equ. (4.44)]. After implementing some conversions that are shown in [80], the sc momentum contribution in the transverse plane is given by

$$\Delta p_x = \frac{1}{mc} \int F_x dt = \frac{\pi/2}{eE_0 \sin(\phi_0)} E_{sc,x}. \quad (4.44)$$

$E_{sc,x} = \frac{n_0}{4\pi\epsilon_0} \mathcal{E}_x$  describes the transverse space charge field in the rest frame defined by the line density at the bunch center  $n_0$ . Furthermore, the normalized field  $\mathcal{E}(x)$  is introduced with a dimension of an inverse length.

Due to the momentum change in the **transverse phase space**, the space charge force provides an emittance contribution. The momentum kick  $\Delta p_x$  is mainly affected by the transverse space charge field  $E_{sc,x}$  which is defined by the volume density of the charge distribution and the bunch volume itself. According to the slice model the transverse space charge field  $E_{sc,x}$  differs in the slices because of the individual slice charges  $q_{\text{slice}}(\zeta)$ , the transverse slice size  $\sigma_{x,\text{slice}}(\zeta)$  and the defined slice width  $\Delta\zeta$ . The individual transverse momentum changes in the slices leads to different slice emittance ellipse rotations, and thus to an increase of the total projected emittance.

Implementing the momentum change that is due to sc effects displayed in Formula (4.44) into the general form for the projected transverse emittance [see Formula (4.4)] provide the transverse sc emittance contribution

$$\epsilon_x^{sc} \approx \frac{\pi/4}{\alpha k \sin(\phi_0)} \frac{I_{\text{avg}}}{I_A} \mu_x(A) \quad (4.45)$$

where  $\alpha$  is the already defined RF field strength,  $I_{\text{avg}}$  is the beam average current and  $I_A$  is the Alfvén current [80]. The space charge emittance factor  $\mu_x$  represents the dependence of the space charge emittance contribution on the bunch charge distribution and the beam dimension considering the aspect ratio  $A = \sigma_x/\sigma_z$ , i.e., the ratio of the transverse beam width to the bunch length.

As a result of the nonlinear charge distribution in the bunch, an additional sc emittance growth occurs. This effect leads to a nonlinear transverse force that causes nonlinear ellipse rotations. Further, the slice emittances are not longer necessarily conserved. An evidence for such nonlinear sc forces are an s-shape in the transverse phase space ellipse.

It must be noted that space charge effects also set a limit to the extractable **bunch charge** at the photocathode during the emission process. The bunch charge can be increased by adjusting the intensity of the drive laser. The bunch charge is only linear to the laser energy at small values. At higher laser energies the dependence starts to become nonlinear since the extracted electrons create a growing external field that counteracts the accelerating field [see Fig. 4.14].

The absolute space charge limit is reached when the space charge field is equal to the applied accelerating field  $E_z$ . In this case the *rms* minimum size of a cylindrical bunch with radius  $R$  for a requested bunch charge  $q_b$  and applied accelerating field  $E_z$  can be assumed as [43]

$$\sigma_x = \sqrt{\frac{q_b}{4\pi\epsilon_0 E_{\text{acc}}}}. \quad (4.46)$$

It follows that the space charge limit provides a lower bound to the intrinsic beam emittance of

$$\epsilon_{\text{in}}^{\text{SCL}} = \sqrt{\frac{q_b(\hbar\omega - \Phi_{\text{eff}})}{\pi\epsilon_0 m c^2 E_{\text{acc}}}}. \quad (4.47)$$

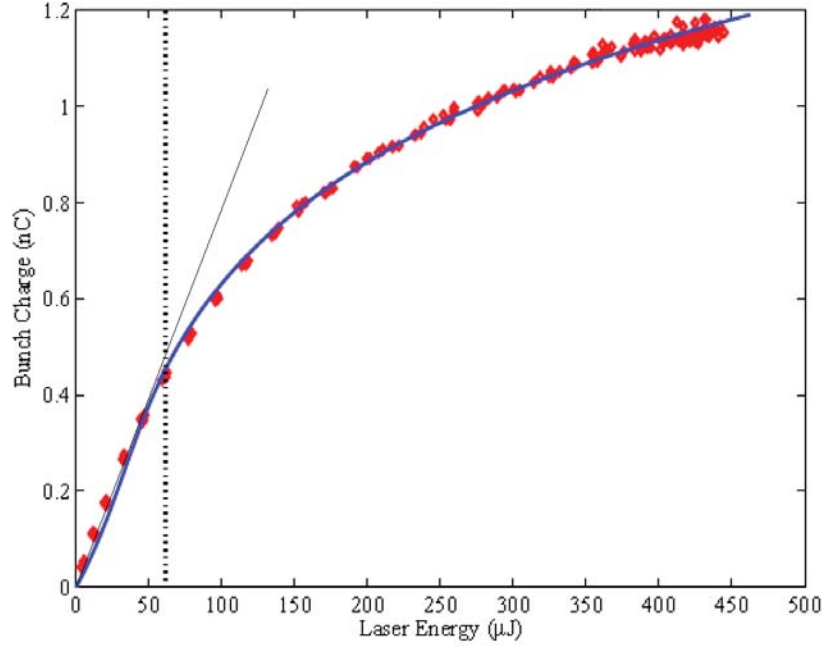


Figure 4.14: Emitted bunch charge over the drive laser energy [43]. The bunch charge converges against the sc limit at a higher laser energy. The data were taken from the LCLS gun operating at a peak cathode field of 115 MV/m. The beam size was constant (0.6 mm radius) but the QE of the photocathode changed [85].

### 4.3.5 Complete beam dynamics in an SRF photoinjector

To provide an interim conclusion, it can be summarized that the four most crucial electron beam parameters are strongly affected by the processes of bunch generation, acceleration, focusing and self-fields. Only the photocathode and the drive laser determine the **bunch charge** during the emission, provided that no particles are lost and no field emission occurs. The space charge effect sets a limit to the maximum extractable bunch charge. The final bunch **energy** is presented by the sum of the electron rest energy  $E_0$ , the mean transverse energy  $MTE$  after emission and the energy gain due to the acceleration in the gun cavity  $E_{acc}$ .

$$E_{tot} = E_0 + MTE + E_{acc}. \quad (4.48)$$

The total **emittance** can be summarized as the square root of the sum of all squared emittance contributions from the different beam path elements and the space charge

[83].

$$\varepsilon_{\text{tot}} = \sqrt{\varepsilon_{\text{in}}^2 + \varepsilon_{\text{rf}}^2 + \varepsilon_{\text{chrom}}^2 + \varepsilon_{\text{geo}}^2 + \varepsilon_{\text{sc}}^2}. \quad (4.49)$$

This expression for the total emittance represents an approximation since the emittances for all emittance contributors are calculated separately and correlations are neglected. Equ. (4.49) can thus be used for a first estimation of the total emittance value. Furthermore, the scaling of the emittance to beam and SRF photoinjector parameters can be analyzed. In order to run an SRF gun in a high brightness mode with the smallest total emittance, as indicated in the given gun design, the emittance must be evaluated for the complete photoinjector. A global parameter optimization based on numerical methods is required for the complete ensemble of beam path elements as a unit.

All emittance contributions are calculated for a 77 pC bunch in the 1.4 cell 1.3 GHz SRF gun in GunLab. The results are plotted as a function of the beam radius at the photocathode as shown in Figure 4.15. The intrinsic and space charge emittances occur right at the cathode. Here, the transverse emittance can be expressed as the product of the transverse beam size and the beam divergence. The linear proportionality of the intrinsic and sc emittance contributions to the cathode radius is visible in Figure 4.15. The RF and solenoid emittance contributions provide an emittance minimum. This minimum originates from a beam size minimum at the gun cavity exit iris and the solenoid entrance, respectively. Smaller cathode radii that increase space charge forces lead to larger beam sizes and consequently to an emittance degradation. A larger cathode radius above this minimum causes a growing beam size due to the beam optics. Figure 4.15 also illustrates that the intrinsic and space charge emittance contributions, together with the chromatic emittance from the solenoid represent the relevant portions of the total transverse emittance. This fact is independent from the corresponding cathode radius. The RF and spheric emittance contributions play a minor part in the total transverse emittance.

Together with the central electron beam parameters, the paraxial ray equation [see Equ. (4.50)] fully characterizes the bunch state and its motion through the SRF photoinjector, and thus the evolution of the *rms* beam envelope, at any point of the photoinjector and at any time of the gun acceleration process.

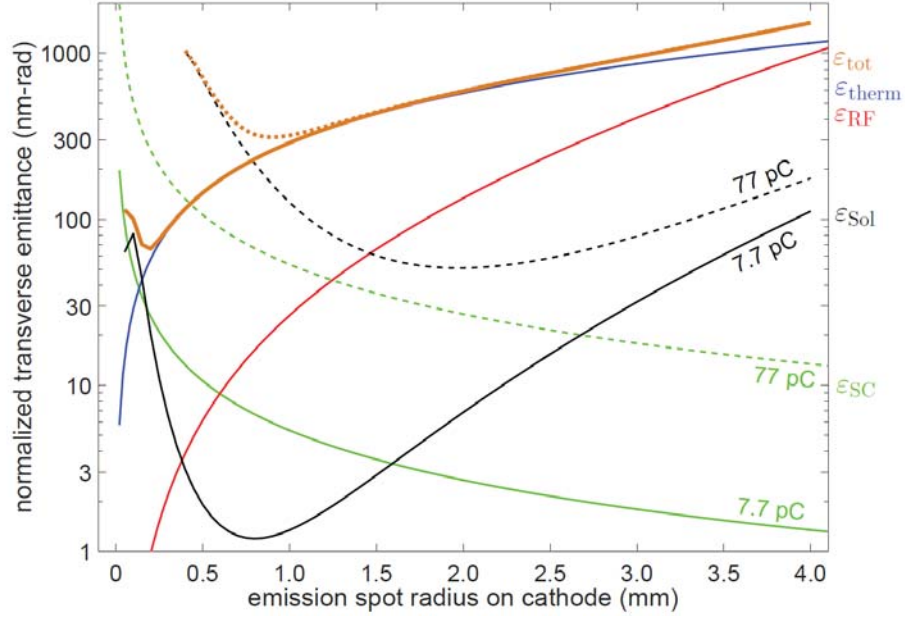


Figure 4.15: Emittance contributions from the photoemission (intrinsic) [blue], the RF field [red], the solenoid aberration effects [black] and the space charge [green] displayed for a diagnostic mode with 7.7 pC bunch charge (solid lines) and the high average current mode of bERLinPro with a bunch charge of 77 pC (dashed lines). The emittance values are calculated for an SRF gun cavity with 30 MV/m cavity peak field. The electrons are emitted by a 3.76 ps long laser pulse and injected to the cavity at the on-crest phase (44.7 deg). The cathode is placed -15 mm behind the cavity back plane. The total emittance is calculated based on Equ. (4.49) [orange curve] (Courtesy Jens Völker, HZB [62]).

In the paraxial limit, the assumptions are made that the bunch moves mainly in the  $z$ -direction  $v_\phi < v_z$ , in an axisymmetric system, close to the  $z$ -axis with a small transverse slope  $r' = dr/ds \ll 1$ . Further, a narrow energy spread is assumed. The Lorentz-force written in cylindrical coordinates together with the Maxwell equations lead to the paraxial ray equation [11]

$$\sigma'' + \frac{\gamma'}{\gamma\beta^2}\sigma' + \frac{\gamma''}{2\gamma\beta^2}\sigma + K^2\sigma - \left(\frac{4p_\phi}{mc\gamma\beta}\right)^2 \frac{1}{\sigma^3} - \frac{\varepsilon_n^2}{\beta^2\gamma^2\sigma^3} - \frac{\kappa_{sc}}{\sigma} = 0. \quad (4.50)$$

$r''$  defines the change of the trajectory slope, within the second terms represents the RF effect of the axial accelerating electric field  $E_z$  on the transverse movement. The impact of the radial electric RF field  $E_r$  causing a radial focusing or defocusing of the beam is displayed in the third term. Additionally, the impact of an external magnetic

force from a solenoid is considered. Here, the factor  $K = qB/2p$  corresponds to the magnetic strength. If the particles provide a canonical angular momentum  $p_\phi$  this contributes further to the beam dynamics equation. The next term displays the outward pressure due to the normalized *rms* emittance. Lastly, the space charge force inside the bunch must be considered. The parameter  $\kappa_{sc}$  in the last term is called the generalized perveance. The dimensionless parameter does not depend on the beam radius but contains the beam current  $I$  and the beam energy  $\gamma$ :

$$\kappa_{sc} = \frac{I}{2I_A \beta^3 \gamma^3}. \quad (4.51)$$

### 4.3.6 Impact of the electron bunch parameters on the beam brightness

The last section established how the diverse processes of the beam generation, first acceleration and manipulation in an SRF gun determine the beam dynamics. Now, the impact of the SRF photoinjector parameters on the most crucial electron beam parameters and, therefore, on the beam brightness will be discussed.

Three of the four electron beam parameters that characterize the bunch also contribute to the 6D brightness [see Formula (4.12)]: The bunch charge  $q_b$ , the transverse emittance  $\varepsilon_{x,y}$  and the longitudinal emittance  $\varepsilon_z$ . The beam energy is specified by the experiment that is driven by the electron source.

In the following discussion, the beam brightness is restricted to the 5D peak brightness [see Formula (4.13)] and the momentum spread of the bunch is neglected. The brightness studies of this dissertation are mainly based on GunLab, a photoinjector designed to operate an ERL or to drive diffraction experiments. Hence, the central beam parameters are given by the transverse emittance and the bunch length. Short bunch lengths enable high peak currents in the ERL, short synchrotron pulses, coherent radiation in an undulator and a high time resolution for time resolved diffraction experiments. The momentum spread in the bunch is frequently used to compress the bunch length [see section 4.4.3]. Thus, it cannot be minimized along the beam line in order to allow this compression process. Furthermore, the momentum spread of the bunch in the keV regime plays a minor role in the synchrotron radiation generation since the radiation power is proportional to the 4th power of the beam energy  $E^4$  [10].

The central task in the photoinjector operation is to maximize the beam brightness. If the 5D peak brightness in equation (4.13) is considered, the beam brightness can be maximized by increasing the bunch charge while minimizing the transverse emittance and the bunch length. As the bunch charge is normally set by the main accelerator and/or the user experiments, the objective is to find a way to render the emittance and bunch length as small and as short as possible.

The next section will answer the question of how a photoinjector can be pushed to a high brightness operation. Several solutions that aim to generate a high brightness beam, to minimize the transverse emittance and the bunch length will be discussed.

## 4.4 Beam Brightness Maximization in an SRF Photoinjector

The beam brightness can be maximized by choosing an appropriate charge distribution and bunch shape at the cathode and by optimizing the transverse emittance and bunch length along the photoinjector beam path.

### 4.4.1 Bunch shape optimization

Following the theory in Section 4.3, internal space charge forces greatly affect the bunch transport right behind the cathode in the non-relativistic section. As already mentioned, nonlinear charge distribution like Gaussian beams cause nonlinear, slice-dependent space charge forces. In order to avoid the additional emittance growth and the subsequent beam brightness degradation, the ideal bunch shape that best preserves the brightness during the transport through the photoinjector is a so called “waterbag” bunch, a uniformly filled, ellipsoidal distribution. In this case, the acting space charge forces are linear and slice-independent. The two different bunch charge distributions are illustrated in Fig. 4.16.

There are different ways to generate such a charge distribution [86]:

- Direct ellipsoidal laser pulse shaping
- “Pancake” laser pulse combined with longitudinal space charge expansion
- “Cigar” laser pulse combined with transverse space charge expansion

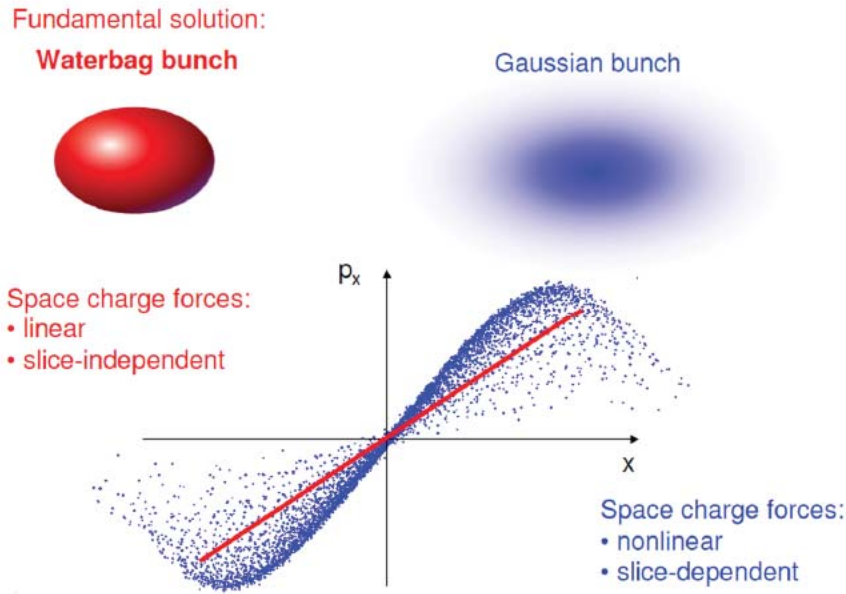


Figure 4.16: “Waterbag” and Gaussian distributed bunches and the corresponding phase spaces [86].

All of these techniques are based on laser shaping. The transverse spot size and the laser pulse length defines the laser pulse volume. In the first approximation, it sets the initial bunch distribution at the photocathode right after the emission process.

In the case of ellipsoidal laser pulse shaping, the photocathode drive laser is elliptically shaped, thereby generating a “waterbag” bunch. Ellipsoidal lasers are part of the latest research and therefore this technique has not yet been fully approved. The photoinjector test stand PITZ at Desy Zeuthen Germany just started to operate an ellipsoidal photocathode laser [87].

Another possibility for brightness maximization by bunch shape optimization is to provide a “pancake” or “cigar” shaped laser pulse. “Pancake” laser pulses are short in the longitudinal direction and illuminate the photocathode with a large transverse spot size. In contrast, laser pulses in the “cigar” regime represent the opposite, with relatively long pulses and small spot sizes. The ellipsoidal bunch shape is then achieved by a longitudinal (“pancake”) or transverse (“cigar”) sc expansion in the non-relativistic part shortly behind the cathode in the photoinjector.

The highest achievable beam brightness at the photocathode can be achieved close to the photoemission saturation, where the sc field on the cathode is equal to



the accelerating RF electric field. For the saturation output charge, a formula can be derived that refers to both the “pancake” and the “cigar” regime. The beam radius at the cathode is expressed by  $R$ . The emission bunch length in the non-relativistic case can be expressed by

$$\Delta z_e = \frac{eE_0}{2m} \Delta \tau_{\text{laser}}^2. \quad (4.52)$$

Here,  $E_0$  describes the accelerating field at the cathode,  $m$  is the electron mass and  $\Delta \tau_{\text{laser}}$  defines the laser pulse length. The theory regarding “pancake” and “cigar” regime is only valid for laser pulse lengths smaller than one RF period.

In the “cigar” regime, the condition  $\Delta z_e > R$  must be fulfilled. The saturation bunch charge can be derived from the Child-Langmuir law as [88]

$$q_{\text{b,cigar}}^{\text{sat}} = I_A \frac{\sqrt{2}}{9} \left( \frac{eE_0 R}{mc^2} \right)^{3/2} \tau_{\text{laser}} \quad (4.53)$$

where  $I_A$  is the Alfvén current. Considering the 5D brightness (4.13) and an transverse normalized *rms* emittance  $\varepsilon_{\text{norm.,x,y}} = \frac{R}{2} \frac{\sigma_p}{mc^2}$  with a *rms* transverse momentum spread  $\sigma_p$ , the cathode brightness limit in the “cigar” regime can be formulated as

$$B \propto \frac{E_0^{3/2} \tau_{\text{laser}}}{\sigma_p^2 \sqrt{R} \Delta z_e}. \quad (4.54)$$

This equation confirms that the beam brightness significantly improves with not only higher gun cavity gradients, but also with shorter and transversely compact laser pulses. The “cigar regime” represents a promising bunch shape to generate and maintain high brightness beams. The long laser pulse length gives an additional control knob for the source optimization by adjusting the temporal laser pulse profile. The relatively long electron bunch can be compressed downstream during the acceleration, when the beam becomes relativistic, using a buncher cavity or a magnetic chicane. The small laser spot size leads to a small intrinsic emittance.

The “pancake” scenario represents the longitudinal counterpart of the “cigar” regime. It occurs when the requirement  $\Delta z_e < R$  is fulfilled. The beam presents an

infinitely thin sheet of charge which is only defined by the surface charge density  $\sigma_{\text{sat}}$ . The saturation bunch charge is then given by [88]

$$q_{\text{b,pancake}}^{\text{sat}} = \sigma_{\text{sat}}\pi R^2 = \epsilon_0 E_0 \pi R^2 \quad (4.55)$$

Due to the proportionality of the saturation bunch charge to the squared laser spot size, the ‘‘pancake’’ brightness limit becomes independent of  $R$  [89].

$$B \propto \frac{E_0}{\sigma_p^2 \Delta z_e}. \quad (4.56)$$

Nevertheless, even though the beam brightness is at its limit at the cathode, the large beam size at the cathode leads to large emittance contributions in the further photoinjector. For that reason, the solenoid needs to largely compensate the emittance.

The laser pulse shaping generates a high brightness beam at the photocathode and the bunch reaches the optimum ellipsoidal shape right after the cathode in the non-relativistic range. It can then be transported through the remaining photoinjector and the following accelerator while it maintains its high brightness level as best as possible. The following sections will present different methods to minimize the two electron beam parameters that most impact the beam brightness: The transverse emittance and the bunch length

## 4.4.2 Emittance minimization

### Minimizing Emittance Contributions in the SRF Gun

Together with nonlinear space charge forces, the photoinjector components lead to an emittance growth in the SRF gun. Equation (4.49) displays all contributions of the different beam path elements and the contribution that occurs from space charge to the transverse normalized emittance. To minimize the total emittance, the individual components must be decreased.

The intrinsic emittance [see Equ. (4.18)] is directly proportional to the transverse laser spot size  $\sigma_x$  on the cathode. The emittance can be reduced significantly with a smaller laser diameter. Moreover, a good cathode treatment during its preparation,

transport and operation that leads to a high and constant quantum efficiency  $QE$ , can improve the intrinsic emittance significantly. The reason is that the  $QE$  is proportional to  $\sqrt{(\hbar\omega - \phi_{\text{eff}})}$  and therefore proportional to the intrinsic emittance  $\varepsilon_{\text{in},x,y}$ .

The laser spot size also affects the RF emittance contribution [see Formula (4.34)]. The squared dependence represents a powerful adjustment for decreasing the RF contribution to the total emittance. Again, the task is to minimize the laser spot size on the cathode. Furthermore, due to RF defocusing the emittance contribution is proportional to the bunch length  $\sigma_z$  while the second RF emittance contribution provides a  $\sigma_z^2$  dependency. Thus, the bunch length and therefore the laser pulse length should also be minimized to limit the RF emittance contribution.

The chromatic and spheric emittances from the solenoid [see Equ. (4.38) and (4.39)] are proportional to the second and fourth power of the beam size at the solenoid entrance. The beam size at the solenoid can be controlled if the magnet is placed as close as possible to the gun cavity. Thereby, drift space is avoided between the cavity and the solenoid which would otherwise enable the bunch to become defocused up to the solenoid entrance due to the RF defocusing effect of the cavity exit. Further, a small initial spot size of the laser represents again a good starting point for a moderate beam size at the solenoid entrance and therefore for small emittance contributions.

Finally, the space charge determines the lower limit of the beam emittance by the space charge limit (see Equ. (4.47)) if no further emittance contributions from the RF gun and the solenoid would occur. The space charge emittance contribution in formula (4.45) can be minimized by freezing the space charge force. This is achieved by accelerating the beam fast with a high gun gradient because the radial defocusing sc force decreases with  $1/\gamma$ . The space charge emittance contribution is, therefore, indirect proportional to the field strength  $\alpha$  of the SRF gun. The transverse emittance also decreases when minimizing the peak current  $I_{\text{peak}}$  of the bunch. Since the bunch charge and the average current are often determined by the experiment for which the accelerator is used, this is a rather impractical solution. The emittance space charge component  $\varepsilon_{\text{sc},x,z}$  is affected by the charge distribution  $\mu_{x,z}$  of the electrons in the bunch. The task is thus to maximize the distance between the particles in the bunch in order to decrease the Coulomb repulsion force, and to simultaneously keep the bunch volume as compact as possible. The two extremes of a large transverse beam

size and a short bunch length - a “pancake” beam - and a small transverse size and a long bunch length - a “cigar” shape - fulfill these conditions. As already mentioned, in the case of a pancake beam, the maximum extractable surface charge density is only set by the gun field at the cathode. In the cigar-regime, higher bunch charges can be extracted from the cathode since only a small part of the bunch contributes to the space charge field [43].

In addition to minimizing the different emittance components by decreasing the laser spot size and the laser pulse length by a suitable placement of the solenoid, by fast acceleration with high gun gradients and by choosing a specific particle distribution, emittance compensation is also applicable with the solenoid magnet.

### Solenoid Emittance Compensation

The slice model helps to theoretically derive the transverse emittance compensation with the solenoid. Misaligned slices lead to an increased projected transverse emittance, as the projected emittance is formed by the superposition of the individual slices with their corresponding form, slice emittance, and orientation. Hence, a minimum projected emittance can be achieved when all slices have nearly the same, preferably small slice emittances and angles of the ellipses in the phase space. This is exactly the case right after the emission of the electron bunch. The thermal emittance stays just about constant over the bunch length. Therefore, each slice provides the same slice emittance. After the emission process RF and space charge forces act on the slices because of the finite bunch length and different slice charges. The ellipses of the slices transform in different ways in the phase space. They are displaced and distorted in relation to each other. In order to compensate this mismatch, a radial force is required to rotate the phase space ellipses. The radial focusing then depends on the settings in the focusing channel of the photoinjector. Figure 4.17 illustrates the described process.

The theory of emittance compensation for an RF photoinjector with a solenoid magnet placed around the gun cavity has been illustrated by Serafini and Rosenzweig [90]. In their explanation, the paraxial ray equation describing the beam envelope evolution is solved for Brillouin flow. In this assumption the sc force is balanced by the focusing axial magnetic field and, therefore, the corresponding transverse beam size  $\sigma_{\text{eq}}$  is maintained as constant in this equilibrium. The conditions for a Brillouin flow are: a low emittance beam ( $\frac{\epsilon_n^2}{\gamma^2 \beta^2 \sigma^3} \rightarrow 0$ ), a zero angular momentum  $p_\phi$  and no

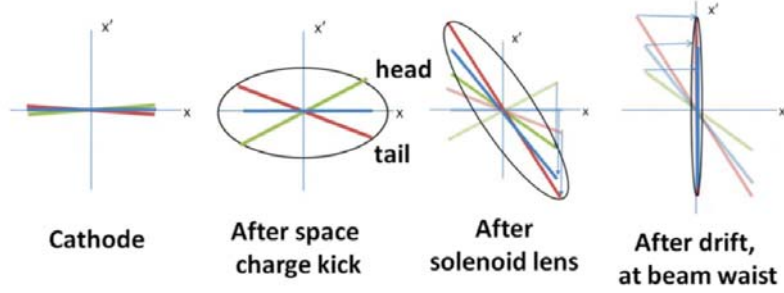


Figure 4.17: Orientation of the beam slices along the beam path. Starting aligned at the cathode, the slices mismatch due to space charge effects. The solenoid causes a slice alignment at or near the beam waist and the projected transverse emittance goes through a minimum [43].

acceleration. Thus, the envelope equation is linearized [see Equ. (4.50)]. The beam in a Brillouin equilibrium fulfills no radial acceleration  $\sigma_{\text{eq}}'' = 0$  with a equilibrium solution  $\sigma_{\text{eq}} = \frac{\sqrt{\kappa_{\text{sc}}}}{K^2}$ , i.e., the ratio of the generalized perveance of the sc effects and the magnetic field strength of the solenoid.

The beam starts at the cathode with all slices showing nearly the same peak current and propagating with the slice size  $\sigma_{\text{eq}}$  in the Brillouin flow. Afterwards, the equilibrium beam size in the photoinjector depends on the slice charge density and thus on the geometric factor  $g(\zeta)$ . Serafini and Rosenzweig then solve the paraxial ray equation for beam sizes with a small initial perturbation  $\delta\sigma(\zeta, 0)$  around the equilibrium value

$$\sigma(\zeta, 0) = \sigma_{\text{eq}}(g(\zeta)) + \delta\sigma(\zeta, 0). \quad (4.57)$$

Setting the expression into the envelope equation and solving this differential equation leads to perturbed trajectories that oscillate around the equilibrium beam size

$$\sigma(\zeta, z) = \sigma_{\text{eq}}(g(\zeta)) + \delta\sigma(\zeta, 0) \cos(\sqrt{2}Kz + \phi(\zeta)). \quad (4.58)$$

Independent of the slice charge, the focusing strength of the solenoid defines the oscillation frequency of the slices. The oscillation amplitudes are given by the initial beam size perturbation of the slices depending on the individual current values [90]. The

phase shift  $\phi(\zeta)$  is added to the original theory of Serafini and Rosenzweig [62]. Since they derive the emittance compensation of an RF photoinjector, the solenoid field starts right at the cathode. Therefore, no initial slice mismatching must be taken into account. In the case of an SRF photoinjector, the solenoid cannot be placed around the gun cavity as all magnetic field lines are excluded by the superconducting material due to the Meissner effect [58]. As a result, the focusing channel starts downstream the beam path close to the cavity exit. The additional parameter  $\phi(\zeta)$  indicates the initial slice misalignment at the focusing channel entrance.

The oscillations cause an additional emittance contribution beside the emittance impacts due to the beam path elements and the space charge effects presented in section 4.3. The oscillation contribution can be derived from the beam size  $\sigma(\zeta, z)$  and its derivative  $\sigma'(\zeta, z)$  according to Equ. (4.4). The slice emittances are averaged over  $\zeta$  in order to display the projected emittance contribution

$$\varepsilon \sim \sigma(\zeta, 0)\sigma_{\text{eq}}(I_{\text{peak}})\frac{K}{2}|\sin(\sqrt{2}Kz)|F(K, z, \phi(\zeta)). \quad (4.59)$$

Assuming all slices match at the cathode, a re-alignment takes place at certain positions behind the cathode, which are defined by the solenoid strength. At those positions, the projected emittance has local minima. Although the beam size oscillates with the same frequency, its phase is shifted by  $\pi/2$ .

This emittance compensation model by Serafini and Rosenzweig is now adopted to an SRF photoinjector. Compared to an RF photoinjector, where the focusing channel starts right at the cathode, which consists of the solenoid and the radial RF cavity focusing, the focusing and emittance compensation in an SRF gun is only based on the solenoid magnet and the drift space behind. The focusing of the RF wave is not strong enough to realign the slices. The momentum spread imparted to the bunch in the RF field leads to a solenoid magnetic strength  $K$  that does not stay constant in the focusing channel. In order to drive the emittance compensation process in an SRF gun the slices start with beam sizes  $\sigma(\zeta, 0)$  that are bigger than the equilibrium width  $\sigma_{\text{eq}}(\zeta)$ . Hence, the space charge term in the paraxial ray equation can be neglected.  $\delta\sigma$  is too large to solve the equation with the small perturbation theory. First of all, the solenoid magnet focuses the beam until its beam size is close to  $\sigma_{\text{eq}}(\zeta)$ . Then, the beam slice starts to oscillate, as was predicted by Serafini and Rosenzweig. The

space charge becomes important again. The focal point of the solenoid is reached at a beam waist of  $\sigma_{\text{eq}}$ . The two minima in the projected emittance lie in the vicinity of the beam waist at the so-called emittance compensation points [62].

The mathematical description of these two transverse emittance minima can be found in [91]. Fig. 4.18 shows the beam divergence as a function of the beam size during the emittance compensation process for two different slices, one in the bunch center with a high slice charge (red curve) and a low charge slice (green curve) at the bunch head or tail.

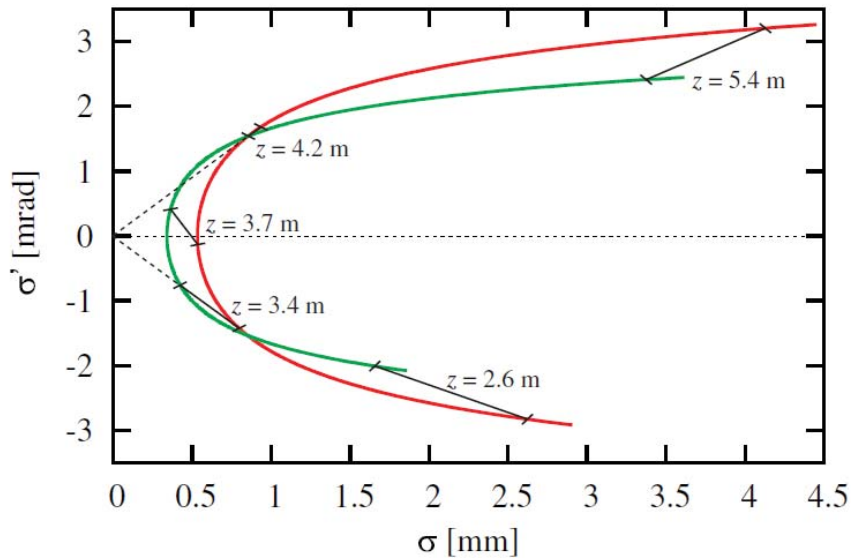


Figure 4.18: Divergence as a function of the beam size during the emittance compensation process. The red curve represents a high charged slice at the bunch center. The green curve corresponds to a low charge slice at the head or the tail of the bunch. Points corresponding to the same longitudinal position  $z$  are connected with a black line [91].

Points corresponding to the same longitudinal position are connected with black lines. The beam waist is indicated by the smallest beam size values and does not show any detectable slice divergence. Around this beam waist, the two curves cross each other and the extension of the position-connecting lines run directly through the point of origin. Therefore, the ellipses are aligned at these two points. The overall emittance contribution is affected by the beam size mismatch resulting from the aligned slices. In the presented example, the first emittance minimum at 3.4 m provides a higher transverse emittance contribution due to the strong beam size mismatch of

around 0.4 mm between the analyzed slices. If a large slice emittance or a large beam size mismatch occurs, the first emittance minimum might be attenuated so that only one emittance minimum can be detected. This is the case in some optimization results that will be presented in Chapter 6.

Figure 4.19 shows that emittance compensation also works with an SRF photoinjector and a solenoid magnet behind the gun cavity. The small emittance growth behind the solenoid can be referred to as nonlinear space charge effects that increase the emittance values of the individual slices. The difference between the projected emittance values and the slice emittance values in the emittance compensation point results from the misalignment of the slices which cannot be fully compensated.

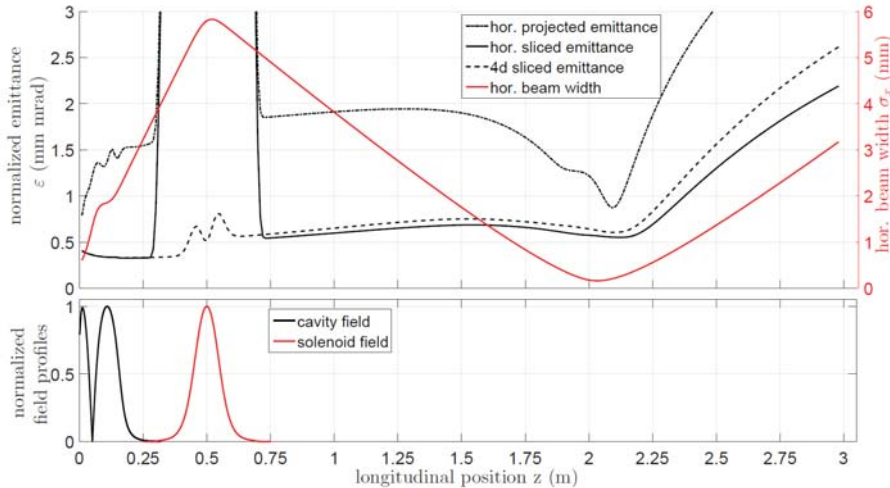


Figure 4.19: Evolution of the horizontal beam size (red curve), the horizontal projected emittance (dashed line) and the slice emittance (black curve) along the beam axis. The emittance compensation point follows shortly behind the beam waist at  $z=2.1$  m (Courtesy Jens Voelker, HZB [62]).

If a booster section follows on the photoinjector, the entrance of the booster must be placed close to the emittance compensation point in order to maintain the minimized emittance value in the subsequent injection line up to the main linac.

The next section will offer several solutions in order for minimizing the bunch length and to, thereby, maximize the beam brightness.



### 4.4.3 Bunch compression

Equ. (4.13) showed that the maximum beam brightness can be reached by minimizing the bunch length. Furthermore, short bunches enable high peak currents that are required for several experiments in the advanced accelerator physics, e.g., linear colliders or single pass FELs. Formula (4.60) represents the indirect proportionality between the peak current and the *rms* bunch length  $\sigma_z$ :

$$I_{\text{peak}} = \frac{q_b}{\sigma_z}. \quad (4.60)$$

Several strategies lead to small bunch lengths. They can be classified according to the following four categories:

- 1) Generate short bunches directly at the electron source
- 2) Bunch compression is due to RF effects
- 3) Bunch compression is reached by manipulating the longitudinal bunch shape
- 4) Select only one part of the bunch during the beam transport

The first three methods are usually applied to photoinjectors. The suggestion of using only a small slice of the bunch to keep the bunch length short applies a concurrent undesired reduction of the bunch charge and causes a decrease in the peak and average current.

In order to generate short bunches in photoinjectors, the pulse length of the drive laser must be reduced. Equ. (4.52) displays the correlation between the laser pulse duration and the formation length of the bunch. A moderate transverse laser spot size on the cathode balances space charge effects. The electron bunch is then emitted in a pancake shape. Depending on the drive laser, bunch lengths in the sub-ps range can be achieved.

### Energy Chirping

If further bunch compression is required the longitudinal compression effect of the RF cavity can be applied and the longitudinal phase space can be manipulated with a magnetic chicane or velocity bunching. All three methods are based on a correlation

between the energy and the longitudinal position of the particles in the bunch. This energy chirp is imparted on the bunch in any RF cavity that is operated off-crest at phase  $\phi$ . The energy chirp can be derived considering a particle at position  $\zeta = \Delta t/c$  that is relative to the reference particle at  $\zeta = 0$  inside the bunch [see Fig. 4.20].

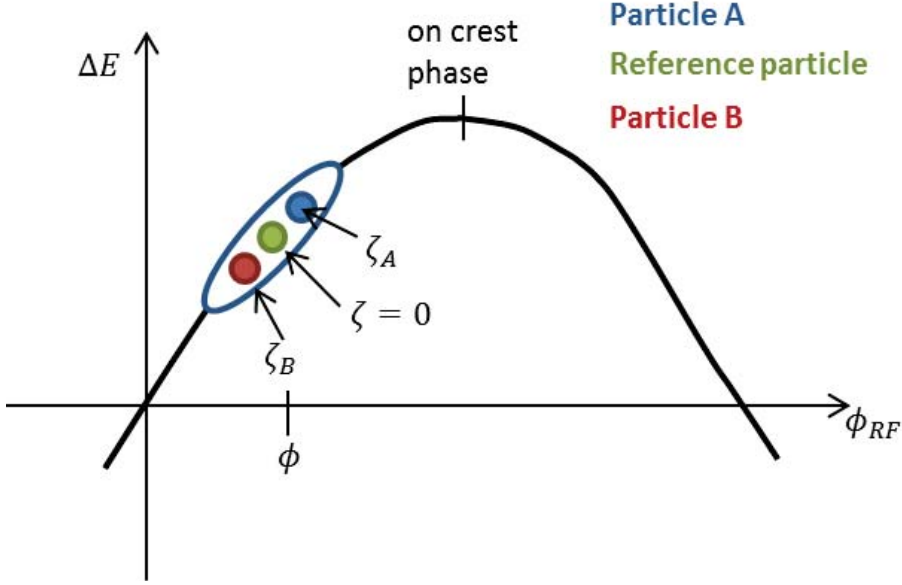


Figure 4.20: The bunch is injected at phase  $\phi$  to the RF cavity. Particle A in the rear part of the bunch achieves a higher energy gain than the reference particle and the particle B in the bunch front due to the time dependent RF wave.

Due to Equ. (4.21) the particle observes a longitudinal accelerating field  $E_z$

$$E_{z,\zeta} = E_{z,0} \cos(kz) \sin(\omega t_{\text{ref}} - \omega \Delta t + \phi). \quad (4.61)$$

Here  $E_{z,0}$  describes the accelerating peak gradient.

Integrating the  $E_z$  field over the cavity length leads to an energy gain  $\Delta E_\zeta$  of the particle at position  $\zeta$ . The final particle energy  $E_f(\zeta)$  behind the gun cavity is given by the initial energy and the energy gain.  $E_f(\zeta)$  depends on the position of the electron  $\zeta$  in the bunch.

$$E_f(\zeta) = E_i + \Delta E = E_i + eV_0 \sin(k\zeta + \phi) \quad (4.62)$$

with  $E_i$  representing the initial energy of the bunch before it enters the RF cavity.  $V_0$  is the accelerating peak voltage. The presented method exploits the finite length of the bunch expanding the bunch energy spread  $\Delta E$

$$\Delta E = \frac{\Delta E_\zeta}{E_f(\zeta = 0)} = \frac{eV_0}{E_i + eV_0 \sin(\phi)} [\sin(k\zeta + \phi) - \sin(\phi)]. \quad (4.63)$$

The linear chirp can be calculated from the derivation of the energy spread  $\Delta E$  with respect to the particle position  $\zeta$  in the bunch.

$$h = \frac{d\Delta E}{d\zeta} = \frac{eV_0 k \cos(\phi)}{E_i + eV_0 \sin(\phi)} \Big|_{\zeta=0}. \quad (4.64)$$

Therefore, the bunch energy spread can be expressed in first order by the linear chirp  $h$  [92]

$$\Delta E_0 = h\zeta + \mathcal{O}(\zeta)^2. \quad (4.65)$$

It follows that small beam energies lead to high energy chirps and a strong bunch compression.

In order to impart an energy chirp on the bunch the RF field of the gun cavity can be used. Alternatively, a separate cavity can be added to the beam path. These so called buncher cavities are mostly placed behind the photoinjector and they operate at zero-crossing. Therefore, a buncher cavity does not provide any net acceleration but it imprints an energy-time correlation to the bunch. K. Sakaue presented a new innovative method in 2014 [93]. He combined a conventional 1.6 cell gun cavity with an attached energy chirping cell (ECC) (see Fig. 4.21). Due to its cavity geometry, the bunch enters the ECC cell near the zero-crossing phase that leads to a maximum energy spread.

Based on the energy chirping effect the bunch compression that is caused by RF effects can be analyzed.

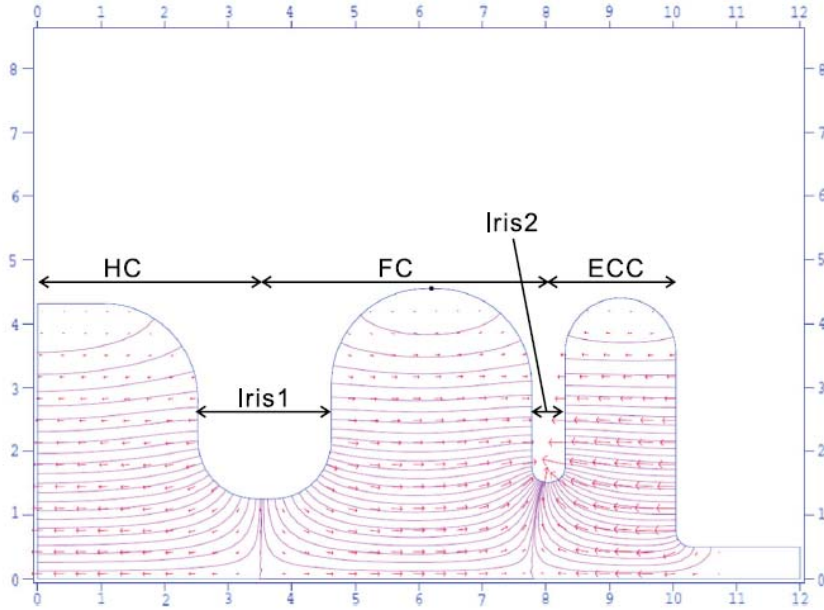


Figure 4.21: Profile of an ECC-RF Gun. The ECC cell is attached to a 1.6 RF cavity with one half-cell (HC) and one full-cell (FC) [93].

### Bunch Compression caused by RF Effects

Bunch compression, which is the result of RF effects, is the only method mentioned above that can be observed in any SRF gun without actively manipulating the photoinjector parameters or additional elements in the beam path further. The bunch compression is based on the phase slippage of the bunch, as described in Formula (4.28) [80]. Two electrons in the bunch, one at the reference position and one in the bunch tail, are injected from the cathode to the RF field at phase  $\phi_0$  and  $\phi_0 + \Delta\phi_0$  respectively. Both electrons are accelerated by the RF field in a different way caused by the phase shift. Therefore, the phase difference  $\Delta\phi$  will not stay constant but will shrink during the acceleration if the tailing electron is energetically higher than the reference particle. The quotient of the final phase difference  $\Delta\phi_\infty$  at the cavity exit after the phase slippage to the initial phase difference  $\Delta\phi_0$  represents the bunch compression factor

$$\frac{\Delta\phi_\infty}{\Delta\phi_0} = 1 - \frac{\cos(\phi_0)}{(2\alpha \sin^2(\phi_0))}. \quad (4.66)$$

This form of bunch compression only depends on the accelerating field strength  $\alpha$

and the injection phase  $\phi_0$ . Since a low energy bunch in the SRF gun cavity suffers from the strong impact of its internal space charge forces, the bunch length compression merely leads to a suppression of the bunch expansion that is induced by the space charge. As a consequence, further bunch compression is required using velocity bunching or a magnetic chicane.

### Velocity/Ballistic Bunching

Another concept for bunch compression combines an RF structure for energy chirping and a drift space. This method is usually applied at low energies [92]. Since

$$\frac{d\zeta}{dz} = \frac{\gamma}{\sqrt{\gamma^2 - 1}} \neq 0 \quad (4.67)$$

with  $\gamma$  describing the Lorentz factor, the particles in the bunch provide a significant difference in their velocities behind the RF structure. If the energy chirping leads to larger energy particles in the bunch tail compared to the leading ones, the bunch will be compressed in the drift line [see Fig. 4.22] while the longitudinal phase space correlation is removed. It follows that the bunch injection phase must be smaller than the on-crest phase,  $\phi_0 < \phi_{\text{oncrest}}$ .

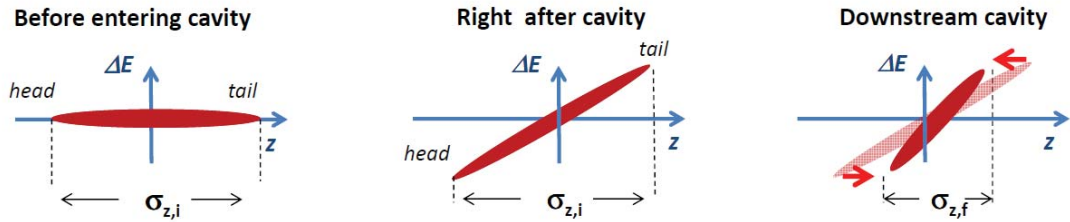


Figure 4.22: The evolution of the longitudinal phase space along the beam line is displayed. After the phase space ellipse is rotated due to momentum chirping in the RF cavity, the bunch length  $\sigma_z$  is compressed in the drift space downstream the cavity [92].

The final bunch length  $\sigma_{z,f}$  is given by the initial bunch length  $\sigma_{z,i}$  at the cavity entrance, the bunch energy spread  $\sigma_{E,i}$  and the  $R_{56}$  element of the transfer matrix of the beam path [94].

$$\sigma_{z,f} = \sigma_{z,i} + R_{56}\sigma_{E,i}. \quad (4.68)$$

The sum of the energy spread, due to the chirp, and the uncorrelated energy spread of the bunch define the total energy spread. The uncorrelated energy spread of a photoinjector stems from the temperature of the cathode as well as the spectral width of the laser. The total final bunch length can be written as

$$\sigma_{z,f} = \sigma_{z,i}(1 + R_{56}h) + R_{56}\sigma_{\Delta E, \text{uncorr}}. \quad (4.69)$$

The uncorrelated energy spread term always sets the minimum bunch length. A small transfer matrix element  $R_{56}$  reduces the final bunch length significantly.  $R_{56}$  is defined by the drift space, with the parameter  $L$  corresponding to the drift length

$$R_{56} = -\frac{L}{\gamma^2}. \quad (4.70)$$

Hence, the final compressed bunch length depends on a suitable choice of the drift length  $L$ . In order to avoid overcompression, the drift space is limited to the point where the rotation of the longitudinal phase space leads to an ellipse standing upright, as it is shown in Fig. 4.22 (right). Further, Equ. (4.70) confirms that low energy beams are required for an adequate bunch length compression if this method is applied. When a separate RF cavity which is entered by the bunch at zero-crossing  $\phi=0$  deg is used, the compression process is referred to as “ballistic bunching” because no net acceleration occurs. Otherwise this method is called “velocity bunching”.

### Further Bunch Compression Methods

#### Magnetic Chicane

A magnetic chicane can also be added to the beam path behind the photoinjector to minimize the bunch length. The beam is guided through a sequence of magnets that provide a uniform magnetostatic field over a defined range. Dipole magnets are usually installed in the beam path to serve as dispersive elements. Since the electron beam should preserve its initial direction, magnetic chicanes normally consist of four magnets (C-shape) [see Fig. 4.23].

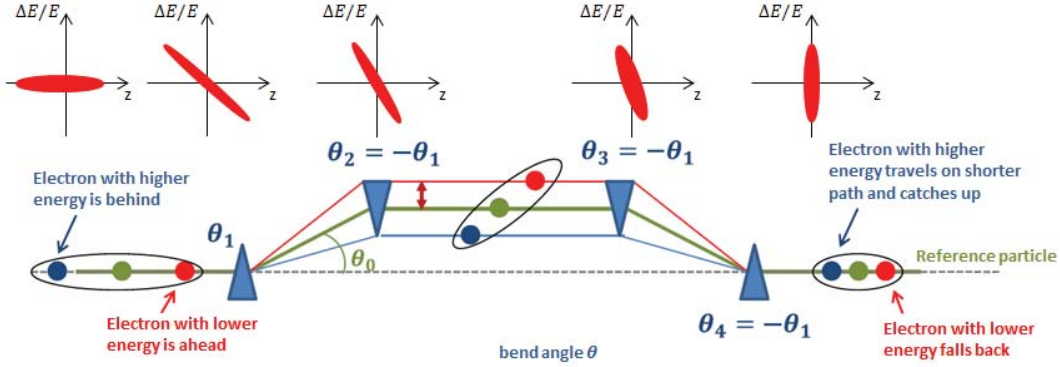


Figure 4.23: Bunch compression in a C-shape magnetic chicane [92].

The idea of bunch compression is based on the characteristic property of the trajectory of particles with different energies to have different total path lengths in the magnet. The bending radius depends on the particle momentum as well as on the constant magnetic field. An off-energy particle with a momentum  $p_0 + \Delta p$  will observe a different bending radius and, thus, it will follow a different path way within the magnet.

Unlike bunch compression which is based on velocity/ballistic bunching, magnetic compression is usually applied to relativistic beams [94]. Therefore, all particles move with the same velocity  $v \approx c$ , without changing their longitudinal position in the bunch ( $\frac{d\zeta}{dz} \approx 0$ ). Nevertheless, the energy chirp ( $\frac{d\zeta}{dE} \neq 0$ ) leads to different path lengths in the dipole which correspond to different arrival times. Thereby, the bunch is time-compressed.

Particles in the bunch tail can catch up with particles positioned in the bunch head if their path way in the magnet is shorter than the way of the other particles [see illustration in Fig. 4.23]. From this correlation, it can be deduced that the bunch must be energy chirped in a way that allows for tail particles to be injected closer to the on-crest phase than head particles which then gain more energy during acceleration. This can be achieved with an injection phase  $\phi < \phi_{\text{on-crest}}$ .

The final bunch length can be expressed again with Equ. (4.68). The  $R_{56}$  is defined by the transfer matrix of the whole magnetic chicane (dipoles and drift spaces).

If the bunch starts short at the cathode or if it is precompressed, bunch lengths of

tens of fs (*rms*) can be reached with a magnetic chicane. Additionally, an appropriate design of the dipole edge angles provides a vertical focusing. Furthermore, placing other magnetic elements between the dipoles can correct nonlinear effects. Still, implementing bend magnets in the beam path causes some unwanted effects, such as emittance growth due to the synchrotron radiation in the dipoles. A further disadvantage is that space-charge effects can lead to a degradation of the horizontal phase space. Both effects influence the maximum achievable beam brightness. Finally, the compression in a magnetic chicane can only be applied at a relativistic energy behind the photoinjector. Further acceleration in a booster section before the bunch enters the magnetic chicane is recommended. This concept is running counter to a compact beamline setup.

### Velocity Bunching by Serafini et al.

The term “velocity bunching” also represents another bunch length compression method as suggested by L. Serafini and M. Ferrario in 2001 [95]. This method is based on a phase space rotation without implying an energy chirp on the bunch.

The bunching starts after the bunch has exited the SRF gun and after the transverse emittance of the bunch has been compensated. In this method bunch compression is thus completely separated from transverse bunch optimization. Then, the low energy (several MeV) bunch with a low emittance is guided through a traveling wave cavity with a phase velocity  $\beta_r$ , which is slightly smaller than the velocity of light  $c$ . The electrons interact with the longitudinal electric field of the traveling wave.

The bunch evolution, due to the interaction with the traveling wave, can be illustrated via plotting a set of Hamiltonians in the  $\gamma$ - $\phi$ -phase space [see Fig. 4.24]. The separatrix (bold line) encloses any particle orbits that represent the trajectories of bunches and that are trapped in the accelerating phase of the RF wave. The horizontally dashed line marks the resonant energy of the RF wave  $\gamma_r = \sqrt{1 - \beta_r^2}$ .

Figure 4.25 displays a close-up of the lower portion of the energy-phase space plot in Fig. 4.24. The particles are injected on a trapped orbit inside the separatrix, with energy  $\gamma_0$  and at the zero-crossing phase  $\phi_0$  (see Point A in Fig. 4.25). In order to illustrate the basic idea of velocity bunching, it is assumed that the injected bunch does not provide an initial energy spread. As the bunch velocity is slower than the phase velocity of the RF wave, the bunch slips back in phase while it is accelerated in the cavity. Meanwhile, the bunch is rotated in the phase space. The bunch length



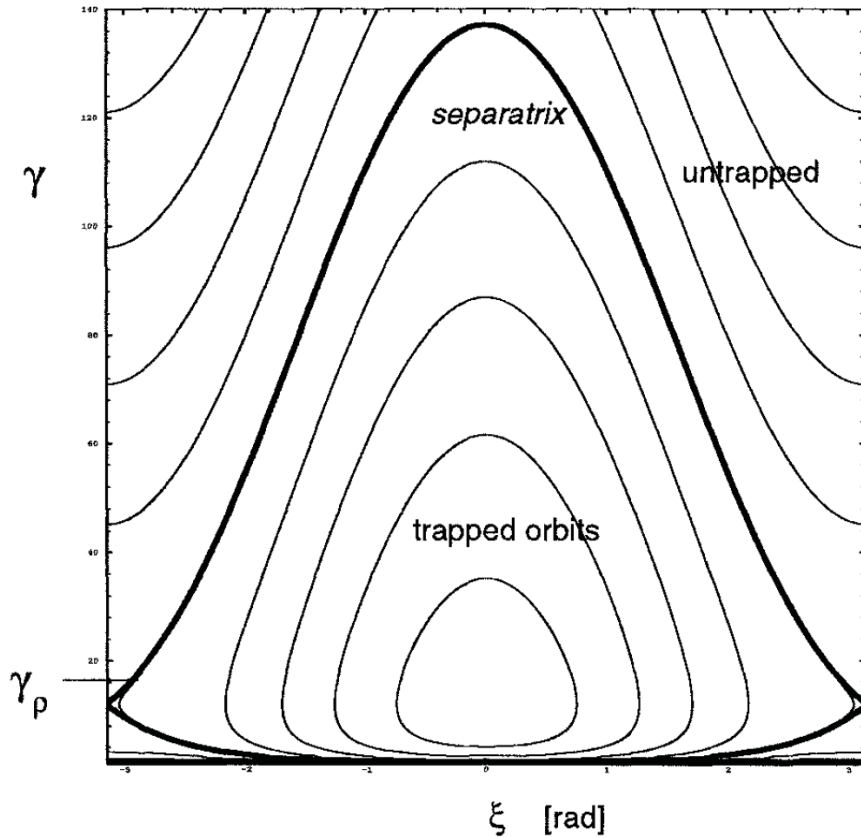


Figure 4.24: Hamiltonians in the  $\gamma$ - $\phi$ -phase space. The separatrix is marked with the bold line [95].

shrinks until point B is reached where the bunch has a beam energy equal to  $\gamma_r$ . At this point, the contour lines in the plot nearly parallel the  $\gamma$  axis that leads to the shortest possible bunch length and the maximum energy spread. A full quarter rotation of the bunch is achieved. In order to avoid a renewed increase in the bunch length, which would be caused by the contour of the phase lines, the bunch must be extracted from the cavity at point B (energy  $\gamma_r$ ). For an idealized bunch without an initial energy chirp, the bunch length at point B should only differ from zero due to nonlinearities in the phase space that are set to the bunch between point A and B.

To calculate a realistic final bunch length after velocity bunching, an initial energy spread and a phase deviation from the injection phase at point A in Fig. 4.25 must be considered. Because of a finite phase spread, the longitudinal beam ellipse extends over several constant Hamiltonian lines at the injection point A in the energy-phase diagram (see Fig. 4.26(a)). During the acceleration and the phase slippage in the

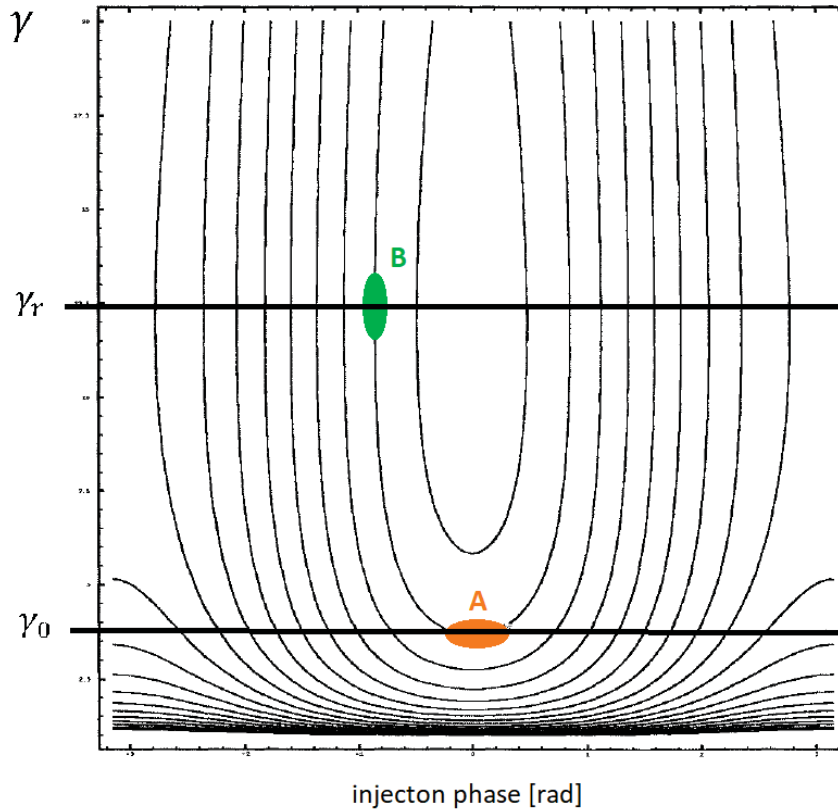


Figure 4.25: Bunch compression by a phase slippage of the bunch in the  $\gamma$ - $\phi$ -phase space [95].

traveling wave cavity, different parts of the ellipse transform in different ways. The initial beam ellipse is heavily distorted at the extraction point B as shown in Fig. 4.26(b). Nonlinear correlations leading to a longitudinal emittance growth must be considered in this bunch compression technique, as well.

In order to maximize the beam brightness and, therefore, to control the transverse emittance during the bunching process, solenoid magnets can be placed around the traveling wave cavity.

#### 4.4.4 Summary of transverse and longitudinal bunch compression methods in SRF guns

Emittance and bunch length minimization that achieve high brightness electron beams can be implemented in different ways in SRF guns. Short bunches are generated with a drive laser which produces compact laser pulses. Additional bunch compression

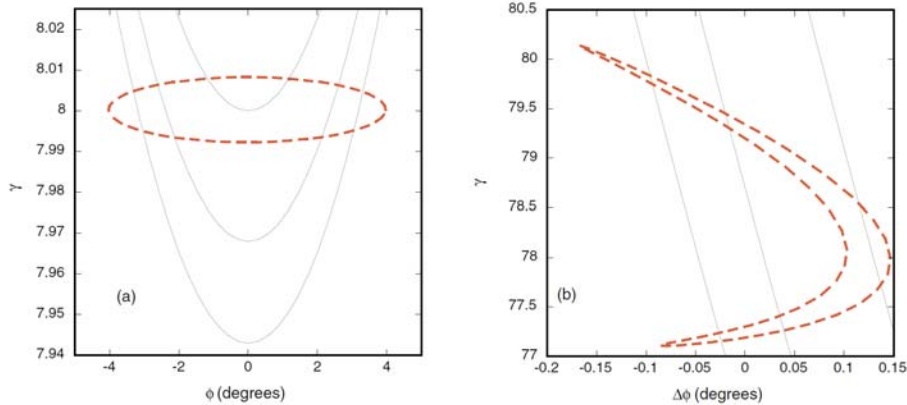


Figure 4.26: (a) The ellipse that represents the beam distribution at the injection (red dashed line) overlaps several phase contours (black lines). The ellipse transforms to the beam phase space shown in Figure (b) and is extracted at point B [96].

occurs due to RF effects. Furthermore, the drift length between the SRF Gun exit and a subsequent booster can be used for velocity bunching based on an energy chirp that is implemented in the RF cavity. This leads to a short enough bunch length of the generated bunch to inject the beam into an accelerator facility, such as an ERL. If further bunch compression is required in an ERL in order to operate an insertion device within the recirculator, this can be mostly achieved in the dispersive section of the first arc. In case that the SRF gun operates as a stand-alone facility driving a user experiment that requires ultra-short bunches, a buncher cavity based on velocity bunching with a phase space rotation can be added to the beam line. The undesired emittance growth and the space consuming setup render magnetic chicanes an unfavorable method for the bunch compression of high brightness electron beams.

## 4.5 Emittance-Bunch Length Trade-off

The preceding section presented several possibilities to minimize the transverse emittance and bunch length. The great challenge of maximizing the beam brightness is to minimize the emittance and bunch length simultaneously. A trade-off between these two parameters turns this task into an impossible one. The idea of a trade-off is shown in Fig. 4.27. If one parameter is minimized the other parameter increases. The best brightness results can be achieved in the compromise region between a small emittance and a short bunch length.

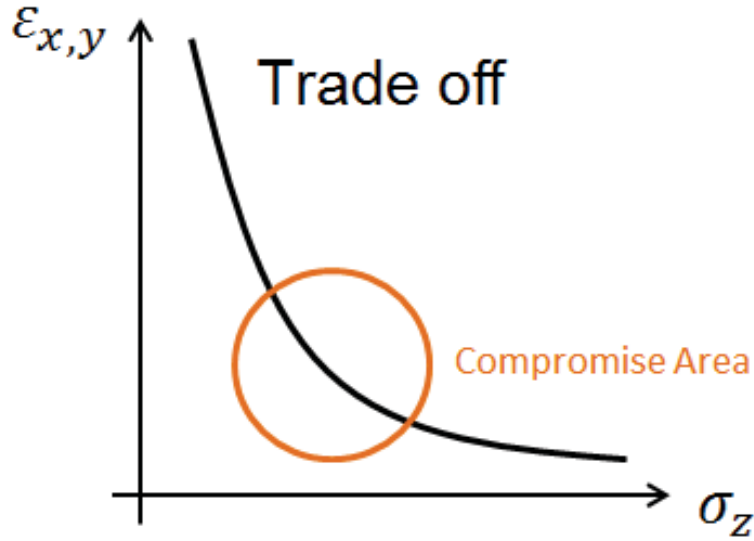


Figure 4.27: Trade-off between the transverse emittance and bunch length. The values on the curve depend on the gun design and operation parameters. The best results are achieved in the compromise region of small emittances and short bunch lengths.

Beginning with formula (4.13), the trade-off ideally represents an ISO-brightness curve that can be described by the  $\varepsilon \propto 1/\sqrt{\sigma_z}$  dependency, with a constant, maximum achievable beam brightness along the front. This condition is fulfilled right at the cathode, where only the intrinsic emittance impacts the transverse phase space. The trade-off between the intrinsic emittance at the cathode and the bunch length can be derived from the electrostatic space charge field inside a bunch, expressed in Equ. (4.41) in section 4.3.4. Since the transverse emittance at the cathode and in any beam waist is given by the product of the beam size  $\sigma_x$  and the beam divergence  $\sigma'_x$  without correlations, the following trade-off of the emittance and bunch length can be found based on the beam size-bunch length dependency shown in Equ. (4.42):

$$\varepsilon_{\text{in},x} \propto \frac{1}{\sqrt{\sigma_z}}. \quad (4.71)$$

Afterwards, the bunch phase space volume is affected by the RF cavity field, the solenoid and space charge effects. Consequently, the  $\varepsilon_x \propto 1/\sqrt{\sigma_z}$  dependency is no longer valid. The trade-off trend between the transverse emittance and the bunch length cannot be further expressed in one formula, as the total emittance summarizes

different emittance contributions from various beam path elements that show different bunch length dependencies. The two RF emittance terms turn out to be proportional to the single and the squared bunch length [see Formula (4.34)]. The solenoid does not impact the longitudinal phase space in the first order. Therefore, the chromatic or geometric emittance contributions present no bunch length dependency. Moreover, the space charge emittance contribution shows a direct proportionality to the beam current that is indirectly proportional to the bunch length [see Equ. (4.45)].

The additional correlation between RF, solenoid and sc effects requires that the phase space evolution in the photoinjector must be considered as a whole. The minimum achievable phase space volume and thus the maximum beam brightness, depends on the drive laser (laser pulse volume), the cavity (peak field, phase) and the solenoid (magnetic field, position in the beamline) settings as well as on the design of the whole injector. This leads to an optimum trade-off curve functioning as an envelope of the different ISO-brightness curves for different SRF gun settings, as illustrated in Fig. 4.28.

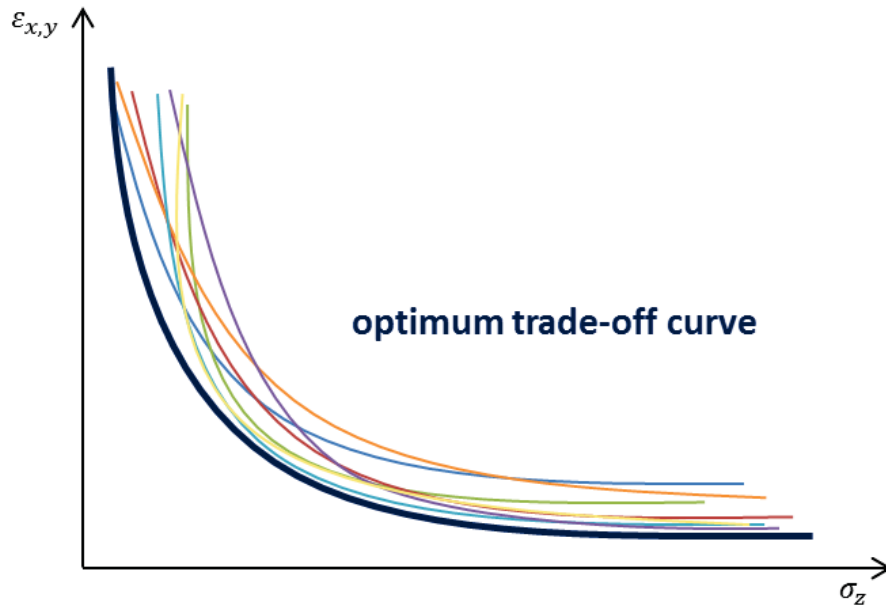


Figure 4.28: The optimum trade-off curve as an envelope of the different ISO-brightness curves for different SRF gun settings.

It is impossible to find the trade-off curve analytically since the beam dynamics of the different beam path elements, the correlations and nonlinear effects represent a complex system. Therefore, a numerical optimization based on particle tracking

through the whole SRF photoinjector is required. The following chapter will introduce a simulation tool to model the beam dynamics in an SRF photoinjector and to optimize the transverse emittance and bunch length in a way that maximum beam brightness can be achieved in any SRF gun. The envelope trade-off curve between emittance and bunch length is the foundation for the result in the optimization program.

## Chapter 5

# Optimization of an SRF Photoinjector

The overall goal for all electron injector designs is to maximize the beam brightness, no matter if an SRF photoinjector is applied as an electron source for a future accelerator driving a light source or as a direct beam source. In order to maximize the beam brightness for different applications, it must be considered that the emittance and bunch length and their trade-off derived in chapter 4.5 determine the brightness. For a space charge dominated beam, both bunch parameters are significantly affected by drive laser, gun and solenoid parameters. Therefore, the task is to find the brightness limit of an SRF photoinjector dependent on gun parameter settings. A global optimization of the SRF injector setting is necessary to achieve a high brightness mode. Moreover, the main bunch characterizing parameters, the transverse emittance and the bunch length, define the trade-off. Beside the high brightness operation, the reduction of a global SRF photoinjector optimization on optimizing the trade-off represents a fast and simple approach with a high accuracy.

To summarize the optimization problem:

Minimizing two conflicting objectives (trade-off), i.e. the transverse emittance and bunch length, leads to a maximization of the beam brightness. They depend on several decision variables given by the drive laser, cavity, solenoid and design settings of the SRF photoinjector. Fig. 5.1 provides an overview of all gun elements and parameters the transverse emittance and bunch length and, therefore, the beam brightness depend on. Most of them are already mentioned in the formulas of section 4.3 describing the transverse and longitudinal beam dynamics in an SRF gun.

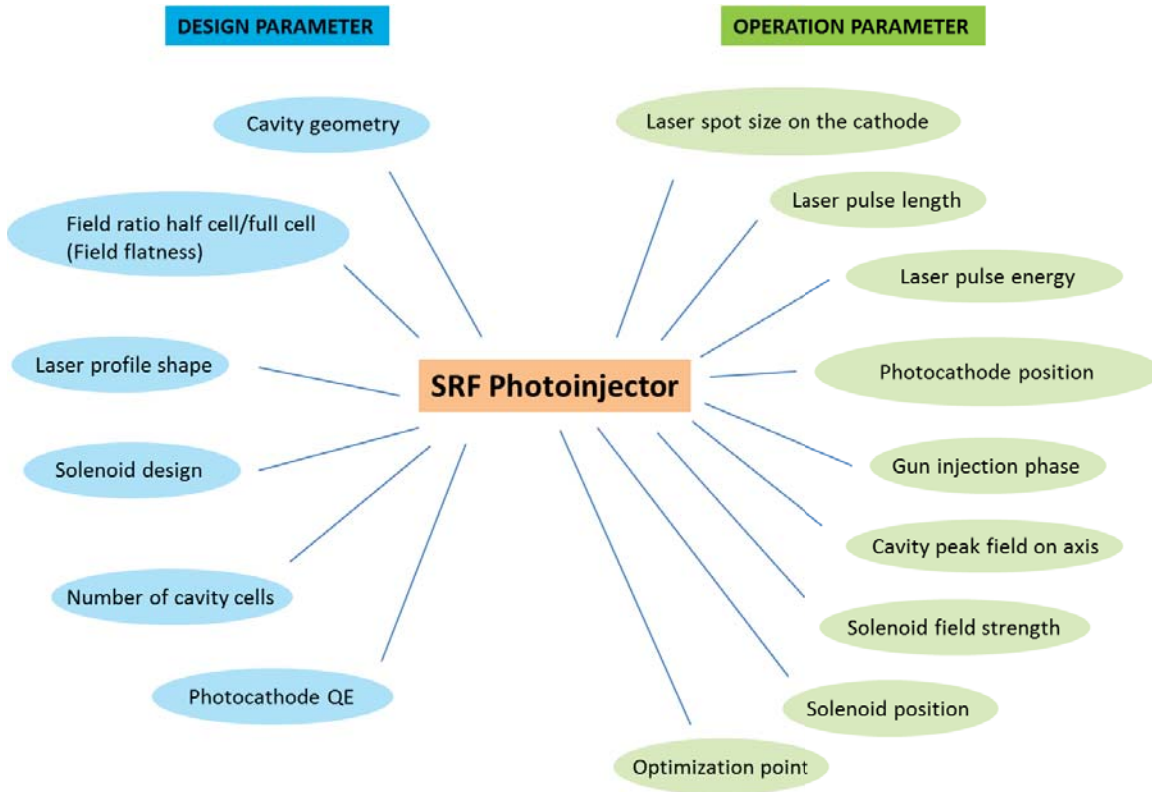


Figure 5.1: Overview of photoinjector design and operation parameters that impact the transverse emittance and the bunch length.

It is critical to control all these parameters simultaneously and constantly, and to find an optimum setting to reach a gun performance with a maximum beam brightness. In order to evaluate the beam brightness at a defined point behind the photoinjector and the quality of a selected photoinjector setting, the transverse emittance and bunch length must be calculated at this position.

## 5.1 Particle Tracking

The nonlinear, non-conservative forces that act in the SRF photoinjector, together with the transition from non-relativistic to relativistic beam velocities make an exact description of the beam dynamics challenging. Analytical, usually linear models offer an approximation including an idealized numerical approach to depict the non-conservative space charge force. As a promising alternative, a particle tracking program simulates the particle phase space transformation through the gun, considering all beam path elements with a significant impact on the electron beam dynamics as well as space charge effects. The 6D beam phase space dimension is determined at



defined positions and at the evaluation and optimization point. The tracking tool ASTRA has been used to simulate said beam propagation.

ASTRA (A Space Charge Tracking Algorithm) was developed by Klaus Floettmann and co-workers at DESY Hamburg [97]. This powerful tool simulates the phase space evolution of a particle beam in an accelerator structure.

The bunch charge is divided in a user-defined number of point-like macroparticles with the same sub-charges. Selecting photoemission for electron generation, the ASTRA generator converts the input parameters of the drive laser to a starting particle distribution. Afterwards, ASTRA tracks the macroparticles under the influence of external fields from the beam path elements and internal self fields including 2D or 3D space charge calculations. The bunch phase space distribution as well as the transverse and longitudinal projected emittances, the bunch length, the kinetic energy and further bunch parameters are provided as outputs after defined time steps, as well as at the user-defined stopping position of the simulation. A detailed description of the ASTRA tracking procedure, intensively used in the optimization program that was developed during this thesis, can be found in Appendix A and in [98].

In recent years, accelerator scientists used the code intensively, especially for simulations and design studies of photoinjectors.

Figure 5.2 shows the results of the ASTRA tracking for one particular SRF photoinjector setting. The evolution of the transverse emittance and bunch length from the photocathode to the stopping point (2.5 m behind the cathode) is displayed. Moreover, the bunch is fully characterized at 2.5 m. Table 5.1 summarizes the photoinjector settings and final beam parameters. This example of ASTRA tracking for 100,000 macroparticles including a 2D space charge calculation took around 12 minutes on a HZB high-performance-computing Linux cluster with 64 cores.

In order to evaluate the smallest emittances and bunch lengths and thus the maximum achievable beam brightness of a given photoinjector design, the particle tracking process must be repeated several thousand times for different electron gun settings. Running multiple ASTRA processes simultaneously reduces the optimization time significantly. Computer software like MATLAB (matrix laboratory), a multi-paradigm numerical computing environment based on the programming language C, fulfills the requirements for running parallel ASTRA simulations [99]. This approach generates different parameter settings in MATLAB by randomly assigning values to the pho-

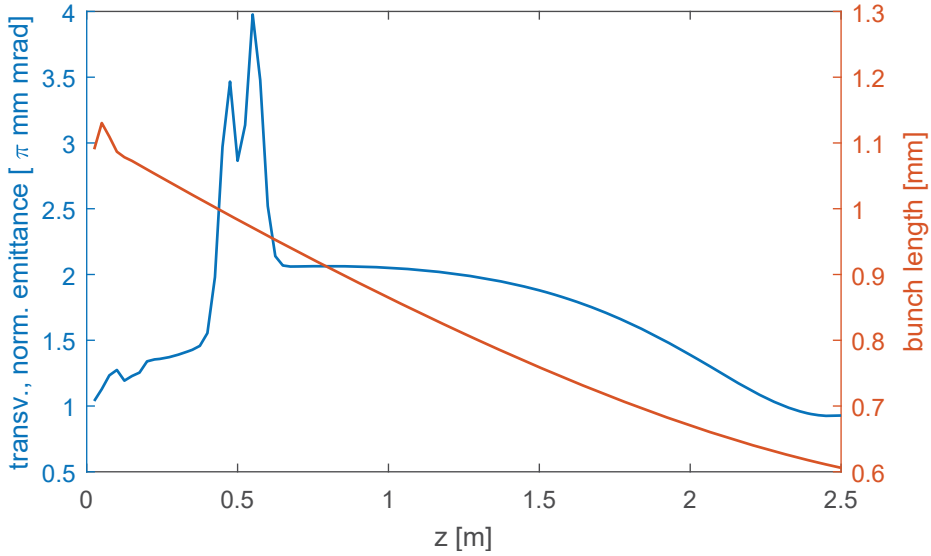


Figure 5.2: Evolution of the transverse emittance and the bunch length along the beamline for one photoinjector setting. The results are obtained with the ASTRA tracking tool.

Table 5.1: Photoinjector settings and final beam parameters at 2.5 m for an ASTRA tracking example

Parameter	Value
Laser spot size	0.46 mm ( <i>rms</i> )
Laser pulse length	5.7 ps
Cathode position	-1.0 mm
Injection phase	-28.7 deg
Cavity peak field	30 MV/m
Solenoid position	0.51 m
Solenoid field	101.8 mT
Bunch length	2.06 ps
Beam size	1.45 mm
Beam transv. divergence	0.28 mrad
Transv., norm. emittance	0.93 mm rad
Kinetic energy	2.49 MeV

toinjector parameters. MATLAB then passes the input settings to ASTRA and starts the tracking operation while running a predefined number of ASTRA processes at the same time. The task is to select those photoinjector settings that lead to the smallest transverse emittances and shortest bunch lengths in the obtained results.

Several optimization strategies exist for finding the best photoinjector parameter

settings for a high brightness mode and for discovering the phase space limits of the SRF gun. The goal for this optimization procedure is to always minimize the objectives (here the transverse emittance and bunch length), depending on various decision variables (gun parameter settings). The following section introduces three different optimization approaches and explains why multi-objective optimization is the preferred strategy in the dissertation at hand.

## 5.2 Optimization Strategies

### 5.2.1 Swarm optimization

Swarm optimization is the consequent continuation of parallel ASTRA tracking and a straightforward approach in multi-parameter optimization. This method does not include an evolutionary optimization process at all. The objectives are calculated for various decision variables. Thus, the transverse emittance and bunch length are evaluated for different gun parameter settings and designs using a particle tracking program like ASTRA (repeat the calculation for Fig. 5.2 several times). Parallel processing of ASTRA helps to save computational run time. Each setting corresponds to one particular point in the emittance-bunch length phase space. All settings together built a swarm-plot of possible solutions while the contour of the plot provides the optimum front of the objectives.

The number of free decision variables in the injector as well as their variation possibilities (continuous or step-wise) defines the number of calculations for a complete swarm-plot. Assuming a 7-dimensional problem, that is to say an SRF photoinjector with seven free operation parameters as decision variables (i.e., laser spot size, laser pulse length, cathode position, gun cavity phase, cavity peak field, solenoid field and solenoid position), with only five variations per parameter,  $5^7 \approx 78,000$  calculations must be conducted. Photoinjector parameters with a broad range in their settings that even allow a continuous variation render the number of calculations infinite. Therefore, it is necessary to reduce the number of calculations. Selecting only a defined number of settings solves this issue.

Figure 5.3 shows the results for 10,000 different settings of the current GunLab design at HZB. The free photoinjector parameters as decision variables are chosen randomly within their design ranges, that are summarized in Table 5.2. The emittance and bunch length values are then calculated in separate ASTRA runs, 20 simultaneous simulations each time. However, the process needs several days for one complete swarm plot.

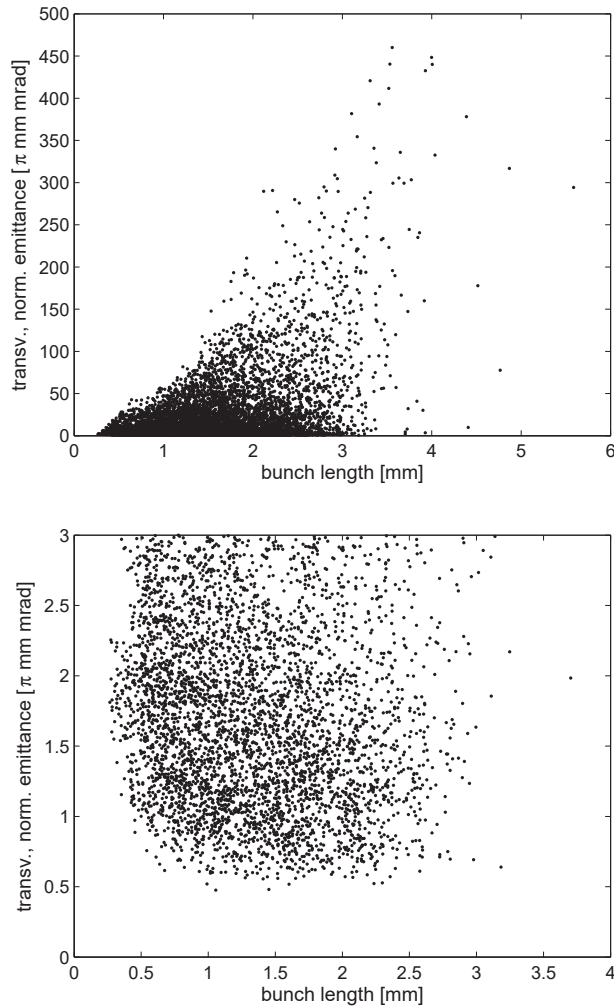


Figure 5.3: (a) Swarm plot for 10,000 different photoinjector settings in GunLab. (b) Close-up of the compromise region of small emittance and short bunch length. A trend to the trade-off between transverse emittance and bunch length can be identified.

The disadvantage of the swarm optimization strategy is that even after thousands of ASTRA simulations only a few solutions lie on the optimum curve that has been manually placed by the user. Therefore, the envelope merely represents an estimate of the optimum. In order to achieve a satisfying precision in the envelope curve, several thousands of photoinjector settings must be simulated even if only the best settings at the lower edge of the swarm are of interest. This inelegant method is very time-consuming.

Table 5.2: Limits of the photoinjector parameters resulting from the current GunLab design

Parameter	Range	Unit
Laser Spot Size	0.1 - 1.5	mm ( <i>rms</i> )
Laser Pulse Length	0.5 - 8.5	ps
Cathode Position	-2.5 - 0	mm
Injection Phase	-30.0 - 30.0	deg
Cavity Peak Field	15 - 40	MV/m
Solenoid Position	0.46 - 0.60	m
Solenoid Field	0.05 - 0.5	T

An optimization process is necessary which selects only solutions that satisfy the requirements on the objectives best. Then, unwanted solutions in the swarm that are far off the optimum edge, are immediately rejected from the solutions pool. Time is saved and the optimum front is clearly determined. In addition, the chosen algorithm increases the number of solutions on the optimum curve.

The structure of such complex decision problems, the optimization of multiple competing criteria, is well known from other real-world problems. It is one example of what are known as cost-performance problems in business economics where the minimization of production costs and increase of product quality and performance standard are opposite objectives. Since the problem is omnipresent in many fields and not only in research, physics or especially in accelerator physics, other, non-physical areas can offer optimization strategies.

### 5.2.2 Single-objective optimization

Single objective optimization provides an alternative to swarm optimization and the described issues. Combining the  $k$  objectives  $z_1, \dots, z_k$  to a single one  $z$  by using the weighted sum method reduces the multi-objective problem. A new single criterion function, defined by the user, has to be optimized [100]:

$$\min/\max \quad z = w_1 z'_1(x) + w_2 z'_2(x) + \dots + w_k z'_k(x) \quad (5.1)$$

with  $\sum w_i=1$ .

Single objective optimization always ends with a single solution. One weight vector yields one solution in the single point design. Finding a correct choice in the weights poses a great challenge since different weights lead to different solutions. Therefore, large regions of parameter space remain unexplored. The diversity of the population of optimum solutions is limited. This runs the risk of ending up in a local optimum without finding the global optimum in the gun settings, or in the case of multiple global optima, to figure out one solution only. Another disadvantage of this method is that the weight vector does not consider trade-offs between the weighted objectives. It follows that the optimization works with a simplified theoretical model.

### 5.2.3 Multi-objective optimization

Multi-objective optimization provides a solution which optimizes a number of conflicting objective functions simultaneously while considering all limiting variables and constraints in a multidimensional parameter space. A multi-objective decision problem is defined as follows [101]:

$$\begin{aligned} & \text{minimize/maximize} && z_k(x_1, \dots, x_n), k = 1, 2, \dots, K; \\ & \text{subject to} && g_j(x_1, \dots, x_n) \geq 0, j = 1, 2, \dots, J; \\ & && x_i^L \geq x_i \geq x_i^U, i = 1, 2, \dots, n. \end{aligned}$$

Given an  $n$ -dimensional decision variable vector  $\mathbf{x} = x_1, \dots, x_n$  in the solution space  $X$ , the optimization will find a vector  $\mathbf{x}^*$  that optimizes a given set of  $K$  objective functions  $z(\mathbf{x}^*) = z_1(\mathbf{x}^*), \dots, z_K(\mathbf{x}^*)$ . The solution space  $X$  is generally subject to a series of  $J$  constraints, such as  $g_j(\mathbf{x}^*) = b_j$  for  $j = 1, \dots, J$ , and limits of the decision variables  $x_i^L \geq x_i \geq x_i^U$ . The set of all feasible non-dominated solutions in  $X$  (population) is referred to as the Pareto optimum set characterized by the circumstances that the solutions cannot be further improved in one objective without degradation of at least one of the remaining objectives or constraints [see Fig. 5.4]. The Pareto optimum is named after Vilfredo Pareto (1848-1923) who used this theory in his studies of economic efficiency [102]. The corresponding objective function values in the objective space are called the Pareto front. All points in the front are equally optimal. For many problems, the number of Pareto optimum solutions is enormous (maybe infinite). Finally, the user of the optimization tool chooses one solution out of the Pareto optimum front that fits the characteristics of the problem best.

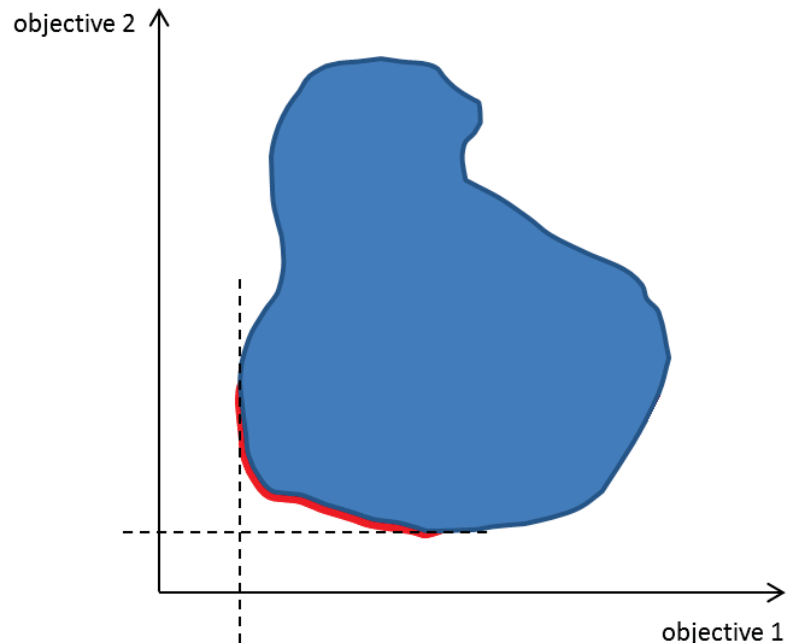


Figure 5.4: Pareto-optima (red highlighted) of a 2D objective space. In this example, the optimization task is to minimize both objectives.

There are several so called MOGA algorithms (multi-objective generic algorithm) that can be implemented to solve a multi-objective optimization problem. MOGA algorithms are potent tools and widely used in accelerator physics, such as the high brightness optimization of a DC gun [103], [104], the lattice optimization of the advanced light source storage ring at BNL [105], and the design of the LCLS-II linac configurations [106]. The great advantage of MOGAs is that they do not require the user to prioritize, to scale, or to weight objectives. Most MOGA algorithms vary in their particulars but share some common properties. The basic steps of a typically MOGA algorithm, illustrated in Fig. 5.5 are the following:

- 1) Randomly initialize a population
- 2) Evaluate objective functions under consideration of all constraints (Evaluator)
- 3) Select best solutions (Selector)
- 4) Apply variator (crossing and mutation of the solutions variables in the mating pool)
- 5) Evaluate the objectives for the new offspring solutions

- 6) The offspring solutions and the most dominant solutions (mating pool) survive for the next generation
- 7) Termination criteria stop the optimization loop.

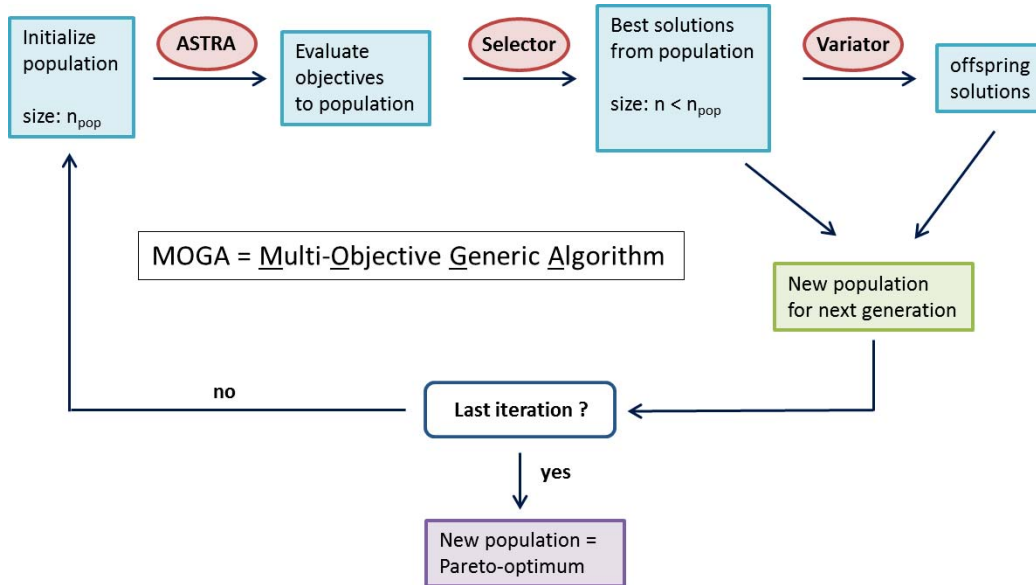


Figure 5.5: Overview of the basic steps in a MOGA algorithm.

In the first step, all decision variables and their limits are handed to the program. Further, a parent population is initialized by assigning random values to the decision variables. A realistic gun model with RF and solenoid fields is used to evaluate the objectives at a certain optimization point, which in our case lies behind the photoinjector, in the tracking and space charge code. The field distributions of the RF cavity and the solenoid used in the tracking, can be generated with specialized simulation codes or taken from bunch measurements. Afterwards, the algorithm maps out the best solutions. Here, the MOGA algorithms differ in the domination criterion and their strategy with which they select the most dominant solutions. Most of them assign fitness values to the solutions in the current population, due to the convergence and diversity, rating how well the solutions satisfy the optimization constraints and objectives. In the following step, the selector chooses the best, most dominant solutions based on the fitness values and puts them in an archive. In order to create new offspring solutions, a variator that is typically based on crossing and mutation, is used. Crossing represents the most important variation of the population. Two results are selected from the archive through using a stochastic operator



(binary tournament selection) several times. Then, a crossing of several or all values of the decision variables creates new non-dominated solutions. This strong modification leads to solutions in unexplored parts of the objective space. In the mutator, small perturbations are set to several or all decision variable values of a randomly selected solution. Mutation reintroduces diversity to the population, and it prevents the focusing to local optima. The offspring solutions from the mixing and mutation process build a new population for which the tracking program again evaluates the corresponding objectives. In the last step, the archive solutions combined with the offspring solutions build the new population and survive for the next generation. The process then starts again and continues with the fitness value assignment and the selection process. The program stops due to user-defined termination criteria like, for example, a predefined number of generations or all solutions in the population reach a desired fitness value. The aim is always to figure out a final population after the last iteration, the Pareto-optimum set, that consists only of solutions that satisfy the objectives at an acceptable level and solutions that are not dominated by other solutions. Therefore, MOGA will always find the global optimum but due to conflicting objects, one solution that optimizes each objective function is almost impossible. Since a MOGA algorithm needs more than one iteration in the described procedure to find the Pareto optimum curve, the algorithms are described as evolutionary. Furthermore, most MOGAs are elite-preserving because the particular population which is provided to the subsequent generation includes not only off-spring solutions but also the most dominant solutions of the last iteration.

The algorithm that is used to run the multi-objective optimization of the photoinjector is selected according to whether it fulfills the following three goals [107]:

- 1) Find best-known Pareto-front close to real Pareto-front, a subset of Pareto-optimum is ideal
- 2) Capture the limits of the objectives (outer parts of the front)
- 3) Pareto-optimal set must be uniformly and diversely distributed over the front to gain a whole picture of the trade-off curve (reducing fitness of solutions in densely populated areas)

In order to achieve solutions that are as close as possible to the real Pareto-front of the photoinjector, the algorithm must trigger a particle tracking program which

uses real RF and solenoid fields. Further, the mutation process in the algorithm allows small improvements of the current solutions towards the true Pareto-curve. The limits of the objectives can be figured out separately if weights are implemented in the objective function. The crossing operator of the algorithm leads to significant changes in the gun settings that consequently reach outer parts of the Pareto-front (second goal). Crossing also helps to gain solutions that are spread over the whole Pareto-front. Nevertheless, to guarantee a uniform distribution which is also diverse in its decision variables, the algorithm must rank the solutions due to their crowding distance in addition to their dominance. Therefore, only algorithms with dominance and density-based rankings are considered to run the multi-objective optimization. NSGA II (Non-dominated Sorting Genetic Algorithm) [108] and SPEA2 (Strength Pareto Evolutionary Algorithm) [109] are the most well-known and widely used algorithms that use density and dominance rankings for fitness assignments.

### NSGA II

NSGA II is based on the standard MOGA algorithm presented above but it uses a special dominance ranking procedure in the selector that is shown in Fig. 5.6 [108]. The population  $Q_{it}$  of iteration  $it$  consists of the archive  $P_{it}$ , from the last iteration, combined with the offspring solutions  $R_{it}$ . The population  $Q_{it}$  is of the size  $2N$ . A two-step model helps to select the most-dominant solutions out of  $Q_{it}$  to form a new population of the length  $N$ . First, the population  $Q_{it}$  is categorized according to non-dominated classes in the so-called non-dominated sorting. Then, the new population is filled with whole fronts until all slots are occupied. The remaining classes are deleted. Normally the last dominance class allowed must be further rejected since there are not enough remaining slots in the new population. The points that lead to the highest diversity of the population are chosen. Therefore, the distance to the next neighbor in the objective space is calculated for each solution in the last front during the step of “crowding distance sorting”. The last dominance class in the new population is rearranged due to decreasing crowding distances. Then the remaining space in the new population is filled with solutions that show the highest crowding distance of the last front.

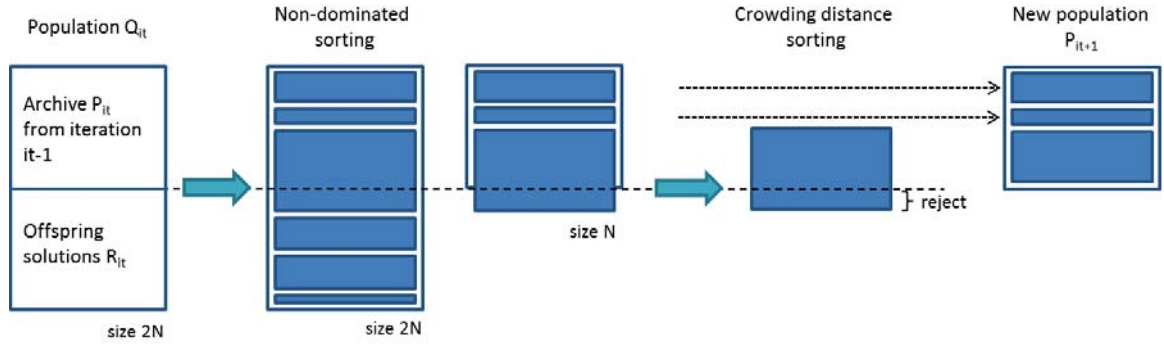


Figure 5.6: Selection process of dominant solutions in the NSGA II algorithm.

## SPEA2

The selector of the SPEA2 algorithm uses a two-step model with fitness assignment and environmental selection in order to reduce the population  $Q_{it}$  of size  $2N$  to the new population of length  $N$  [109]. Fig. 5.7 summarizes the procedure in a flow chart. First, the algorithm evaluates the so-called raw fitness for each solution in population  $Q_{it}$  based on the dominance criterion: Comparing all solutions with each other, solution  $i$  dominates solution  $j$  if solution  $i$  is not worse in all objectives and better in at least one objective than solution  $j$ . Fig. 5.8 illustrates the dominance criterion for two objectives that should be minimized, such as in the case of the transverse emittance and bunch length.

Each individual  $i$  is assigned a strength value  $S(i)$  that represents the number of Pareto-dominated solutions by  $i$ . The raw fitness  $R(i)$  of individual  $i$  is then calculated by summing up the strength values of all dominators in population  $Q_{it}$  of individual  $i$ . Therefore, a raw fitness value of  $R(i)=0$  corresponds to a non-dominated solution while a high  $R(i)$  value indicates undesired dominated solutions. However, the procedure will fail if a majority of the solutions do not dominate each other. Since there is the risk to gain a sort of niche result with many individuals that have the same raw fitness value and do not dominate each other, meaning that they cannot be selected due to their dominance, the fitness assignment is complemented by a density function. Adapting the  $k$ -th nearest neighbor method, the density of a solution  $i$  is calculated using the distance to the  $k$ -th nearest solution in the population, where  $k$  is the square root of the population size,  $k = \sqrt{N_{\text{pop}} + N_{\text{arch}}}$  [109]. The density  $D(i)$  is defined as follows

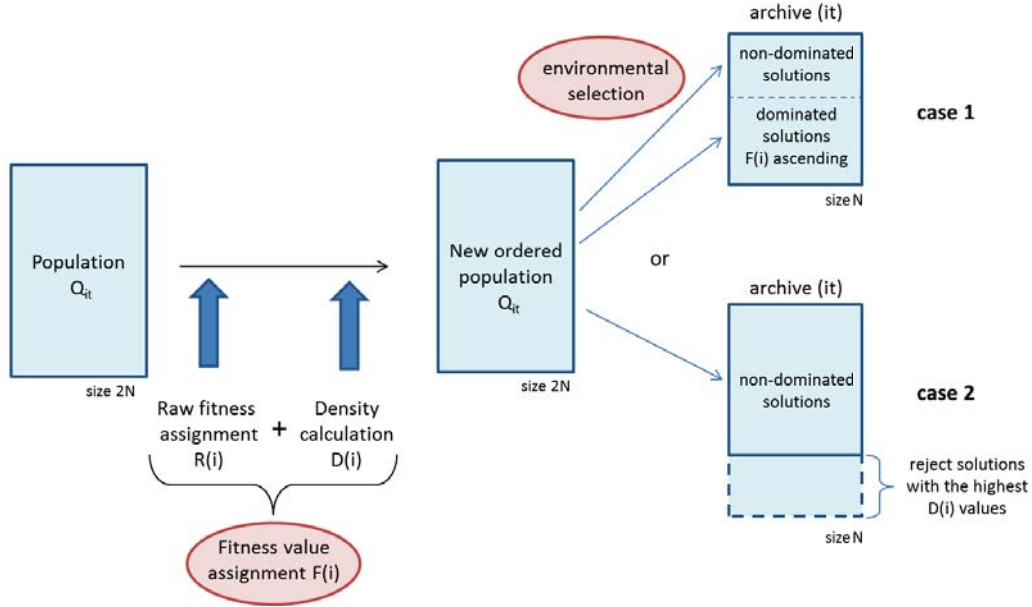


Figure 5.7: Selection routine in the SPEA2 algorithm.

$$D(i) = \frac{1}{\sigma_1^k + 2} \quad (5.2)$$

where  $\sigma_1^k$  is the distance between solution  $i$  and solution  $k$  of the current population  $Q_{it}$ . In order to ensure that the dominator is greater than zero and that the density is  $D(i) < 1$ , 2 is summed up to the distance in the denominator of Equ. (5.2). Finally, the sum of the raw fitness  $R(i)$  and the density  $D(i)$  of solution  $i$  gives the total fitness function  $F(i)$

$$F(i) = R(i) + D(i). \quad (5.3)$$

After the fitness assignment is finished, the so-called *environmental selection* starts to fill a new archive based on the fitness values of the individuals in the current population. In the first iteration, the *archive(it)* offers more free slots than non-dominated solutions exist in  $Q$ . The algorithm copies non-dominated solutions to the new pool first. Then, all remaining individuals in  $Q$  are sorted due to their fitness value and they are filled to the new archive until all places are left. After several iterations, the number of non-dominant solutions with  $R=0$  might exceed the *archive(it)* size.

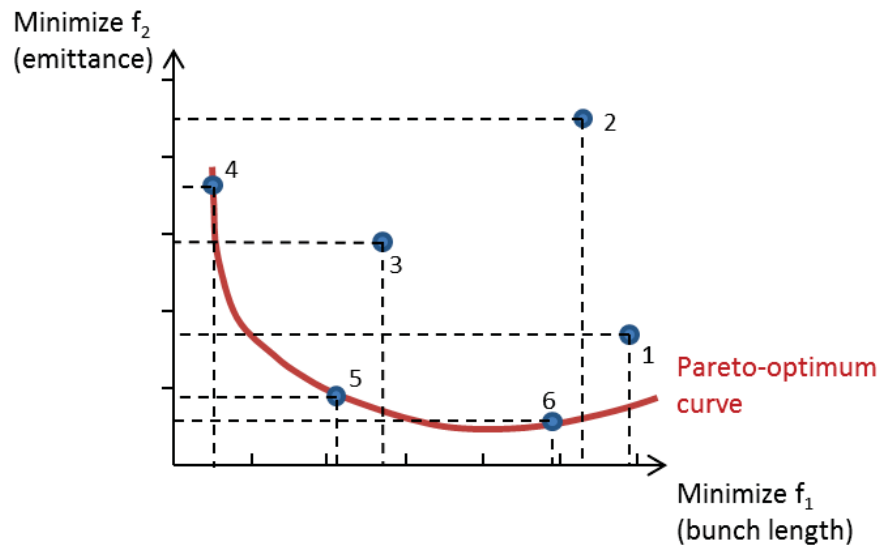


Figure 5.8: Illustration of the dominance criterion: Solution 1, 2 and 3 in the population are dominated by solution 4, 5 and 6. Solution 4, 5 and 6 are Pareto-optima since the objectives cannot be improved without an degradation in the second objective.

In that case, the archive is filled with all Pareto-optimum solutions. A truncation operator reduces the population to the archive size. The SPEA2 algorithm calculates the mean Euclidean distances of all chromosomes to their neighbors. Lastly, the solutions in the *archive(it)* are sorted according to their diminishing distances to each other, and the archive is cut to its defined size  $nArchive$ .

If one compares the two MOGA algorithms NSGA II and SPEA2 to each other, SPEA2 provides the significant advantage that the density function is evaluated and considered in the fitness value for all solutions of the population. NSGA II takes the crowding distance and therefore the density of an individual into account for solutions of a single non-dominated class only. It follows that the SPEA2 algorithm is more promising regarding the preservation of diversity over several generations to achieve a uniform, equally distributed Pareto-optimum curve as an optimization result, and to fulfill the MOGA algorithm goals mentioned above. This advantage is also confirmed by Ah King et al. who compared both algorithms by solving a multi-objective optimization problem [110]. The SPEA2 algorithm offered a significantly higher diversity in the Pareto-optimum front explained by the higher diversity maintenance strategy of SPEA2. Further, SPEA2 showed strong convergence in the optimization process due to its better distributing ability. However, the optimization

using the SPEA2 algorithm takes a longer time and needs more computational power.

In order to achieve the best results optimizing an SRF photoinjector due to its transverse emittance and bunch length, the SPEA2 algorithm was selected to solve this multi-objective optimization problem.

The following section analyzes the optimization tool that was developed in the course of this doctoral thesis. The tool is based on a SPEA2 algorithm implemented in a MATLAB script that uses ASTRA as a tracking code to simulate the beam dynamics along the beam path of the photoinjector.

### 5.3 Multi-Objective Optimization Program for an SRF Photoinjector

The presented optimization tool aims to find parameter and design settings for an SRF photoinjector that lead to a small transverse beam emittance and short bunch length at a chosen optimization point and, hence, to a high brightness electron beam at that point [41].

The program code is divided into a main script that was written in MATLAB with several sub-functions outsourced in further MATLAB scripts. MATLAB was chosen since it offers a simple, diverse and fast programming code. The complex optimization process can be clearly structured in the main script with essential optimization steps outsourced in sub-functions. Nevertheless, the whole optimization code can run in the same computational environment. Further, MATLAB is independent of the computer operation system and it can also run on Linux clusters like those offered by the HZB. MATLAB provides the opportunity to refer to external programs in a script, such as the simulation and tracking program ASTRA. As the structure of the ASTRA output has a matrix shape, MATLAB is able to read and to process the ASTRA output parameters. The included plotting function enables the display of the optimization results in the same script. Finally, MATLAB offers the possibility to create a user interface in order to make the handling of the optimization tool more comfortable and commercial.

The main optimization steps in the script based on the presented algorithm SPEA2 follow the MOGA procedure shown in Fig. 5.5. Detailed flow charts for each optimization step are shown in the Figures 5.9, 5.10, 5.11, 5.12, and 5.13.

## 1) Parameter Initialization

The decision variables that impact the objectives and their limits are initialized first. The decision variables of a photoinjector can be separated into two groups: the operation parameters and the design parameters [see Fig. 5.1]. Operation parameters, such as the laser spot size, the laser pulse length, the cathode position, the gun phase, the gun acceleration gradient, the solenoid field or the solenoid position can be adjusted during the operation of the SRF gun or in short shut-downs. Their limits are given by the design of the different components like the photocathode drive laser or the RF cavity, providing constraints to the optimization. Design parameters that include geometric parameters of the RF cavity or of the solenoid as well as temporal laser pulse profile shape are specified in the design phase of a photoinjector project. Afterwards, these parameters are fixed. The cavity design targets the accelerating field profile, and it also determines the field flatness, that is the ratio of the RF field in the half-cell to the full-cell of the cavity. The solenoid design determines the focusing field pattern in the injector. In case the design of the whole SRF photoinjector or single elements needs to be optimized to improve the corresponding objectives, the limits are defined by the user within a reasonable range.

Moreover, the optimization variables set further constraints. The variator probability is defined. Furthermore, the maximum number of iterations  $MaxIt$  is limited to 200 loops in order to prevent an infinite run time for finding only non-dominated solutions. Therefore, the variable  $MaxIt$  represents one termination condition of the optimization. Furthermore, the size of the population  $n_{pop}$ , as well as the size of the archive  $n_{archive}$ , are defined. Usually, an equal number of solutions in the population and in the archive is chosen in order to ensure an equal weight distribution to the archive and the population. The archive contains the best solutions of the last iterations, while the population is filled with new offspring solutions. In order to receive a first trend of the Pareto optimum curve, 50 solutions per population and per archive are sufficient. In order to achieve a detailed view of the front and variable gun settings in the region of interest in the objective space, 100 up to 200 solutions per pool are recommended. The program initializes the first population  $pop(1)$  by randomly assigning  $n_{pop}$  times values to the decision variables. One complete set of decision variables corresponds to one complete gun parameter setting. Nevertheless, it must be noted that values are never assigned to the solenoid field if the operation parameters represent the decision variables. The solenoid field strongly depends on

the beam energy given by the selected gun gradient and gun phase. Therefore, the tool always calculates the required solenoid field for beam focusing from the particle distribution in front of the solenoid in the “objective evaluation” step. The objectives are evaluated for all parameter settings (solutions) in the parent population  $pop(1)$ . Outsourcing this step in a separate MATLAB sub-function is the best option to receive a clear structure in the main script. The initialization step is summarized in Fig. 5.9.

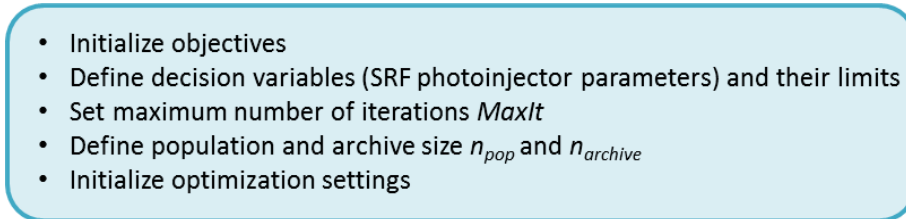
- 
- Initialize objectives
  - Define decision variables (SRF photoinjector parameters) and their limits
  - Set maximum number of iterations  $MaxIt$
  - Define population and archive size  $n_{pop}$  and  $n_{archive}$
  - Initialize optimization settings

Figure 5.9: Initialization of the optimization parameters.

### 2) Objective Evaluation

The task of this sub-function is to calculate the objectives for all gun settings in the population at the optimization point. A particle tracking program is, therefore, required to simulate the photoemission as well as the tracking through the whole beam path. The mentioned program ASTRA is implemented in the script. For an evaluation of the objectives for a given population the parameter settings of the population are transferred to the sub-function as input values. In a first step, the script inserts the values of the different solutions in the population in the Generator and ASTRA input files. The resulting data are  $n_{pop}$  Generator and ASTRA files. Then, the function refers the input files to the generator to calculate the  $n_{pop}$  input distributions for the ASTRA run. At this point, parallel processing reduces the computational run time significantly. The start distributions are transferred to ASTRA. In a first ASTRA run, ASTRA only calculates the particle distributions for each Generator output file up to the solenoid, reducing the beam path to the cathode and the RF cavity in the process. The particle tracking program includes space charge forces in the calculation. Another sub-function determines the corresponding solenoid fields for each gun setting in the population by calculating the beta function at the optimization point for each ASTRA distribution and different solenoid fields separately. Then, the most suitable solenoid field for each distribution is chosen by beta function minimization.



Now, the solenoid fields are inserted to the ASTRA input files as well. Since there is no space charge included in the beta function calculation, the determined solenoid field values are modulated up to 10%. A second ASTRA run based on the original parameter values and the calculated solenoid field tracks the particle distributions up to the optimization point. Then, the objectives of the optimization are selected from the final ASTRA distributions for each gun setting, and are saved. Since the parent population is randomly initialized, some parameter settings with an unfavorable choice in the decision variables end in the loss of particles during the tracking. The program figures out the indices of these solutions. Finally, the sub-function hands the objectives, the indices of solutions with only partially tracked particles and the ASTRA output files back to the main script.

In the main script solutions with partially tracked particles (unstable solutions) as well as solutions with a solenoid field equal to zero are deleted from the population. If the transverse emittance is one of the objectives which must be minimized, solutions with the solenoid being switched off represent a local optimum since emittance contributions from the solenoid [see Equ. (4.38) and (4.39) in chapter 4.3.3] are avoided.

After the initialization is finished, the program enters the main loop where the Pareto optimum is figured out starting from the parent population  $pop(1)$  in several iterations. In the first step, a mating pool  $Q$  is created by adding all solutions of the current population as well as all elements from the archive. In the first iteration only the gun settings from  $pop(1)$  are filled to  $Q$ . In the  $t$ -th iteration, population  $pop(t)$  consists of the offspring solutions of iteration  $t-1$  while the archive includes the most dominant solutions of iteration  $t-1$ . Both sets are summed up to the pool  $Q$ . Fig. 5.10 presents a flow chart of the “objective evaluation” step. The program continues with the selector process.

### 3) Selector

In the *Selector* the program follows the dominance criterion and the fitness value assignment of the standard SPEA2 algorithm [see Fig. 5.11]. Afterwards, the *Environmental Selection* is used to fill the archive  $archive(it)$  of the current iteration  $it$  with dominant solutions from the mating pool  $Q$ . This procedure is based on the fitness value  $F$  of each individual in  $Q$  as an entrance criterion.

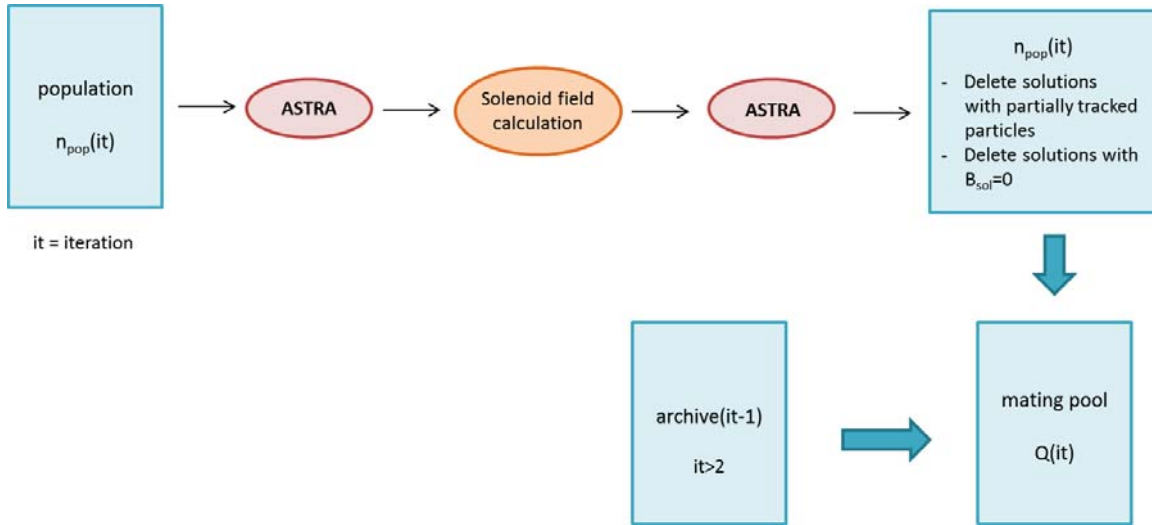


Figure 5.10: Objective evaluation based on the particle tracking program ASTRA.

Before the termination criterion is inquired, all ASTRA files of the current archive are saved. An additional sub-function plots the objectives of all solutions in a separate figure. This procedure ensures the documentation of the evolution of the Pareto optimum curve over all iterations for the user of the program.

#### 4) Termination of the Main Loop

The program considers two termination conditions to stop the run of the main loop [see Fig. 5.12]. The iteration number is compared to the set number of maximum iteration  $MaxIt$  first. In case the last iteration is reached, the program will stop. Otherwise, the procedure verifies if the  $archive(it)$  consists only of Pareto dominant solutions, i.e.  $R_i=0$  for all  $i=1, \dots, n_{archive}$ . Most runs end because of this condition as  $MaxIt$  is set to a high number by the user. The script continues with modulations of the  $archive(it)$  to create a new population if some dominated solutions remain in  $archive(it)$  and if they can be further improved.

#### 5) Variator

In order to create new offspring solutions, a crossing- and mutation-based variator is used. Figure 5.13 summarizes the procedure in the variator. One (mutation) or two (mixing) solutions are selected several times out of the archive via the stochastic operator *binary tournament selection*. This sub-function randomly chooses two solu-

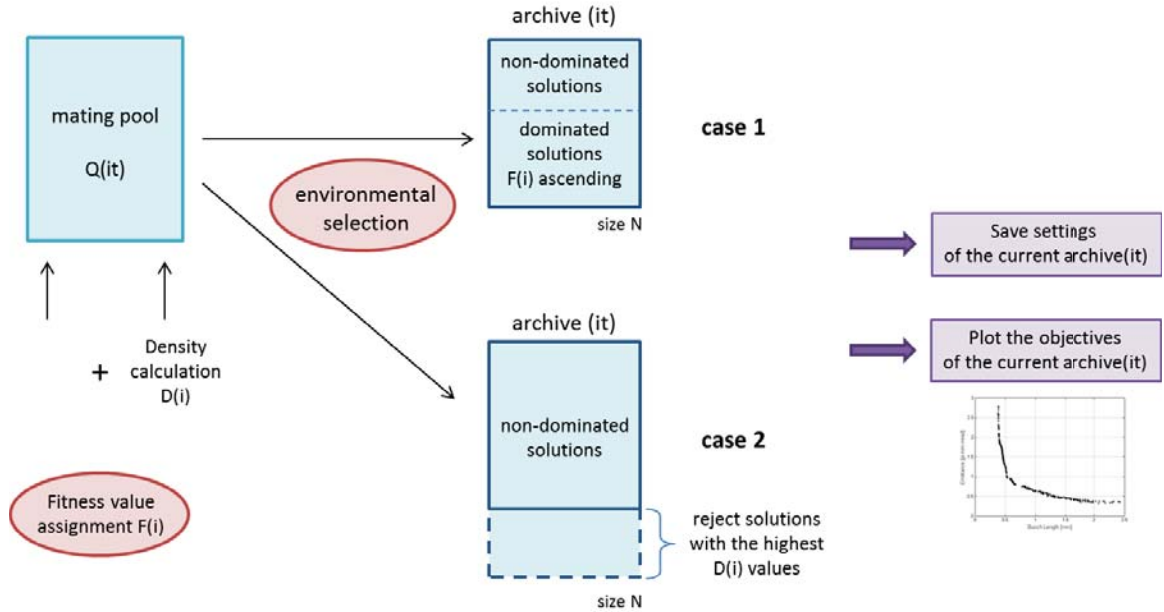


Figure 5.11: Environmental Selection following the SPEA2 algorithm.

tions from the archive. It figures out the more dominant one based on their fitness values, and transfers all decision variables of the selected solution back to the main script. In the case of *Mixing*, binary tournament selection is implemented twice in the program to select two dominant solutions,  $X1$  and  $X2$ , from the  $archive(it)$  that can be mixed up. The mixing subfunction is employed on each decision variable of the selected individuals separately. In order to create two new offspring solutions  $Y1$  and  $Y2$ , the decision variables (here  $x1$ ,  $x2$ ) are mixed up using a normal distributed random weight  $\alpha$ :

$$y_1 = \alpha \cdot x_1 + (1 - \alpha) \cdot x_2 \quad (5.4)$$

$$y_2 = \alpha \cdot x_2 + (1 - \alpha) \cdot x_1 \quad (5.5)$$

Afterwards, the sub-function controls whether the generated offspring decision variables fulfill all optimization constraints, particularly the defined limits of the decision variables. Then, the mixing sub-function returns the new decision variables as an output to the main program script. The crossing process of two solutions is repeated several times in a loop. The number of mixing runs depends on the user-defined probability  $p_{\text{Mix}}$ . Crossing represents the most important variation of the

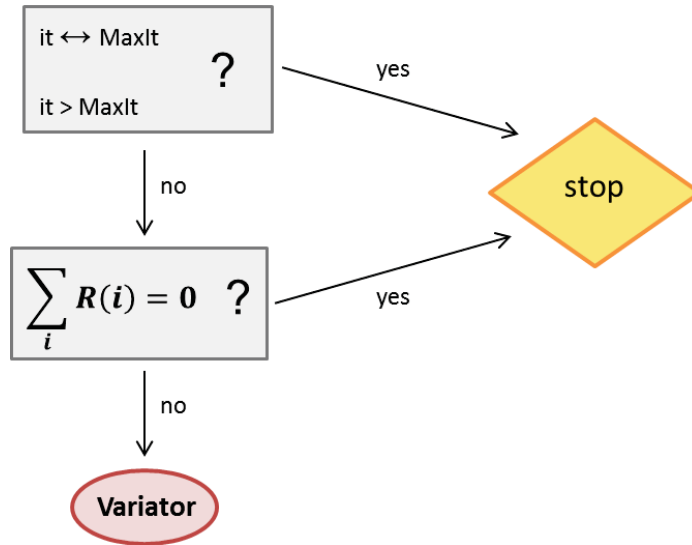


Figure 5.12: Termination criteria in the SPEA2 algorithm.

population since this strong modification leads to solutions in unexplored parts of the objective space. In order to guarantee a uniform distribution over the whole Pareto front,  $p_{\text{Mix}}$  is often set to high values of 0.6, ..., 0.9. All new offspring solutions are stored in the crossing population of the current iteration  $popc(it)$ .

The second variator mutates solutions from the archive. The *binary tournament selection* chooses one solution in a common way. Subsequently, the *Mutator* separately varies the decision variables by a small, random perturbation (up to  $\pm 10\%$  of the former value). If the mutated value falls within the limits of the corresponding decision variable, it is returned to the main script. The probability of mutation, and therefore the number of iterations in the loop of the sub-function *Mutation*, is given by  $p_{\text{Mut}}=1-p_{\text{Mix}}$ . The mutation prevents that the optimization encounters island solutions of local minima. Nevertheless, even if mutation preserves the diversity of the population, it contributes only slightly to the evolution of the population. Hence, the probability of mutation is always smaller than for the mixing procedure. The mutated solutions are saved in the new population  $popm(it)$ .

In the last step of the variator, the objectives for the new offspring solutions are evaluated using the sub-function that was introduced at an earlier point in this dissertation with particle tracking in ASTRA. After deleting untracked particle solutions and individuals with a switched off solenoid, the populations for the next iteration

$it+1$  are prepared. The offspring solutions from mixing and mutation represent the next population  $pop(it+1)$  while the current  $archive(it)$  is renamed to  $archive(it+1)$  which contains the fittest parameter sets from iteration  $it$ . This step fulfills the requirement of elite-preservation.

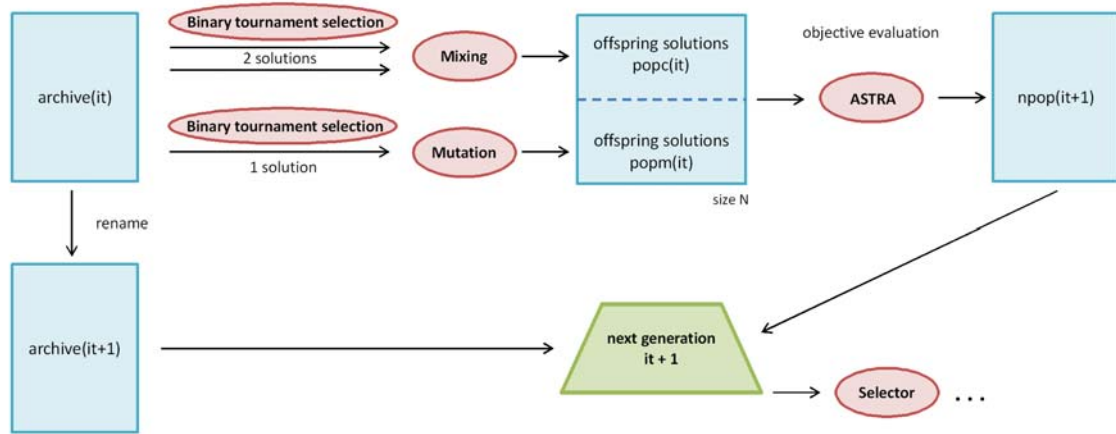


Figure 5.13: As a final step in the optimization procedure, offspring solutions are created by mixing and mutation of randomly selected solutions from the current archive.

The multi-objective optimization program enters the next generation turning back to the step of mating pool  $Q$  creation and fitness value assignment in the selector.

## 5.4 Applications of the Developed Optimization Tool

This program represents a potent tool for SRF guns. The optimization results provide information on the performance limit of the SRF gun and include the theoretical brightness limit. Further, the Pareto optimum set contains an amount of stable operation parameter settings to generate a high brightness beam. The correlation between the operation parameters and the beam dynamics from the photoemission to the optimization point are gained as a side product. Furthermore, an existing photoinjector design can be improved by using the design parameters, e.g. for the cavity geometry, as decision variables in the optimization.

The program is universal since it is able to optimize any SRF gun in the world. It is easily implementable into another design by exchanging the RF and solenoid fields as well as the position of the components in the beam path of the ASTRA input files. In addition, the script optimizes an SRF photoinjector independently from its application. Adjusting the bunch charge and the limits of the drive laser, the RF cavity and the solenoid, the multi-objective optimization program will provide stable parameter settings for an electron source (ERL, FEL) or a stand-alone facility (UED). Moreover, the program is flexible since the objectives and decision variables can be varied or extended. This means that the objectives are not restricted to the transverse emittance and the bunch length. Any parameter, for example, energy, the energy spread, the coherence length, the bunch charge a.s.o., that is obtained or calculated from an ASTRA simulation can be optimized as an objective. Operation or design parameters of the SRF gun can be added to the decision variables, e.g., the form of the temporal laser pulse profile.

The multi-objective optimization program is developed and used in this thesis to optimize several different objectives for SRF photoinjectors of different designs (HZB, HZDR) and for different applications (ERL, FEL, UED). The next chapter will present the corresponding results obtained during this dissertation.

# Chapter 6

## Multi-Objective Optimization Results

### 6.1 SRF Photoinjector Optimization without Solenoid Field Correction

Referring to the considerations of the preceding chapters, the following chapter presents the optimization results of SRF photoinjectors for different applications.

First, the photoinjector design of GunLab is optimized for a high brightness operation of the ERL facility bERLinPro. The ERL mode requires a high average current mode of 100 mA that corresponds to 77 pC bunch charge at a repetition rate of 1.3 GHz [8]. Besides the high charged beam, a compact 6D phase space with small transverse emittances  $\varepsilon_{x,y} < 1$  mm mrad and short bunch lengths  $\sigma_z$  within the range of a few ps must be achieved behind the photoinjector to fulfill the bERLinPro high brightness specifications.

The first optimization approach sets the gun operation parameters as decision variables on which the objectives depend. These variables are: The laser spot size, the laser pulse length, the cathode position, the cavity injection phase, the cavity peak field, the solenoid field and the solenoid position. They can be adjusted in the commissioning or during the photoinjector operation. Their limits are defined by the laser, the cathode, the cavity, and the solenoid design of GunLab, and of the future electron source setup in the bERLinPro facility. All parameters are summarized in Table 5.2 in the previous chapter, including their corresponding ranges. After the first optimization runs it became obvious that the cavity gradient cannot be set as a free parameter in the optimization. The optimization always prefers the highest peak field defined as an upper limit in the decision variable. This effect will be discussed

in detail in section 6.2. As a result, the cavity peak field is fixed and the optimization procedure is repeated to obtain results for medium or low acceleration fields, as well.

The transverse emittance and bunch length should be minimized at the optimization point. This position must provide a measurement station to compare the simulation values with the real beam properties and to verify the optimization results. A screen station with several YAG screens and a slit mask for emittance measurements using the slit scan technique is placed 2.5 m behind the photocathode in the diagnostic beamline of GunLab. This value is set as the  $z_{\text{stop}}$ -parameter in the ASTRA tracking. Additionally, the number of particles, as well as the space charge grid with the number of radial and longitudinal grid cells, must be chosen in the ASTRA input script. In accordance with numerical studies (see Appendix B) referring to the optimization program, the particle number is restricted to 10,000 macro particles. 30 radial and 40 longitudinal cells are used for the space charge calculations. The optimization starts with a random population of 50 parameter sets in order to limit the run time. This amount is sufficient to figure out the trend of the optimum curve, and to check if the complete phase space of the derived optimum solutions fulfill the requirements on the electron beam. For a detailed discussion, 100 or 200 solutions per population are used (see Appendix B.2.2). The maximum number of generations during the optimization process of the photoinjector is defined as a stop criterion and set to 200 iterations. Normally, the procedure finishes when all parameter sets in the archive reach a raw fitness value  $R=0$ . The MATLAB script always runs 20 ASTRA trackings in parallel on a high-performance-computing Linux cluster at HZB.

Figure 6.1 shows how the evolutionary algorithm improves the start population to the Pareto-optimum in several iterations. In the beginning, 200 different parameter sets are defined by randomly assigning values to the decision variables, thus the operation parameters of the photoinjector. Some of the parameter sets lead to maximum emittances that lie above 700 mm mrad, whereas others cause a bunch length longer than 25 ps. The first evidence showing that the program with the included optimization criterion works, is the clearly visible trend towards the expected trade-off curve after five iterations. In the 15<sup>th</sup> generation the Pareto-curve is already identifiable. The last iterations reduce the archive to only dominant solutions achieved after the 22<sup>nd</sup> iteration in a fine tuning process.



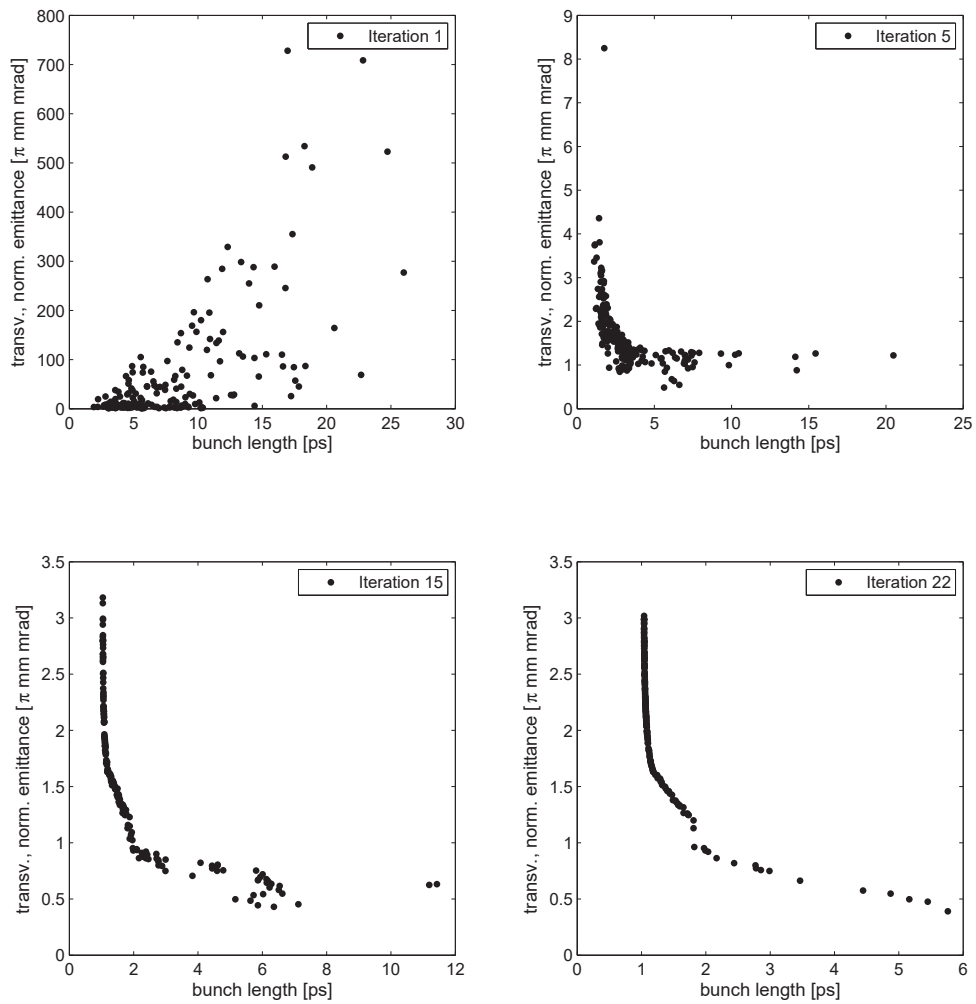


Figure 6.1: Evolution of the emittance and bunch length limit of the current SRF photoinjector design of Gunlab. The optimum curve is calculated in an evolutionary approach with a MOGA algorithm.

The resulting Pareto-optimum front (22<sup>nd</sup> iteration) contains the smallest transverse emittances and bunch lengths that can be achieved with the present gun design using a bunch charge of 77 pC and a gun peak field of 30 MV/m. The whole optimization was done in 104 hours. Therefore, the optimization program is not suited for in situ operation during the commissioning of GunLab or beam dynamic measurements. But the prepared results from the optimization tool can facilitate the commissioning process and it saves time to tune the GunLab test facility and later bERLinPro to

a high brightness mode using one of the optimum settings for the photoinjector elements.

Compared to the swarm optimization technique, the multi-objective optimization is more effective since the optimum front is found fast with fewer start settings. The resolution of the Pareto-curve is much better, as all resulting gun parameter sets are located on this front. If the curve generated by multi-objective optimization is added to the swarm plot, the MOGA based optimization demonstrates a clear superiority towards swarm optimization (see Figure 6.2). Only dominant photoinjector sets for small transverse emittances and short bunch lengths are part of the final population. The optimum curve noticeably represents the envelope of the swarm settings.

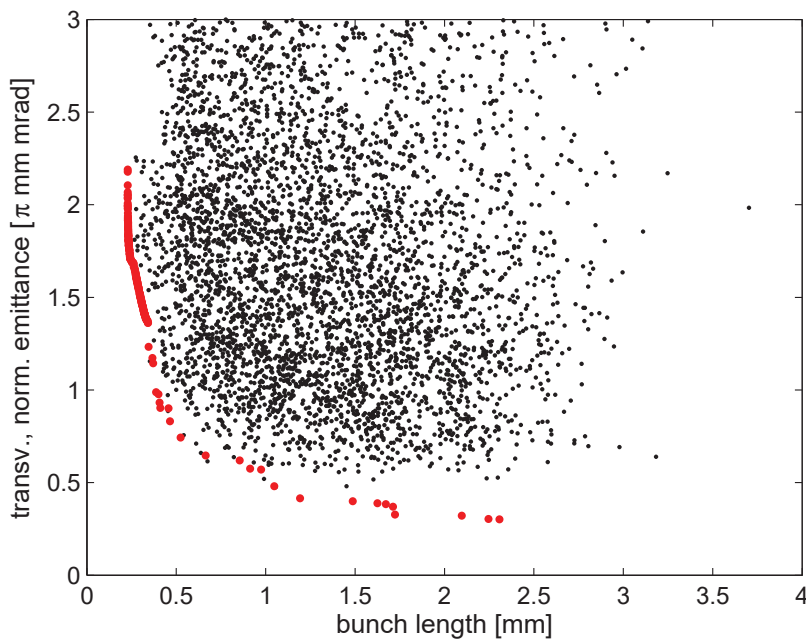


Figure 6.2: Results for a swarm optimization (77 pC bunch charge and 40 MV/m cavity peak field) of the GunLab photoinjector are compared to the Pareto-optimum front achieved by multi-objective optimization. The Pareto-curve represents the envelope of the swarm settings.

In order to discuss single parameter sets and their phase spaces in the optimum curve, the optimization process is repeated with 200 gun settings in the initial population. The resulting Pareto-front is shown in Figure 6.3. All settings are stable with respect to small perturbations in the set values of the photoinjector elements

(see Appendix B).

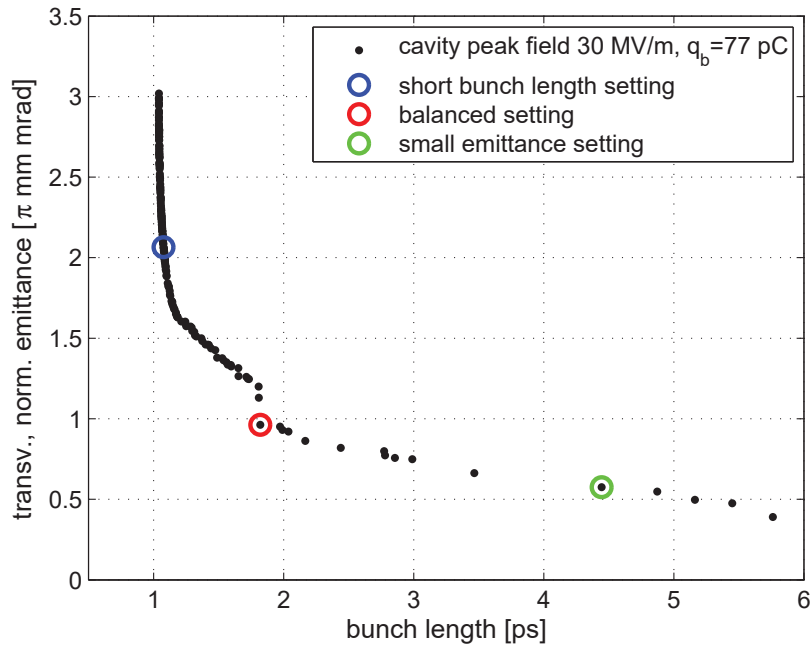


Figure 6.3: Pareto-front for 77 pC bunch charge and a cavity peak field of 30 MV/m. Gun parameter settings in the short bunch length mode (blue), compromise region (red) and small emittance mode (green) are highlighted.

It has to be mentioned that small edges and steps in the Pareto-optimum curve are usually caused by changes in the photoinjector parameters that determine the shape of the curve. The front always displays the envelope of different optimum curves (ISO-brightness curves see Chapter 4.5) following the photoinjector operation parameters as decision variables.

In order to operate the photoinjector test facility Gunlab or the electron source of bERLinPro, the transverse and longitudinal phase spaces distributions must be controlled. Furthermore, the evolution of the most important beam parameters characterizing the transverse and longitudinal phase space must fulfill the requirements of a convergent beam in both planes. Therefore, some parameter sets along the optimum curve are selected for phase space studies (marked blue, red, and green in Figure 6.3). Considering the ERL mode, the focus is on the transverse emittance which already has to be small in the injection line. Arrangements are being prepared for further compression of the bunch length in the first arc of the main ring of bERLinPro. For

that reason, the phase space evolution of the important parameter sets in the compromise region between small emittance and short bunch lengths (red marked in Figure 6.3), and in the low emittance mode (green marked in Figure 6.3), are analyzed first.

### 6.1.1 Beam parameter evolution in the compromise region

The parameter set in the compromise region leads to a final transverse emittance of 0.96 mm mrad. The bunch length reaches a value of 1.82 ps (0.54 mm). Hence, the optimized setting fulfills the bERLinPro specifications already in the injection line. Figure 6.4(a) and (b) present the evolution of the beam size, the transverse emittance, the bunch length, and the longitudinal emittance along the  $z$ -axis.

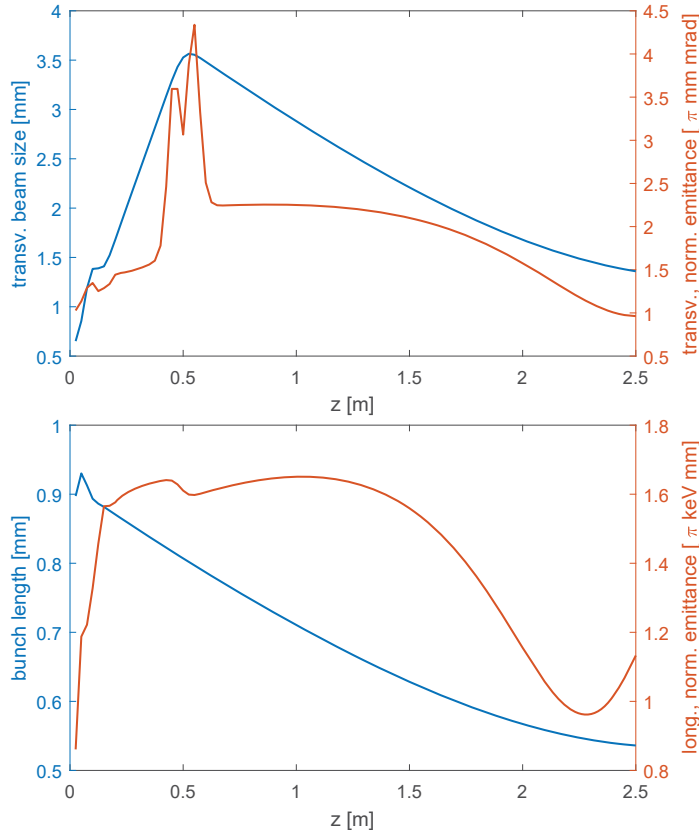


Figure 6.4: Evolution of the beam size and the transverse emittance [top: (a)] and the bunch length and the longitudinal emittance [bottom: (b)] along the  $z$ -axis from the photocathode to the optimization point at 2.5 m. The results are given for a parameter setting in the compromise region (marked red in Fig.6.3). The optimization was subjected to a 77 pC bunch charge and a cavity peak field of 30 MV/m.

The initial beam size is dominated by the laser spot size at the cathode, which is chosen with a rather small size of 0.49 mm (*rms*). The small initial beam size minimizes the contribution of the intrinsic emittance to the total projected emittance (see Chapter 4.3.1). After a first space charge and RF field dominated beam size growth in the cavity, the transverse bunch size is focused by the solenoid magnet placed 0.5 m behind the photocathode (see Figure 6.4(a)). The focal point of the beam is located close to the optimization point at 2.5 m.

The transverse emittance is mainly determined by the beam size and thus by the laser spot size at the cathode (see Figure 6.4(a)). The strong emittance growth in the solenoid can be traced back to the transverse beam rotation (Larmor rotation [111]) inside the solenoid. The Larmor rotation cannot be described by decoupled horizontal and vertical equations of motion since the projected phase space distributions are not independent. The additional momentum distribution in the phase spaces produces an increased projected emittance. This effect can be compensated by using the 4D phase space  $(x, x', y, y')$  or by a transformation in the Larmor system which is associated with the beam rotation in a solenoid field.

According to the theory of Serafini and Rosenzweig (see Chapter 4.4.2), the emittance compensation of the solenoid leads to the projected emittance minimum being situated close to the optimization point. The emittance compensation point of the solenoid magnet follows shortly behind the focal point. The optimization chooses a solenoid peak field on axis of 102.9 mT that moves the emittance compensation point of the beam to the optimization point as close as possible. The beam energy at the solenoid entrance is also considered in this process. This effect of emittance compensation is presented in Figure 6.4(a).

The bunch is generated at the photocathode with a rather long laser pulse length of 4.44 ps. In order to counteract the space charge effects right after the bunch emission (see Equ. (4.44) in Chapter 4.3.4), the optimization program tends to choose a longer laser pulse length if the laser spot size is kept compact on the photocathode. Longitudinal space charge interactions cannot be neglected in the low energy part of the injector. This effect leads to a first bunch extension in the cavity [see Fig. 6.4 (b)]. The bunch is injected -30 deg relative to the on-crest phase. Strong RF chirping at this phase combined with the drift space up to the optimization point at 2.5 m leads to bunch compression, which is due to velocity bunching (see Chapter 4.4.3). Close to the optimization point, the slope of the bunch compression is attenuated by space charge effects. In this region, the transverse and longitudinal phase spaces are well focused, whereas the bunch has not yet reached an ultra-relativistic velocity. It

is, thus, still space charge dominated. Nevertheless, a short bunch length of 1.82 ps (0.54 mm) is reached.

Finally, Figure 6.4 (b) displays the longitudinal emittance. This parameter is impacted by the bunch length and the energy spread. The maximum of the longitudinal emittance is reached close to the cavity exit. Since the beam was generated by a long laser pulse and the velocity bunching process has not yet started, the bunch length is rather long at this position. Furthermore, the energy spread is at its maximum at the cavity exit due to the imprinted energy chirp. The bunch length and the energy spread are decreased in the drift space simultaneously that leads to a longitudinal emittance minimum shortly before 2.5 m. The minimum energy spread at 2.5 m corresponds to 0.1% of the beam energy and, thus, fulfills the bERLinPro requirement on the relative energy spread.

### 6.1.2 Beam parameter evolution in the low emittance regime

Figures 6.5(a) and (b) show the beam size, transverse emittance, bunch length, and the longitudinal emittance evolution for the low emittance mode.

The laser spot size is comparable to the spot size in the compromise region. Due to a cathode retreat of -2 mm, the bunch is additionally focused by the radial part of the electric RF field of the cavity. This effect leads to a smaller slope in the beam size growth induced by the space charge. The solenoid focuses the beam behind the cavity with a strong axial magnetic field of 115.0 mT. The focal point is clearly in front of the emittance compensation point [see Fig. 6.5(a)].

The transverse emittance can be slightly minimized in the accelerating structure [see Fig. 6.5(a)]. This effect is supported by the small laser spot size on the cathode as well as by the cathode retreat and the corresponding radial focusing in the cavity. In order to perfectly match the emittance compensation at the optimization point, the solenoid is placed close to the cavity (0.48 m behind the photocathode) so that the emittance compensation starts right behind the cavity exit. The first and the second emittance minimum due to the beam oscillations can then be observed [see theory Chapter 4.4.2 and Fig. 4.18]. The smaller transverse emittance value (0.58 mm mrad) compared to the compromise region is achieved through the smaller laser spot size on the cathode, a cathode retreat, a stronger solenoid field, and by positioning the solenoid next to the cavity exit.

Additionally, the laser pulse length is enlarged to a size of 6.36 ps compensating the

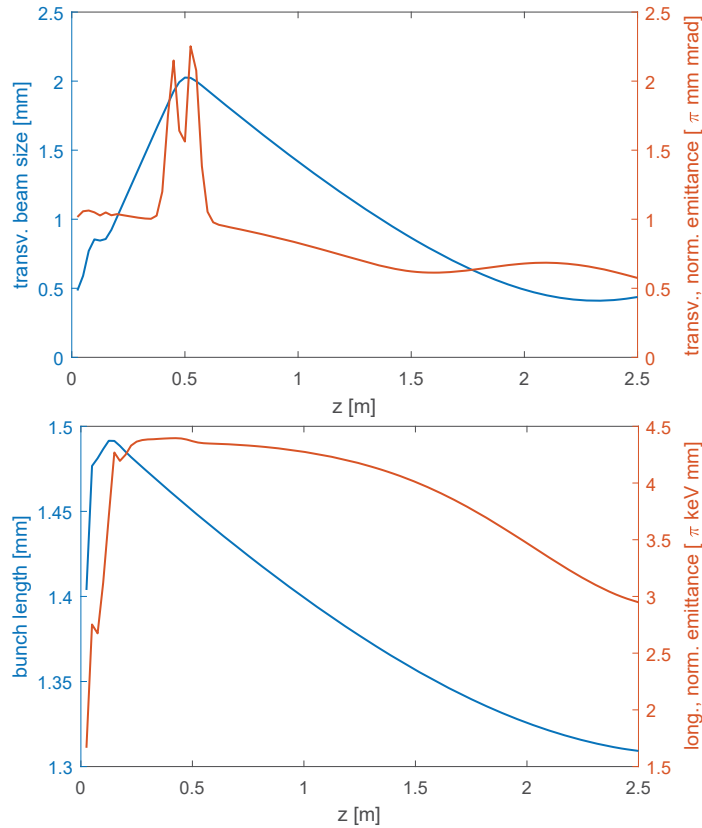


Figure 6.5: Evolution of the beam size and the transverse emittance [top: (a)] and the bunch length and the longitudinal emittance [bottom: (b)] along the  $z$ -axis from the photocathode to the optimization point at 2.5 m. The results are given for one parameter setting in the low emittance mode (marked green in Fig.6.3).

space charge pressure of the minimized laser spot size. The gun injection phase of  $-13.1$  deg is set closer to the on-crest phase than the setting in the compromise area. This phase setting leads to a more moderate RF chirping and small velocity bunching. The bunch is compressed down to 4.44 ps (1.31 mm) and remains convergent in the longitudinal plane [see Fig. 6.5(b)].

The final longitudinal emittance at 2.5 m shown in Fig. 6.5(b), lies clearly above the longitudinal emittance value of the compromise region as the bunch length and the energy spread are only slightly focused in the drift line behind the gun cavity exit. However, the relative energy spread at 2.5 m for the presented low emittance example holds the value of 0.1% and, therefore, follows the bERLinPro scenario.

To summarize, the focus of this end of the Pareto-optimum curve is, nevertheless, on the small transverse emittance.

Analyzing Figure 6.4(b) and Figure 6.5(b) again, the emittance compensation point appears to lie slightly behind the optimization point. This observation gives rise to the question of whether the transverse emittance improves further if the optimization point is added as a free parameter to the optimization procedure. To answer this question, the  $z_{\text{stop}}$  value in the ASTRA routine is set to 7.0 m. The initial population is now optimized towards minimum emittance values and their corresponding bunch lengths, independent of the position of emittance compensation.

### 6.1.3 Pareto-optimization with a variable optimization point

Figure 6.6 displays the result of the Pareto-optimum curve.

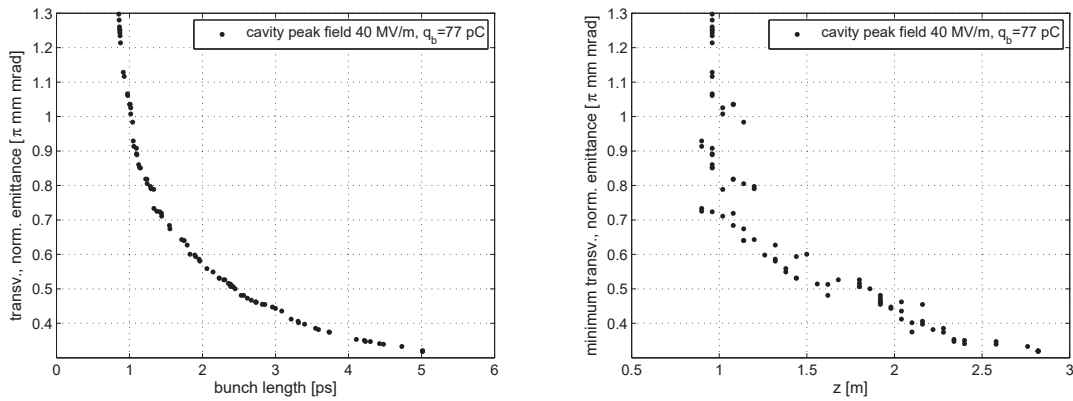


Figure 6.6: (a) The Pareto-optimum curve for an optimization procedure that includes minimum emittance values with a variable optimization point (decision variable). (b)  $z$ -positions of minimum transverse emittances. The absolute emittance minimum (0.31 mm mrad) is achieved at 2.8 m.

The optimum curve presents a smoother contour compared to the optimization result with a fixed reference point. The achieved minimum transverse emittance at 2.5 m can be improved by 30% to 0.31 mm mrad [see Fig. 6.6(b)]. This minimum is located 2.8 m behind the cathode. Therefore, the result confirms that the transverse emittance can further be decreased behind the chosen stopping point of the simulations.

This effect comes into play when a booster section is added to the photoinjector, providing further beam acceleration in one or several linac cavities. The entrance of the booster is normally placed close to the emittance compensation point to preserve the small emittance value during the acceleration through the whole booster. A booster



entrance close to the 2.8 m matches the smallest achievable emittance of the current SRF photoinjector design using the corresponding gun parameter set determined by the multi-objective optimization tool [see Fig. 6.7]. The booster position (iris position of the first 2-cell cavity) in the bERLinPro injection line is currently planned at 3.2 m behind the cathode and, therefore, slightly behind the evaluated optimum [8].

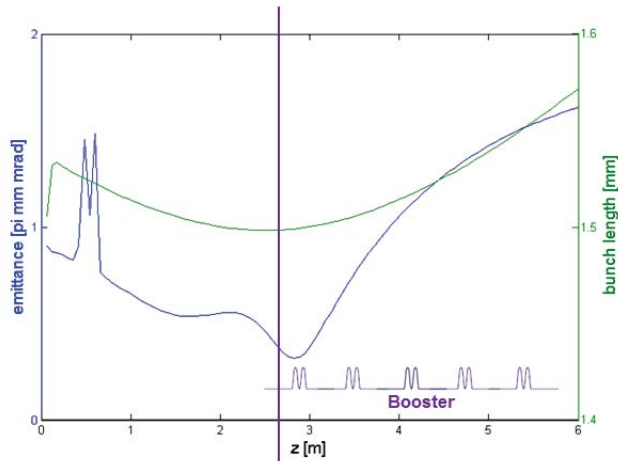


Figure 6.7: Beam parameter evolution along the beamline from the photocathode to 7.0 m corresponding to the case of a minimum transverse emittance of 0.31 mm mrad at the optimization point. If the entrance of the booster is placed close to the emittance compensation point the small emittance value can be preserved during the acceleration through the whole booster.

Nevertheless, the optimization point for the presented optimization results in the thesis at hand remains at 2.5 m since the screen station at this position in the Gunlab beamline and its slit mask makes the transverse phase space characterization possible and, thus, the verification of the optimization results.

#### 6.1.4 Beam parameter evolution in the short bunch length regime

Short pulses are required for some user experiments that can be conducted behind the SRF photoinjector or in the injection line of an ERL. When diffraction experiments are performed in a pump-probe-setup, the electron bunch length determines the time resolution of the diffraction patterns. Therefore, a gun parameter set in the short bunch length mode is analyzed (marked blue in Figure 6.3 and parameter evolution in Figure 6.8(a) and (b)).

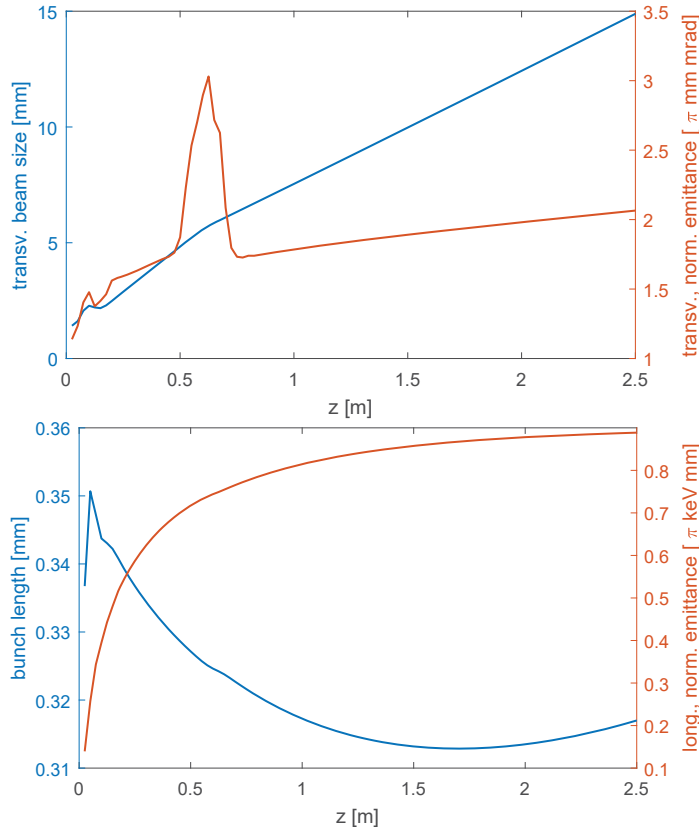


Figure 6.8: Evolution of the beam size and the transverse emittance [top: (a)] and the bunch length and the longitudinal emittance [bottom: (b)] along the  $z$ -axis from the photocathode to the optimization point at 2.5 m. The results are given for a parameter setting in the short bunch length mode (marked blue in Fig.6.3). The optimization is subjected to 77 pC bunch charge and a cavity peak field of 30 MV/m.

The required short bunch length is achieved by a short laser pulse of 2.57 ps at the cathode and a strong RF focusing with an injection phase of -30 deg, relative to the on-crest phase, followed by velocity bunching. The strong energy chirping leads to a growth in the longitudinal emittance that is located in the area between the cathode and 1 m in the beamline. Afterwards, the bunch length and the energy spread stay nearly constant and the longitudinal emittance does not change anymore. A nonlinear distribution of the longitudinal phase space makes a detailed analysis of the evolution of the longitudinal emittance along the beamline challenging. The final longitudinal emittance at 2.5 m is rather small with a value below  $1 \pi$  keV mm.

As a consequence of the selected short laser pulse length, the laser spot size is set to its upper parameter limit of 1.5 mm (*rms*) on the photocathode that also affects

an enlarged intrinsic emittance and an initial beam size [see Fig. 6.8(a)]. In the short bunch length mode, the optimization tool tries to minimize the emittance by avoiding solenoid emittance contributions. Since the impact of the chromatic aberration is proportional to the squared beam size and the spheric aberration grows with the fourth power of the beam size, solenoid emittance contributions increase the total transverse emittance significantly [see Equ. (4.38) and (4.39)]. Through this reason, the solenoid axial field is optimized to its minimum value of 50 mT. Neither radial focusing in the beam size, nor an emittance compensation point can be observed in Fig. 6.8(a). The transverse emittance is nearly constant behind the solenoid providing only a small slope. Based on these observations, the parameter set is selected as an optimum by the procedure. The beam is appreciably divergent. A similar trend can be seen in the beam size and emittance evolution of other parameter sets in the short bunch length region of the optimum curve. Furthermore, it can be observed that the optimization program strategically switches off the solenoid in order to minimize the transverse emittance in a low current mode, which is preferred for diffraction experiments in order to obtain small phase spaces.

### 6.1.5 Correction of the solenoid field

Up to this point, the solenoid field strength was a free decision variable in the optimization program, randomly chosen in the first population and selected independent of the other gun parameters. However, according to the solenoid theory (see Chapter 4.3.3), the focusing strength is not only defined by the axial magnetic field but also by the momentum of the particles that move into  $z$ -direction. The beam momentum is set by the cavity peak field and the chosen gun injection phase of the individual parameter set that is also a free decision variable in the algorithm. Hence, the axial magnetic field of the solenoid cannot be selected independent of the gun phase and the fixed cavity gradient. Therefore, it cannot be used as a free parameter in the optimization.

In a first approach to solve this problem, different lookup tables including the gun phase, the cavity peak field, the cathode position, and the corresponding solenoid field are prepared. The magnetic fields are calculated in ASTRA trackings along the Gunlab beamline that use five test particles and neglect space charge effects to save run time. The gun phase is divided into steps of 0.5 deg from -30 deg to 30 deg, while the cavity peak field varies from 15 MV/m to 30 MV/m in 5 MV/m steps. Six different cathode positions from -2.5 mm to 0 mm are considered. The results contain the

## 6. Multi-Objective Optimization Results

solenoid field which shows all five particles crossing the beam axis at 2.5 m behind the cathode. In the optimization the calculated solenoid fields from the lookup table are varied by  $\pm 10$  mT to compensate the neglected space charge effects.

The strategy fails at a cathode position of -1.5 mm. If the cathode is drawn back relative to the back plane of the gun cavity, the radial electric field of the RF wave can be used for a first beam focusing in the radial plane. This radial RF focusing is increased at larger cathode retreats. The focusing point of the RF field slips into the solenoid at a cathode position of -1.5 mm. No further transverse focusing by the solenoid magnet occurs. The solenoid field is set to 0 mT in the lookup table. Below -1.5 mm, the focal point lies in the cavity, and the beam is already divergent at the solenoid magnet. An additional focusing effect of the magnet can be observed. These effects for the two cathode positions -1.5 mm and -2.0 mm are illustrated for different solenoid field strengths in Figure 6.9.

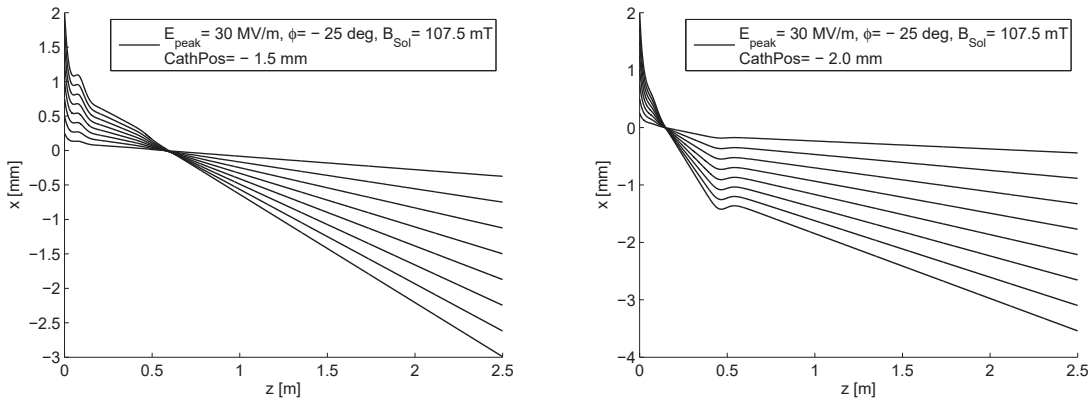


Figure 6.9: Left(a): Tracking of eight particles along the beamline starting with a cathode retreat of -1.5 mm. The acceleration field is set to 30 MV/m with an injection phase of -25 deg, the solenoid focuses with 107.5 mT. Space charge is neglected in this ASTRA tracking. The focusing point of the RF field lies in the solenoid. No solenoid performance can be detected due to the already compact beam size.

Right(b): Tracking for eight particles along the beamline starting at a cathode position of -2.0 mm. The cavity and solenoid settings correspond to the tracking conditions of Fig. 6.9(a). The strong focusing of the RF field with a focusing point at 15 cm behind the cathode allows an impact of the solenoid.

Another disadvantage of this procedure is that individual lookup tables must be calculated for different bunch charges and optimization points ( $z_{\text{stop}}$ ). This time-consuming technique requires nearly 3,000 ASTRA trackings for each bunch charge and each optimization point to compile one complete lookup table for all possible

photoinjector settings.

As an alternative, the required focusing field of the solenoid can be calculated from the transverse bunch distribution at the cavity exit aiming for a minimized transverse phase space at the optimization point. Therefore, the  $\beta(z)$ -function represents a measure of the local beam size along the beam path  $z$ . The ASTRA tracking in the optimization process is interrupted behind the cavity ( $z=0.30$  m). The  $\beta(z)$ -function is evaluated at the optimization point using the bunch distribution from the ASTRA output at 0.30 m, as well as the transfer matrix between cavity axis and optimization point. The transfer matrix includes a drift space between cavity and solenoid, the solenoid transfer itself, and an additional drift space from the solenoid to the optimization point. The  $\beta(z)$ -function at 2.5 m is calculated for different solenoid fields between 0.1 mT and 200 mT changed by 0.1 mT steps. Finally, the smallest transverse phase space ( $\beta(z)$ -function) and its corresponding solenoid field are selected from the results. The solenoid magnetic field is added to the gun parameter setting. Afterwards, the ASTRA tracking is repeated for the whole beam line up to the optimization point using the calculated solenoid field. Since space charge effects are now considered, the calculated magnetic field is randomly modified by a maximum variation of 10%. This procedure is applied to all parameter sets in the current population. The great advantage of this technique is that the procedure evaluating the bunch distribution at the cavity exit, includes space charge effects. Therefore, more precise results in the calculated solenoid field can be achieved. The run-time of the additional ASTRA tracking up to 0.30 m behind the photocathode must be accepted.

## 6.2 SRF Photoinjector Optimization with Solenoid Field Correction

Figure 6.10 shows the optimum curve of the optimization with the described solenoid magnet correction [41]. Again, the Pareto-front is clearly evaluated. This result is compared to the first optimization in which the axial magnetic field of the solenoid was a free parameter [see Fig. 6.11]. Both curves fit very well in the compromise region between small emittances and short bunch lengths, as well as in the low emittance mode. The new optimized front shows a better resolution with more parameter sets at the low emittance end. Here, small deviations in the emittance values of the

## 6. Multi-Objective Optimization Results

---

small curve can be traced back to the statistical error of the optimization process (Appendix B.3.3). The optimum curve obtained with solenoid correction also explains the edge in the curve shape without solenoid correction at a bunch length of 1.7 ps and an emittance of 1 mm mrad. At this point in the optimum curve, the solenoid field changes from around 100 mT, to achieve small emittance values, to the solenoid field minimum of 50 mT, to achieve bunch lengths shorter than 1.7 ps. Although the optimization with solenoid correction does not provide parameter settings with such short bunch lengths, the evolution of the beam size and the emittance are convergent and controlled.

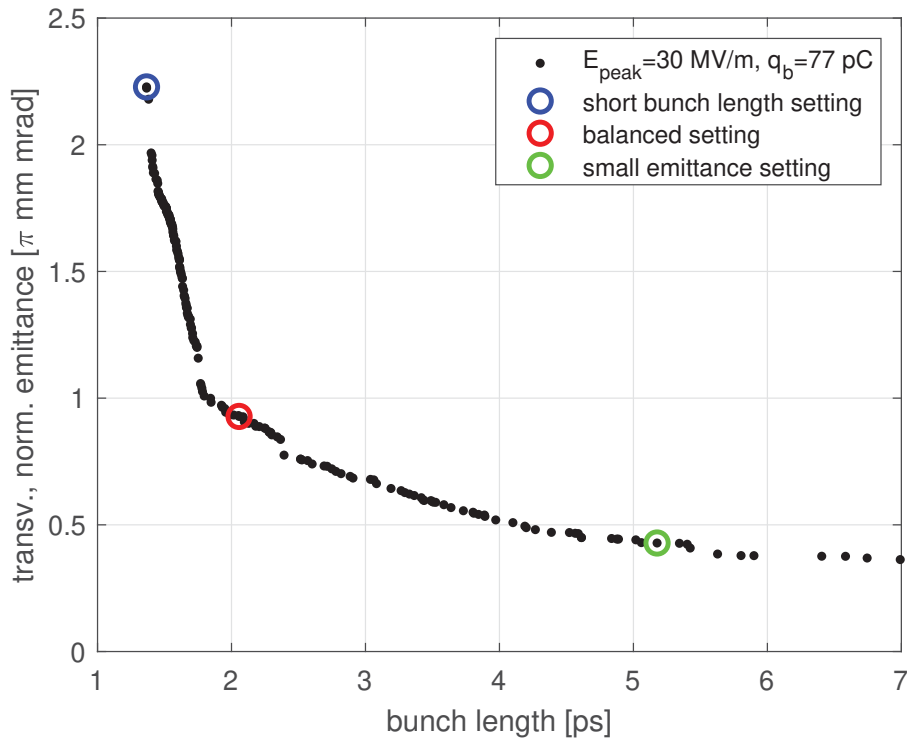


Figure 6.10: Pareto-front for 77 pC bunch charge and a cavity peak field of 30 MV/m including a solenoid field correction. Gun parameter settings in the short bunch length mode (blue), compromise region (red) and small emittance mode (green) are highlighted.

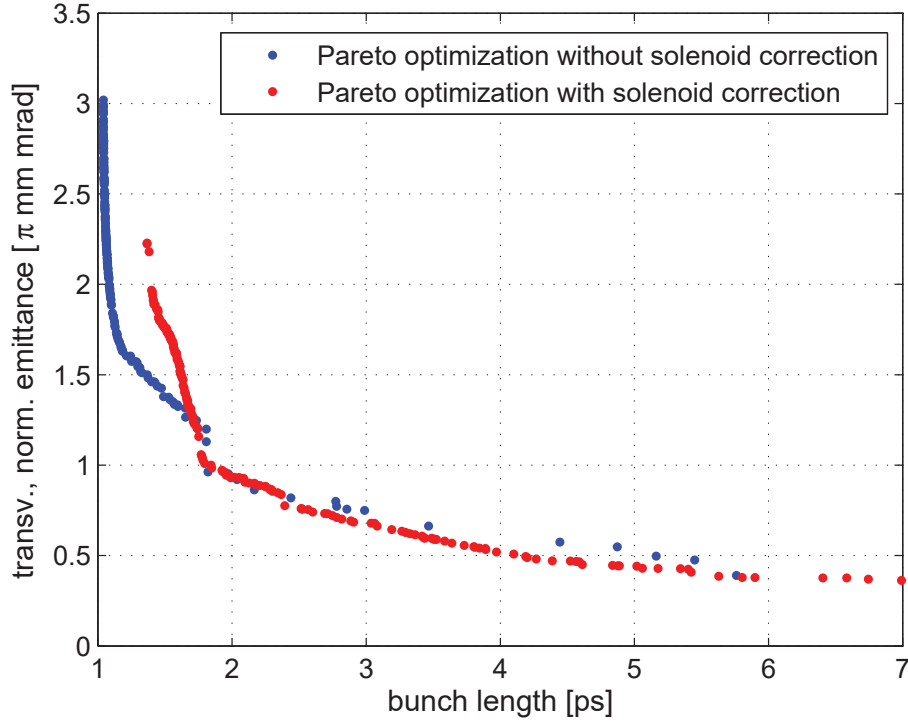


Figure 6.11: Comparison of the Pareto-optimum curves without (blue) and with (red) solenoid correction.

### 6.2.1 Beam parameter evolution in the short bunch length mode

The controlled transverse and longitudinal phase spaces are illustrated in Figure 6.12(a) and (b) for one point in the short bunch length region of the optimum front (marked blue in Figure 6.10).

In short bunch length mode, a short laser pulse of 3.16 ps generates the bunch. This value is slightly above the selected laser pulse length in the optimization without solenoid correction (2.57 ps). After the photoemission, the bunch is compressed by velocity bunching using a maximum gun cavity injection phase of -30 deg relative to the on-crest phase (see Figure 6.12(b)). The bunch length reaches its minimum value at 2.0 m behind the photocathode. Therefore, the bunch is longitudinally over-focused at the optimization point (2.5 m) since the transverse phase space has to be controlled simultaneously. However, a final bunch length of 1.4 ps (0.4 mm) at a high charge (77 pC) represents a short beam.

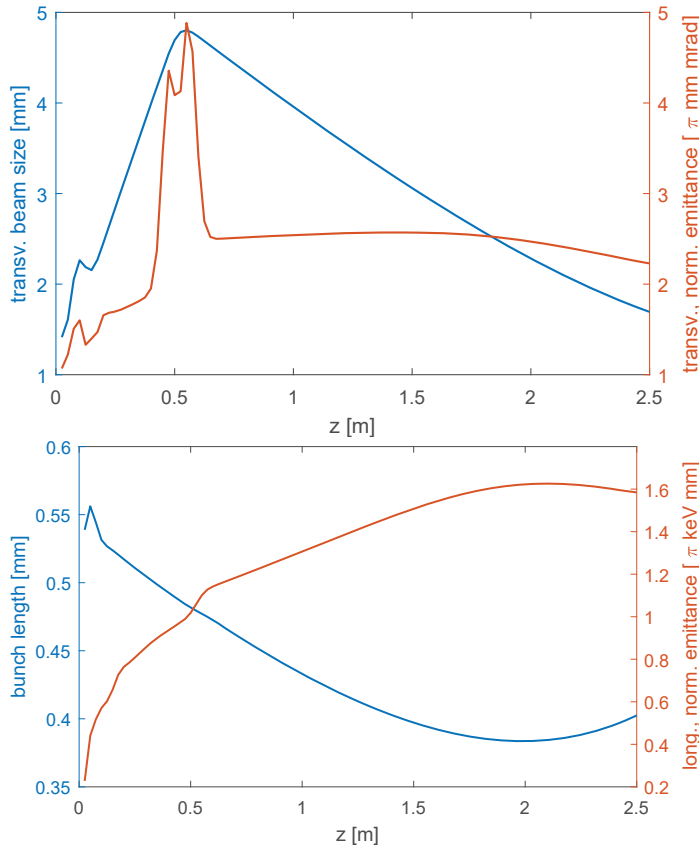


Figure 6.12: Evolution of the beam size and the transverse emittance [top: (a)] and the bunch length and the longitudinal emittance [bottom: (b)] along the  $z$ -axis from the photocathode to the optimization point at 2.5 m. The results are given for one parameter setting in the short bunch length regime (marked blue in Fig.6.10). The optimization is subjected to 77 pC bunch charge and a cavity peak field of 30 MV/m. The solenoid field is adjusted to the beam energy that is defined by the gun gradient and the selected injection phase.

The evolution of the longitudinal emittance in Fig. 6.12(b) is comparable to the one without solenoid correction in the optimization. The minimum of the energy spread corresponds to the bunch length minimum at 2 m following the theory of velocity bunching. However, the longitudinal emittance increases until 2.0 m, becomes nearly constant at 2.0 m before it slightly starts to decrease. Strong space charge and non-linear effects act on the initially “pancake”-shaped beam at the photocathode, during the acceleration in the RF cavity, and the velocity bunching in the drift. The longitudinal phase space evaluation in the following section [see Section 6.2.2] will underline that the longitudinal emittance can no longer be described by linear transformations along the  $z$ -direction. This deformation of the longitudinal phase space makes the interpretation of the longitudinal emittance challenging. A higher energy spread at



2.5 m leads to an increased relative energy spread of 0.3% and a longitudinal emittance of  $1.5\pi$  keV mm. The slightly enlarged longitudinal phase space compared to the short bunch length results in the optimization without solenoid correction [see Fig. 6.11] is a consequence of the more compact and controlled transverse beam parameters. However, the results are still interesting for an application in the short bunch length regime.

Fig. 6.12 demonstrates that the solenoid correction provides the desired control of the transverse phase space in the short bunch length regime. The beams size as well as the transverse emittance are successfully minimized at the optimization point. In order to counteract strong space charge effects and to allow a prioritized strong bunch length focusing, the beam size and the transverse intrinsic emittance starts with maximum values at the cathode (maximum laser spot size of 1.5 mm). A moderate focusing of the solenoid with 0.96 T follows. The solenoid is placed at 0.52 m behind the cathode. It, thus, is distanced further away from the cathode than the selected solenoid positions in the compromise and small emittance regions. Therefore, the transverse beam focusing and the emittance compensation starts later, relative to the longitudinal compression. As an effect of this distancing and the moderate solenoid field, the focal point of the solenoid and the emittance compensation point is not fully reached at the optimization point at 2.5 m (see Figure 6.12(a)). The optimization selects a gun parameter set that balances the compressed bunch length (at 2.0 m) and the minimum emittance (behind 2.5 m) at the optimization point.

## 6.2.2 Phase space evaluation in the short bunch length regime

In this section, the transverse and longitudinal phase spaces corresponding to the short bunch length mode are discussed.

The transverse phase space of a bunch including 10,000 macroparticles is evaluated at the optimization point.

The bunch has a round shape and is symmetrically distributed in the transverse plane [see Fig. 6.13(a)]. The particle distribution is flattop-shaped as defined by the radial laser distribution. The shape is preserved during the beam transport through the SRF photoinjector. The large laser spot size on the photocathode and a merely moderate beam focusing from the solenoid leads to a rather large beam size at the

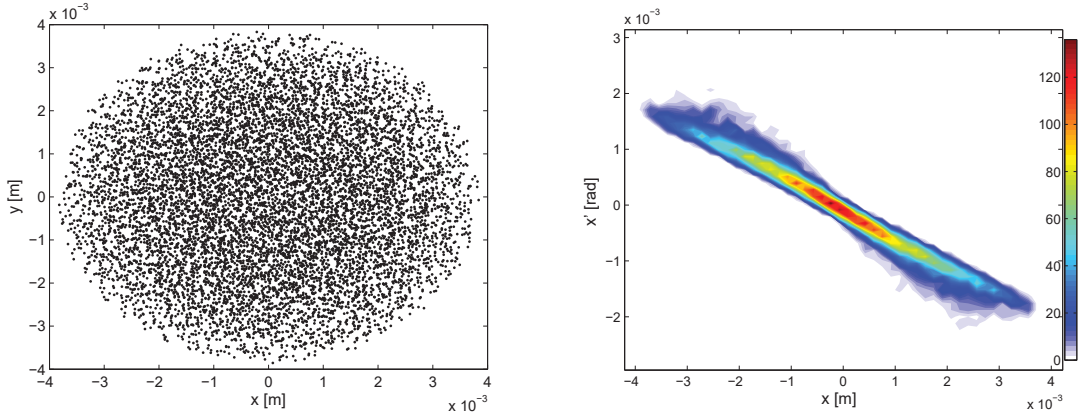


Figure 6.13: The transverse phase space distribution at the optimization point at 2.5 m. The results show the transverse bunch distribution (left (a)) and the transverse phase space distribution (right (b)) for a parameter setting in the short bunch length region.

optimization point. The focus is clearly on a short bunch length. As shown in Fig. 6.12(a), neither the focus point of the solenoid magnet, nor the emittance compensation point are reached at the optimization point. The slope of the transverse phase space ellipse in Fig. 6.13(b) confirms that the beam is still convergent. Moreover, some slices at the head and the tail of the bunch mismatch but will be aligned at the emittance compensation point behind 2.5 m. Only a small twist in the transverse phase space occurs indicating that nonlinear effects act on the bunch. Due to the large beam size in the transverse plane, transverse space charge effects are mostly controlled.

Fig. 6.14(b) represents the longitudinal phase space in the short bunch length regime at the optimization point.

The interpretation of the longitudinal phase space poses a challenge and requires an analysis of the longitudinal phase space evolution along the beamline. Because of space charge and nonlinear effects that act on the ultrashort bunch (“pancake”-regime at the cathode), a twisted S-shape in the longitudinal phase space occurs in the gun cavity already. Furthermore, to reach an ultrashort bunch, a strong energy chirp is imprinted on the bunch by selecting a gun injection phase of -30 deg relative to the on-crest phase. As a consequence, the phase space distortion - induced by nonlinear and longitudinal space charge - is reinforced during the velocity bunching in the drift space. The energy spread shrinks along the  $z$ -axis towards the focusing

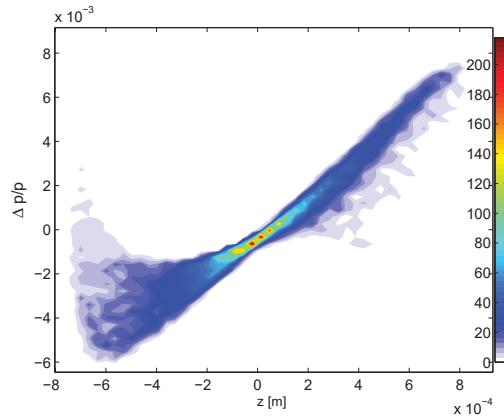


Figure 6.14: The longitudinal phase space distribution at the optimization point at 2.5 m. The result is displayed for a parameter setting in the short bunch length region.

point. This decrease in the energy spread leads to a rotation of the ellipse in the longitudinal phase space. Fig. 6.14 shows a positive slope of the phase space ellipse at the optimization point indicating that the phase space is evaluated behind the longitudinal focusing point [see also Fig.6.12(b)]. During the bunch compression by velocity bunching high energy particles in the bunch tail catch up at the center of the bunch. This effect is caused by the positive energy spread of the tail particles and, in the end, the bunch is consequently compressed. It is observed that the reference particle in the bunch center is pushed forward by the tail particles and whereby it gains velocity. Simultaneously, the bunch head particles slow down relative to the reference particle. The phase space distribution at the bunch head turns towards a smaller relative energy spread that can be observed in Fig. 6.14. To summarize, the nonlinear longitudinal phase space distribution results from nonlinear forces and space charge effects that act on the bunch, and from a strong bunch compression along the beamline.

### 6.2.3 Beam parameter evolution in the compromise region

Fig. 6.15 displays the evolution of transverse and longitudinal beam parameters along the beamline for a setting in the compromise region between small emittance and short bunch length (marked red in Figure 6.10). The parameter evolution is comparable to the results from an optimization without solenoid correction (see Figure 6.4(a) and (b)).

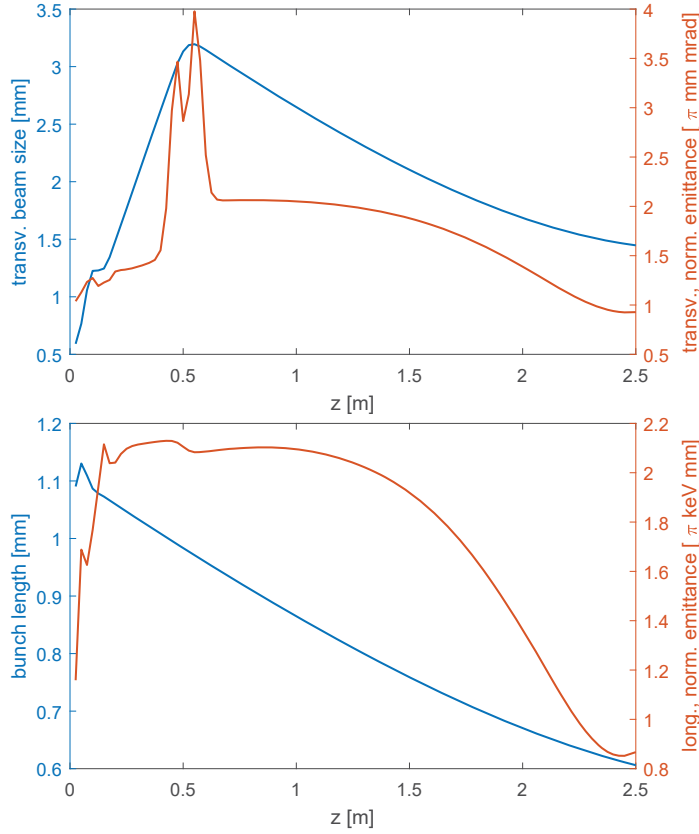


Figure 6.15: Evolution of the beam size and the transverse emittance [top: (a)] and the bunch length and the longitudinal emittance [bottom: (b)] along the  $z$ -axis from the photocathode to the optimization point at 2.5 m. The results are given for a parameter setting in the compromise region (marked red in Fig.6.10). The optimization is subjected to a 77 pC bunch charge and a cavity peak field of 30 MV/m. The solenoid field is adjusted to the beam energy which is defined by the gun gradient and the selected injection phase.

The transverse beam size and emittance are well focused which was achieved by a small laser spot size on the cathode (0.46 mm), a cathode retreat of -0.5 mm, and a strong solenoid field of 101.8 mT. However, as shown in Fig. 6.15(a), the beam is not completely focused, yet, at 2.5 m and has not fully reached its emittance compensation point. Therefore, a shift in the optimization point, as demonstrated in section 6.1.3, would allow smaller emittance values.

The laser pulse driving the photoemission process in the compromise mode has a tendency towards a “cigar”-shaped-regime. The bunch is generated by a rather long laser pulse of 5.7 ps. Afterwards, the bunch is focused by velocity bunching that is triggered with a gun injection phase of -28.7 deg relative to the on-crest phase. The bunch compression is also visible in the bunch length evolution along the beamline in

Fig. 6.15(b). The bunch length minimization is not finished at the optimization point of 2.5 m. Additionally, the second curve in 6.15(b) reflects the longitudinal emittance evolution of the bunch. The longitudinal emittance is defined by the bunch length compression as well as the energy spread reduction during the velocity bunching process. A minimum of 0.86 keV mm is reached close to the optimization point.

The corresponding transverse and longitudinal phase spaces will be discussed in the subsequent section.

### 6.2.4 Phase space evaluation in the compromise region

The transverse and longitudinal phase space of a bunch in the compromise region is analyzed in the following section.

Fig. 6.16(a) plots the bunch distribution in the transverse plane.

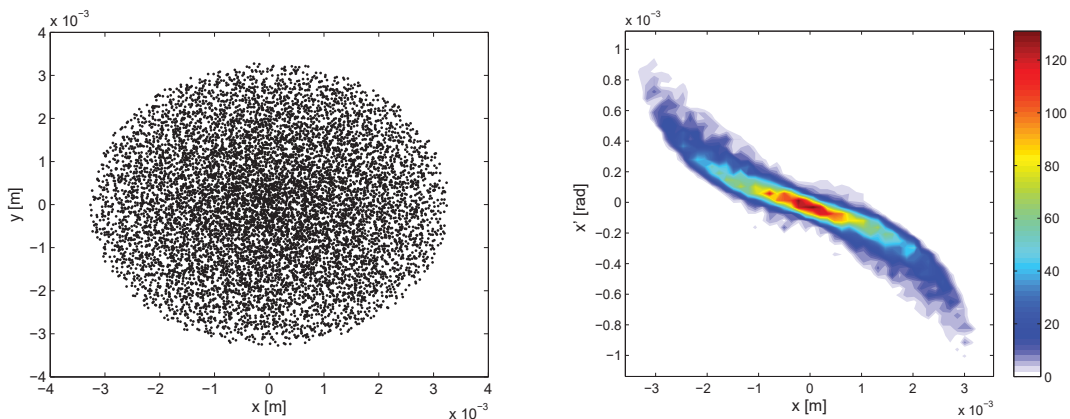


Figure 6.16: The transverse phase space distribution at the optimization point of 2.5 m. The results show the transverse bunch distribution (left (a)) and the transverse phase space distribution (right (b)) for one parameter setting in the compromise region.

The bunch is symmetric, round-shaped and flattop-distributed. Therefore, the transverse x-y-distribution - originally defined by the photocathode drive laser - can be preserved during the beam transport through the SRF photoinjector and the subsequent drift until 2.5 m.

The evolution of the transverse emittance in Fig. 6.4(a) shows that the optimization point lies slightly before the focus point of the solenoid and the emittance compensation point. The orientation and slope of the ellipse in the transverse phase space

verifies that the bunch is still convergent in the transverse plane [see Fig. 6.16(b)]. Close to the emittance compensation point, only a few particle slices mismatch at the head and the tail of the bunch. All other slices are already well aligned and prove a successful emittance compensation by the solenoid. A small S-shape in the transverse plane can be observed. The distortion of the phase space is mostly space charge dominated since it occurs primarily in the bunch center that includes high charged slices. Furthermore, as the bunch is close to the focusing point of the solenoid [see beam size evolution in Fig. 6.15(a)], the transverse phase space is particularly sensitive to the nonlinear effects by the solenoid magnet.

The longitudinal phase space distribution in Fig. 6.17 confirms that the bunch compression by velocity bunching is not finished at the optimization point. Particles in the tail of the bunch provide a higher momentum than particles in the center or at the front. Only a slight S-curvature which is due to nonlinear effects can be detected.

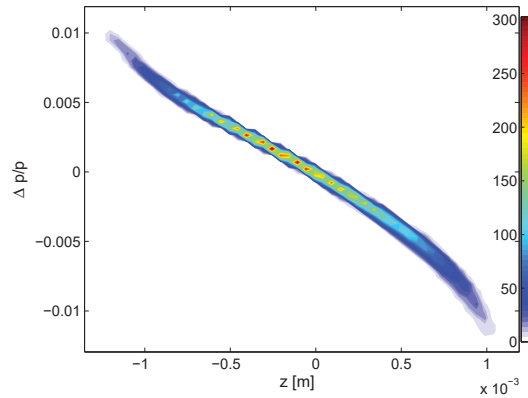


Figure 6.17: The longitudinal phase space distribution at the optimization point of 2.5 m. The plot shows the longitudinal phase space distribution for a parameter setting in the compromise region.

The transverse and longitudinal phase spaces in the compromise region, a particular important region at the Pareto-optimum curve for the high brightness operation of an SRF photoinjector, provide promising results including fully controlled bunch parameters and phase spaces with limited impacts from nonlinearities and space charge effects.

### 6.2.5 Beam parameter evolution in the low emittance region

Finally, the beam parameter evolution for one parameter setting in the low emittance regime is analyzed in detail in Fig. 6.18 (setting marked green in Figure 6.10). The

results are equal the corresponding evolution of the transverse and longitudinal beam parameters of the optimization without the solenoid correction. The solenoid correction mostly influences the results in the short bunch length regime.

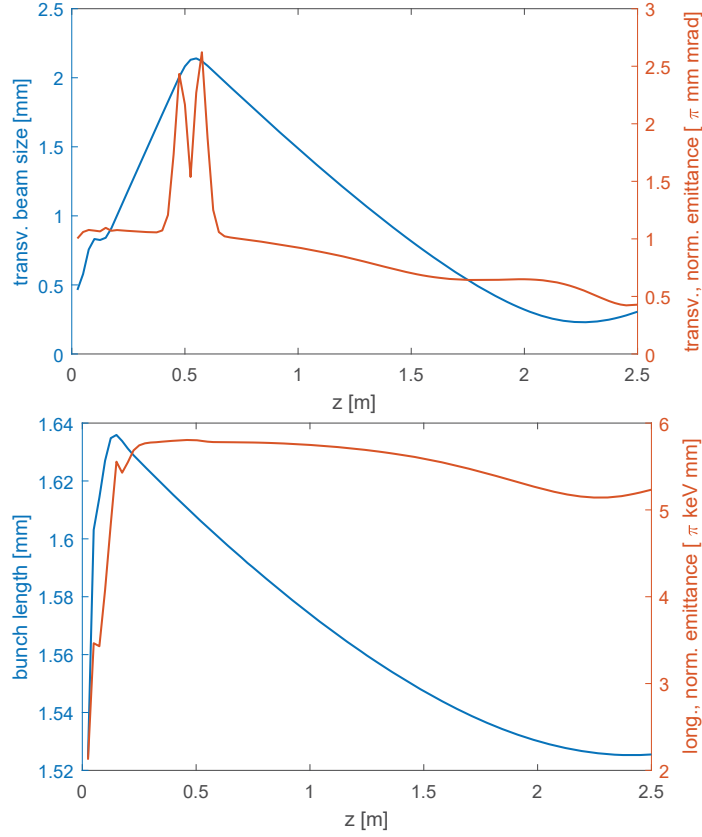


Figure 6.18: Evolution of the beam size and the transverse emittance [top: (a)] and the bunch length and the longitudinal emittance [bottom: (b)] along the  $z$ -axis from the photocathode to the optimization point at 2.5 m. The results are given for a parameter setting in the low emittance regime (marked green in Fig.6.10). The optimization is subjected to a 77 pC bunch charge and a cavity peak field of 30 MV/m. The solenoid field is adjusted to the beam energy which is defined by the gun gradient and the selected injection phase.

In the selected setting for the low emittance mode, a “cigar”-shaped laser pulse illuminates the cathode. The small laser spot size of 0.41 mm minimizes the intrinsic emittance contribution right at the photocathode. Additionally, the photocathode is retracted by -1.5 mm for a maximum radial focusing field that acts on the generated electrons already when they escape from the cathode material. The strongest transverse focusing is achieved by the solenoid with a maximum magnetic field of 113.9 mT on axis. These photoinjector settings lead to a well-focused beam at the

optimization point as displayed in Fig. 6.18(a). The beam size minimum is reached at the focus point at 2.25 m. Furthermore, full emittance compensation is achieved a few cm before the optimization point.

The evolution of the longitudinal phase space is summarized in Fig. 6.18(b). Since the aim is to reach the lowest possible transverse emittance, the bunch length remains almost constant from the cathode to the evaluation point. In order to avoid a space charge dominated growth in the longitudinal plane due to the transverse compression, the bunch is generated with a rather long laser pulse (6.8 ps) (“cigar”-regime). Moreover, a gun injection phase close to the on-crest phase (-8.3 deg) does not add a strong energy chirp to the bunch. As a consequence, the bunch is controlled in the longitudinal direction and only slightly compressed (compressed by 0.1 mm). The minimum bunch length is located close to the optimization point.

As a moderate energy chirp acts on the bunch the energy spread slowly decreases along the beamline. The evolution of the longitudinal emittance, thus, follows the trend of the bunch length and the energy chirp [see Fig. 6.18(b)]. A longitudinal emittance minimum occurs close to the lower limit in the energy spread and the minimum in the bunch length.

### 6.2.6 Phase space evaluation in the low emittance regime

The well-focused bunch with a beam width in the range of  $500 \mu\text{m}$  (*rms*) is symmetrically distributed in the transverse plane [see Fig. 6.19(a)]. Less than 100 macroparticles out of 10,000 lie in a small halo region. These particles are part of enlarged slices at the head and the tail of the bunch caused by strong space charge effects [see Fig. 6.19(b)]. Furthermore, due to a mismatch in the particle momenta [see Fig. 6.20], the focusing effect of the solenoid is disturbed.

As shown in Fig. 6.18(a), the focusing point of the solenoid at 2.25 m can be found before the optimization point. The orientation of the transverse phase space ellipse in Fig. 6.19(b) verifies that the bunch starts to diverge again. The transverse emittance is evaluated shortly behind the emittance compensation point [see Fig. 6.18(a)]. Therefore, some slices at the end of the bunch and in the center begin to become mismatched again. However, most of the slices are well aligned. No significant S-shape in the transverse phase space is detectable. Otherwise, such a shape would give an indication of nonlinear effects.



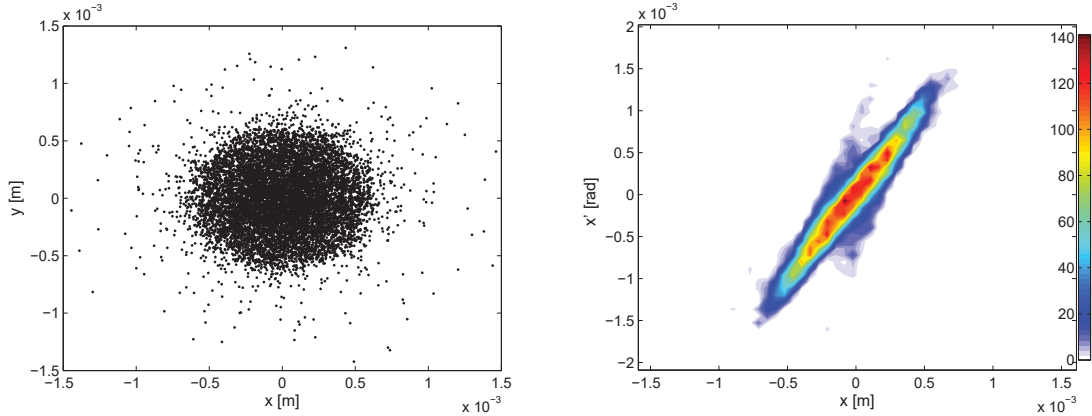


Figure 6.19: The transverse phase space distribution at the optimization point of 2.5 m. The results show the transverse bunch distribution (left (a)) and the transverse phase space distribution (right (b)) for one parameter setting in the low emittance region.

The longitudinal phase space in Fig. 6.20 shows a nonlinear distribution. The RF curvature in the cavity is imaged by the longitudinal phase space due to the long laser pulse length of 7 ps and a gun injection phase of  $-8.3$  deg relative to the on-crest phase. Following Fig. 6.18(b), the bunch length, the energy spread and, therefore, the longitudinal emittance change only slightly along the beam path. Consequently, significant change in the longitudinal phase space evolution does not appear to occur between the cathode and the optimization point. The optimization point matches approximately the longitudinal focus point [see Fig. 6.18(b)], i.e., the moderate bunch length compression is finished. The negative energy spread values of the bunch tail displayed in Fig. 6.20 confirm that the longitudinal focus point lies close to the optimization point. A few particles in the tail of the bunch show a slightly higher energy than the particles located close behind the bunch center. One explanation could be that these particles are pushed to smaller  $z$ -values by the bunch center providing a high-particle density. In that case, the higher particle energy in the tail would be an effect of the longitudinal space charge. Moreover, this effect can originate in the photoelectric emission of the relatively long bunch. At this point, it must be mentioned that the faithful simulation of the photoemission process means a challenge to the particle tracking program ASTRA.

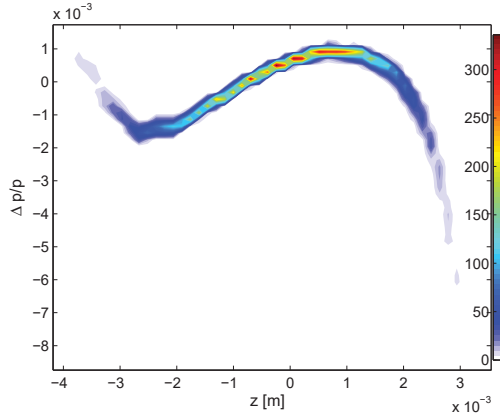


Figure 6.20: The longitudinal phase space distribution at the optimization point at 2.5 m. The result displays the longitudinal phase space distribution for a parameter setting in the low emittance region.

### 6.2.7 Discussion of the phase spaces

To summarize, the presented phase spaces in the short bunch length mode and low emittance regime underline that the ends of the Pareto-optimum curve uncover the limits of the SRF photoinjector system. The discussion of the phase spaces is challenging since the final bunch distributions correlate with the impact of photoinjector parameter settings, transverse and longitudinal space charge effects, nonlinearities from the RF field and the solenoid, and the simulation limit of the photoemission process in ASTRA. Here, the simple linear SRF photoinjector theory is no longer applicable. Moreover, these correlations and nonlinearities complicate a correct interpretation of the beam parameter evolution, and of the longitudinal emittance in particular.

However, the phase space results provide an important evidence regarding the bunch evolution in the transverse and longitudinal plane from the photocathode until the optimization point and beam dynamic effects in the SRF photoinjector, as well as beyond. If a fully controlled transverse and longitudinal phase space is required for a special application of the SRF photoinjector, modifying the optimization tool is advisable. As a solution, the optimization of slice values instead of *rms* parameters could work. Additionally, an adjustment of the space charge grid in dependence on the randomly selected laser pulse volume to provide a constant number of macroparticles per grid cell can provide a better control of the space charge effects. Numerous changes can be implemented into the optimization tool moving the focus of the opti-

mization results to the current application. It is expected that the lowest transverse *rms* emittance and shortest *rms* bunch length values that were discovered in this dissertation can no longer be retained under the same optimization conditions (bunch charge, acceleration peak field). Further constraints added to the optimization procedure, e.g., concerning the phase space or the space charge control, will limit the achievable objectives values. As a result, general multi-objective optimization which refrains from further constraints is the best initial approach in terms of the primary task of the developed optimization tool: to explore the limits of the transverse *rms* emittance and *rms* bunch length for a high brightness electron beam of a given SRF photoinjector design.

### 6.2.8 Impact of the beam and the photoinjector parameters on the Pareto-optimum curve

The optimization results can be used to determine suitable parameter sets for laser, gun and solenoid that support a stable operation of the SRF photoinjector in a high brightness mode. The table in Figure 6.21 displays the decision variables of one 77 pC beam setting in the balanced region of small emittance and short bunch length (highlighted). Here, the bunch charge of 77 pC corresponds to a high average current operation desired for the bERLinPro facility. All photoinjector parameter values fit very well within their design limits.

Yet, the Pareto-optimum front offers information about how the photoinjector parameters and the bunch charge impact the beam dynamics and define the beam brightness limit of the SRF photoinjector. The following sections analyze the influence of the different parameters in detail.

#### Impact of the bunch charge

Figure 6.21 shows a Pareto-curve in the optimization point for two different bunch charges [41]. While 7 pC corresponds to a low current commissioning and diagnostic mode, the bunch charge of 77 pC represents the high average current bERLinPro specification. Fig. 6.21 illustrates the strong dependence of the available minimum emittance and bunch length values on the bunch charge. Compared to the low current mode, the higher space charge at 77 pC leads to a strong emittance growth in the transverse plane. The bunch length is less affected as the longitudinal space charge component decreases fast with the beam acceleration and can, thus, be neglected (see Chapter 4.3.4).

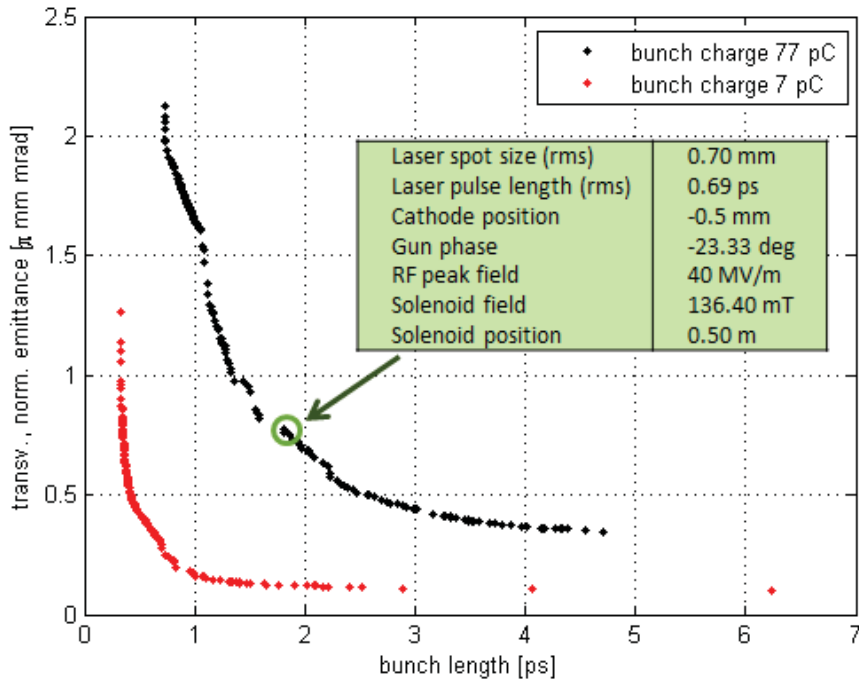


Figure 6.21: Pareto-optimum curve for 7 pC bunch charge (diagnostic mode) and 77 pC bunch charge (high average current mode at bERLinPro).

### Impact of the gun parameters

Figure 6.22 plots the curves of the 77 pC multi-objective optimization for different cavity gradients [41]. The energy dependency of the electron beam accelerated by various cavity peak fields leads to different Pareto-curves. The values of both objectives can be significantly decreased with a high energy beam accelerated by a maximum gun gradient. In this case, space charge effects that impact the radial and longitudinal planes can be reduced [see Chapter 4.3.4].

Figure 6.22 also explains why the cavity peak field cannot be set as a decision variable in the optimization process. The optimization program will always set the acceleration peak field to its upper limit of the decision variable range in order to reach the best emittance and bunch length values. Consequently, the optimization process is repeated for different cavity peak fields separately.

Gun parameter settings that fulfill the requirements of bERLinPro ( $\epsilon_x < 1$  mm mrad and  $\sigma_z < 6$  ps) can be found for a 77 pC bunch charge at cavity peak fields lying above 20 MV/m. The optimization results illustrated in Figure 6.22 confirm the demand for high RF fields in the gun cavity. Still, the risk of multipacting and field emission

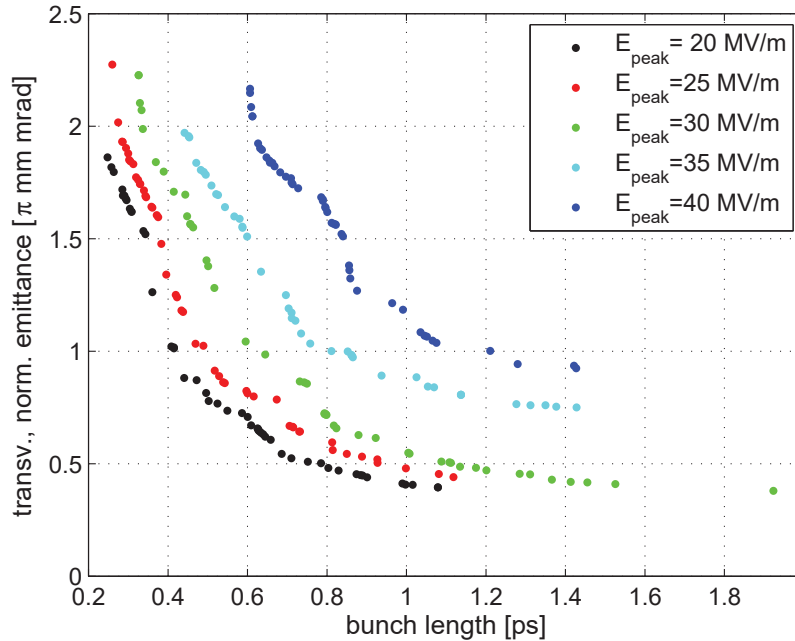


Figure 6.22: Pareto-curves for different gun cavity peak fields on axis (20 MV/m to 40 MV/m) with 77 pC bunch charge.

grow with higher cavity fields in the same way.

The current gun cavity 1.0 in Gunlab is specified for a theoretical maximum field of 60 MV/m on the beam axis <sup>1</sup>. A cavity field of 34.9 MV/m could be measured in the horizontal cavity test stand at HZB [see Fig. 3.9]. Following Figure 6.22 both objectives cannot be significantly improved above 35 MV/m in the optimization. Therefore, a moderate cavity peak field of 35 MV/m with controlled field effects is aspired.

Beside the cavity peak field, the impact of the other photoinjector parameters on the transverse emittance and bunch length can also be analyzed based on the optimization results. Following the theory from Chapter 4.3, the transverse emittance in the gun is mainly affected by the laser spot size, the cathode position and the solenoid, while the bunch length is defined by the laser pulse length and the gun phase. The impact of the laser pulse volume will be discussed in a separate section in detail. Figure 6.23(a)-(d) summarizes the impact of the main parameters of the cathode, the gun cavity and the solenoid. Figure 6.23(a)-(d) display the same Pareto-optimum curve for a bunch charge of 77 pC and a cavity peak field of 30 MV/m. The color map

<sup>1</sup>Private communication Axel Neumann.

## 6. Multi-Objective Optimization Results

indicates four different gun parameters in their defined ranges as a third dimension.

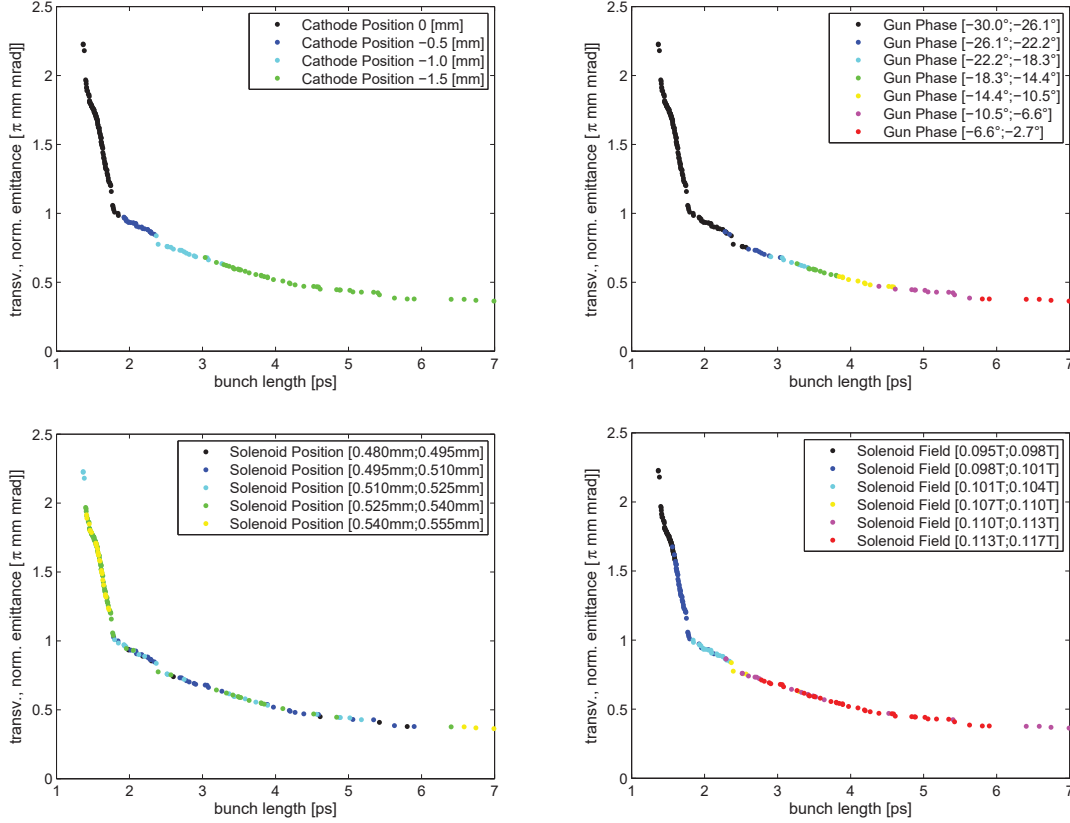


Figure 6.23: Dependency of the Pareto-optimum curve on the cathode position [top left: (a)], the gun injection phase [top right: (b)], the solenoid position [bottom left: (c)], and the solenoid field [bottom right: (d)]. The optimization is done for a 77 pC beam accelerated by an field gradient of 30 MV/m.

Analyzing the cathode position in Figure 6.23(a), it can be observed that the cathode is strongly retreated for smaller transverse emittances. This trend confirms the theory of radial RF focusing in the cathode tube in front of the half cell. The most compact transverse phase space can be achieved with a maximum cathode retreat of -2.5 mm.

A comparable effect can be observed in the longitudinal plane. The bunch compression in the SRF photoinjector is given by velocity bunching. Due to the theory of bunch compression [see Chapter 4.4.3], velocity bunching requires a strong energy chirp to be imprinted on the bunch. This energy chirp is defined during the gun injection phase. Figure 6.23(b) shows the development of the gun phase along the optimum front. At short bunch lengths, the gun phase significantly diverges from the

on-crest phase that provides maximum acceleration and minimum energy chirping. The slope of the energy over the phase increases at negative injection phases relative to the on-crest phase. A maximum compression can be observed at a phase of  $-30$  deg relative to the on-crest phase. Gun phases close to the on-crest phase lead to moderate longitudinal focusing but maximum acceleration in the low emittance arm of the Pareto-curve.

The effect of the solenoid parameters, the longitudinal position and magnetic field strength, on the objectives, especially on the transverse emittance, is displayed in Figure 6.23(c) and 6.23(d). The solenoid is mounted on a motorized moving frame, which allows an overall alignment of the magnet to the real beam axis and a longitudinal movement along the  $z$ -axis of several centimeters [62]. The solenoid position does not have such an obvious impact as other photoinjector parameters. Moreover, the position is not continuously changed along the optimum front [see Figure 6.23(c)]. However, a trend in the low emittance mode and short bunch length regime can be observed. In order to receive a maximum focusing in the transverse plane (small emittance) the solenoid is placed close to the cavity exit. The emittance compensation starts right after the acceleration and the emittance compensation point is moved next to the optimization point. Therefore, the selection of the solenoid position provides a fine-tuning process in the optimization towards small transverse emittances. For short bunch lengths that are smaller than 1.7 ps, it can be observed that the optimization program trends to position the solenoid several centimeters away from the cavity exit. In this case, the drift space between cavity and solenoid can already be used for velocity bunching in the longitudinal plane without causing a simultaneous radial compression that would enlarge space charge effects. As a consequence, the focus and emittance compensation point of the solenoid are often moved behind the optimization point in the short bunch length regime.

The solenoid field increases towards the small emittance end of the Pareto-optimum curve [see Figure 6.23(d)]. This is expected since the solenoid presents the most important strategy to minimize the transverse emittance. Acting as an optical lens, a high solenoid field provides a strong radial focusing that sets the focal point and the emittance compensation point close to the solenoid and next to the optimization point.

### Impact of the laser parameters

An analysis of the Pareto-optimum front for a bunch charge of 77 pC and 30 MV/m cavity peak field shows a change in the slope of the curve at a transverse emittance of 1 mm mrad and a bunch length of 1.7 ps. This edge can be traced back to a change in the laser pulse parameters. The Pareto-optimum front at small bunch lengths is specified by “pancake”-shaped bunch distributions, caused by short laser pulse lengths  $\sigma_{\text{laser},z}=0.9 \dots 3.1$  ps and large laser spot sizes  $\sigma_{\text{laser},x}=1.3 \dots 1.5$  mm. Together with the velocity bunching which uses the cavity and the drift space behind the solenoid magnet, the short emission length enables the photoinjector to provide short bunches at the optimization point. The laser spot size and, thus, the initial electron beam size are maximized to counteract space charge effects. Smaller emittances are achieved in a “cigar”-regime. Longer pulses  $\sigma_{\text{laser},z}=5.3 \dots 8.6$  ps allow for smaller laser spots  $\sigma_{\text{laser},x}=0.3 \dots 0.7$  mm that minimizes the intrinsic emittance, one of the most important emittance contributions. Figure 6.24 depicts the “pancake”- and the “cigar”-regime [41].

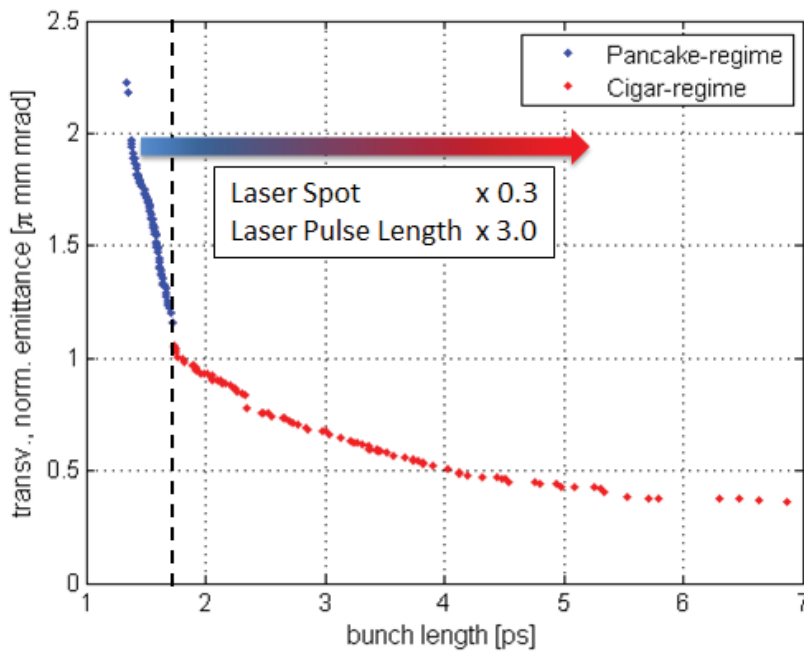


Figure 6.24: “Pancake”- and “cigar”-shaped bunch distributions in the Pareto-front for a 77 pc bunch charge and an acceleration gradient of 30 MV/m.



In addition, the optimized laser pulse duration and spot size settings are analyzed in relation to the final *rms* bunch length in Fig. 6.25(a) and (b).

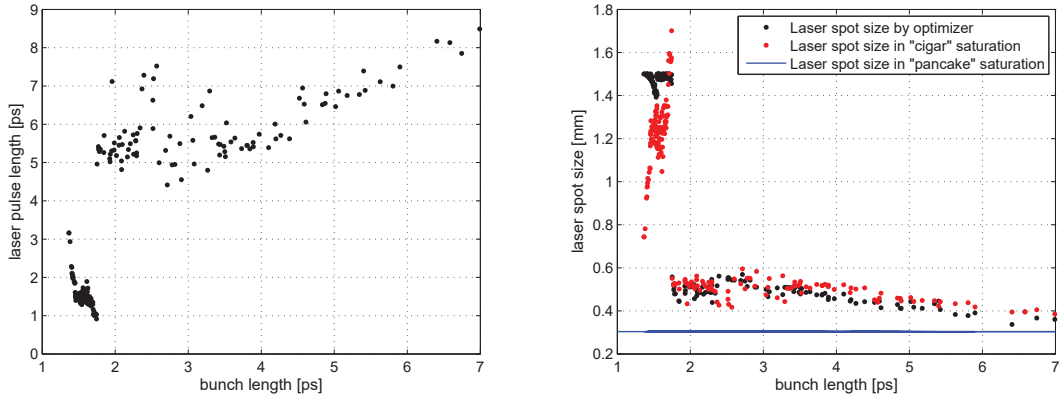


Figure 6.25: Laser pulse length (left (a)) and laser spot size (right (b)) versus the final bunch length for the 77 pC Pareto-optimum solutions. The optimized laser spot size is compared with the calculated spot size in the saturation for the “pancake”- and “cigar”-shaped-regime.

Figure 6.25(a) shows the expected increase in the final bunch length when the bunch is generated with a longer laser pulse. A clear difference between the “pancake”-regime at short bunch lengths and the “cigar”-regime can be detected. As shown in Fig. 6.25(a), the shortest bunch lengths are not generated with ultrashort laser pulses. It is assumed that the velocity bunching is more effective if the energy chirp is imprinted on a slightly longer bunch of 2 ps to 3 ps length. In low emittance mode, the bunch length increases approximately linear to the laser pulse length.

Figure 6.25(b) presents the laser spot sizes selected by the optimizer in relation to the final bunch length (black dots). The calculated laser width in saturation in the “pancake”- and “cigar”-regimes are added based on Equ. 4.55 and 4.53. In the “cigar”-regime, the results fit very well. Therefore, it can be assumed that the photoemission of the SRF photoinjector operates close to the maximum cathode brightness discussed in chapter 4.4.1. In the “pancake”-regime the laser spot size is clearly maximized in order to achieve short bunch lengths and to counteract corresponding space charge effects. Therefore, the transverse beam brightness is not further optimized. The optimization program prevents a charge emission close to the saturation to avoid a longitudinal electron bunch expansion at the photocathode.

## 6.3 Application-Specific SRF Photoinjector Optimization

Until this point, multi-objective optimization has determined the performance limit of the current SRF gun design at HZB. The best achievable transverse emittance and bunch length values corresponding to different photoinjector settings were figured out for different gun gradients and bunch charges. Usually, different applications set a stronger focus on only one of the two objectives while the total beam brightness must be maintained at a high level.

### 6.3.1 Optimization of an SRF photoinjector for ERL operation

#### 3-cavity booster section

The operation of an ERL facility that utilizes an SRF photoinjector as an electron source requires a small transverse emittance as early as in the injection line of the accelerator. The bunch length can be further compressed after merging the beam in the main ring. Thus, the focus is clearly on the transverse emittance along with the high beam brightness that must always be ensured. Pareto-optimum results regarding the balanced compromise region and settings from the low emittance branch at the optimum front are of special interest for the high brightness ERL mode.

The injection line of an ERL is the distance between the photoinjector and the merger, where the bunch is coupled to the main recirculation ring. It normally consists of an additional acceleration section, the so-called booster, as well as steerer magnets for transverse beam offset corrections, quadrupole sequences to focus the beam in the transverse plane and beam diagnostic tools. The booster section consisting of one or several multi-cell SRF cavities is implemented for further acceleration and longitudinal bunch compression based on ballistic bunching. The booster shows the strongest impact on the electron beam dynamics, which poses the question of whether the beam properties of the optimized photoinjector settings can be preserved through the booster without degrading emittance and bunch length.

First evidence can be found in older optimization results for the bERLinPro design. The best settings for the whole injection line of bERLinPro from the photocathode, through the photoinjector and the three 2-cell booster section until the merger was evaluated by using a swarm optimization tool developed at HZB [112].

Since this program neglects space charge effects, the swarm optimization process is combined with a space charge optimizer (SCO) <sup>2</sup>. The SCO implements transverse but not longitudinal space charge forces in the beam dynamics calculations. A stable parameter set for the gun cavity (gun injection phase, cavity peak field), the solenoid (solenoid field), the booster section (three cavity phases, three cavity peak fields) and the quadrupoles (quadrupole gradients), was found for a 77 pC high average current beam, as is summarized in Table 6.1. The program is not able to optimize the emission process. Therefore, the laser pulse parameters are derived from a desired initial bunch distribution behind the cathode that functions as a starting point of the optimization process.

Table 6.1: Stable parameter setting for the bERLinPro injection line determined by swarm optimization and SCO [112]

Parameter	Value	Unit
Laser spot size	0.38	mm ( <i>rms</i> )
Laser pulse length	7.21	ps
Cathode position	-1.5	mm
Injection phase gun cavity	-4.78	deg
Gun cavity peak field	30	MV/m
Solenoid position	0.46	m
Solenoid field	0.112	T
Booster cav 1 peak field	4.83	MV/m
Booster cav 1 phase	-90 (zero crossing)	deg
Booster cav 2 peak field	-16.52	MV/m
Booster cav 2 phase	0 (on-crest)	deg
Booster cav 3 peak field	-16.52	MV/m
Booster cav 3 phase	0 (on-crest)	deg

Afterwards, the determined injection line setting is used to evaluate the bunch phase space at 10.5 m behind the cathode in the diagnostic line of bERLinPro using the particle tracking program ASTRA. A projected transverse emittance in the horizontal plane of 0.34 mm mrad, and a bunch length value of 5.18 ps [1.55 mm] can be achieved. The result is plotted together with the Pareto-optimum curve obtained by multi-objective optimization of a 77 pC bunch and at 30 MV/m gun cavity peak field in Figure 6.26 <sup>3</sup>.

<sup>2</sup>Private communication Michael Abo-Bakr.

<sup>3</sup>Private communication Bettina Kuske.

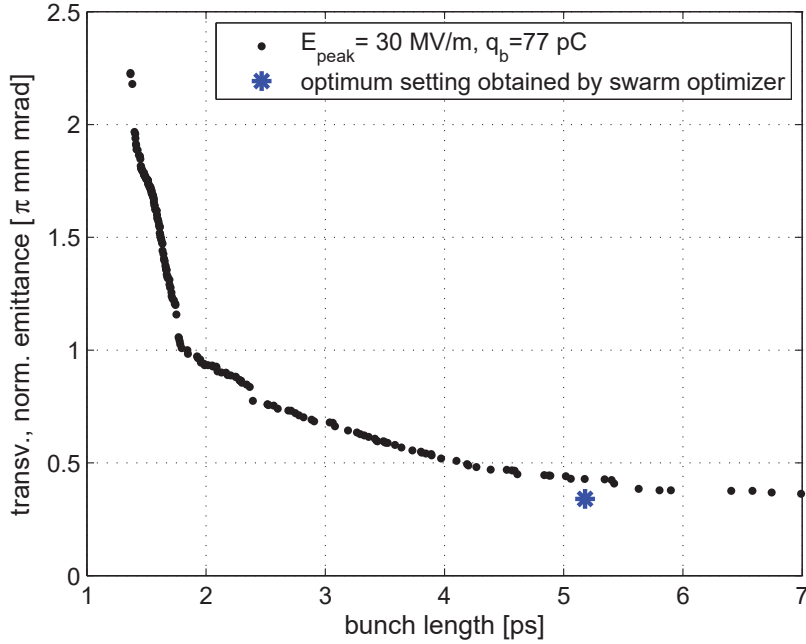


Figure 6.26: Comparison of the Pareto-curve obtained with multi-objective optimization with the optimum setting of the currently planned bERLinPro setup calculated with a swarm optimizer including SCO [112].

There is one parameter setting at a transverse emittance of 0.43 mm mrad and 5.18 ps [1.53 mm] bunch length at the Pareto-optimum front that can be compared with the achieved result by swarm optimization for the injection line. Beside the deviation in the transverse emittance value, which will be discussed later, the photoinjector and beam parameters of both methods match very well. The parameter sets for the photoinjector for both points are summarized in Table 6.2:

Table 6.2: Comparison of two stable parameter settings for the bERLinPro photoinjector as determined by the Pareto-optimization, and swarm and SCO combined optimization

Parameter	Pareto-optimum	bERLinPro SCO	Unit
Laser spot size	0.39	0.38	mm ( <i>rms</i> )
Laser pulse length	6.78	7.21	ps
Cathode position	-1.5	-1.5	mm
Injection phase gun cavity	-6.33	-4.78	deg
Gun cavity peak field	30	30	MV/m
Solenoid position	0.49	0.46	m
Solenoid field	0.115	0.112	T

The optimum photoinjector settings evaluated with the two different optimization techniques are very compatible and almost identical in their settings. The comparison confirms the multi-objective optimization to be a powerful tool for finding stable parameter settings to operate an ERL in high brightness mode. Multi-objective optimization also pushes the SRF photoinjector to its physical limits.

Nevertheless, a slightly smaller transverse emittance of 0.34 mm mrad is obtained using the SCO optimizer. The reason for that emittance are the different optimization points, at which the emittance is calculated in relation to the phase space distribution. While the multi-objective optimization stops at 2.5 m behind the cathode, the SCO optimizer evaluates the beam phase space at 10.5 m in the bERLinPro diagnostic line. The transverse emittance is further decreased by RF focusing in the booster. Due to the additional acceleration and hence, the higher beam energy, space charge effects can be controlled better than in the photoinjector beam. As a consequence, a smaller emittance value corresponding to the selected bunch length can be achieved. This example shows that for the selected Pareto-optimized photoinjector setting the prepared electron bunch can be transported through the current bERLinPro booster design and setting, as well as through the rest of the injection line without any beam quality degradation.

Now, the task remains to observe whether all optimized high brightness settings on the Pareto-optimum curve can be traced through the booster. The small values of the two objectives must be conserved or, if possible, even improved during the transport to the stopping position at 7.0 m behind the cathode. Therefore, the optimization is repeated with positioning the optimization point at the entrance of the booster section at 3.2 m behind the cathode. Then, ten points along the curve are selected by way of example and they are transformed through the three booster cavities using the booster setting optimized by SCO [see Table 6.1 and Figure 6.27].

The electron beam parameters are evaluated by ASTRA tracking 7.0 m behind the photocathode. Figure 6.27 displays the optimized emittance and bunch length results behind the photoinjector ( $z=3.2$  m) and behind the booster section ( $z=7.0$  m).

The bERLinPro injection line is optimized by the SCO optimizer in a way that the transverse emittance is minimized in the photoinjector based on cathode retreat, RF focusing and solenoid emittance compensation. The bunch length is controlled

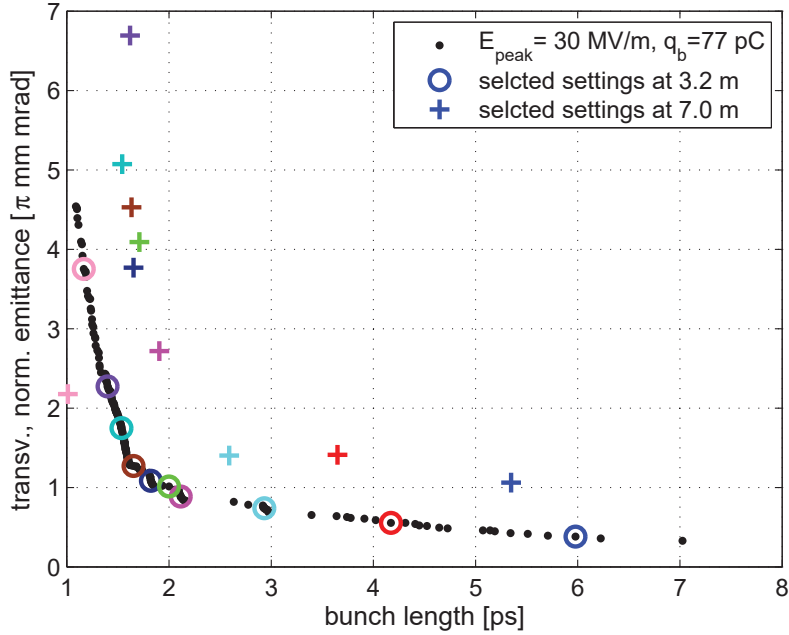


Figure 6.27: The Pareto-optimum curve for a 77 pC bunch accelerated with a 30 MV/m peak field on axis, and evaluated at 3.2 m behind the cathode. Ten parameter settings are selected (colored circles). The beam is tracked through the gun and the booster using these settings and the current bERLinPro booster set summarized in Table 6.1 (colored asterisks correspond to the circles with the same color).

by the laser pulse length and the gun injection phase but it can be foreseen that the booster section provides the main bunch compression. Consequently, the first booster cavity runs at zero crossing. The bunch is injected at a phase of  $-90$  deg relative to the on-crest phase. No net acceleration occurs but the bunch possesses a maximum energy chirp for ballistic bunching. The second and third cavities operate on-crest at high gradients to accelerate the bunch to 6.5 MeV. Hence, the injection line works in a two step 6D phase space optimization, starting with the transverse phase space in the photoinjector which is then followed by the longitudinal phase space optimization in the booster section.

This discovery also occurs in the ASTRA results of the ten selected points. The bunch length evolution along the beam axis is controlled. For short bunches smaller than 2 ps (0.6 mm) at the booster entrance (short bunch length region [“pancake”], compromise region at the Pareto-optimum front) no further significant bunch compression can be obtained. The bunch is already too short due to the velocity bunching induced by the photoinjector. Nevertheless, the booster holds the small bunch length

values. For bunch lengths above 2 ps (0.6 mm) a strong compressing effect of the booster is found in the bunch length evolution plots.

Analyzing the transverse emittance evolution along the beam axis presents an emittance growth in the booster section that can be observed at most of the selected points. Only the maximum transverse emittance setting at the booster entrance ( $> 3 \text{ mm mrad}$ ) can be decreased by RF focusing. Since the ERL mode aims for transverse emittances smaller than  $1 \text{ mm mrad}$ , this solution is only of minor significance. At the other selected points on the optimum curve, the emittance growth in the booster section can be explained with sc effects if the bunch is already strongly compressed in the longitudinal plane before the booster entrance.

It follows that the longitudinal compression of the bunch by photoinjector induced velocity bunching before the booster should be restricted. In order to avoid emittance growth in the booster which would counteract the emittance compensation by the solenoid, a bunch with a moderate bunch length above 3.5 ps (1 mm) must be injected to the booster section.

As a consequence, regarding best beam performance, the multi-objective optimization of the photoinjector and the booster section are expedient [113].

The presented optimization program can be adjusted to the new optimization goals rather quickly. The optimization criterion of the two objectives is retained. The ASTRA tracking is extended through implementing the three additional booster cavity field profiles. Adding seven additional decision variables to the optimization, the position of the whole booster section (the distances between the cavities are fixed), three cavity peak fields and three cavity phases poses a bit of a challenge since the optimization procedure becomes more time-consuming. The design range of the booster section is summarized in Table 6.3. In order to receive a first overview of the Pareto-optimum front and to save computational run-time, the number of solutions in the optimization population is restricted to  $n_{\text{pop}}=50$ . A look at the numerical studies discussed in the Appendix B.2.2 clarifies that the transverse emittance is overestimated. A higher number of selected parameter settings in the parent population is required for a detailed study.

Figure 6.28 shows the Pareto-optimum curve for the optimization of the SRF photoinjector together with the 3-cavity booster of bERLinPro for a bunch charge of 77 pC, a gun cavity gradient of 30 MV/m and at an optimization point of 7.0 m. Compared to the results of the photoinjector optimization at 2.5 m, the transverse

## 6. Multi-Objective Optimization Results

Table 6.3: Limits of the booster parameters following the current bERLinPro design

Parameter	Range	Unit
Booster position	3.01 - 3.41	m
Booster cav 1 peak field	1 - 20	MV/m
Booster cav 1 phase	-100 - 10	deg
Booster cav 2 peak field	1-20	MV/m
Booster cav 2 phase	-100 - 10	deg
Booster cav 3 peak field	1-20	MV/m
Booster cav 3 phase	-100 - 10	deg

emittance values with corresponding bunch lengths can be significantly improved. Here, the RF field of the booster cavities is used for transverse compression. Better results are achieved in both objectives with Pareto-optimized settings as compared to the presented results obtained with the swarm optimizer for a transverse emittance of 0.34 mm mrad and a bunch length of 5.18 ps [plotted in Fig. 6.26 and 6.28 as an asterisk]. This outcome verifies the ability of the developed optimization tool to improve the high brightness performance of the SRF photoinjector and the ERL injection line.

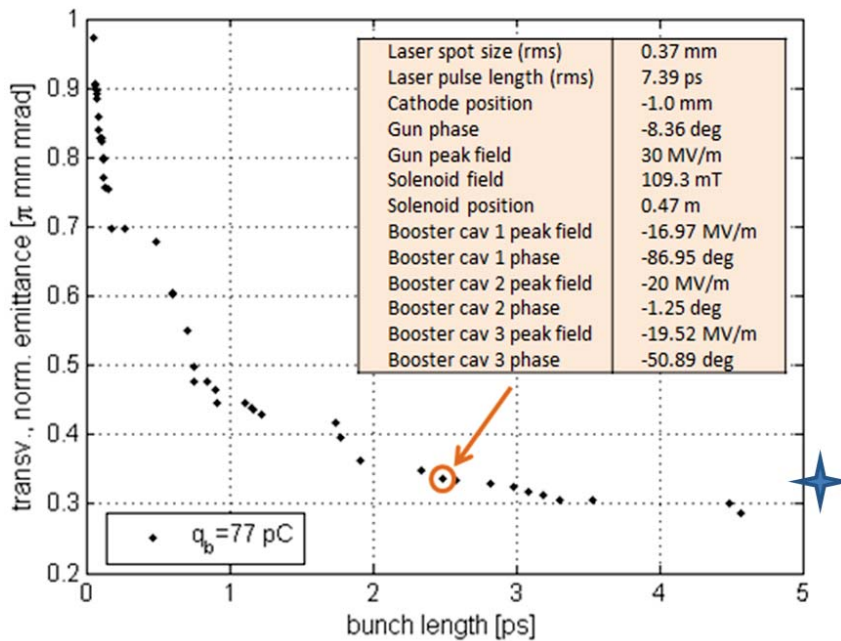


Figure 6.28: Results of the multi-objective optimization of an SRF photoinjector combined with a booster section consisting of three 2-cell superconducting cavities. The blue asterisk marks the optimization result obtained with the SCO optimizer.



One parameter setting is selected from the optimum curve representing the bERLin-Pro specification with a final energy of 6.5 MeV [8]. The decision parameter values are given in the table in Fig. 6.28

The values of the photoinjector settings are comparable to the result of the SCO optimizer. The slightly longer laser pulse length in the multi-objective optimization scenario is precompressed through velocity bunching. Therefore, the smaller injection phase to the gun cavity of -8.36 deg (compared to -4.75 deg in the swarm optimization) imparts a stronger momentum chirp on the bunch. In comparison to the SCO solution with a cathode retreat of -1.5 mm, less cathode retreat of -1 mm is determined by the Pareto-optimizer. Nevertheless, the smaller radial RF focusing and the 109 mT solenoid field are still sufficient for an emittance compensation point right after the booster entrance. The booster section should always begin directly before the emittance compensation point to maintain the small emittance values through the booster.

Regarding the determined booster setting, it is exceptional that the Pareto-optimizer is able to set the first cavity in the sequence to a zero crossing phase. A maximum energy chirp and almost no net acceleration are thereby imprinted on the bunch at a phase of -86.95 deg. This provokes a bunch compression by ballistic bunching. The second cavity operates on-crest at a phase of -1.24 deg and a maximum gradient of 20 MV/m to reach a final bunch energy of 6.5 MeV. Only the last cavity set differs from the SCO results. The Pareto-optimization also pushes the cavity gradient to its upper limit for the beam acceleration. Still, the cavity phase is far away from the on-crest phase with -50.89 deg. This effect can be explained with the transverse emittance that starts to decrease in the third booster cavity. In order to counteract the strong sc effects that lead to a mitigation of the longitudinal focusing or even to a defocusing process, an additional longitudinal compression by velocity bunching is implemented on the bunch.

These effects can also be observed in the evolution plots of the beam size, the transverse emittance, the bunch length, and the longitudinal emittance along the  $z$ -axis as displayed in Figure 6.29.

The booster is placed 3.02 m behind the cathode. The values representing the transverse emittance rise at this position, just before the absolute emittance minimum is reached at the emittance compensation point [see Fig. 6.29(a)]. After a first

## 6. Multi-Objective Optimization Results

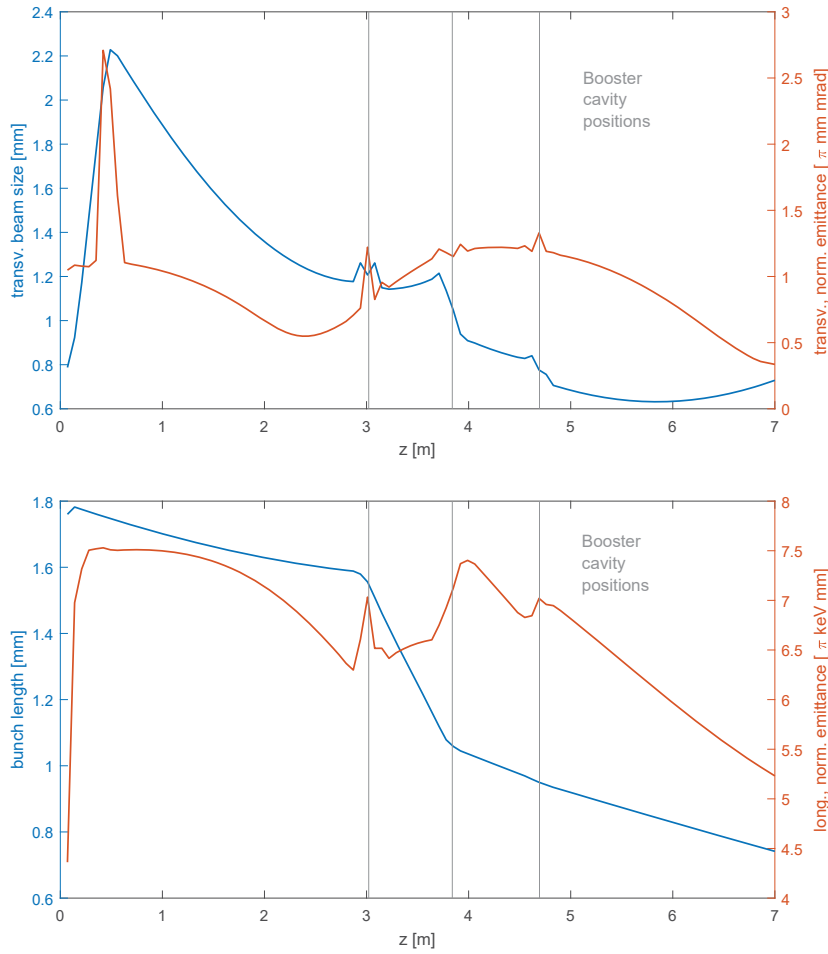


Figure 6.29: Evolution of the beam size and the transverse emittance [top: (a)] and the bunch length and the longitudinal emittance [bottom (b)] along the  $z$ -axis from the photocathode through the three booster cavities and to the optimization point at 7.0 m. The results are given for a parameter setting in the low emittance regime (marked orange in Fig.6.28). The optimization is subjected to a 77 pC bunch charge and a cavity peak field of 30 MV/m.

emittance growth in the booster up to the position at 3.8 m, the transverse phase space decreases mainly due to beam size minimization by RF focusing of the booster cavity. This effect can also be seen in the beam size evolution in Figure 6.29(a). The emittance compensation point is located close to the focal point of the booster section.

After a moderate focusing due to the momentum chirping of the RF gun cavity field at  $-8.36$  deg phase, the bunch length is strongly compressed by ballistic bunching in the first booster cavity [see Fig. 6.29(b)]. The on-crest acceleration in the second cavity attenuates the slope of the bunch compression. This slope can be maintained

in the last booster cavity even though the transverse phase space is also minimized by imprinting an additional momentum chirp on the beam to trigger velocity bunching. The longitudinal emittance remains nearly constant behind the gun cavity exit. Even though the bunch length is strongly compressed, the energy chirping in the first and the third booster cavity cause a growth in the energy spread, which prevents a decrease in the longitudinal emittance value. The relative energy spread at 7 m is 1.8%. Since the bunch compression process is not completely finished at this position, the values for the relative energy spread and the longitudinal emittance are not significant and can be further minimized before the bunch is merged to the main ERL ring.

### **5-cavity booster section**

As a design case study, the optimization process is repeated for a booster section consisting of five 2-cell SRF cavities. Eleven additional decision variables require long run times and a large number of solutions in the parent population of the optimization process. The Pareto-optimum results for an SRF photoinjector supplemented with a three and a five cavity booster section are plotted in Fig. 6.30.

As a result, the transverse emittance can be improved by around 10% due to the transverse RF focusing induced in the last two booster cavities. It was shown in the optimization of the injector with three booster cavities [see Fig. 6.29] that the emittance minimization starts in the last booster cavity. The effect can be extended if two additional cavities are added to the section. The bunch compression is mainly based on the energy chirping in the first booster cavity. An extension of the booster section does not impact the resulting ballistic bunching. Therefore, the achieved bunch lengths behind the five cavity booster section are comparable to the results with three booster cavities. To summarize, the beam brightness can be further maximized with two additional booster cavities due to the emittance decrease.

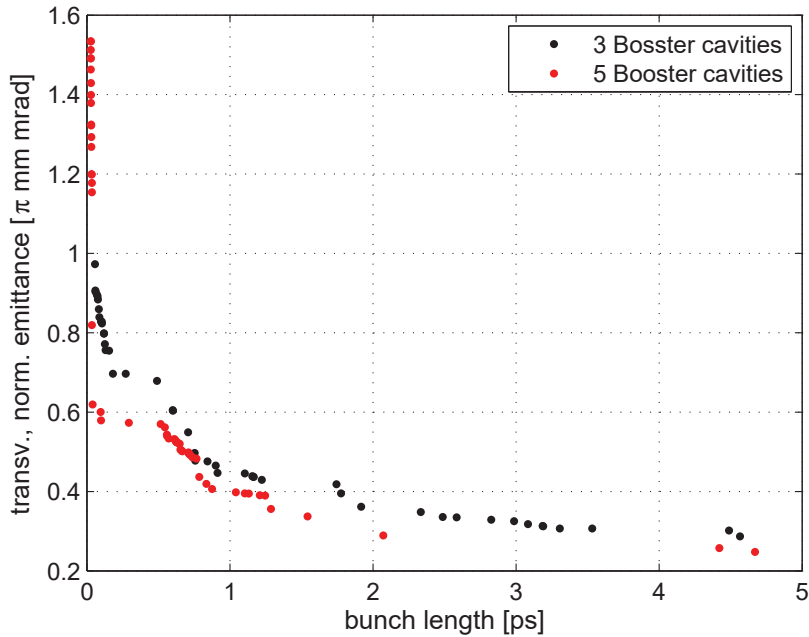


Figure 6.30: Comparison of the Pareto-optimum curves for an SRF photoinjector combined with a three cavity booster section (black curve) and combined with a five cavity booster section (red curve).

### Comparison of the 5-cavity booster optimization results with the Cornell high brightness dc photoinjector

The Pareto-optimization of the SRF photoinjector at HZB supplemented with a 5-cavity booster section allows a comparison with former Pareto-optimization results of the DC photoinjector at the Cornell University. In this case, a multivariate optimization tool based on a SPEA2 algorithm, was developed at the Cornell University to optimize the high brightness, high current DC injector designed for the Cornell ERL prototype [103, 114]. The injection line displayed in Fig. 6.31 consists of a high-voltage DC gun followed by two focusing solenoid magnets with a buncher cavity in between. After a short drift, five 2-cell booster cavities followed by a 3 m long drift line complete the setup.

Figure 6.32 represents the Pareto-optimum curve for the DC injector for 80 pC bunch charge (left) and the already shown optimum front of the bERLinPro injection line including a 5-cavity booster section (design study).

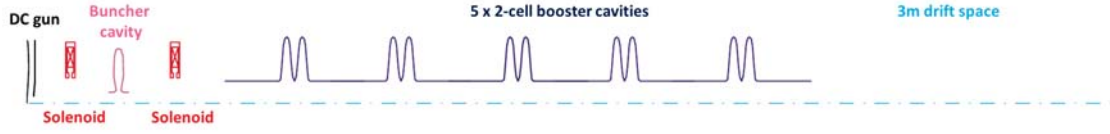


Figure 6.31: Injection line of the ERL prototype at the Cornell University including a DC gun, two solenoids, a buncher cavity and a five cavity booster section [103].

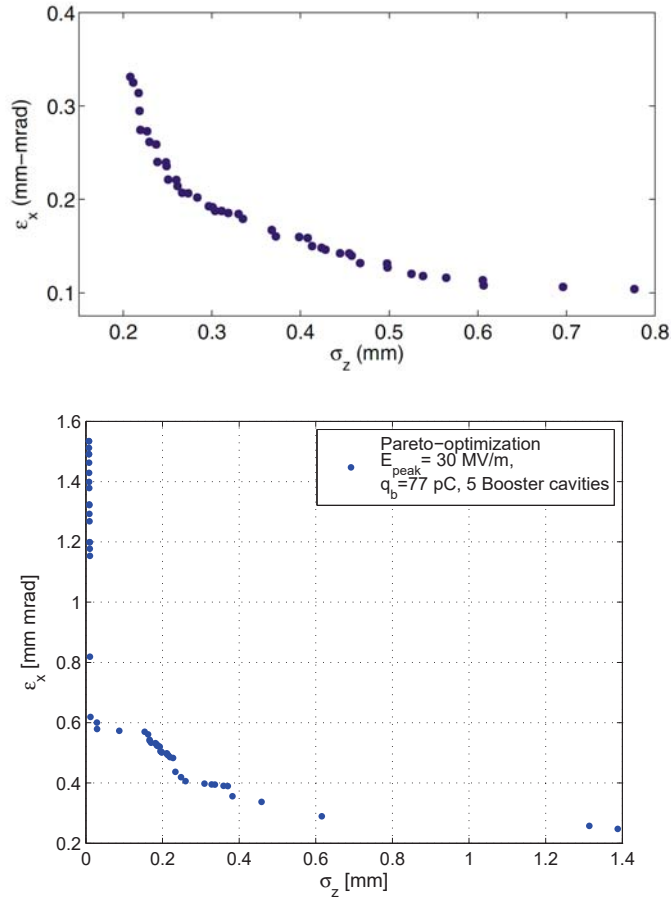


Figure 6.32: Comparison of the Pareto-optimum results for the DC injector at the Cornell University and the SRF photoinjector at HZB.

(a) top: Pareto-front of the DC injector with five booster cavities for a bunch charge of 80 pC [103].

(b) bottom: Pareto-optimum settings for the SRF photoinjector (GunLab design) and five booster cavities at HZB for a bunch charge of 77 pC.

In general, the shape of the Pareto-optimum curve for the DC injector is close to the results presented in this work. Therefore, the optimum front does not represent one smooth ISO-brightness curve, but an envelope of several trade-offs for different injector settings.

At first sight, a smaller transverse beam emittance can be achieved at comparable bunch lengths using a DC injector. However, some modifications in the DC injector beamline compared to the bERLinPro beam path, must be considered. The transverse emittance is already minimized at the photocathode of the Cornell DC gun using a 19 ps (*rms*) long bunch in the space charge dominated regime. The rather long initial bunch length counteracts space charge effects due to a compression in the transverse plane. Afterwards, the transverse phase space is further minimized by an additional solenoid in the beam path compared to the SRF photoinjector setup. An acceleration to 12.6 MeV in the Cornell injector that corresponds to nearly twice the energy in the bERLinPro injection line, reduces a space charge induced emittance growth. Finally, the transverse emittance is analyzed 3 m behind the exit of the last booster cavity. The trade-off curve of the SRF photoinjector combined with a booster section is directly evaluated at the booster exit (7 m). Fig. 6.33 displays the evolution of the transverse emittance and bunch length in the bERLinPro injector for one parameter setting of the Pareto-optimum curve in Fig. 6.32 (bottom). The plot shows that the transverse emittance has not reached its minimum value at the booster exit. Therefore, smaller emittance values that are comparable to the results from the DC injector, can be achieved after a drift space behind the booster section of the SRF photoinjector source.

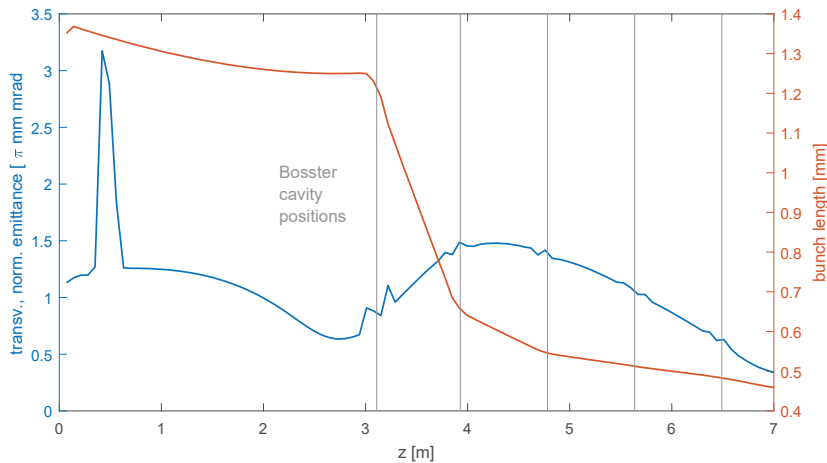


Figure 6.33: Evolution of the transverse emittance and the bunch length along the beamline including five booster cavities.

The optimization of the SRF photoinjector with booster section demonstrates that ultrashort bunch lengths can be achieved with the setup. Even though the Cornell injector setup includes a buncher cavity for bunch compression, the lower bunch length limit lies at  $200\ \mu\text{m}$ . The buncher cavity is mainly applied to compress the initially long bunches of the “cigar”-shaped drive laser. Moreover, the five booster cavities of the DC injector focuses on a beam acceleration while the Pareto-optimization of the SRF injector selects booster settings that allow a further bunch compression by ballistic and velocity bunching.

Additional constraints in the presented SRF photoinjector optimization code can set the focus on a small transverse emittance and a high final beam energy in the bERLinPro injector, as well. The first arc of the ERL ring also enables further bunch compression.

To summarize, the comparison of the Pareto-optimization results for the studied SRF photoinjector with the DC injector at Cornell University confirms the quality of the developed optimization tool. As a result, a stable operating SRF photoinjector can be at least equivalent in its high brightness performance to a DC injector.

### 6.3.2 Optimization of an SRF photoinjector for ultra-short pulses

The motivation behind this mode is to operate an ultra-fast electron diffraction user experiment with an SRF photoinjector. The photoinjector is then used as a stand-alone facility. UED enables the study of molecular structural dynamics with atomic resolution on a femtosecond timescale [40]. Driving a UED experiment requires short electron bunches to obtain a sufficient time resolution in the diffraction pattern. Thus, one main focus of the electron beam quality clearly lies on the shorter bunch lengths compared to the ERL application. Moreover, the transverse emittance must be controlled in order to reach a high transverse coherence length that is defined by Formula (6.1)

$$L_{\perp} = \frac{\hbar}{m_e c} \frac{\sigma_r}{\varepsilon_r} \quad (6.1)$$

where  $\sigma_r = \sqrt{\sigma_x^2 + \sigma_y^2}$  describes the *rms* bunch radius and  $\varepsilon_r = \sqrt{\varepsilon_x^2 + \varepsilon_y^2}$  is the radial *rms* emittance [115]. As a measure for the length of the probe beam where spatial coherence occurs, the transverse coherence length is decisive of the quality of the diffraction pattern. The sample with its individual atomic distances sets the lower

limit to the required coherence length for successful diffraction experiments. Materials with great domains that should be investigated represents a challenging obstacle, as the measurement needs a spatial coherence of the electron beam of several tens of nanometers.

Furthermore, the coherence length is directly proportional to the probe beam size. A beam with a maximum spatial coherence length offers a beam size that covers most of the sample while the transverse emittance is small. This can be achieved by generating a quasi-laminar beam with a minimized transverse divergence. A transversely compact beam that does not overlap the sample and a maximum coherence length that results from a large spot size, represent a further trade-off. A compromise has to be found.

However, together with the desired short bunch length for a high temporal resolution, the requirement of a small emittance aspires high peak brightness, again. Several ten thousand electrons must additionally hit the sample to achieve a sufficient diffraction pattern. This requires a highly charged bunch of several fC due to the ultra-short bunch length and the compact transverse phase space. Finally, the probe beam must offer an energy up to the MeV range so that an analysis of the sample layers under the target surface becomes possible. All electron beam requirements for a UED experiment are summarized in Table 6.4 [42].

Table 6.4: Electron beam requirements for driving a UED experiment

Requirements on beam	Range
relativistic	$E_{\text{kin}}=1 \dots 3 \text{ MeV}$
low (rel.) energy spread	$\approx 10^{-4}$
ultra-short	$\sigma_t \leq 50 \text{ fs}$
compact	$\varepsilon \leq 200 \mu\text{m rad}$ $\sigma_x \leq 100 \mu\text{m}$
highly charged	number of electrons $\approx 10^5$
high repetition rates	up to MHz

The high-quality beam production together with a variable output energy from keV to MeV range, renders an SRF photoinjector an interesting choice for a UED electron source. A first feasibility study concerning the required beam properties is carried out using the multi-objective optimization program.

As for the ERL, the required high brightness is achieved by minimizing the transverse emittance and bunch length behind the photoinjector while controlling the beam size



at the sample. The beam properties are evaluated at the sample position that is set as the stopping point in the particle tracking process of the optimization. As a first approach, the Gunlab photoinjector test facility is optimized for UED application with a sample holder that is assumed at the screen station located at 2.5 m behind the cathode. The same ERL-based, cavity, and solenoid photoinjector designs as before are used in the optimization code. This is sufficient for a first case study to determine if the required beam properties can, in general, be fulfilled. Moreover, the implementation of a UED experiment in an ERL injection line can be analyzed. Nevertheless, a high performance UED setup driven by an SRF photoinjector as a stand-alone facility requires a separate cavity and solenoid design optimization in an additional step.

In order to optimize the ERL source for a UED application, the ps regime drive laser is replaced in the optimization decision variables by a laser emitting 10 fs to 100 fs long pulses. The bunch charge is reduced to a few fC.

Figure 6.34 shows the Pareto-optimum curve for three different bunch charges, 10 fC, 50 fC and 100 fC [41].

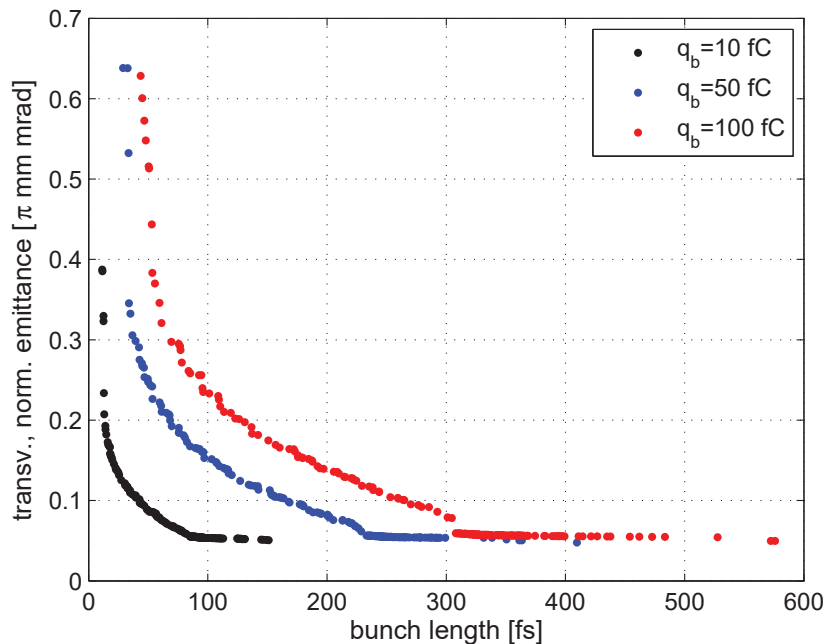


Figure 6.34: The Pareto-optimum curves for three different bunch charges 10 fC, 50 fC and 100 fC. The gun cavity peak field is set to 20 MV/m. As can be seen, the space charge strongly impacts the emittance-bunch length trade-off.

The impact of the space charge on the Pareto-front can clearly be identified from the 10 fC towards the 100 fC curve. The space charge in the compact bunches are mainly determined by the laser pulse volume at the photocathode.

When the SRF gun settings are analyzed, a difference in the laser pulse shaping occurs, compared to the ERL mode, as is illustrated in Fig. 6.35 and 6.36. Instead of optimizing the laser pulse volume towards a “pancake”-regime for short bunch lengths, the laser pulse length is maximized to 100 fs to generate ultra-short bunches, while the laser spot size on the cathode is moderate with around  $700 \mu\text{m}$  (*rms*). The relatively long laser pulse length builds a starting point for a strong energy chirping in the RF cavity that results in velocity bunching in the drift space. This leads to the realization that ultra-short laser pulses are not necessarily required for highly temporal resolved diffraction experiments. Starting at a bunch charge of 100 fC towards higher charged beams, a trend to the “pancake”-regime can be observed in the short bunch length mode again.

In the compromise region of the optimum curves, the initial laser pulse volume reaches a “cigar”-shape. The laser pulse length remains at 100 fs whereas the laser spot size is decreased to obtain small emittance values. Space charge effects driven by the small emittance prevent the bunch length from being further compressed in the longitudinal plane towards ultra-short values in the range of several tens of femtoseconds.

Towards the low emittance end of the optimum front, the initial bunch distribution is determined by a compact laser pulse in both planes instead of the “cigar”-shaped known from the ERL optimization. The laser spot size (0.1 mm) and the laser pulse length (10 fs) are set to their lower limits. The bunch length is only slightly decreased by velocity bunching. The focus is clearly on a compact transverse phase space which is induced by compact laser spots and strong focusing fields of the solenoid magnet.

Comparing the three plots in Fig. 6.35, a continuous increase of the laser width towards higher bunch charges in order to achieve ultrashort bunches can be observed.

An analysis of the three Pareto-optimum curves in Fig. 6.34 with respect to the ability of their beam properties for UED starting at 10 fC uncovers several parameter sets that satisfy the desired bunch length of less than 50 fs. The compact bunch lengths allow for a corresponding high temporal resolution in combination with suitably short and well-synchronized laser pulses. Thus, even ultra-fast processes in the sample can be visualized. The corresponding transverse emittance and beam

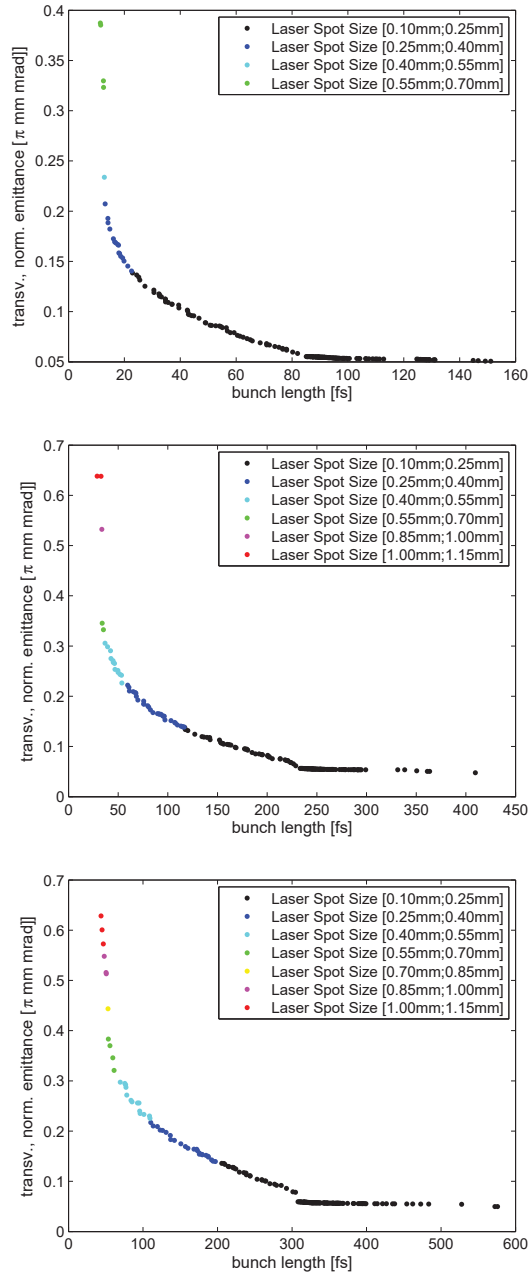


Figure 6.35: Dependency of the Pareto-optimum curve on the laser spot size. Higher bunch charges require larger laser spots on the cathode to reach ultra-short bunches. This finding indicates that strong space charge effects act in the compact electron bunch.

size values also fulfill the UED specifications. The beam size ranges from  $120\ \mu\text{m}$  to  $150\ \mu\text{m}$  in the short bunch length region. Supplementary apertures can be added to the beamline if a transverse spot size of  $< 100\ \mu\text{m}$  is required for compact samples. However, the relatively large emittance values above  $100\ \text{nmrad}$ , together with the

## 6. Multi-Objective Optimization Results

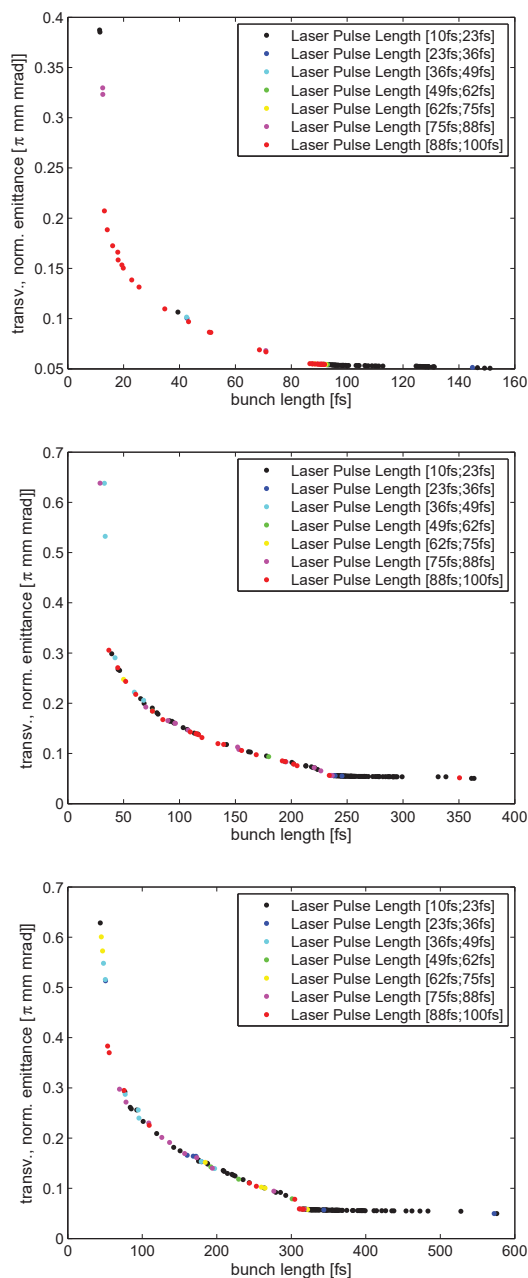


Figure 6.36: Dependency of the Pareto-optimum curve on the laser pulse length.

compact beam size, limit the coherence length to 0.6 nm at its maximum in the low bunch length mode [see Fig. 6.37]. Considering a usual test sample of a thin gold foil with a lattice parameter of 4.078 Å, the coherence length is still sufficient to conduct a UED experiment with a high-quality diffraction pattern.

In general, the coherence length increases up to a value of 1.3 nm towards smaller emittance values along the Pareto-optimum curve. The decline of the coherence length

that starts at 80 fs bunch length can be traced back to a strong focusing of the beam size by an increased solenoid field. If the sample requires a larger transverse coherence length to cover greater domains, a setting at the end of the compromise area or in the low emittance mode of the optimum curve can be selected. The bunch length must then be further compressed in front of the sample by a buncher cavity or by adding a magnetic chicane to the beamline [see the discussion of bunch compression techniques in Chapter 4.4.3].

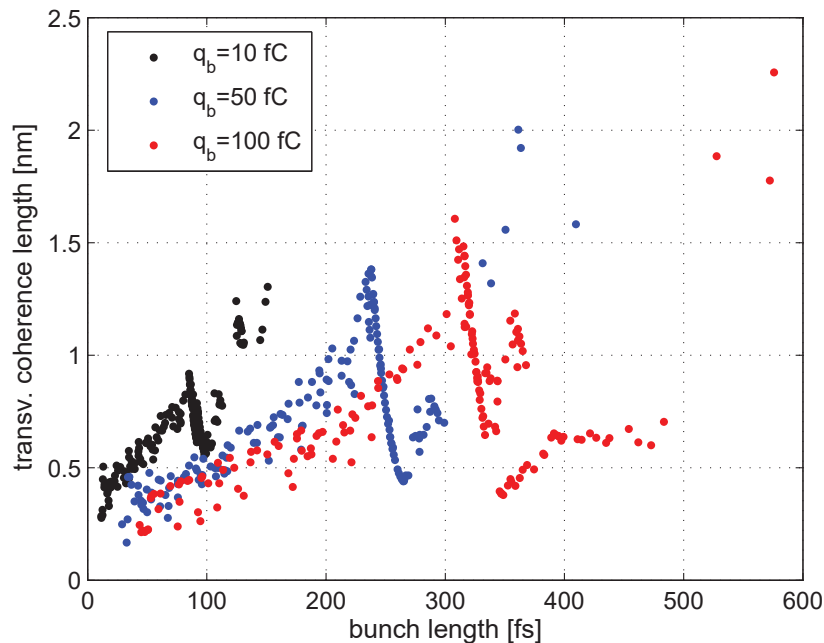


Figure 6.37: Transverse coherence length over bunch length for three different bunch charges. The coherence length was calculated from the beam parameters achieved in the Pareto-optimization for UED, as illustrated in Fig. 6.34.

Regarding the optimum front for a 50 fC bunch charge, only a few gun parameter settings reach a bunch length that is shorter than 50 fs. In this area, the transverse emittance exceeds 200 nm rad, which results in a transverse coherence length below 0.5 nm [see Fig. 6.37]. This value limits the spectrum of suitable samples for UED. Appreciably higher coherence lengths above 1 nm occur at bunch lengths that are longer than 200 fs. Additional bunch compression can counteract the constrain in the time resolution of the diffraction patterns.

## 6. Multi-Objective Optimization Results

---

At 100 fC, short pulses are only possible with an insufficient coherence length as illustrated in Fig. 6.37. In order to benefit from the coherence length maximum of 1.5 nm at 300 fs bunch length, before the solenoid field starts to minimize the beam size and the coherence length, a parameter setting in the compromise region must be selected in the setup together with a bunch length compression method.

Overall, it can be summarized that short bunch length settings only lead to the desired, suitable results for low charged beams.

One setting for the current SRF photoinjector design at HZB fulfilling all UED requirements is presented in Fig. 6.38 (a) and (b) for 10 fC. The corresponding photoinjector setting and beam parameters at the target are summarized in Table 6.5 and 6.6.

Table 6.5: Stable parameter setting for a 10 fC UED experiment in Gunlab determined by Pareto-optimization.

Parameter	Value	Unit
Laser spot size	0.19	mm ( <i>rms</i> )
Laser pulse length	100	fs
Cathode position	0	mm
Injection phase gun cavity	-30	deg
Gun cavity peak field	20	MV/m
Solenoid position	0.60	m
Solenoid field	0.068	T

Table 6.6: Beam parameters at the sample for one selected UED setting

Parameter	Value	Unit
Bunch length	37.07	fs
Beam size	0.14	mm ( <i>rms</i> )
Beam transverse divergence	0.28	mrاد
Norm., transv. emittance	0.11	mm mrad
Transv. coherence length	0.50	nm
Kinetic energy	1.68	MeV

The beam is well focused in all three planes at the sample. Figure 6.38 shows the strong focusing in the longitudinal plane by velocity bunching and in the transverse plane by the solenoid magnet. The beam is overfocused in the longitudinal plane.

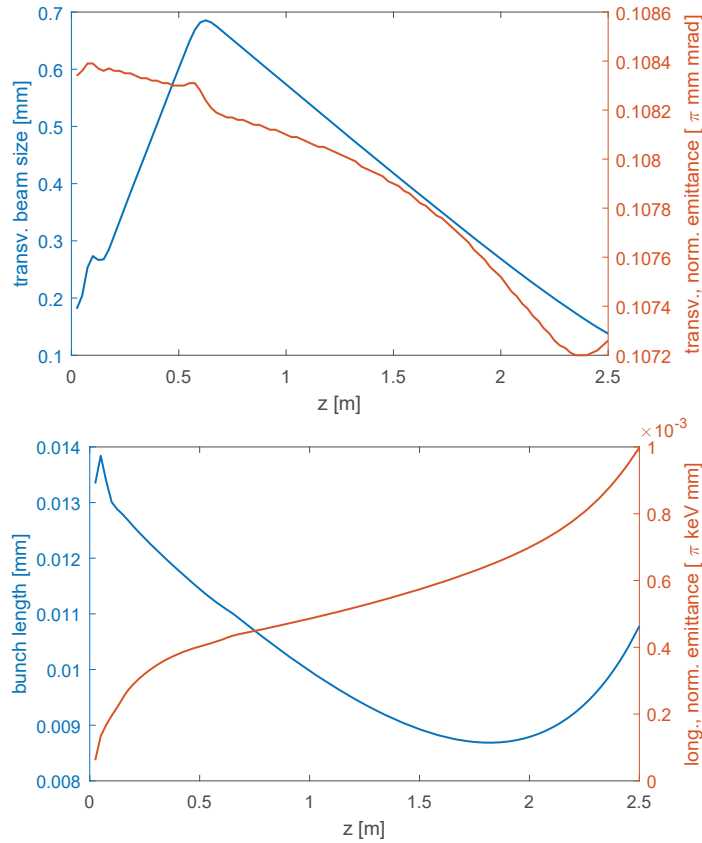


Figure 6.38: Evolution of the beam size and transverse emittance [top: (a)] and the bunch length and the longitudinal emittance [bottom: (b)] along the  $z$ -axis, from the photocathode to the UED experiment with the sample position at 2.5 m. The optimization is subjected to a 10 fC bunch charge and a cavity peak field of 20 MV/m.

Therefore, the bunch length, the energy spread and the longitudinal emittance start to increase again [see Fig. 6.38(b)] at a short distance away from the optimization point. The relative energy spread of 0.1‰ is ultra-low and supports the quality of the diffraction pattern in the UED experiment. Starting with a small intrinsic emittance at the cathode due to the small laser spot size, the total transverse emittance is kept nearly constant along the beam path. In spite of the strong longitudinal compression, the resulting space charge effects that lead to growth in the transverse direction can be controlled.

The compact transverse beam size of  $140 \mu\text{m}$  does not require a further aperture in front of the target. Therefore, no electrons in the beam halo are cut away and the low charge of 10 fC provides a sufficient number of electrons for a high-quality diffraction pattern.

The gun cavity peak field on axis is restricted to 20 MV/m in all three optimization runs, which leads to a moderate beam energy of 1.7 MeV at the UED sample. The energy is sufficient for UED experiments that are classically conducted with a probe beam that shows an energy in the keV range [115]. The MeV beam opens the possibility to analyze deeper layers in the sample structure. Yet, as the diffraction angle is inversely proportional to the beam energy (Bragg law [116]), the spots in the diffraction pattern move closer to the zeroth maximum for high energy beams. The detector must be placed a certain distance away from the sample to benefit from the divergence of the deflected beam in the drift. The moderate energy value of 1.7 MeV enables that the detector is placed close to the sample. This provides a compact setup.

An optimization procedure with an acceleration gradient of 30 MV/m in the gun cavity achieves desirable, shorter bunch length at comparable transverse emittance values as at 20 MV/m, while the beam energy increases to 2.5 MeV on average. This is illustrated in Figure 6.39. Choosing samples with a structure that will not be damaged by heating of a higher energetic bunch would render increased gun gradients possible to reach a better beam brightness.

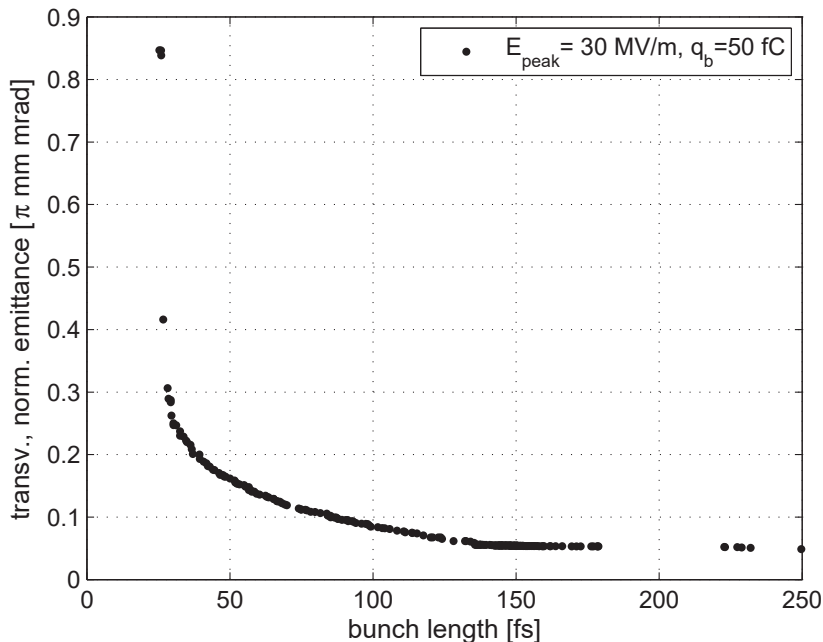


Figure 6.39: Optimization results for an UED application of an SRF photoinjector. The acceleration gradient for the 50 fC bunch is set to 30 MV/m.



The first approach in the multi-objective optimization program was the high brightness operation of an SRF photoinjector with the transverse emittance and bunch length as its objectives. Even if the transverse emittance cannot be neglected for UED, from the user perspective, the transverse coherence length represents the most important transverse beam parameter that combines all characterizing parameters of the transverse phase space. Consequently, it is crucial to maximize the coherence length. In a further step, the objectives of the optimization are adjusted for the UED application of the SRF gun, using a minimum bunch length and a maximum transverse coherence length in the dominance criterion. At the same time, the ability of the program to optimize objectives that differ from the ERL scenario can be verified.

Figure 6.40 illustrates the new optimum curves for the three bunch charges, 10 fC, 50 fC and 100 fC. The trend towards shorter bunch lengths at smaller bunch charges can be detected again and confirms the sc theory. Compared to the  $\varepsilon_x$ - $\sigma_z$ -optimization, coherence lengths distinctly above 1 nm can be achieved easily. Thus, it is sensible to set the transverse coherence length as an objective in the optimization in order to improve the photoinjector performance in UED. Analyzing Fig. 6.40 shows that the section at the optimum front with the approximately linear slope in the coherence length towards higher bunch lengths is determined by an increase in the beam size while the transverse emittance stays constant. This linear increase of the transverse coherence length relative to the bunch length was also observed in multi-objective optimization studies done for DC and normal-conducting RF guns by Gulliford et al. [117], [118]. Nevertheless, the maximum coherence values above 2 nm are achieved by ultra-small emittances. The corresponding small beam size value limits a further improvement of the spatial coherence but cannot be avoided.

The optimization of the injection line in section 6.3.1 demonstrated that the transverse emittance and bunch length can further be minimized by tracing the beam through the booster. The quality of the UED experiment benefits from the improved beam properties. Therefore, it is considered to use the bERLinPro injection line setup at HZB for UED. A booster section, however, also leads to a higher beam energy which excludes sensible samples, such as liquids due to the occurring evaporation. An electron beam which is generated in an SRF photoinjector and accelerated in a booster still represents an interesting probe beam for many samples. Consequently, a first feasibility study is presently conducted in a master thesis at HZB based on the optimization code that was developed during this dissertation.

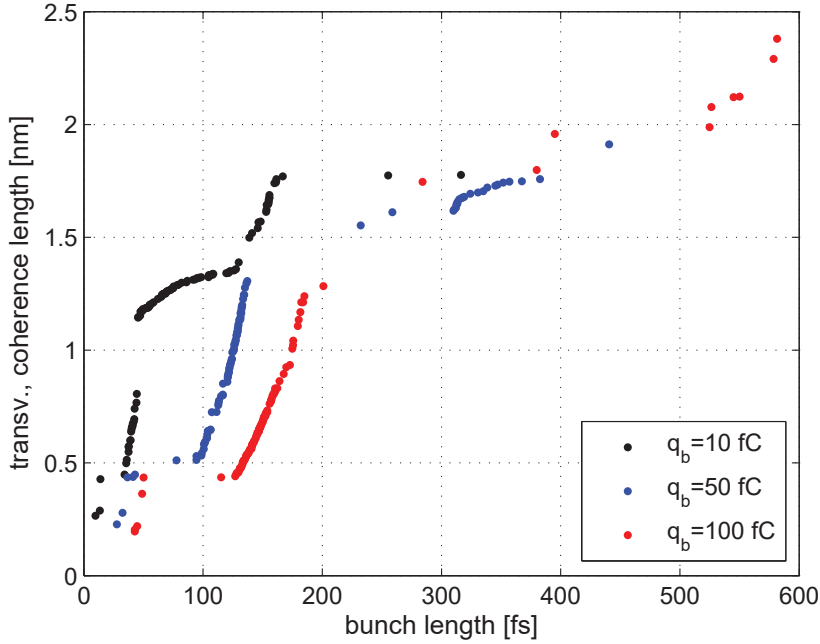


Figure 6.40: Pareto-optimization for the two objectives transverse coherence length and bunch length for three different bunch charges 10 fC, 50 fC and 100 fC.

### 6.3.3 Gun cavity design study based on Pareto-optimization

In order to fully explore the possibilities of the developed Pareto-optimizer, a first design optimization is realized [113]. Up to this point, the decision variables of the optimization process are restricted to the operation parameters that can be changed with less effort during the photoinjector and booster commissioning, and during the run, as well. Now, a first gun cavity design optimization is implemented which considers the field flatness  $FF$  that is defined as the ratio of the on-axis peak field of the half-cell compared to the on-axis peak field of the full-cell in the photoinjector [see Equ. (6.2)] [54]

$$FF = \frac{E_{peak,half-cell}}{E_{peak,full-cell}}. \quad (6.2)$$

A field flatness value below 100% describes a field enhancement in the full-cell, while field flatness above 100% corresponds to a higher field in the half-cell than in the full-cell. A balanced peak field (100% field flatness) between half- and full-cell is desired at all times. Yet, the challenging manufacturing of the superconducting gun

cavities as well as tuning processes during the cavity commissioning cause deviations from the desired 100% field flatness state.

The goal is to determine the impact of the cavity design on the transverse emittance and bunch length and consequently, on the peak brightness. Eight different cavity fields from a 59% up to a 204% field flatness are displayed in Figure 6.41.

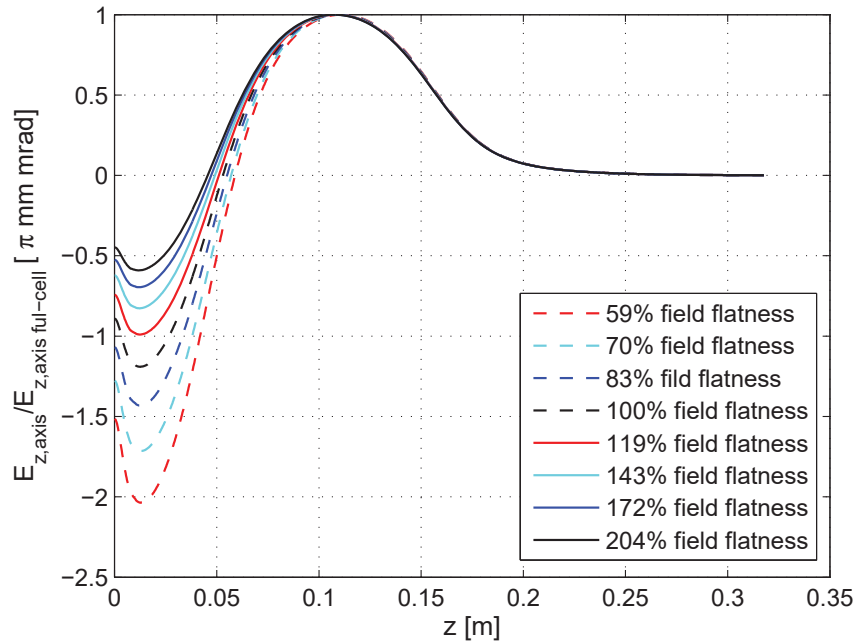


Figure 6.41: Field distributions in the gun cavity for eight different field flatness values from 59% to 204%.

In order to compare the beams that are accelerated with different field flatness in the SRF gun cavity, the final beam energy is set to 2.3 MeV (bERLinPro specification). The gun cavity gradients and injection phases are selected accordingly. The Pareto-optimum fronts are evaluated at 2.5 m behind the cathode, thus the optimization is restricted to the SRF photoinjector without a booster section. The optimum results are plotted in Figure 6.42 with a 100% field flatness displayed in the red curve and field enhancement in the full-cell. Figure 6.43 presents the Pareto-fronts for field enhancement in the half-cell.

The conspicuous discrepancy in the optimum solutions of all Pareto-curves between short and moderate bunch lengths can be traced back to a cut in the injection phase settings. In order to achieve the lower limit of the bunch length of each field

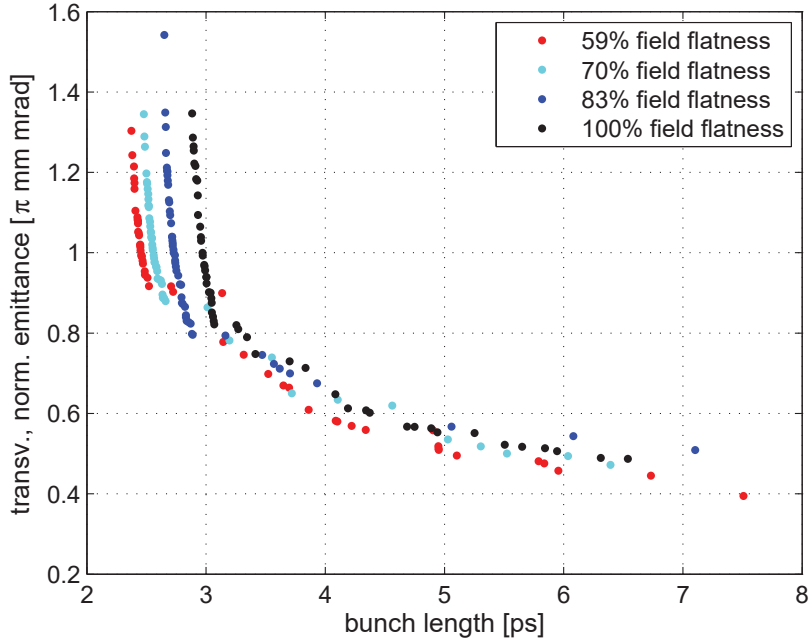


Figure 6.42: Pareto-curves for 100% field flatness (red) and for field enhancement in the gun cavity full-cell.

flatness optimum front, the gun phase is set far away from on-crest at phases that provide a strong momentum chirp on the bunch. At the branch where smaller emittance and longer bunch length occur in the curve, the injection phase continuously changes from small phase values towards the on-crest phase.

The bunch length can be significantly decreased towards higher field flatness, i.e., higher fields in the half-cell. This decreasing of the bunch length is possible because of the fact that the total momentum chirp of the cavity imprinted on the bunch does not only depend on the gun gradient and injection phase, but it is directly impacted by the field flatness, too. As illustrated in Fig. 6.44, the momentum spread (absolute value) grows towards higher fields in the half-cell and, thus, higher field flatness values. This leads to stronger velocity bunching and shorter bunch lengths at the optimization point.

The effect can also be observed in the Pareto-optimum curves in Fig. 6.42 and Fig. 6.43 in the minimization of the bunch length towards higher field flatness values. Nevertheless, the field enhancement in the half-cell and cavity peak fields cause different acceleration voltages in the half-cell. Depending on that detail, the bunches

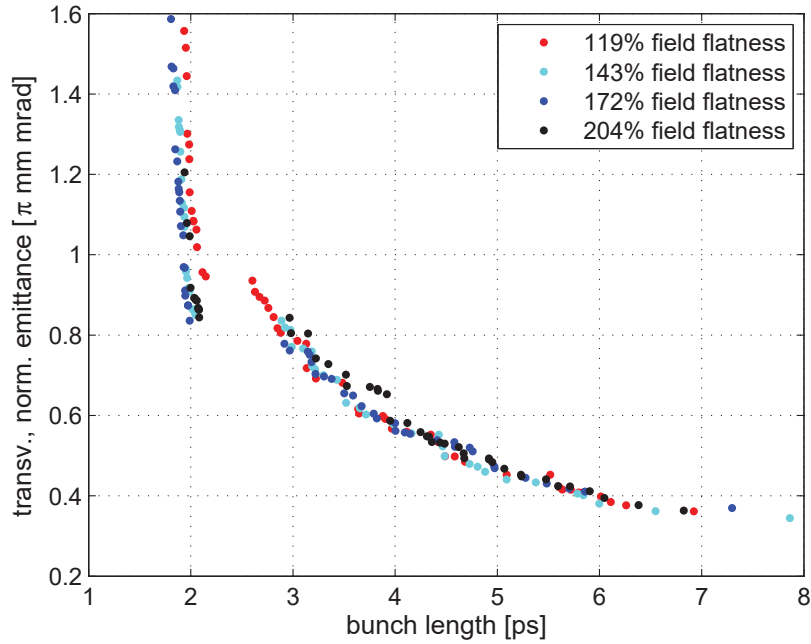


Figure 6.43: Pareto-curves for field enhancement in the gun cavity half-cell.

are injected at different times into the full-cell (phase slippage). If the field flatness is at 120%, the corresponding total momentum spread is not further increased but it converges and even decreases above a 150% field flatness [see Fig. 6.44]. Therefore, the bunch length cannot be compressed further. The Pareto-fronts start to move towards longer bunch lengths again (red curve in Fig. 6.43).

Additionally, a moderate improvement of the transverse emittance at higher fields in the half-cell can be observed. It can be traced back to stronger RF focusing by high radial electric fields at the photocathode. A constant cathode retreat of 1.5 mm, implemented into all field flatness optimization runs, supports this effect. Although an obvious stronger impact of the field flatness on the longitudinal phase space is still detected.

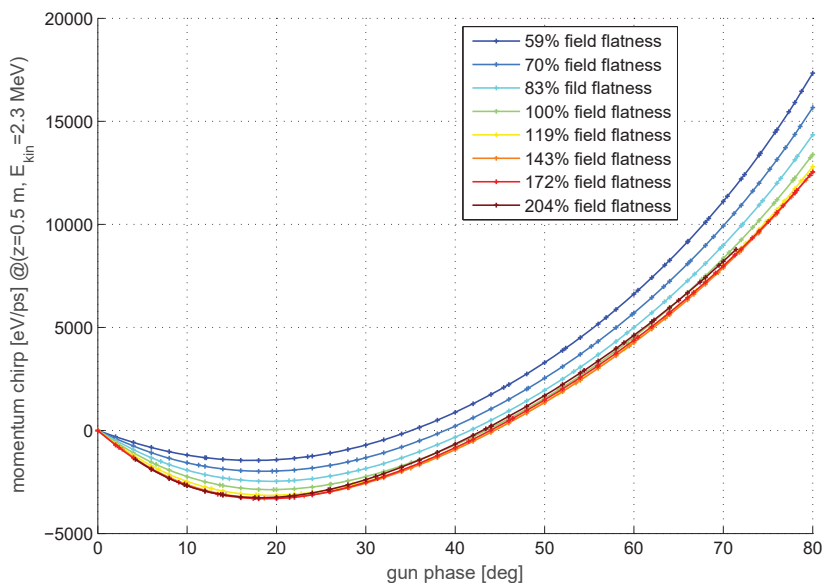


Figure 6.44: The dependency of the momentum chirp on the gun injection phase and field flatness. The momentum chirp is imprinted on the bunch by the RF cavity. The presented data correspond to the 2.3 MeV final kinetic energy that the electron beam reaches at the cavity exit ( $z=0.5$  m).

Even though the peak brightness can be maximized at a field flatness of around 120% by reaching the smallest emittance and shortest bunch length values, higher peak fields of up to 40 MV/m are required to achieve a beam energy of 2.3 MeV. The maximum cavity fields on axis over the corresponding bunch length are illustrated for the eight different field flatness values [see Fig. 6.45]. These high gradients pose a great challenge for the sc cavity operation and make a field flatness of 100% most desirable.

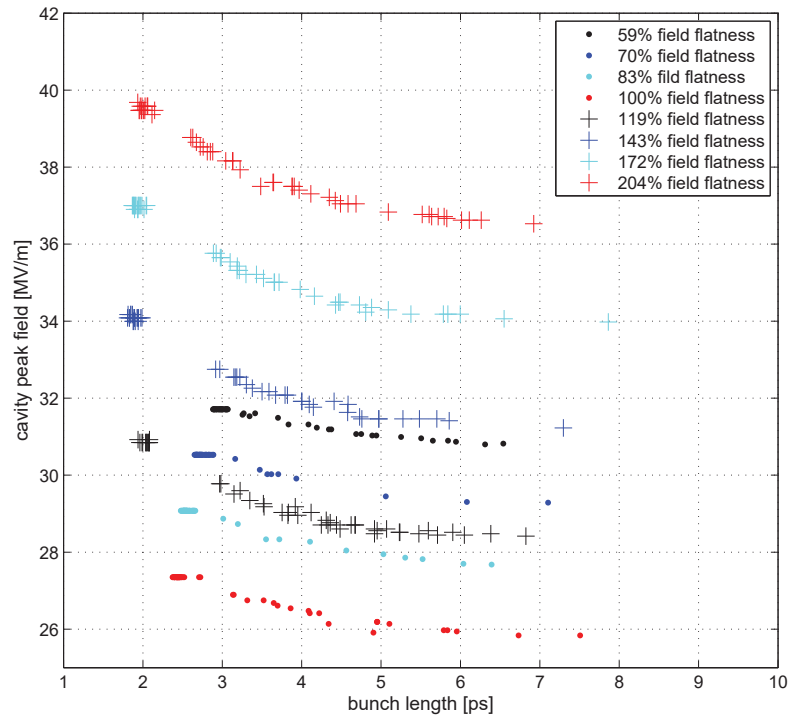


Figure 6.45: Gun cavity peak field on axis for the eight different field flatness values required to accelerate the electron beam to a final kinetic energy of 2.3 MeV at the cavity exit.

## 6.4 SRF Gun at Helmholtz-Zentrum Dresden-Rossendorf

In order to demonstrate the flexibility of the developed optimization tool, the program is adjusted so that it applies the approach of multi-objective optimization to the SRF photoinjector at Helmholtz-Zentrum Dresden-Rossendorf (HZDR), Germany. This injector is used as an electron source for the ELBE linac, a research facility for the generation and acceleration of high brightness, low emittance electron beams [119]. An overview of the current setup can be found in Fig. 6.46.

An important application concerning the accelerated electron beam at the ELBE facility is the operation of an FEL for a semiconductor spectroscopy as well as the generation of THz radiation. Currently, the FEL experiment FELBE [121] and the THz generation TELBE [122] are mainly driven by an electron beam generated in

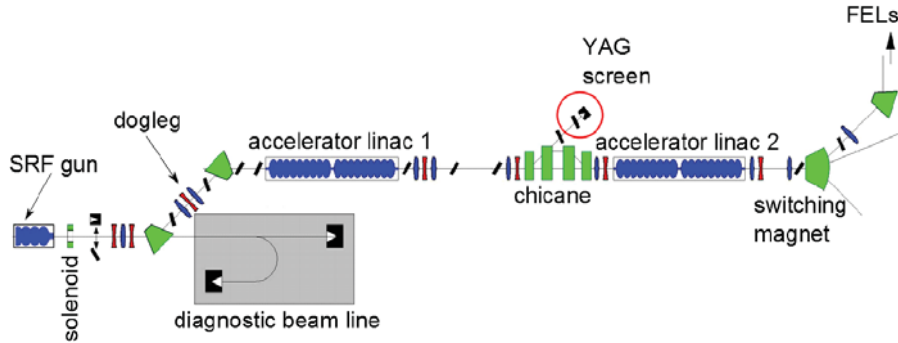


Figure 6.46: SRF photoinjector and ELBE beamline at HZDR, Germany [120].

the second electron source (thermionic injector) due to criteria of stability. Nevertheless, a test runs that aim for the first SRF photoinjector generated electron beam operating a THz experiment [123]. Therefore, the Pareto-optimization of the SRF photoinjector at HZDR also opens the possibility of extending the demonstration of the optimization program to cover various, high charge SRF gun applications.

The optimization setup was adjusted by merely changing the RF field distribution and the solenoid field profile in the ASTRA input tracking file. The cavity peak field is set to 20 MV/m which represents a realistic value also achieved in the SRF photoinjector operation. Besides a diagnostic mode with a bunch charge of 20 pC, a high bunch charge mode of 100 pC, 200 pC and 300 pC to ensure high peak currents for, e.g., an FEL operation is considered. Fig. 6.47 presents the resulting Pareto-optimum fronts for the different bunch charges.

The strong impact of the space charge effects that increase with an ascending bunch charge can be clearly detected in the curves of Fig. 6.47. Therefore, a significant emittance growth to values above 10 mm mrad for bunch charges of 200 pC and 300 pC is observed. In order to operate the ELBE facility, a transverse emittance below 3 mm mrad and a bunch length shorter than 15 ps is required [120]. Several parameter settings in the curves from a 20 pC to a 200 pC bunch charge fulfill these requirements. It is expected that in the case of a 300 pC bunch charge, an emittance around 3 mm mrad can be achieved with a corresponding bunch length of approximately 12 ps. The output of the optimization program does not provide any parameter settings in this area on the Pareto-optimum curve. As an alternative, the transverse emittance can be controlled by a moderate RF focusing that is triggered



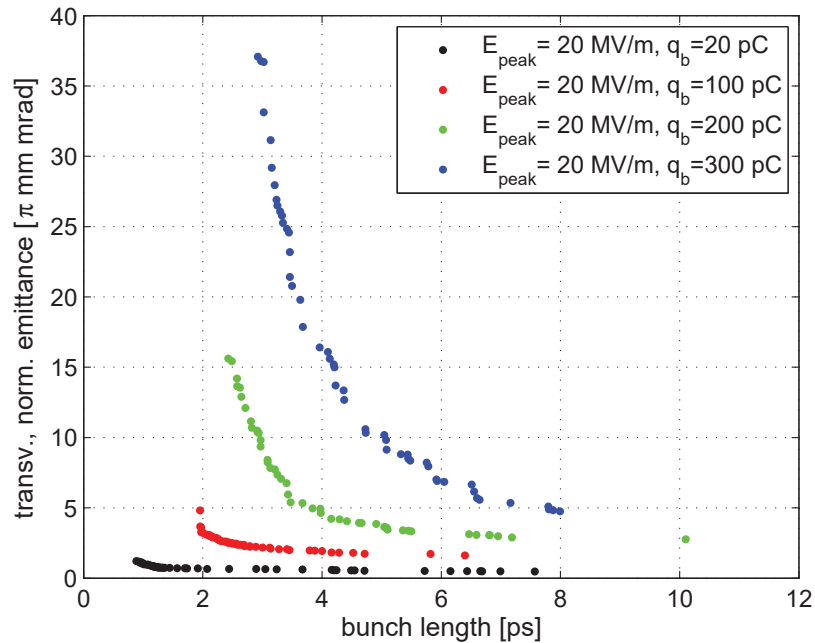


Figure 6.47: Pareto-optimum results for the SRF photoinjector at Helmholtz-Zentrum Dresden-Rossendorf. A low charge mode (20 pC) as well as a FEL mode (100 pC, 200 pC, 300 pC) to achieve high peak currents are considered.

by the radial RF field contribution in the ELBE linac cavities.

In order to drive the FEL facility in a high charge mode, further emittance compensation and, in particular, bunch compression is required. Therefore, the magnetic chicane in the ELBE beamline provides a bunch compression facility [see Fig. 6.46].

To summarize, the successful implementation of the developed multi-objective optimization program for the SRF photoinjector at HZDR demonstrated that the tool is able to optimize other SRF photoinjector designs for a high brightness, low emittance operation.



# Chapter 7

## Summary and Outlook

This thesis examined the high brightness performance of high average current SRF photoinjectors. The aim was to figure out the conditions for operating an SRF photoinjector in a high brightness mode. In the course of this analysis, the limiting factors of such an operation mode were also identified. For that reason, long established and current theories on beam dynamics in SRF photoinjectors were studied to understand the processes acting in the injector. Based on this theoretical analysis, the beam parameters that impact the beam brightness were determined, while this dissertation also analyzed how these beam parameters are affected by the photoinjector settings. Using the gained knowledge, an innovative optimization tool for a high brightness SRF photoinjector performance was developed representing the central part of the thesis at hand.

### 7.1 Conclusion

It was shown in the theory chapter that the electron beam brightness is primarily defined by the transverse emittance and bunch length. Both beam parameters are heavily influenced by the operation and design parameters of the photoinjector. Several strategies for an individual minimization of the transverse emittance induced by emittance compensation, and for minimizing the bunch length by using compression were introduced. However, the transverse emittance and bunch length always entail a trade-off and, thus, a simultaneous minimization of both parameters is almost impossible. As a consequence, the optimization of the SRF photoinjector towards a high brightness performance presents a typical multi-objective optimization problem with two objectives (transverse emittance, bunch length) that have to be optimized depending on several decision variables (photoinjector design and operation parameters). Up to this point, the improvement of the SRF photoinjector performance was

based on such time-consuming methods as single particle tracking that was repeated several times for different photoinjector settings, or as swarm optimization generating multiple dominated solutions. This dissertation developed an innovative optimization program which is able to find stable parameter settings out of a population. This selection allows the user to run the SRF photoinjector in a high brightness mode. A multi-objective generic algorithm was chosen for the optimization process. Compared to the previous optimization methods, a MOGA uses a strong dominance criterion in order to select the best solutions out of the population. Furthermore, the algorithm allows the user to hand as much optimization decisions as possible to the program, for example the selection of the best settings. Another significant advantage of the developed tool is that the architecture of the optimization program makes the finding of several Pareto-optimum solutions that cover the whole objective space possible, instead of finding only one local optimum as a result of one optimization run.

The functionality and standard optimization procedure were successfully demonstrated in the high brightness operation of the current SRF photoinjector test stand GunLab at HZB. In a high average current mode corresponding to a 77 pC bunch charge, a minimum transverse emittance of 0.36 mm mrad in a low emittance mode and the shortest bunch length of 1.3 ps in a short bunch length regime could be achieved. Several optimized photoinjector settings along the Pareto-optimum curve fulfill the requirements of the ERL project bERLinPro at HZB on the electron source. A further optimization run confirms that a transverse emittance down to 0.31 mm mrad can even be reached at an optimization point that is positioned further away from the cathode (here 2.8 m). The results of the Pareto-optimum curve can additionally be used for beam dynamics studies. The evolution of the most important beam parameters and of the transverse and longitudinal phase spaces confirms the strong impact the photoinjector parameters have, especially the laser pulse volume, the gun injection phase, the cavity peak field and the solenoid field on the beam. Due to the various Pareto-optimum solutions in the front, the developed optimization program allows to analyze the changes in the beam parameters and the phase spaces from a short bunch length to a low emittance regime - another advantage compared to the single solution optimization or the particle tracking. In particular, the shift of the focus from a short bunch  $\sigma_z < 2$  ps corresponding to moderate emittance  $\varepsilon_{x,y} > 0.8$  mm mrad towards a low emittance  $\varepsilon_{x,y} < 1$  mm mrad corresponding to a longer bunch length  $\sigma_z > 2.5$  ps can be observed in the evolution plots. Finally, the optimization program makes it possible to study the impact of the photoinjector settings

on the beam quality. Beside a strong trend towards higher cavity peak fields on axis, a moderate cathode retreat of -1 mm, an off-crest gun phase of around -28 deg, and a solenoid field on axis of around 100 mT lead to the best transverse emittance and bunch length values and therefore, to the highest beam brightness. At the same time, the emittance and bunch length results along the Pareto-optimum curve represents the achievable beam performance limits of the current SRF photoinjector design of GunLab. The program allows a simple, fast, and global evaluation of these limits compared to other optimization techniques presented in this work.

It is expected that changes in the design of the photoinjector elements strongly influence the electron beam parameters. Especially the cavity provides three important operation parameters for the optimization: The injection phase, the RF field and the aperture for the cathode (cathode position). One aim of the dissertation at hand was to prove the usability of the presented optimization tool for photoinjector design parameters that can be taken as decision variables in the optimization. The field flatness of a gun cavity and its deviation from the desired 100% represent a great challenge in the gun cavity manufacturing and the SRF photoinjector research. The doctoral thesis presents first results for a field flatness study of the current gun cavity with the developed multi-objective optimization program. The investigation of the impact of the field flatness, especially on the bunch length, demonstrates the diverse applicability of this powerful tool. For the first time, it could be verified that a field enhancement in the half-cell can lead to shorter bunch lengths while the transverse emittance stays nearly constant. Still, this field enhancement corresponds to a higher peak field in the gun cavity which is required to keep the final beam energy on the desired value.

Along with these general studies of the high brightness operation by the SRF photoinjector, its application as an electron source for ERL, UED and FEL experiments was considered. The aim was to demonstrate the successful multi-objective optimization by using the developed tool for different SRF photoinjector applications. This was initially done for the ERL mode. Based on the particle tracking with ASTRA, the program could be easily adjusted by adding a booster section to the tracking beamline and additional decision variables (booster parameters) to the optimization procedure. The Pareto-optimum was evaluated for the bERLinPro scenario at HZB. Compared to the results obtained from the standard swarm optimizer, better results in the transverse emittance (0.28 mm mrad) and bunch length (4.6 ps) are achieved.

The optimization of the three booster cavities means a great success since the program was able to select zero-crossing and on-crest acceleration settings on its own. A design case study of the SRF photoinjector together with a 5-cavity booster section allowed a successful comparison of the high brightness performance of an SRF photoinjector and a DC injector. The results obtained with the developed Pareto-optimizer confirm that an SRF photoinjector is able to operate in a high brightness mode, at least equivalent compared to a DC injector.

The applications of the optimized high brightness, high average current electron beam in the ERL are numerous. One interesting approach is the combination of an ERL together with a single-pass FEL. It is based on the high average beam power that is achieved by accelerating the high average current beam to energies up to the GeV range in the ERL linac. The high power FEL would allow the operation of EUV lithography experiments, a next-generation lithography technology that enables the imaging from nanostructures below 20 nm on wafers [24]. Since the optics in the setup will absorb most of the EUV light at the desired wavelength of 13.5 nm, a bright source is crucial. An ERL FEL optimized for high brightness, high average current beam, will provide a promising alternative to the currently investigated laser-driven plasma light sources.

The optimization of an SRF photoinjector that is used as a stand-alone facility for a UED experiment revealed that the program is also applicable in low charge mode. After implementing a fs photocathode drive laser in the optimization routine, ultrashort bunch lengths that were smaller than 20 ps were achieved. This result provides a time-resolution that allows to resolve ultrafast processes in the sample of a UED experiment. Users in material science, chemistry, biology, or medicine are particularly interested in visualizing ultrafast transitions in the sample that do not proceed from the initial to the final state. An ultrashort bunch length allows to investigate non-equilibrium reaction states, i.e., of molecular crystals or nanostructures. Furthermore, the electron beam energy in the lower MeV range allows to investigate deeper layers in the sample compared to standard keV-electron guns. The promising optimization results confirm that an SRF photoinjector presents an interesting option for a UED electron source. A future Pareto-optimization of the SRF photoinjector design and operation parameters can aim for attosecond short pulses that would allow to extend the current research from the investigation of atomic motion in the sample to the electron scale.

Additionally, the multi-objective optimization in the UED mode was performed for

the transverse coherence length and the bunch length as the objectives. The results point out that in order to investigate greater domains in a sample with a transverse coherence length above 10 nm, further beam manipulation is required behind the photoinjector. Nevertheless, the successful optimization shows that the developed program is flexible in its objectives and can easily be adjusted to the requirements of the specific SRF photoinjector application that has to be analyzed.

The optimization of the SRF photoinjector at HZDR also underlined the flexibility of the developed program to easily adjust the tool for the optimization of any photoinjector in the world. If additional bunch compression and emittance compensation are applied to the beam, the investigated injector is able to drive an FEL experiment at a high bunch charge of several hundreds of pC.

To summarize, the introduced program is able to find stable parameter settings for any SRF photoinjector design, independent from the electron beam application and the subsequent accelerator type.

However, the evaluation of the transverse and longitudinal phase spaces indicated that the optimization results, especially in the short bunch length mode and the low emittance regime, represent the physical limits of the analyzed SRF photoinjector. The correlation and superposition between the transverse and longitudinal space charge effects, as well as nonlinearities from the RF field and the solenoid pose some challenges for the interpretation and lead to nonlinear phase spaces.

A future modification of the developed program could implement slice values instead of the currently used *rms* values as objectives. It is expected that this step will improve the resulting phase spaces, but the minimum achievable *rms* emittance and bunch length will increase. Moreover, the calculation of reliable slice emittance values requires a much higher number of macroparticles that extend the ASTRA particle tracking run-time and, therefore, the optimization run-time significantly.

Real field distributions can improve the simulation of the emission and acceleration process in the gun cavity. Currently, ASTRA calculates the radial RF field contribution from the longitudinal 1D RF field input. As a result, the calculated RF field obtained by cylindrical symmetric expansion in the radial direction differs from the real radial field contribution, in particular at the photocathode <sup>1</sup>.

Moreover, an adjustment of the used space charge grid for each randomly chosen

---

<sup>1</sup>Private communication Axel Neumann.

photoninjector setting in the optimization will improve the calculation of the space charge that acts on the bunch and will thereby improve the analysis of the resulting change in the beam dynamics, as well.

A verification of the optimization tool with beam dynamic measurements at an SRF photoninjector can provide further valuable insights on how the optimization tool can be further developed and perfected. The modification, e.g. by implementing dark current or observed instabilities of SRF photoninjector elements, can bring the optimization results closer to reality. Understanding the limiting factors of the SRF photoninjector based on the optimization program can, consequently, improve the high brightness performance of the SRF photoninjector in operation.

### 7.2 Outlook

The developed multi-objective-optimization program has a great potential to be used for the optimization of other parts of the accelerator or at least of the whole facility. The modifications of the developed optimization program are numerous. The basic concept of particle tracking for different, randomly chosen accelerator settings, the evaluation of consequent beam properties at a chosen final position at the beam line, and the selection of the best settings following a dominance criterion are universally applicable to different accelerator types and experiments. Therefore, the introduced MOGA optimizer represents a very significant tool in the accelerator research.

However, the operation of accelerators becomes more and more complex and it, therefore, increases the requirements on optimizer systems. An accelerator is a dynamic, non-stationary behavior system with many parameters that must be monitored and controlled. Many components with interacting sub-systems lead to complex beam dynamics, including nonlinear beam physics. The beam diagnostics are limited in some facilities or the outcomes are not fully used to control the beam (i.e. profile and image measurements). The future in accelerator physics will pose various challenges for the optimization work.

A better control and an improved operation performance is always of great interest as science goals can be achieved and new particle beam applications become possible. Furthermore, accelerator operation costs can be lowered by saving time, improving the energy efficiency, avoiding unintended shut-down times, and reducing the labor of the operator, who in turn can work on hardware solutions. This leads to a global



optimization of the accelerator operation.

Although (MOGA) Optimization procedures successfully meet several of these challenges, the implemented particle tracking simulations with space charge calculations are time-consuming. Moreover, the number of parallel working simulation runs are limited by the available clusters. Following these arguments, conducting an online-optimization of a greater part of the accelerator operation parameters parallel to the accelerator run is impossible. Further estimations, e.g., for the space charge calculation or nonlinear beam dynamics, only result in a limited and simplified accelerator model.

As presented in this thesis, mathematical optimization with an evolutionary algorithm already includes a type of artificial intelligence when the developed program finds the best solution based on a human-defined dominance criterion. However, the optimization of an accelerator is currently split into a theoretical approach that is based on particle tracking and simulations and into experimental studies. Usually, the measurement results are compared to the simulation outcomes. Afterwards, the operator tries to find the driving effects that lead to the deviations and adjusts the accelerator model used in the optimization. This procedure is performed manually and is based on human intelligence.

In a new approach, an artificial intelligence, which is able to recognize correlations, to learn (machine learning) and to improve the accelerator performance on its own, replaces the operator. The application of machine learning techniques based on neural networks steps beyond the current optimizer potential. Machine learning represents a subset of artificial intelligence. Figure 7.1 summarizes the correlations between artificial intelligence, machine learning, neural networks and mathematical optimization. Together with its learning paradigms, machine learning with its strategy of classification, clustering and dimensionality reduction build the framework for neural networks. Mathematical optimization is applied in this context, as well, contributing with evolutionary algorithms and swarm intelligence to the adjustment of input weights or the topology of the neural networks. Many different architectures of neural networks, consisting of single neurons, feed-forward networks, recurring forms, and learning strategies are available [124].

Machine learning is already widely approved in high energy physics but represents a rather new strategy in accelerator physics. Fig. 7.2 shows the standard procedure of machine learning using a neural network in a flow chart. Now, the strategy com-

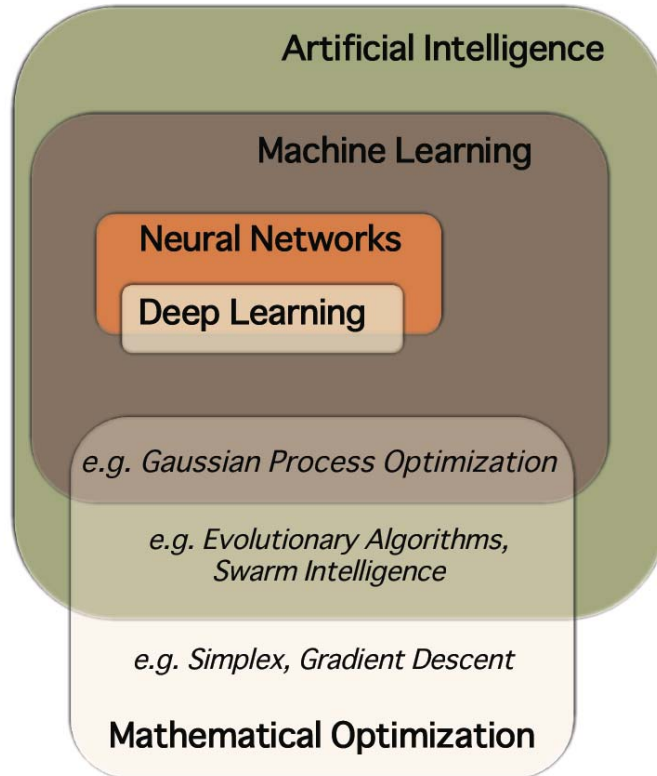


Figure 7.1: Correlation between artificial intelligence, machine learning, neural networks and mathematical optimization (multi-objective optimization) [125].

bines the theoretical and experimental approach. The input (i.e. a parameter set for the accelerator) is handed to the model as well as to the accelerator that starts the operation. The results of both processes are compared. The neural network acquires the consistencies and deviations in the beam parameters and it receives additional information about the system under investigation. Machine learning enables an internal optimization that varies the model and the accelerator settings in accordance with the gained information of the neural network [125].

The procedure of machine learning can be implemented in a new accelerator operation strategy illustrated in Fig. 7.3. The internal optimizer provides an input to the model that was adjusted to the real accelerator performance by machine learning. In a following step, the output of the model is compared to defined criteria. If all criteria are met, the optimizer input is used for the accelerator operation, as well. The obtained measurements from the accelerator are used as a feedback to further improve the model. In the case that the output of the model does not fulfill the

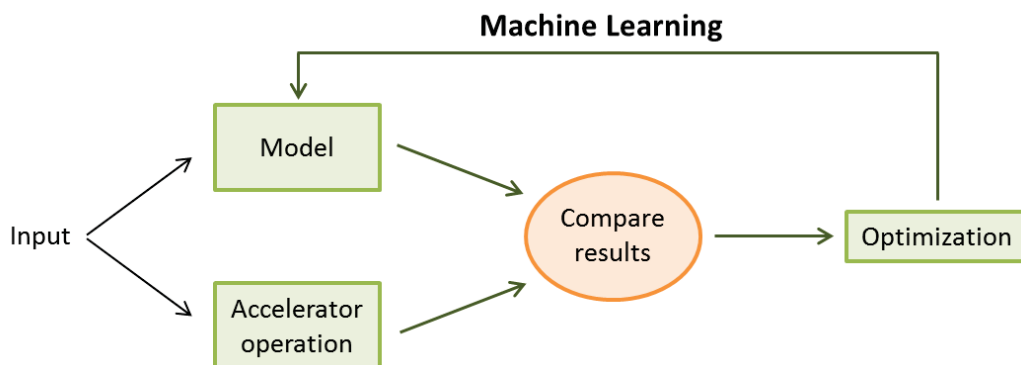


Figure 7.2: The machine learning procedure in an accelerator physics context.

requirements, the system is further optimized until all criteria can be achieved and the accelerator starts its operation.

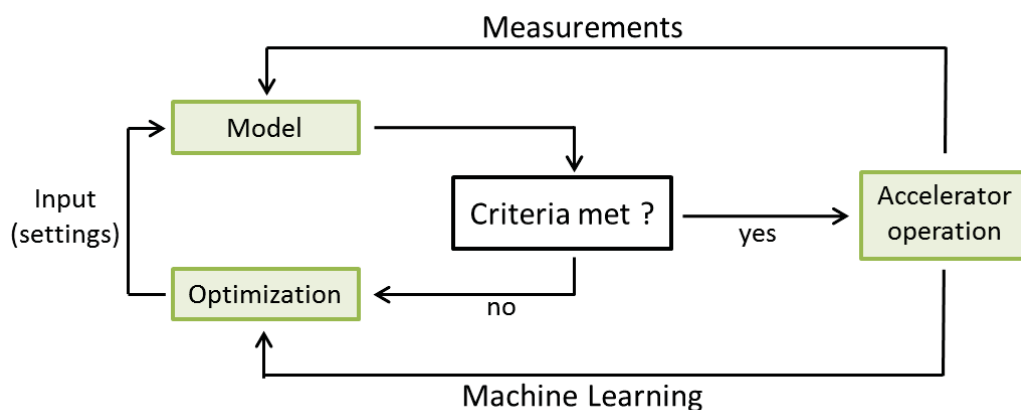


Figure 7.3: New optimization strategy for an accelerator based on artificial intelligence and machine learning.

The procedure of neural-networked-based machine learning allows the specification of set values (operation and design parameter settings) that are gained by the self-identified prediction of beam dynamics. Furthermore, accelerator optimization and online modeling as well as data analysis can be performed [126, 125].

A first approach, comparable to the outline of this dissertation, is the prediction of the transverse normalized emittance which is achieved for the photocathode RF injector of the FAST facility at FERMILAB [125]. The neural network tool evaluates suitable gun parameter settings based on the laser spot size. This work is motivated by the asymmetry in the initial laser distribution on the photocathode and its abil-

## 7. Summary and Outlook

---

ity to cause an emittance asymmetry and downstream an emittance growth in the photoinjector. The gun phase and solenoid fields are then tuned for compensation. The neural network model uses measurement data, such as the gun phase, the solenoid field, and an online image of the current laser spot profile as input values. The output values of the neural network procedure include the average beam energy, the predicted transverse normalized emittance, as well as beta and alpha function values depending on the gun phase and the solenoid field. The results are shown in Fig. 7.4 for 0 deg RF phase presenting a good evidence to former simulation results obtained with the tracking code PARMELA. Afterwards, the machine learning function calculates the minimum emittance and the corresponding gun settings, and trains the neural network.

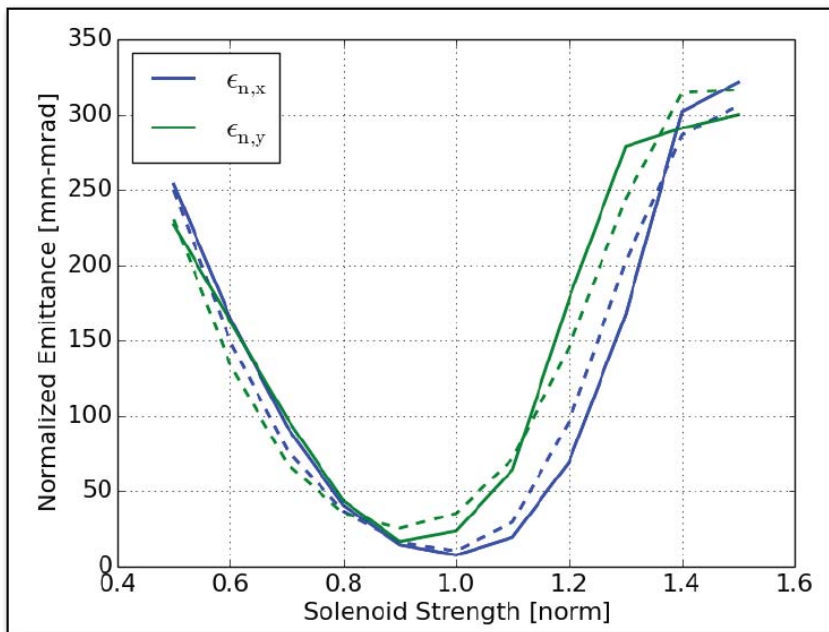


Figure 7.4: Predictions of the transverse normalized emittance depending on the solenoid field focusing for the RF injector of the FAST facility at FERMILAB [127]. The dashed lines are predictions from a neural network while the solid lines are achieved by simulations with the 2D particle simulation program PARMELA [128, 125].

Machine learning and neural networks have the potential to push the optimization and operation of the future high performance accelerators to the next level. Increased computational capability, new network architectures, and improved opti-

mization methods open new perspectives but their complexity requires the expertise and advise of machine learning experts.

The thesis at hand represents a link between single-objective optimization based on particle tracking and a global optimization with neural networks and integrated machine learning procedures. The results are a significant step towards an improved, high brightness SRF photoinjector performance regarding relevant operation and design parameters.



# Appendices

---



# Appendix A

## ASTRA Tracking Procedure

The starting point for the tracking is a particle distribution that is defined by the user or provided by the ASTRA generator. The generator converts an input distribution which represents an incoming photon pulse from a photoemission drive laser into a 3D particle distribution [98]. Therefore, the generator requires parameters like the transverse size, the pulse length, the initial kinetic energy, and the cathode material (metal = Fermi-Dirac distribution, semiconductor = isotropic) as an input. Furthermore, to receive a realistic tracking result, the type of simulated particles and the bunch charge must be defined. Possible particle types for the tracking are electrons, positrons, protons and hydrogen ions. The whole bunch charge is divided in a user-defined number of point-like macroparticles with the same sub-charges.

After generating a starting particle distribution, the ASTRA program tracks the particles under the influence of external and internal fields including 2D or 3D space charge calculations. ASTRA bases its tracking process on the programming language “Fortran 90”. The 3D tracking itself uses a Runge-Kutta integration of the fourth order with fixed, user-defined time steps [98]. The simulation of the emission process is the first step of the tracking process. The transverse distribution of the drive laser or the given input file defines the initial bunch distribution. The laser pulse length that was set in the user input of the generator is converted into the *rms* value of the emission time. According to the finite timing spread of the initial particle distribution, the space charge field rises continuously during the emission process. ASTRA performs a complete recalculation of the space charge field after each user-defined time step. This calculation is a time-consuming procedure. Additionally, the field of the mirror charge of the bunch is taken into account when the bunch is emitted from the cathode and is added to the bunch field.

After each particle has been emitted, the beam is tracked through all elements in the beam path, i.e., cavities, solenoids, quadrupoles, dipoles, and apertures set in a Cartesian coordinate system. ASTRA takes their position in the 3D space and, in the case of a cavity or a solenoid, takes the field strength and the field map as input values [98]. In a last step, ASTRA provides the phase space distribution as well as the transverse and longitudinal projected emittance, bunch length, kinetic energy, and further bunch parameters as outputs after each time step and at the user-defined stopping position of the simulation.

ASTRA offers a 2D cylindrical grid and a 3D algorithm for space charge calculations, respectively, tracking the process from the emission to the stopping position [98]. The space charge algorithm in the presented optimization is restricted to a cylindrical grid, since the 3D algorithm does not implement features to simulate the emission of particles from a cathode - one of the most essential steps in a photoinjector. Further, 3D calculations use much more grid cells. These calculations require a large number of macro-particles to achieve a sufficient number of particles in each grid cell and thereby to avoid statistical problems. Using a cylindrical grid, the bunch is divided in a user-defined number of radial rings and longitudinal slices. The number of grid cells and the number of macro-particles must be adjusted. A constant charge density inside the rings is assumed. Outside the grid, the charge decreases in a  $1/r$  extrapolation. The space charge is integrated into the tracking code assuming the space charge field to be an external field in the Runge-Kutta integration. Since calculating the space charge field for all grid cells at each Runge-Kutta time step takes too much time, the field and the grid size scale with beam parameters, such as the beam size, the beam energy, etc. ASTRA does not run a recalculation of the space charge field until the scaling factor of the field exceeds a user-defined limit.

# Appendix B

## Settings and Numerical Studies for the Developed Multi-Objective Optimization Program

### B.1 Settings for the ASTRA Simulations

The goal of the ASTRA simulation in the optimization process is always to bring the particle tracking through the SRF photoinjector and a subsequent booster section as close to reality as possible. Only then, a reliable prediction of the expected beam properties at selected points along the beamline can be made. A successful optimization strongly depends on the chosen settings in ASTRA [98]. A decisive parameter is the number of macroparticles  $N_{\text{part}}$  which determines the start distribution and the space charge calculation, especially in the non-relativistic part of the accelerator starting at the photocathode. In addition, the parameters of the space charge grid that define the number of grid cells used to calculate the sc force for each cell, play an important role. As mentioned in chapter 5.1, a cylindrical grid is chosen dividing the beam into  $N_{\text{rad}}$  equidistant radial and  $N_{\text{long}}$  longitudinal cells [see illustration in Fig. B.1]. The total number of particles is divided into the cells with less particles in the outer grid cells following the transverse and the longitudinal particle distribution. Nevertheless, a sufficient number of macroparticles per grid cell must always be ensured for realistic space charge calculations. The three parameters consequently depend on each other and must be chosen all together.

An appropriate setting for  $N_{\text{part}}$ ,  $N_{\text{rad}}$ ,  $N_{\text{long}}$  is derived from several test runs using the particle tracking program ASTRA. In a first run, the number of particles and sc grid cells of five points on the Pareto-optimum curve (Gunlab design, 77 pC,

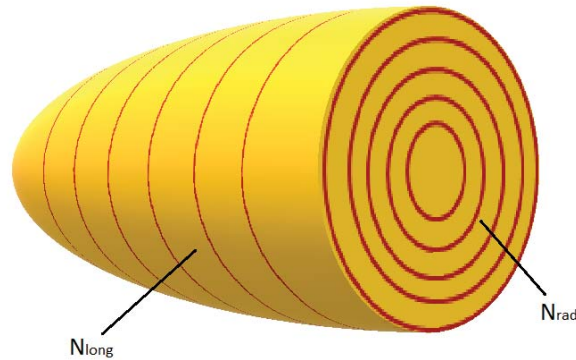


Figure B.1: Illustration of the ASTRA space charge grid.  $N_{rad}$  describes the number of radial grid cells,  $N_{long}$  gives the number of longitudinal sc cells.

30 MV/m cavity peak field on axis) are varied step-wise within a range from 1,000 to 100,000 macroparticles, 10 to 70 radial grid cells and 10 to 70 longitudinal sc slices. Separate ASTRA runs calculate the corresponding transverse emittance and bunch length values for the different start settings. In a first result, it can be determined that the transverse emittance is only affected by the number of macroparticles and the parameter  $N_{rad}$  while the bunch length in the longitudinal plane is influenced by the number of longitudinal grid cells  $N_{long}$ . As a consequence, the transverse and longitudinal plane are assumed to be uncorrelated and can be analyzed separately. Furthermore, the upper limit for the two grid cell parameters is restricted to 50, since no further modification in the beam parameter values can be observed.

For a detailed analysis, the transverse emittance is calculated for one point in the compromise region of the Pareto-front depending on the number of particles  $N_{part}$  and the radial sc grid number  $N_{rad}$ . The results are presented in Fig. B.2.

In general, a higher number of grid cells allows a more detailed calculation of the space charge forces acting inside the bunch. Hence, the sc emittance contribution can be calculated more precisely. Shown in Fig. B.2, the transverse emittance increases towards higher numbers of radial grid cells. The transverse emittance converges above  $N_{rad}=30$ . For statistical reasons resulting from the fixed number of particles per run and the finite transverse beam size, an enhancement of the radial grid cells does not further improve the sc calculation since an insufficient number of particles per cell occurs. Furthermore, the computational run-time of one ASTRA simulation

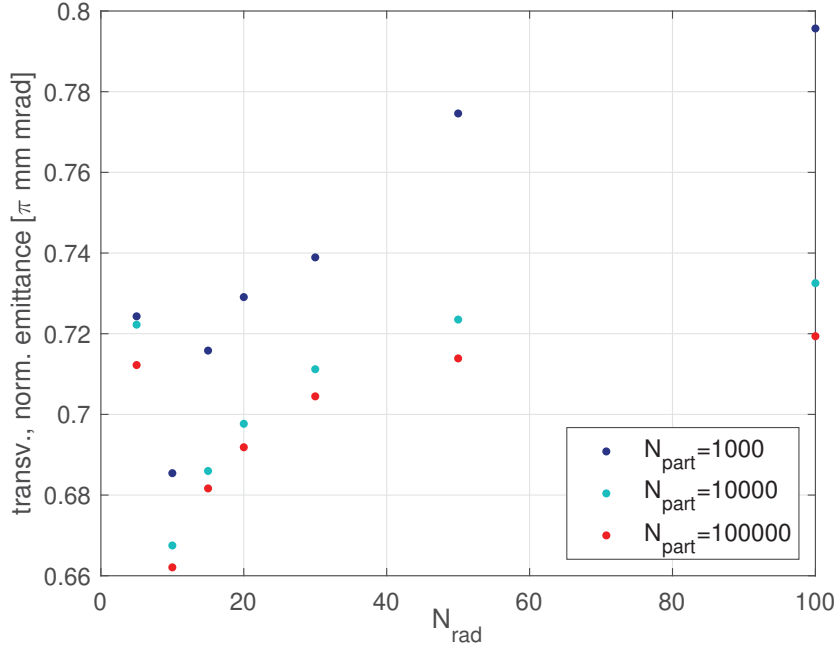


Figure B.2: The dependency of the transverse emittance on the number of radial grid cells  $N_{\text{rad}}$  and the number of macroparticles  $N_{\text{part}}$ .

significantly grows since the calculations for more grid rings take more time. As a consequence, a moderate number of radial grid cells for the sc calculation of  $N_{\text{rad}}=30$ , already in the convergence region, is selected.

In order to satisfy statistical requirements, the particle number must be increased with the number of sc cells simultaneously. Statistical inaccuracies cause the obvious deviation of the emittance values by approximately 4% for a particle number  $N_{\text{part}}=1,000$ . More particles improve the statistics. A convergence towards a higher number of macroparticles can be observed, again. The particle number is restricted to 10,000 as a compromise between an emittance output value recognizing the sc contribution and a controlled, acceptable computational run-time. Fig. B.2 proves that the emittance is then slightly overestimated by 1%. The procedure was repeated for different photoinjector settings in the short bunch length mode, the compromise mode, and the low emittance regime. The results are comparable to the result presented above with an overestimated emittance of around 1%. Still, a space charge grid adjusted to the selected laser pulse volume and the initial bunch distribution allows a constant number of macroparticles per grid cell and would provide a more accurate space charge calculation. Otherwise, such a space charge grid adjustment for each photoinjector setting in the population is time-consuming and required a higher

number of macroparticles for some settings. This would increase the tracking time of ASTRA tremendously, meaning that the new run-time of the optimization procedure must be analyzed. Afterwards, it has to be considered if a more precise space charge calculation through this extension of the optimization procedure justifies the longer optimization run-time.

The same procedure is repeated for the longitudinal number of grid slices  $N_{\text{long}}$ . The impact of  $N_{\text{long}}$  on the calculated bunch length is displayed in Figure B.3.

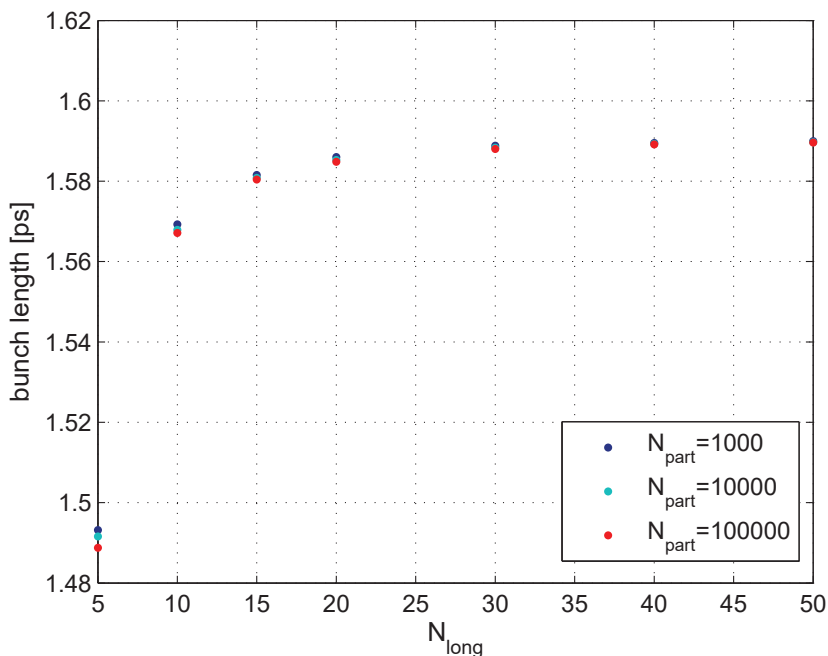


Figure B.3: The dependency of the bunch length on the number of longitudinal grid cells  $N_{\text{long}}$  and the number of macroparticles  $N_{\text{part}}$ .

The number of macroparticles does not impact the calculated bunch length value. If a moderate number of macroparticle  $N_{\text{part}}=10,000$  is selected to save optimization run time, 40 longitudinal grid cells are sufficient. The number is slightly above the radial one. The chosen point in the compromise region already starts in the “cigar”-regime with a relatively long laser pulse length of 5 ps. Such a length requires more grid cells in the  $z$ -direction for a detailed description of the sc effects in the non-relativistic region of the SRF photoinjector.

Additional particle tracking runs with different sc grid and particle number settings are performed for optimized points in the short bunch length region and the small emittance area of the Pareto-optimum curve. The results verify the outcomes described above and confirm the choice for the ASTRA settings of 10,000 macroparticles, 30 radial grid rings and 40 longitudinal grid slices in the space charge calculation.

## B.2 Settings for the Optimization

### B.2.1 Variator probability

Following the MOGA algorithm, the optimization changes the current population of settings by *Mixing* and *Mutation* to create a new pool of solutions in each iteration. The parameter settings that are changed are selected randomly by the function of *Binary Tournament Selection*. It is, overall, possible that one solution is mixed with another one and afterwards it is mutated during one iteration. The probabilities of the *Mixing* and *Mutation* procedure,  $p_{\text{Mix}}$  and  $p_{\text{Mut}}$ , state how many parameter settings of the archive are selected to be mixed and mutated. In the current optimization setup,  $p_{\text{Mix}}$  is set to 0.8 while  $p_{\text{Mut}}$  is equal to 0.2. The *Mixing* process strongly varies the decision variables in the parameter settings, and thus the objective values. As a result, *Mixing* is an important function to cover the whole objective space quickly. Accordingly, the *Mixing* probability must be chosen distinctly above 50%. The *Mutation* function sets small perturbations to the decision variable values that ensure the stability of the parameter settings in the final population. Small deviations in the SRF photoinjector parameters will not cause a significant increase in the objectives. However, a higher probability of *Mutation* in the variator leads to longer run times of the optimization, as only small changes are implemented on the parameter settings, and thus on the objectives. A *Mutation* probability  $p_{\text{Mut}}$  far below 50% is advisable. In the commissioning phase of the optimization tool, different probability values were tested between 50% and 95% for  $p_{\text{Mix}}$ , and 5% up to 50% for  $p_{\text{Mut}}$ . The precise values for  $p_{\text{Mix}}$  and  $p_{\text{Mut}}$  are mostly empirical choosing a compromise between an optimum exploitation of the objective space with stable parameter settings and a tolerable optimization run-time.

While the *Mixing* process plays primary role in the beginning of the optimization procedure in order to spread solutions over the whole objectives space, the *Mutation* allows the relevant fine-tuning of the best settings in the last iterations. However, an adjustment of the variator probabilities during the optimization process is not required. In the first iterations, the fitness value  $F$  [see Equ. (5.3)] is dominated

by the density function that is mainly affected by the *Mixing* process. In the last runs, all settings in the population provide nearly the same density value. Therefore, their dominance expressed in the raw fitness value  $R$  is improved in small steps by the *Mutation* variator and they become more important in the total fitness  $F$ . The selector picks the best settings out of the pool according to the fitness values, and thus weights the impact of the *Mixing* and *Mutation* variator during the iterations.

### **B.2.2 Number of parameter settings per population and resolution of the Pareto-optimum curve**

In the initialization of the optimization the number of different gun parameter settings  $n_{\text{pop}}$  in the population must be defined. This value remains constant over all iterations. The most dominant settings of the last iteration in the archive, together with the new pool of solutions generated by the variator, always compose the total population of each iteration. The number of settings in the population is one of the most important parameters of the optimization as it significantly impacts the optimization run-time. ASTRA calculates the beam parameters along the beam path for each parameter setting in the population. Since the used cluster limits the number of ASTRA runs that can be operated in parallel, a higher number of solutions in the population can expand the required optimization run-time to several weeks. Otherwise, the number of parameter settings defines the resolution of the Pareto-optimum curve. A higher number of different parameter settings allows to determine the shape of the final optimum curve in more detail. This fact is illustrated in Fig. B.4.

The lower limit of  $n_{\text{pop}}$  is empirically set to 50 solutions in order to ensure a minimum covering of the optimum front. Optimization runs with  $n_{\text{pop}}=50$  are useful in the commissioning phase of the optimization tool to receive a first overview about the shape of the curve and the objective range, as well as to detect first trends in the photoinjector settings and beam parameters. For a detailed analysis, up to 200 solutions are required. Then, the Pareto-optimum curve is nearly continuous with a well spread in the transverse emittance and bunch length values inside their limits. The run-time of  $n_{\text{pop}}=500$  settings reaches approximately one month that makes such a high number of settings per population not advisable considering the limited information gain relative to  $n_{\text{pop}}=200$ .



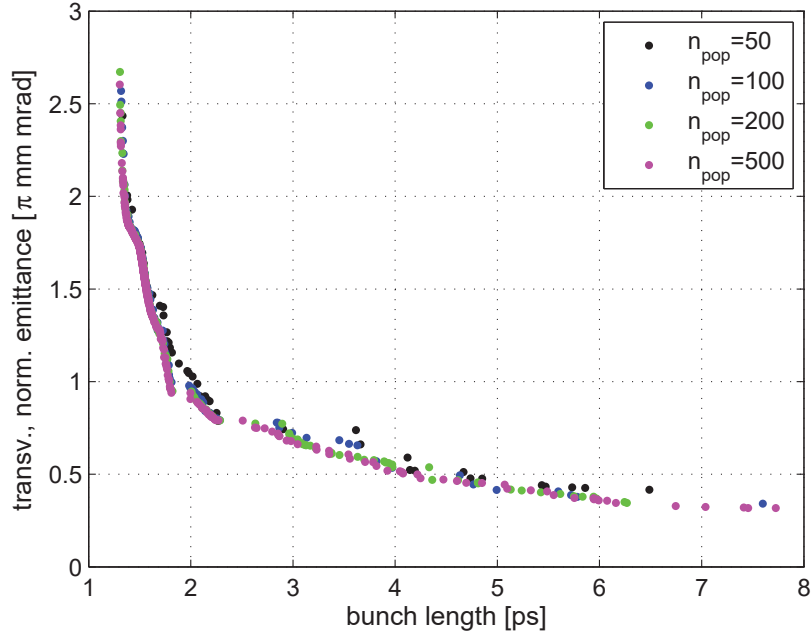


Figure B.4: Dependency of the resolution of the Pareto-optimum curve on the number of Photoinjector settings per population. Population sizes from  $n_{\text{pop}}=50$  to  $n_{\text{pop}}=500$  are plotted.

## B.3 Properties of the Pareto-Optimum Front

### B.3.1 Convergence of the optimum curve

The termination criterion stops the iterative optimization procedure if the raw fitness values of all settings in the current population equals zero, or if a defined maximum number of iterations is reached. Following the first condition, the optimum curve with the corresponding objectives cannot be further improved. Moreover, the front must always converge in the previous iterations towards this final optimum position in the objectives space with only small improvements. The convergence of one Pareto-optimum curve for an SRF photoinjector in an ERL mode with 77 pC bunch charge and 30 MV/m cavity peak field on the axis is displayed in Fig. B.5.

Figure B.5 illustrates that the solutions in the population are optimized fast towards the trade-off shape. Starting in iteration 40, the points on the curve slowly converge into the Pareto-optimum based on small mutations in the parameter settings. In the last 10 iterations, fewer improvements of the front can be observed. The curve of the last iteration represents the expected envelope of the previous ones.

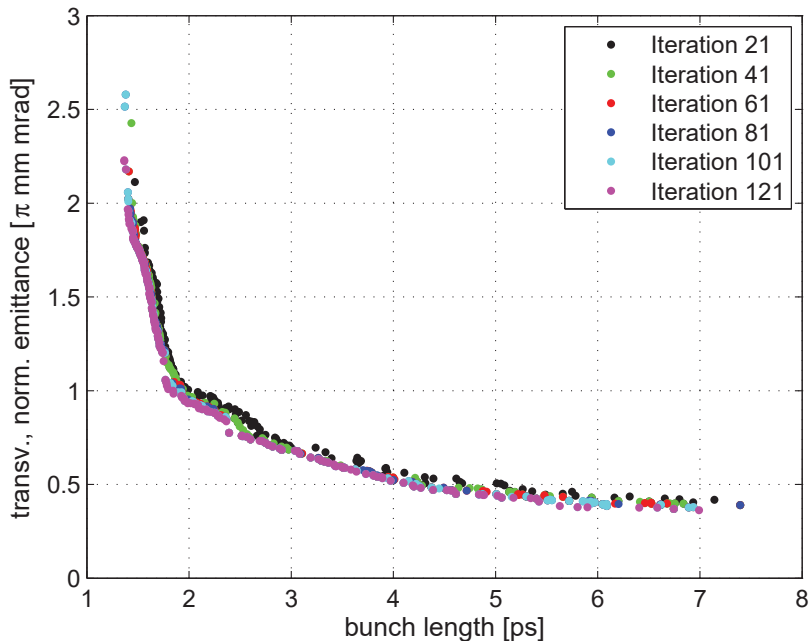


Figure B.5: Convergence of the optimization results towards the Pareto-optimum curve starting in iteration 21 of 121 in total. The last iteration is equal to the envelope of all curves.

### B.3.2 Reproducibility of the Pareto-optimum curve

One requirement for the program is that a repetition of the optimization procedure leads to comparable results regarding the shape and the position of the optimum front in the objective space. Nevertheless, due to the randomly chosen start settings and randomly selected settings for *Mixing* and *Mutation* in the variator, an identical Pareto-optimum with the same parameter settings in the population is impossible in consecutive runs. The random number generator is seeded anew at the beginning of each optimization procedure in relation to the current time by the function “shuffle” [99].

Figure B.6 shows ten optimization runs for a bunch charge of 77 pC and a 30 MV/m acceleration gun gradient. The bunch length values can be reproduced much better than the transverse emittance, most obviously at the short bunch length end of the optimum front. The reason for that is that the bunch length is only affected by the laser pulse length and the gun phase. The longitudinal sc effects plays a minor role since the sc force decreases with  $\gamma^{-3}$  [see Chapter 4.3.4]. Therefore, the lower bunch length limit in the optimum curve is mainly dominated by the optics of the SRF

gun that cannot be further improved for a bunch length focusing at the optimization point of 2.5 m behind the cathode. In comparison, the RF field, the solenoid and the sc effects influence the transverse emittance. The reproducibility is less effective with deviations of up to 20% in the low emittance end of the optimum curve. However, each optimization run works with only 50 solutions per population. It is expected that the deviations decrease with a higher number of parameter settings as the objective space is covered much better. Therefore, an optimization run with 500 solutions is performed, thus containing the same amount of different parameter settings (10 times 50 solutions) as for the reproducibility study. As shown in Figure B.4, the high-resolution Pareto-front represents the envelope of the low parameter set optimization runs.

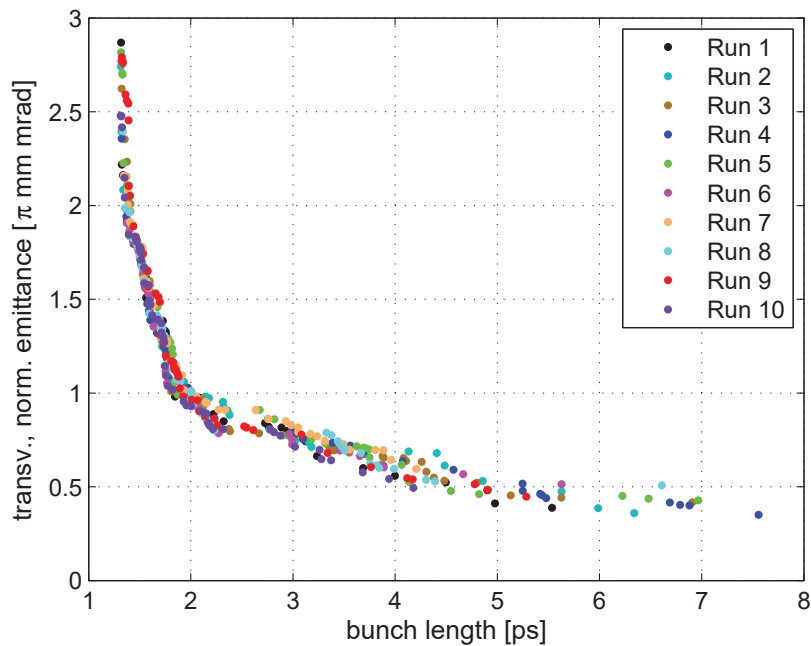


Figure B.6: Reproducibility of the Pareto-optimum curve demonstrated in ten runs with 50 settings per population.

To conclude, the Pareto-optimum is reproducible. The accuracy depends on the number of solutions in the population. More parameter settings allow a more precise evaluation of the optimum curve and the corresponding performance limit of the facility that is optimized. In contrast, the optimization run time increases. A compromise of a moderate population size of 100 to 200 solutions is recommended.

### B.3.3 Error estimations for the transverse emittance and bunch length

As usual for simulations and optimization results, no error bars are displayed in the presented optimum curves in this thesis. The uncertainties of the emittance and bunch length values are, nevertheless, estimated in this section.

Three sources of uncertainties distort the emittance and bunch length simulation values:

- Statistical error of the emittance and bunch length calculation
- Statistical uncertainty due to the ASTRA setting
- Statistical uncertainty due to the number of parameter sets per population

The particle tracking program ASTRA calculates the normalized *rms* emittance value of a beam based on the second moment of the particle distribution of all macroparticles  $N_{\text{part}}$  [98]. The bunch length is defined as the *rms* length of the beam, consisting of the macroparticles, along the  $z$ -axis. Statistical errors of the *rms* emittance and bunch length are then given by  $1/\sqrt{N_{\text{part}}}$ .

The statistical error on the transverse emittance due to the number of macroparticles  $N_{\text{part}}$  can also be detected in Fig. B.2 in section B.1. The uncertainty is estimated by 1% based on the sc grid cell study at  $N_{\text{rad}}=30$  and  $N_{\text{part}}=10,000$ , and thus fulfills the  $1/\sqrt{N_{\text{part}}}$  dependency. The statistical error of the  $N_{\text{part}}$  setting on the *rms* bunch length is far below one per mil and therefore neglected [see Fig. B.3].

Moreover, the setting of the grid for sc calculations lead to a statistic uncertainty of the emittance and bunch length values. As shown in Fig. B.1 and Fig. B.3 in section B.1 the radial and longitudinal number of grid cells impacts the final beam parameters.  $N_{\text{rad}}$ , set to 30 radial rings distorts the transverse emittance by 2%. The statistic uncertainty of the bunch length due to the longitudinal grid number amounts to only one per mil.

Finally, as demonstrated in Fig. B.4 in section B.3.2, the number of photoinjector settings per population  $n_{\text{pop}}$  in the optimization process has a strong impact on the transverse emittance and a moderate impact on the bunch length. At the lower limit of only  $n_{\text{pop}}=50$  settings per population, an uncertainty regarding the transverse

emittance is estimated to 20% while around 5% occur for the bunch length. The uncertainty can be significantly suppressed for higher solution numbers.

To summarize, the contribution of the number of photoinjector settings per population dominates the total error of the transverse emittance and the bunch length in the optimization results.

### B.3.4 Stability of the Pareto-optimum settings

Measurements in the SRF photoinjector verify the optimization results and additionally contribute to an improved model of the electron source. The optimized gun parameter settings can significantly facilitate the commissioning and operation of the high brightness injector. However, the photoinjector elements can only be set with finite precision. Thus, small deviations in the set values of the parameters must not cause severe variations in the objective values, which would indicate island solutions with local minima in the optimum curve. The stability of the optimum parameter sets is one of the most crucial requirements concerning the Pareto-optimum curve. In order to prove the stability of the resulting Pareto-front, the optimum settings are varied in a realistic range corresponding to the parameter accuracy of the current SRF photoinjector at HZB, as summarized in Table B.1. The laser spot size is assumed as stable since it is imaged on the cathode by a fixed aperture.

Table B.1: Accuracy estimations of the photoinjector parameters following the current GunLab design

Parameter	Range	Unit
Laser Spot Size	-	mm ( <i>rms</i> )
Laser Pulse Length	0.02	ps
Cathode Position	0.1	mm
Injection Phase	0.03	deg
Cavity Peak Field	$10^{-4}$ · peak field	MV/m
Solenoid Position	10	$\mu\text{m}$
Solenoid Field	0.1	mT

The ASTRA tracking was repeated for a 77 pC bunch for 200 Pareto-optimum parameter sets randomly varied based on the parameter ranges displayed in Table B.1. The original Pareto-optimum curve for a 77 pC bunch charge beam accelerated with a 30 MV/m cavity gradient together with the verified settings are plotted in Fig. B.7.

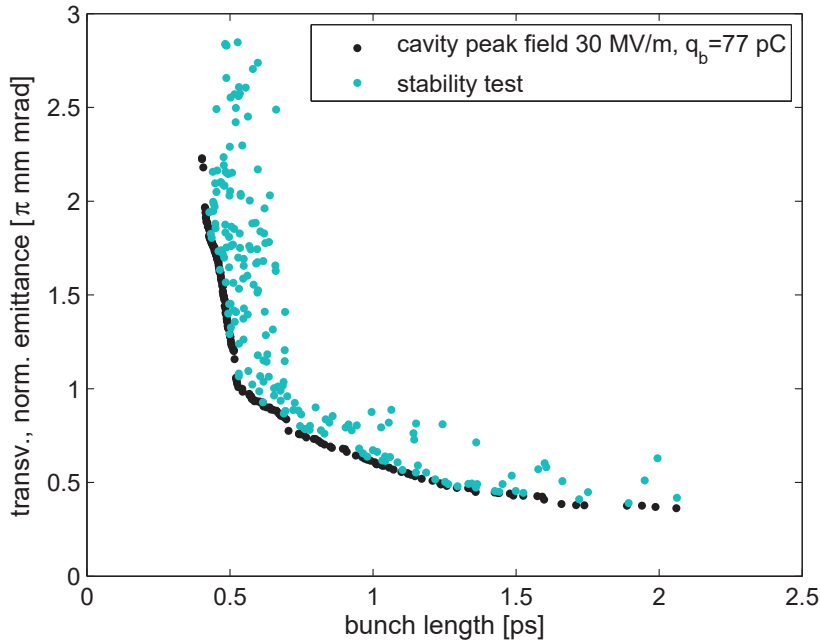


Figure B.7: Stability analysis of the Pareto-optimum curve for a 77 pC bunch charge beam accelerated at 30 MV/m. The blue points represent the optimum photoinjector settings varied by small deviations.

Fig. B.7 confirms that the Pareto-optimum front represents stable settings to run the SRF photoinjector in a high brightness mode. The trade-off curve still does not show tremendous deviations in the transverse emittance and bunch length values. The impact on the settings in the low emittance regime can be mainly traced back to the variation in the cavity peak field and the variation of the cathode position. A deviation towards a smaller gradient in the cavity shifts the Pareto-optimum results towards higher transverse emittance values, as was already discussed in section 6.2.8. A deviation in the cathode retreat causes a different radial focusing electric field component in the cavity and, thus, again higher emittance values. The strongest impact on the electron beam parameters can be observed in short bunch length mode. The emittance and bunch length growths are mainly caused by an interaction of the changes in the RF field (gradient, cathode position), the gun injection phase and the laser pulse length.

Even if most of the Pareto-optimum results still provide a satisfying transverse emittance and bunch length, the photoinjector is, nevertheless, sensitive to variances in the set values. As a consequence, the results confirm the crucial importance of sta-

ble settings in the SRF photoinjector setup and in reliable and precise measurements of the real photoinjector settings. Finally, limiting processes, such as instabilities of the drive laser or the cavity that lead to deviations in the set values must be investigated, eliminated or, if these options are impossible, added to the optimization procedure as a constraint.





# List of Figures

1.1	Beam brightness for different light sources. . . . .	4
2.1	Magnetic lattice of the diffraction limited storage ring of MAX IV. . .	10
2.2	The SASE principle. . . . .	12
2.3	Setup of an energy recovery linac. . . . .	14
2.4	Current and future ERL projects. . . . .	16
2.5	Setup of the ERL test facility bERLinPro. . . . .	17
2.6	Setup of an ultrafast electron diffraction experiment. . . . .	19
3.1	Field potential in the thermionic, photo- and field emission of electrons.	23
3.2	Operation modes of an RF cavity. . . . .	24
3.3	Trend from thermionic injectors to photoinjectors. . . . .	25
3.4	Quality factor measurement in an SRF gun cavity in cw mode. . . . .	27
3.5	Sketch of an SRF photoinjector setup. . . . .	29
3.6	Setup of the GunLab cryomodule at HZB. . . . .	31
3.7	Spectral response measurements of a semiconductor cathode at HZB.	32
3.8	Setup scheme of the current photocathode drive laser at GunLab. . .	33
3.9	Quality factor measurement of the gun cavity in GunLab. . . . .	34
3.10	The GunLab solenoid. . . . .	35
3.11	The GunLab diagnostic beamline. . . . .	36
3.12	Setup of the transverse phase space scanner in GunLab. . . . .	37
3.13	Operation principle of the transverse deflecting cavity (TCav) in GunLab.	38
3.14	Beam position monitor (BPM) in the GunLab diagnostic line. . . . .	40
4.1	Bunch phase space including a reference particle. . . . .	44
4.2	The $1\text{-}\sigma$ -envelope of the transverse projected particle distribution. . .	46
4.3	The slice emittance. . . . .	48
4.4	The photoemission process illustrated based on Spicer's three step model.	52
4.5	Schottky scan. . . . .	53
4.6	$\text{TM}_{01}$ mode in a pillbox shaped cavity. . . . .	57
4.7	The $\text{TM}_{01-\pi}$ mode in an RF cavity. . . . .	58
4.8	Dependency of the kinetic energy of the bunch on the gun phase. . .	61

## LIST OF FIGURES

---

4.9	Radial RF field contribution in a pillbox shaped RF cavity. . . . .	64
4.10	The radial electric field depending on the photocathode position. . . . .	65
4.11	External fields of the RF wave and the solenoid in the photoinjector. . . . .	66
4.12	Field profile of the GunLab solenoid magnet. . . . .	67
4.13	Lorentz contraction of the field lines of a charged particle. . . . .	71
4.14	Space charge limit. . . . .	73
4.15	Emittance contributions from the photoinjector elements. . . . .	75
4.16	“Waterbag” and Gaussian distributed bunches. . . . .	78
4.17	Orientation of the beam slices along the beam path during emittance compensation. . . . .	83
4.18	Divergence as a function of the beam size during the emittance compensation process. . . . .	85
4.19	Evolution of the transverse phase space along the beam axis in the photoinjector. . . . .	86
4.20	Energy chirping. . . . .	88
4.21	Profile of an ECC-RF Gun. . . . .	90
4.22	Evolution of the longitudinal phase space during velocity bunching. . . . .	91
4.23	Bunch compression in a C-shape magnetic chicane. . . . .	93
4.24	Hamiltonians in the $\gamma$ - $\phi$ -phase space. . . . .	95
4.25	Bunch compression by a phase slippage of the bunch in the $\gamma$ - $\phi$ -phase space. . . . .	96
4.26	Bunch compression of a bunch with a finite phase spread. . . . .	97
4.27	Trade-off between the transverse emittance and bunch length. . . . .	98
4.28	The trade-off curve as an envelope of different ISO-brightness curves. . . . .	99
5.1	Overview of photoinjector design and operation parameters. . . . .	102
5.2	Results from one ASTRA tracking. . . . .	104
5.3	Swarm optimization results for GunLab. . . . .	106
5.4	Pareto-optima of a 2D objective space. . . . .	109
5.5	Overview of the basic steps in a MOGA algorithm. . . . .	110
5.6	The NSGA II algorithm. . . . .	113
5.7	The SPEA2 algorithm. . . . .	114
5.8	Illustration of the dominance criterion in the SPEA2 algorithm. . . . .	115
5.9	Initialization of the optimization parameters in SPEA2. . . . .	118
5.10	Objective evaluation in SPEA2. . . . .	120
5.11	Environmental Selection following the SPEA2 algorithm. . . . .	121
5.12	Termination criteria in the SPEA2 algorithm. . . . .	122
5.13	Principles of the variator in the SPEA2 procedure. . . . .	123
6.1	Evolution of the Pareto-optimum front of the current GunLab design. . . . .	127

6.2	Comparison of the results for swarm optimization with the Pareto-optimum front of the GunLab photoinjector. . . . .	128
6.3	Pareto-optimum front of the transverse emittance and bunch length in GunLab (without solenoid correction). . . . .	129
6.4	Evolution of the transv. and long. phase spaces along the beam axis in the compromise region (without solenoid correction). . . . .	130
6.5	Evolution of the transv. and long. phase spaces along the beam axis in the low emittance mode (without solenoid correction). . . . .	133
6.6	Pareto-optimum curve for an optimization with a variable optimization point. . . . .	134
6.7	Beam parameter evolution for the minimum emittance setting with a variable optimization point. . . . .	135
6.8	Evolution of the transv. and long. phase spaces along the beam axis in the short bunch length regime (without solenoid correction). . . . .	136
6.9	Particle tracking through the SRF photoinjector depending on the cathode position. . . . .	138
6.10	Pareto-optimum front of the transverse emittance and bunch length in GunLab (with solenoid correction). . . . .	140
6.11	Comparison of the Pareto-optimum curves without and with solenoid correction. . . . .	141
6.12	Evolution of the transv. and long. phase spaces along the beam axis in the short bunch length regime (with solenoid correction). . . . .	142
6.13	The transverse phase space distribution (short bunch length region). . . . .	144
6.14	The longitudinal phase space distribution (short bunch length region). . . . .	145
6.15	Evolution of the transv. and long. phase spaces along the beam axis in the compromise regime (with solenoid correction). . . . .	146
6.16	The transverse phase space distribution (compromise region). . . . .	147
6.17	The longitudinal phase space distribution (compromise region). . . . .	148
6.18	Evolution of the transv. and long. phase spaces along the beam axis in the low emittance regime (with solenoid correction). . . . .	149
6.19	The transverse phase space distribution (low emittance region). . . . .	151
6.20	The longitudinal phase space distribution (low emittance region). . . . .	152
6.21	Pareto-optimum curve for 7 pC bunch charge (diagnostic mode) and 77 pC bunch charge (high average current mode at bERLinPro). . . . .	154
6.22	Pareto-curves for different gun cavity peak fields. . . . .	155
6.23	Dependency of the Pareto-optimum curve on the photoinjector settings. . . . .	156
6.24	Dependency of the Pareto-optimum curve on the laser settings. . . . .	158
6.25	Laser pulse length and spot size versus the final bunch length for 77 pC. . . . .	159
6.26	Comparison of the Pareto-optimum curve with an optimum setting obtained with a swarm optimizer. . . . .	162

## LIST OF FIGURES

---

6.27	Pareto-optimum settings at 3 m behind the cathode tracked through the current bERLinPro booster set. . . . .	164
6.28	Pareto-optimum front of an SRF photoinjector combined with a three 2-cell booster section. . . . .	166
6.29	Evolution of the transv. and long. phase spaces from the SRF photoinjector through the booster in the low emittance regime. . . . .	168
6.30	Comparison of the Pareto-optimum curves for a 3-cavity and a 5-cavity booster section. . . . .	170
6.31	Injection line of the ERL prototype at the Cornell University. . . . .	171
6.32	Comparison of the Pareto-optimum results for the DC injector at the Cornell University and the SRF photoinjector at HZB. . . . .	171
6.33	Evolution of the emittance and bunch length along the $z$ -axis including five booster cavities. . . . .	172
6.34	The Pareto-optimum curves in the UED mode for three different bunch charges. . . . .	175
6.35	Dependency of the Pareto-optimum curve on the laser spot size in the UED mode. . . . .	177
6.36	Dependency of the optimum result on the laser pulse length in the UED mode. . . . .	178
6.37	Calculated transverse coherence length over bunch length for three different bunch charges. . . . .	179
6.38	Evolution of the transv. and long. phase spaces along the beam axis in the compromise region (UED mode. . . . .	181
6.39	Pareto-optimum curve in the UED mode for a gun gradient of 30 MV/m. 182	
6.40	Pareto-optimum front of the transverse coherence length and the bunch length in the UED mode. . . . .	184
6.41	Field distributions in the gun cavity for eight different field flatness values. . . . .	185
6.42	Pareto-curves for 100% field flatness and for field enhancement in the cavity full-cell. . . . .	186
6.43	Pareto-curves for field enhancement in the cavity half-cell. . . . .	187
6.44	Dependency of the momentum chirp on the gun injection phase and field flatness. . . . .	188
6.45	Cavity peak fields on axis for eight different field flatness values for 2.3 MeV final beam energy. . . . .	189
6.46	SRF photoinjector and ELBE beamline at HZDR. . . . .	190
6.47	Pareto-optimum results for the SRF photoinjector at Helmholtz-Zentrum Dresden-Rossendorf. . . . .	191
7.1	Correlation between artificial intelligence, machine learning, neural networks and mathematical optimization. . . . .	200

---

7.2	Machine learning procedure. . . . .	201
7.3	New optimization strategy for an accelerator. . . . .	201
7.4	Example of the application of a neural network tool for an RF injector. . . . .	202
B.1	Illustration of the ASTRA space charge grid. . . . .	210
B.2	Dependency of the transverse emittance on the number of radial grid cells and the number of macroparticles. . . . .	211
B.3	Dependency of the bunch length on the number of longitudinal grid cells and the number of macroparticles. . . . .	212
B.4	Dependency of the resolution of the Pareto-optimum curve on the number of settings per population. . . . .	215
B.5	Convergence of the optimization results towards the Pareto-optimum curve. . . . .	216
B.6	Reproducibility of the Pareto-optimum curve. . . . .	217
B.7	Stability analysis of the Pareto-optimum curve. . . . .	220

## LIST OF FIGURES

---

# List of Tables

2.1	Main bERLinPro parameters suitable for future X-ray light source applications . . . . .	17
3.1	Electron beam properties for an FEL and a UED application . . . . .	24
5.1	Photoinjector settings and final beam parameters at 2.5 m for an AS-TRA tracking example . . . . .	104
5.2	Limits of the photoinjector parameters resulting from the current GunLab design . . . . .	107
6.1	Stable parameter setting for the bERLinPro injection line determined by swarm optimization and SCO . . . . .	161
6.2	Comparison of two stable parameter settings for the bERLinPro photoinjector as determined by the Pareto-optimization, and swarm and SCO combined optimization . . . . .	162
6.3	Limits of the booster parameters following the current bERLinPro design	166
6.4	Electron beam requirements for driving a UED experiment . . . . .	174
6.5	Stable parameter setting for a 10 fC UED experiment in Gunlab determined by Pareto-optimization. . . . .	180
6.6	Beam parameters at the sample for one selected UED setting . . . . .	180
B.1	Accuracy estimations of the photoinjector parameters following the current GunLab design . . . . .	219





# Abbreviations

ALICE	Accelerators and Lasers in Combined Experiments.
ASTRA	A Space Charge Tracking Algorithm.
bERLinPro	Berlin Energy Recovery Linac.
BESSY II	Synchrotron radiation source at Berliner Elektronenspeicherring-Gesellschaft für Synchrotronstrahlung.
BESSY VSR	Variable pulse-length storage ring project at Berliner Elektronenspeicherring-Gesellschaft für Synchrotronstrahlung.
BNL	Brookhaven National Laboratory.
BPM	Beam Position Monitor.
cBETA	Cornell-BNL ERL Test Accelerator.
cERL	Compact Energy Recovery Linac.
CERN LHC	Large Hadron Collider at European Organization for Nuclear Research.
CsK <sub>2</sub> Sb	Cesium potassium antimonide.
cw	Continuous wave.
DC	Direct current.
DESY PETRA	Positron-Elektron-Tandem-Ring-Anlage at Deutsches Elektronen Synchrotron Hamburg.
DESY REGAE	Relativistic Electron Gun for Atomic Exploration at Deutsches Elektronen Synchrotron Hamburg.
ECC	Energy chirping cell.
ELBE	Electron Linac for Beams with High Brilliance and Low Emittance.
eRHIC	Electrons at Relativistic Heavy Ion Collider.
ERL	Energy Recovery Linac.
EUV	Extreme ultraviolet.
FAST	Fermilab Accelerator Science and Technology.
FEL	Free Electron Laser.
FELBE	Free Electron Laser at the ELBE Facility.
Fermilab	Fermi National Accelerator Laboratory.
FF	Field Flatness.
GSI	Gesellschaft für Schwerionenforschung.
GunLab	Gun Laboratory at Helmholtz-Zentrum Berlin.

HOM	Higher order mode.
HZB	Helmholtz-Zentrum Berlin.
HZDR	Helmholtz-Zentrum Dresden-Rossendorf.
INP	Institute of Nuclear Physics in Novosibirsk.
IR	Infrared.
JAERI	Japan Atomic Energy Research Institute.
KEK	High Energy Accelerator Research Organization in Japan.
LCLS	Linac Coherent Light Source.
LHeC	Large Hadron-Electron Collider at CERN.
linac	Linear accelerator.
MAX IV	Synchrotron storage ring at Lund, Sweden.
MESA	Mainz Energy-Recovering Superconducting Accelerator.
MOGA	Multi-objective generic algorithm.
MTE	Mean transverse energy.
NSGA II	Non-Dominated Sorting Genetic Algorithm.
PARMELA	Phase And Radial Motion in Electron Linear Accelerators (Tracking Code).
QE	Quantum efficiency.
R & D	Research & Development.
RF	Radio frequency.
RHIC	Relativistic Heavy Ion Collider.
rms	Root mean square.
SASE	Self-Amplified Spontaneous Emission.
sc	Space charge.
SCA/FEL	Stanford Superconducting Accelerator/Free Electron Laser.
SCO	Space Charge Optimizer.
SPEA2	Strength Pareto Evolutionary Algorithm.
SRF	Superconducting radio frequency.
TELBE	High-Field High-Repetition-Rate Terahertz Facility at ELBE.
TESLA	TeV-Energy Superconducting Linear Accelerator.
TCAV	Transverse Deflecting Cavity.
UED	Ultrafast Electron Diffraction.
UV	Ultraviolet.
XFEL	European X-Ray Free-Electron Laser.
YAG	Yttrium Aluminium Garnet.
Yb:YAG	Ytterbium Doped Yttrium Aluminium Garnet Laser Crystal.
4GLS	Fourth Generation Light Source.

# Symbols

$A$	Aspect ratio.
$B$	Brightness.
$\vec{B}$	Magnetic field.
$c$	Speed of light.
$D$	Density function.
$\Delta E$	Bunch energy spread.
$\vec{E}$	Electric field.
$E_{\text{acc}}$	Energy gain due to acceleration.
$E_{\text{excess}}$	Electron excess energy.
$E_{\text{laser}}$	Laser pulse energy.
$e$	Elementary electron charge.
$e^-$	Electron.
$E_{\text{kin}}$	Kinetic energy.
$E_0$	Electric peak field on axis.
$\vec{F}_{\text{Lorentz}}$	Lorentz force.
$F$	Fitness value.
$f_{\text{rep}}$	Repetition rate.
$h$	Planck's constant.
$\hbar$	Planck's constant/ $2\pi$ .
$I$	Beam current.
$I_{\text{avg}}$	Average current.
$I_{\text{peak}}$	Peak current.
$it$	Iteration.
$J$	Bessel function.
$K$	Solenoid focusing strength.
$k$	Wave number.
$L_{\text{eff}}$	Effective solenoid length.
$MaxIt$	Maximum number of iterations.
$m$	Electron mass.
$N_e$	Number of electrons.
$N_{\text{long}}$	Number of longitudinal space charge grid cells.
$N_{\text{part}}$	Number of macroparticles.
$N_{\text{ph}}$	Number of photons.
$N_{\text{rad}}$	Number of radial space charge grid cells.
$n_{\text{Archive}}$	Archive size.
$n_{\text{Pop}}$	Population size.

$P_{\text{avg}}$	Laser average power.
$p_{\text{Mix}}$	Probability of mixing.
$p_{\text{Mut}}$	Probability of mutation.
$p_x$	horizontal momentum.
$p_y$	vertical momentum.
$p_z$	longitudinal momentum.
$pop$	Population.
$popc$	Population generated by mixing.
$popm$	Population generated by mutation.
$\Delta p_z$	Momentum difference to the reference particle.
$p_\phi$	Azimuthal momentum.
$Q$	Quality factor.
$q_b$	Bunch charge.
$R$	Raw fitness.
$R_{56}$	Transfer matrix element.
$r$	Radius.
$t$	time.
$V_0$	Accelerating peak voltage.
$\vec{v}$	Velocity.
$z_{\text{stop}}$	Stopping point of the particle tracking in optimization procedure.
$\alpha$	RF field strength.
$\beta$	Ratio of the velocity $v$ to the speed of light.
$\epsilon_{n,\text{chrom}}$	Emittance contribution from chromatic aberration (solenoid).
$\epsilon_{\text{in},x}$	transverse intrinsic emittance.
$\epsilon_{\text{norm.}}$	Normalized emittance.
$\epsilon_{\text{rf},x}$	RF emittance contribution.
$\epsilon_{\text{tot}}$	Total emittance.
$\epsilon_x^{sc}$	Space charge emittance contribution.
$\epsilon_{x,y}$	Transverse emittance.
$\epsilon_{\text{slice}}$	Slice emittance.
$\epsilon_{n,\text{spheric}}$	Emittance contribution from spheric aberration (solenoid).
$\epsilon_z$	Longitudinal emittance.
$\gamma$	Lorentz factor.
$\sigma_{\text{laser},x}$	Transverse laser spot size.
$\sigma_{\text{laser},t}$	Laser pulse length.
$\sigma_{\text{eq}}$	Equilibrium beam size.
$\sigma_{x,y}$	transverse rms beam size.
$\sigma_{x'}$	rms divergence.
$\sigma_z$	Bunch length.
$\phi$	RF phase.
$\phi_{\text{eff}}$	Effective work function.
$\zeta$	longitudinal particle position relative to the reference particle.
$\delta\zeta$	Slice thickness.
$\kappa_{\text{sc}}$	Generalized perveance.
$\omega$	Angular frequency.

# Bibliography

- [1] A. Jankowiak et al. *Technical Design Study BESSY VSR*. Tech. rep. Berlin, Germany: Helmholtz-Zentrum Berlin für Materialien und Energie GmbH, 2015. DOI: 10.5442/R0001.
- [2] D. P. Barber et al. “Discovery of Three-Jet Events and a Test of Quantum Chromodynamics at PETRA”. In: *Physical Review Letters* 43.12 (1979), pp. 830–833. DOI: 10.1103/PhysRevLett.43.830.
- [3] S. Chatrchyan et al. “Observation of a New Boson at a Mass of 125 GeV with the CMS Experiment at the LHC”. In: *Physics Letters Section B* 716.1 (2012), pp. 30–61. DOI: 10.1016/j.physletb.2012.08.021.
- [4] G. Aad et al. “Observation of a New Particle in the Search for the Standard Model Higgs Boson with the ATLAS Detector at the LHC”. In: *Physics Letters Section B* 716.1 (2012), pp. 1–29. DOI: 10.1016/j.physletb.2012.08.020.
- [5] A. Denker et al. “Eye Tumour Therapy in Berlin”. In: *Proceedings of IPAC’10*. Kyoto, Japan, 2010, pp. 64–66. ISBN: 9-789-29083-352-9.
- [6] M. Hachmann and K. Floettmann. “Measurement of Ultra Low Transverse Emittance at REGAE”. In: *Nuclear Instruments and Methods in Physics Research Section A* 829 (2016), pp. 318–320. DOI: 10.1016/j.nima.2016.01.065.
- [7] *Photon Source BESSY II*. (accessed August 1, 2018). URL: [https://www.helmholtz-berlin.de/quellen/bessy/index\\_en.html](https://www.helmholtz-berlin.de/quellen/bessy/index_en.html).
- [8] B. Kuske, N. Paulick, A. Jankowiak, and J. Knobloch. *Conceptual Design Report BERLinPro*. Tech. rep. Berlin, Germany: Helmholtz-Zentrum Berlin für Materialien und Energie GmbH, 2012.
- [9] C. Pellegrini and J. Stöhr. “X-Ray Free Electron Lasers: Principles, Properties and Applications”. In: *Nuclear Instruments and Methods in Physics Research Section A* 500.1 (2003), pp. 33–40. DOI: 10.1016/S0168-9002(03)00739-3.
- [10] K. Wille. *Physik der Teilchenbeschleuniger und Synchrotronstrahlungsquellen*. Stuttgart, Germany: Teubner Verlag, 1996. ISBN: 3-519-13087-4.
- [11] M. Reiser. *Theory and Design of Charged Particle Beams*. Weinheim, Germany: WILEY-VHC, 2008. ISBN: 9-783-52740-741-5.

- [12] D. Einfeld, J. Schaper, and M. Plesko. “Design of a Diffraction Limited Light Source (DIFL)”. In: *Proceedings of the Particle Accelerator Conference 1995*. Vol. 1. Dallas, Texas, USA, 1995, pp. 177–179. DOI: 10.1109/PAC.1995.504602.
- [13] A. Balerna. “Atoms, X-Rays and Synchrotron Radiation”. In: *International School of Modern Physics and Research 2017*. 2017, p. 33.
- [14] P. F. Tavares et al. “The MAX IV Storage Ring Project”. In: *Journal of Synchrotron Radiation* 21.5 (2014), pp. 862–877. DOI: 10.1107/S1600577514011503.
- [15] A. Wolsky. “Low Emittance Machines Part 1 & 2”. In: *Advanced Accelerator Physics Course, CERN Accelerator School*. Trondheim, Norway, 2013, pp. 245–294. DOI: doi:10.5170/CERN-2014-009.331.
- [16] MAX IV. (accessed August 1, 2018). URL: <https://www.maxiv.lu.se/>.
- [17] *The Evolution of Synchrotron Light Sources*. (accessed August 1, 2018). URL: [https://www.helmholtz-berlin.de/projects/berlinpro/erl-intro/index\\_en.html](https://www.helmholtz-berlin.de/projects/berlinpro/erl-intro/index_en.html).
- [18] J. M. J. Madey. “Stimulated Emission of Bremsstrahlung in a Periodic Magnetic Field”. In: *Journal of Applied Physics* 42.5 (1971), pp. 1906–1913. DOI: 10.1063/1.1660466.
- [19] C. Pellegrini. “The History of X-Ray Free-Electron Lasers”. In: *The European Physical Journal H* 37.5 (2012), 659–708. DOI: 10.1140/epjh/e2012-20064-5.
- [20] *High Gain FELs - The SASE Principle*. (accessed August 1, 2018). URL: <http://www.desy.de/~khan/lehre/beschleuniger-ss06/folien/>.
- [21] K. J. Kim, Y. Shvyd’ko, and S. Reiche. “A Proposal for an X-Ray Free-Electron Laser Oscillator with an Energy-Recovery Linac”. In: *Physical Review Letters* 100 (24 2008), pp. 1–4. DOI: 10.1103/PhysRevLett.100.244802.
- [22] W. Decking et al. “Commissioning of the European XFEL Accelerator”. In: *Proceedings of IPAC’17*. Copenhagen, Denmark, 2017, pp. 1–6. ISBN: 9-783-95450-182-3.
- [23] *European XFEL*. (accessed August 1, 2018). URL: <https://www.xfel.eu/>.
- [24] N. Nakamura et al. “Design Work of the ERL-FEL as the High Intense EUV Light Source”. In: *Proceedings of ERL2015*. Stony Brook, New York, USA, 2015, pp. 4–9. ISBN: 978-3-95450-183-0.
- [25] M. Tigner. “A Possible Apparatus for Electron Clashing-Beam Experiments”. In: *Nuovo Cimento* 37 (1965), pp. 1228–1231. DOI: 10.1007/BF02773204.
- [26] T. I. Smith et al. “Development of the SCA/FEL for Use in Biomedical and Materials Science Experiments”. In: *Nuclear Instruments and Methods in Physics Research Section A* 259.1 (1987), pp. 1–7. DOI: 10.1016/0168-9002(87)90421-9.

- [27] D. Proch. “Superconducting Cavities for Accelerators”. In: *Reports on Progress in Physics* 61.5 (1998), p. 441. URL: <http://stacks.iop.org/0034-4885/61/i=5/a=001>.
- [28] G. R. Neil et al. “The JLab High Power ERL Light Source”. In: *Nuclear Instruments and Methods in Physics Research Section A* 557.1 (2006), pp. 9–15. DOI: 10.1016/j.nima.2005.10.047.
- [29] G. H. Hoffstaetter et al. “cBETA, the 4-Turn ERL with SRF and Single Return Loop”. In: *Proceedings of IPAC2018*. Vancouver, British Columbia, Canada, 2018, pp. 635–639. ISBN: 978-3-95450-184-7.
- [30] E. C. Aschenauer et al. *eRHIC Design Study: An Electron-Ion Collider at BNL*. Tech. rep. Berlin, Germany: Helmholtz-Zentrum Berlin, 2014. URL: <https://arxiv.org/abs/1409.1633>.
- [31] M. Sawamura. “Performance and Upgrade of the JAERI ERL-FEL”. In: *Proceedings of PAC2003*. Portland, Oregon, USA, 2003, pp. 3446–3448. DOI: 10.1109/PAC.2003.1289943.
- [32] S. Sakanaka et al. “The First Beam Recirculation and Beam Tuning in the Compact ERL at KEK”. In: *Proceedings of LINAC2014*. Geneva, Switzerland, 2014, pp. 599–602. ISBN: 978-3-95450-142-7.
- [33] S. L. Smith. “The Status of the Daresbury Energy Recovery Linac Prototype (ERLP)”. In: *Proceedings of ERL2007*. Daresbury, UK, 2007, pp. 6–10. DOI: 10.1109/PAC.2007.4440997.
- [34] J. L. Abelleira Fernandez et al. “A Large Hadron Electron Collider at CERN: Report on the Physics and Design Concepts for Machine and Detector”. In: *Journal of Physics G* 39 (2012), pp. 1–630. DOI: 10.1088/0954-3899/39/7/075001.
- [35] D. Simon et al. “Lattice and Beam Dynamics of the Energy Recovery Mode of the Mainz Energy-Recovering Superconducting Accelerator MESA”. In: *Proceedings of IPAC2015*. Richmond, Virginia, USA, 2015, pp. 220–222. ISBN: 978-3-95450-168-7.
- [36] Antokhin E. A. et al. “First Lasing at the High-Power Free Electron Laser at Siberian Center for Photochemistry Research”. In: *Nuclear Instruments and Methods in Physics Research Section A* 528.1 (2004), pp. 15–18. DOI: 10.1016/j.nima.2004.04.009.
- [37] R. Hajima. “Overview of Energy-Recovery Linacs”. In: *Proceedings of APAC 2007*. Indore, India, 2007, pp. 11–14. URL: <http://accelconf.web.cern.ch/accelconf/a07/INDEX.HTM>.
- [38] M. Abo-Bakr et al. “Status Report of the Berlin Energy Recovery Linac Project bERLinPro”. In: *Proceedings of IPAC’18*. yet published; Pre-Release: <http://ipac2018.vrws.de/html/author.htm>. Vancouver, British Columbia, Canada, 2018, pp. 4127–4130. ISBN: 978-3-95450-184-7.



- [39] L. K. Rudge et al. “Single-Shot Multi-MeV Ultrafast Electron Diffraction on VELA at Daresbury Laboratory”. In: *Proceedings of IPAC2015*. Richmond, Virginia, USA, 2015, pp. 2278–2281. ISBN: 978-3-95450-168-7.
- [40] G. Sciaini and J. R. D. Miller. “Femtosecond Electron Diffraction: Heralding the Era of Atomically Resolved Dynamics”. In: *Reports on Progress in Physics* 74.9 (2011), pp. 1–36. DOI: 10.1088/0034-4885/74/9/096101.
- [41] E. Panofski et al. “Multi-Objective Optimization of an SRF Photoinjector for ERL and UED Application”. In: *Proceedings of IPAC’17*. Copenhagen, Denmark, 2017, pp. 3704–3707. ISBN: 9-783-95450-182-3.
- [42] J. Yang et al. “Femtosecond Electron Guns for Ultrafast Electron Diffraction”. In: *Proceedings of IPAC’12*. New Orleans, Louisiana, USA, 2012, pp. 4170–4174. ISBN: 9-783-95450-115-1.
- [43] E. Chiadroni. *Electron Sources and Injection Systems*. Hamburg, Germany, 2016. URL: <http://cas.web.cern.ch/sites/cas.web.cern.ch/files/lectures/hamburg-2016/chiadroni.pdf>.
- [44] R. H. Fowler and L. Nordheim. “Electron Emission in Intense Electric Fields”. In: *Proceedings of the Royal Society of London A* 119.781 (1928), pp. 173–181. ISSN: 0950-1207. DOI: 10.1098/rspa.1928.0091.
- [45] J. Wueppen. “Emission freier Elektronen aus laserinduzierten Plasmen”. PhD thesis. RWTH Aachen University, 2012. URL: <https://core.ac.uk/display/36448248>.
- [46] R. Triveni and D. H. Dowell, eds. *An Engineering Guide to Photoinjectors*. 2014. URL: <https://arxiv.org/abs/1403.7539>.
- [47] A. Arnold and J. Teichert. “Overview on Superconducting Photoinjectors”. In: *Physical Review Special Topics Accelerators and Beams* 14 (2011), pp. 424–428. DOI: 10.1103/PhysRevSTAB.14.024801.
- [48] J. Kühn et al. “A Cu Photocathode for the Superconducting RF Photoinjector of bERLinPro”. In: *Proceedings of IPAC’18*. Vancouver, British Columbia, Canada, 2018, pp. 1247–1250. ISBN: 978-3-95450-184-7.
- [49] J. N. Galayda. “The Linac Coherent Light Source-II Project”. In: *Proceedings of IPAC’14*. Dresden, Germany, 2014, pp. 935–937. ISBN: 9-783-95450-132-8.
- [50] P. G. O’Shea. “High-Brightness RF Photocathode Guns for Single Pass X-Ray Free-Electron Lasers”. In: *Nuclear Instruments and Methods in Physics Research Section A* 358.1 (1995), pp. 36–39. DOI: 10.1016/0168-9002(94)01501-5.
- [51] X. Jin et al. “Highly Spin-Polarized Electron Photocathode Based on GaAs–GaAsP Superlattice Grown on Mosaic-Structured Buffer Layer”. In: *Journal of Crystal Growth* 310.23 (2008), pp. 5039–5043. DOI: 10.1016/j.jcrysgro.2008.07.001.



- [52] H. Chaloupka et al. “A Proposed Superconducting Photoemission Source of High Brightness”. In: *Nuclear Instruments and Methods in Physics Research Section A* 285.1 (1989), pp. 327–332. DOI: 10.1016/0168-9002(89)90474-9.
- [53] D. Kostin et al. ““SRF Gun Cavity R&D at DESY””. In: *Proceedings of SRF2015*. Whistler, BC, Canada, 2015, pp. 1231–1234. ISBN: 9-783-95450-178-6.
- [54] H. Padamsee, J. Knobloch, and T. Hays. *RF Superconductivity for Accelerators*. Ithaca, New York, USA: Wiley-VHC, 2008. ISBN: 0-471-15432-6.
- [55] D. Proch. “The TESLA Cavity: Design Considerations and RF Properties”. In: *Proceedings of the Sixth Workshop on RF Superconductivity*. Virginia, USA, 1993, pp. 382–397.
- [56] A. Neumann. “Photoinjector SRF Cavity Development for BERLinPro”. In: *Proceedings of LINAC2012*. Tel-Aviv, Israel, 2012, pp. 993–995. ISBN: 978-3-95450-122-9.
- [57] R. Brinkmann et al. *TESLA Technical Design Report*. Tech. rep. Deutsches Elektronen Synchrotron Hamburg, 2001. URL: [http://tesla.desy.de/new/\\_pages/TDR\\_CD/PartII/](http://tesla.desy.de/new/_pages/TDR_CD/PartII/).
- [58] W. Meissner and R. Ochsenfeld. “Ein neuer Effekt bei Eintritt der Supraleitfähigkeit”. In: *Die Naturwissenschaften* 21 (1933), pp. 787–788. DOI: 10.1007/BF01504252.
- [59] J. Völker et al. “Introducing GunLab - A Compact Test Facility for SRF Photoinjectors”. In: *Proceedings of IPAC’14*. Dresden, Germany, 2014, pp. 630–632. ISBN: 978-3-95450-132-8.
- [60] A. Neumann et al. “Towards a 100 mA Superconducting RF Photoinjector for BERLinPro”. In: *Proceedings of SRF2013*. Paris, France, 2013, pp. 42–49. ISBN: 978-3-95450-143-4.
- [61] A. Neumann et al. “The bERLinPro SRF Photoinjector System - From First RF Commissioning to First Beam”. In: *Proceedings of IPAC’18*. Vancouver, British Columbia, Canada, 2018, pp. 1660–1663. ISBN: 978-3-95450-184-7.
- [62] J. Völker. “Development of a Compact Test Facility for SRF Photoelectron Injectors”. PhD thesis. Berlin, Germany: Humboldt-Universität zu Berlin and Helmholtz-Zentrum Berlin, 2018. DOI: 10.18452/19322. URL: <http://edoc.hu-berlin.de/18452/20083>.
- [63] T. Kamps et al. “Status and Perspectives of Superconducting Radio-Frequency Gun Development for BERLinPro”. In: *Journal of Physics: Conference Series* 298.1 (2011), pp. 1–5.
- [64] M. A. H. Schmeisser et al. “CsK<sub>2</sub>Sb Photocathode Development for bERLinPro”. In: *Proceedings of ERL2015*. Stony Brook, New York, USA, 2015, pp. 97–99. ISBN: 978-3-95450-183-0.

- [65] L. Cultrera, H. Lee, and I. Bazarov. “Alkali Antimonides Photocathodes Growth Using Pure Metals Evaporation from Effusion Cells”. In: *Journal of Vacuum Science & Technology B* 34.1 (2016), pp. 1–6. DOI: 10.1116/1.4936845.
- [66] *Annual Report 2010*. Tech. rep. Berlin, Germany: Max-Born Institut, 2010. URL: [http://www.mbi-berlin.de/de/research/annuals/2010/annual\\_report\\_2010.pdf](http://www.mbi-berlin.de/de/research/annuals/2010/annual_report_2010.pdf).
- [67] G. Kourkafas et al. “Solenoid Alignment for the SRF Photoinjector of bERLin-Pro at HZB”. In: *Proceedings of IPAC’17*. Copenhagen, Denmark, 2017, pp. 1778–1780. ISBN: 978-3-95450-182-3.
- [68] W. K. H. Panofsky and W. A. Wenzel. “Some Considerations Concerning the Transverse Deflection of Charged Particles in Radio-Frequency Fields”. In: *Review of Scientific Instruments* 27.11 (1956), pp. 967–967. DOI: 10.1063/1.1715427.
- [69] I. Y. Vladimirov et al. “Spectrometer for SRF Gun”. In: *Proceedings of IPAC’14*. Dresden, Germany, 2014, pp. 3608–3610. ISBN: 978-3-95450-132-8.
- [70] P. Forck, P. Kowina, and D. Liakin. “Beam Position Monitors”. In: *Cern Accelerator School 2009* (2009). URL: [apps.fz-juelich.de/pax/paxwiki/images/2/2c/Cas\\_bpm\\_main.pdf](apps.fz-juelich.de/pax/paxwiki/images/2/2c/Cas_bpm_main.pdf).
- [71] *Beam Based Alignment*. (accessed August 1, 2018). URL: <http://www.desy.de/~sahoo/WebPage/Beam%20Based%20Alignment.htm>.
- [72] H. Wiedemann. *Particle Accelerator Physics*. Heidelberg, Germany: Springer Verlag, 2007. ISBN: 978-3-540-49043-2.
- [73] B. v. Borries and E. Ruska. “Versuche, Rechnung und Ergebnisse zur Frage des Auflösungsvermögens beim Übermikroskops”. In: *Zeitung technische Physik* 20 (1939), pp. 225–235.
- [74] W. Pauli. “Über den Zusammenhang des Abschlusses der Elektronengruppen im Atom mit der Komplexstruktur der Spektren”. In: *Zeitschrift für Physik* 31 (1925), pp. 765–783. DOI: 10.1007/BF02980631.
- [75] W. Heisenberg. “Über den anschaulichen Inhalt der quantentheoretischen Kinematik und Mechanik”. In: *Zeitschrift für Physik* 43 (1927), pp. 172–198. DOI: 10.1007/BF01397280.
- [76] W. E. Spicer. “Photoemissive, Photoconductive, and Optical Absorption Studies of Alkali-Antimony Compounds”. In: *Physical Review* 112 (1958), pp. 114–122. DOI: 10.1103/PhysRev.112.114.
- [77] D. H. Dowell and J. F. Schmerge. “The Quantum Efficiency and Thermal Emittance of Metal Photocathodes”. In: *Physical Review Special Topics Accelerators and Beams* 12 (2009), pp. 1–13. DOI: 10.1103/PhysRevSTAB.12.074201.
- [78] D. H. Dowell and other. “In situ Cleaning of Metal Cathodes Using a Hydrogen Ion Beam”. In: *Physical Review Special Topics Accelerators and Beams* 9 (2006), pp. 1–8. DOI: 10.1103/PhysRevSTAB.9.063502.

- [79] M. A. H. Schmeisser. not published. Master thesis. Berlin, Germany: Humboldt-Universität zu Berlin and Helmholtz-Zentrum Berlin, 2014.
- [80] K. J. Kim. “Rf and Space-Charge Effects in Laser-Driven RF Electron Guns”. In: *Nuclear Instruments and Methods in Physics Research Section A* 275.2 (1989), pp. 201–218. DOI: 10.1016/0168-9002(89)90688-8.
- [81] D. H. Dowell. “The Physics of High-Brightness Sources”. In: *Talk at the SLAC Summer Seminar on Electron and Photon Beams 2015* (2015). URL: <https://conf-slac.stanford.edu/sssepb-2015>.
- [82] A. Neumann et al. “SRF Photoinjector Cavity for bERLinPro”. In: *Proceedings of IPAC 2013*. Shanghai, China, 2013, pp. 285–287. ISBN: 978-3-95450-122-9.
- [83] D. H. Dowell. “Beam Optics and Emittance Growth”. In: *Talk at the USPAS 2007* (2007). URL: [http://uspas.fnal.gov/materials/10MIT/Lecture8\\\_EmittanceGrowth\\\_text.pdf](http://uspas.fnal.gov/materials/10MIT/Lecture8\_EmittanceGrowth\_text.pdf).
- [84] M. Ferrario, M. Migliorati, and L. Palumbo. “Space Charge Effects”. In: *Advanced Accelerator Physics Course, CERN Accelerator School*. Trondheim, Norway, 2013, pp. 331–356. DOI: 10.5170/CERN-2014-009.331.
- [85] D. H. Dowell et al. “Commissioning Results of the LCLS Injector”. In: *Proceedings of FEL 2007*. Novosibirsk, Russia, 2007, pp. 276–283. ISBN: 978-1-61738-416-5.
- [86] P. Musumeci. “High Brightness Beam Science”. In: *Talk at the FEIS (Femtosecond Electron Imaging and Spectroscopy) Workshop* (2013). URL: <http://bt.pa.msu.edu/FEIS2013/talks/musumeci.pdf>.
- [87] M. Khojayan, M. Krasilnikov, and F. Stephan. “Studies on the Application of the 3D Ellipsoidal Cathode Laser Pulses at PITZ”. In: *Proceedings of IPAC’14*. Dresden, Germany, 2014, pp. 2958–2961. ISBN: 978-3-95450-132-8.
- [88] D. Filippetto et al. “Maximum Current Density and Beam Brightness Achievable by Laser-Driven Electron Sources”. In: *Physical Review Special Topics Accelerators and Beams* 17.2 (2014), pp. 1–7. DOI: 10.1103/PhysRevSTAB.17.024201.
- [89] I. V. Bazarov, B. M. Dunham, and C. K. Sinclair. “Maximum Achievable Beam Brightness from Photoinjectors”. In: *Physical Review Letters* 102 (10 2009), pp. 1–4. DOI: 10.1103/PhysRevLett.102.104801.
- [90] L. Serafini and J. B. Rosenzweig. “Envelope Analysis of Intense Relativistic Quasilaminar Beams in RF Photoinjectors: A Theory of Emittance Compensation”. In: *Physical Review E* 55 (6 1997), pp. 7565–7589. DOI: 10.1103/PhysRevE.55.7565.
- [91] K. Flöttmann. “Emittance Compensation in Split Photoinjectors”. In: *Physical Review Special Topics Accelerators and Beams* 20 (2017), pp. 1–14. DOI: 10.1103/PhysRevAccelBeams.20.013401.

- [92] S. Di Mitri. “Bunch Length Compressors”. In: *Talk at the CERN Accelerator School for FELs and ERLs* (2016). URL: <http://cas.web.cern.ch/sites/cas.web.cern.ch/files/lectures/hamburg-2016/dimitri.pdf>.
- [93] K. Sakaue et al. “Ultrashort Electron Bunch Generation by an Energy Chirping Cell Attached RF Gun”. In: *Physical Review Special Topics Accelerators and Beams* 17 (2 2014), pp. 1–9. DOI: 10.1103/PhysRevSTAB.17.023401.
- [94] P. Piot. “State-of-the-Art Electron Bunch Compression”. In: *Proceedings of LINAC 2004*. Lübeck, Germany, 2004, pp. 528–532.
- [95] L. Serafini and M. Ferrario. “Velocity Bunching in Photo-Injectors”. In: *AIP Conference Proceedings* 581.1 (2001), pp. 87–106. DOI: 10.1063/1.1401564.
- [96] S. G. Anderson et al. “Velocity Bunching of High-Brightness Electron Beams”. In: *Physical Review Special Topics Accelerators and Beams* 8.1 (2005), pp. 1–22. DOI: 10.1103/PhysRevSTAB.8.014401.
- [97] K. Flöttmann. *ASTRA, A Space Charge Tracking Algorithm*. 2017. URL: <http://www.desy.de/~mpyflo/>.
- [98] K. Flöttmann. *ASTRA Documentation*. 2017. URL: [http://www.desy.de/~mpyflo/Astra\\_manual/Astra-Manual\\_V3.2.pdf](http://www.desy.de/~mpyflo/Astra_manual/Astra-Manual_V3.2.pdf).
- [99] *MATLAB, Matrix Laboratory*. (accessed August 1, 2018). URL: <https://de.mathworks.com/>.
- [100] R. T. Marler and J. S. Arora. “The Weighted Sum Method for Multi-Objective Optimization: New Insights”. In: *Structural and Multidisciplinary Optimization* 41.6 (2010), pp. 853–862. DOI: 10.1007/s00158-009-0460-7.
- [101] K. Deb. *Multi-Objective Optimisation Using Evolutionary Algorithm: An Introduction*. published in Wang, L., NG, A., Deb, K.: *Multi-Objective Evolutionary Optimisation for Product Design and Manufacturing*. London, Great Britain: Springer Verlag, 2011. ISBN: 978-0-85729-617-7.
- [102] V. Pareto, ed. *Manuale di economia politica con una introduzione alla scienza sociale*. Milano, Italy, 1919.
- [103] I. V. Bazarov and C. K. Sinclair. “Multivariate Optimization of a High Brightness DC Gun Photoinjector”. In: *Physical Review Special Topics Accelerators and Beams* 8 (2005), pp. 1–14. DOI: 10.1103/PhysRevSTAB.8.034202.
- [104] I. Bazarov et al. “Comparison of DC and Superconducting RF Photoemission Guns for High Brightness High Average Current Beam Production”. In: *Physical Review Special Topics Accelerators and Beams* 14 (2011), pp. 1–12. DOI: 10.1103/PhysRevAccelBeams.14.072001.
- [105] L. Yang et al. “Global Optimization of an Accelerator Lattice Using Multiobjective Genetic Algorithms”. In: *Nuclear Instruments and Methods in Physics Research Section A* 609.1 (2009), pp. 50–57. DOI: 10.1016/j.nima.2009.08.027.

- [106] L. Wang et al. “MOGA Optimization Design of LCLS-II Linac Configurations”. In: *Proceedings of FEL 2014*. Basel, Switzerland, 2014, pp. 763–768. ISBN: 978-3-95450-133-5.
- [107] A. Konak, D. W. Coit, and A. E. Smith. “Multi-Objective Optimization Using Genetic Algorithms: A Tutorial”. In: *Reliability Engineering & System Safety* 91.9 (2006), pp. 992–1007. DOI: 10.1016/j.ress.2005.11.018.
- [108] K. Deb et al. “A Fast and Elitist Multiobjective Genetic Algorithm: NSGA-II”. In: *IEEE Transactions on Evolutionary Computation* 6 (2 2002), pp. 182–197. DOI: 0.1109/4235.996017.
- [109] E. Zitzler, M. Laumanns, and L. Thiele. *SPEA2: Improving the Strength Pareto Evolutionary Algorithm*. Tech. rep. Swiss Federal Institute of Technology Zurich, 2001, pp. 1–21.
- [110] R. T. F. Ah King, K. Deb, and H. C. S. Rughooputh. “Comparison of NSGA II and SPEA2 on the Multiobjective Environmental/Economic Dispatch”. In: *University of Mauritius Research Journal* 16 (2010), pp. 485–511.
- [111] M. H. Levitt. *Spin Dynamics: Basics of Nuclear Magnetic Resonance, 2nd Edition*. Weinheim, Germany: WILEY-VHC, 2008. ISBN: 978-0-470-51117-6.
- [112] M. Abo-Bakr and B. Kuske. “ASTRA Based Swarm Optimization of the BERLinPro Injector”. In: *Proceedings of ICAP 2012*. Rostock-Warnemünde, Germany, 2012, pp. 281–283. ISBN: 978-3-95450-116-8.
- [113] E. Panofski et al. “Multi-Objective Optimization of an SRF Photoinjector with Booster Section for High Brightness Beam Performance”. In: *Proceedings of IPAC’18*. Vancouver, British Columbia, Canada, 2018, pp. 3193–3196. ISBN: 978-3-95450-184-7.
- [114] I. V. Bazarov and C. Sinclair. “High Brightness, High Current Injector Design for the Cornell ERL Prototype”. In: *Proceedings of PAC 2003*. Portland, Oregon, USA, 2003, pp. 2062–2064. ISBN: 0-7803-7739-7.
- [115] T. van Oudheusden et al. “Electron Source Concept for Single-Shot Sub-100 fs Electron Diffraction in the 100 keV Range”. In: *Journal of Applied Physics* 102.9 (2007), pp. 1–8. DOI: 10.1063/1.2801027.
- [116] M. J. Cowley. *Diffraction Physics*. Amsterdam, North-Holland: North-Holland Personal Library, 1995. ISBN: 0-444-10791-6.
- [117] C. Gulliford, A. Bartnik, and I. Bazarov. “Multi-objective Optimizations of a Novel Cryo-cooled DC Gun Based Ultra Fast Electron Diffraction Beamline”. In: *Physical Review Special Topics Accelerators and Beams* 19 (2016), pp. 1–9. DOI: 10.1103/PhysRevAccelBeams.19.093402.
- [118] C. Gulliford, A. Bartnik, and I. Bazarov. “Multiobjective Optimizations of an RF Gun Based Electron Diffraction Beam Line”. In: *Physical Review Special Topics Accelerators and Beams* 20 (2017), pp. 1–6. DOI: 10.1103/PhysRevAccelBeams.20.033401.



- [119] P. Michel. “The Radiation Source ELBE at the Forschungszentrum Dresden-Rossendorf”. In: *Proceedings of the Nuclear Science Symposium 2008*. Dresden, Germany, 2008, pp. 3078–3080. DOI: 10.1109/NSSMIC.2008.4775006.
- [120] A. Arnold. “Simulation und Messung der Hochfrequenzeigenschaften einer supraleitenden Photo-Elektronenquelle”. PhD thesis. Universität Rostock and Helmholtz-Zentrum Dresden-Rossendorf, 2012.
- [121] W. Seidel et al. “Three Years of cw-Operation at FELBE - Experiences and Applications”. In: *Proceedings of FEL’08*. Gyeongju, Korea, 2008, pp. 382–385.
- [122] U. Lehnert et al. “Conceptual Design of a THz Facility at the ELBE Radiation Source”. In: *Proceedings of FEL 2010*. Malmö, Sweden, 2010, pp. 656–659.
- [123] J. Teichert et al. “Experiences with the SRF Gun II for User Operation at the ELBE Radiation Source”. In: *Proceedings of IPAC’18*. Vancouver, British Columbia, Canada, 2018, pp. 4145–4147. ISBN: 978-3-95450-184-7.
- [124] G. Dreyfus. *Neural Networks: Methodology and Applications*. Berlin, Germany: Springer Verlag, 2005. ISBN: 978-3-540-28847-3.
- [125] A. L. Edelen. “Application of Neural Networks to Modeling and Control of Particle Accelerators”. In: *Talk at the Fermilab Accelerator Physics and Technology Seminar, 8th June 2017* (2017).
- [126] A. L. Edelen et al. “Neural Networks for Modeling and Control of Particle Accelerators”. In: *IEEE Trans. Nucl. Sci.* 63.2 (2016), pp. 878–897. DOI: 10.1109/TNS.2016.2543203.
- [127] D. Edstrom et al. “50-MeV Run of the IOTA/FAST Electron Accelerator”. In: *Proceedings of NAPAC 2016*. Chicago, Illinois, USA, 2016, pp. 326–329. ISBN: 978-3-95450-180-9.
- [128] L. Young and J. Billen. “The Particle Tracking Code PARMELA”. In: *Proceedings of the 2003 Particle Accelerator Conference*. Portland, Oregon, USA, 2003, pp. 3521–3523. ISBN: 0-7803-7739-9.

## Acknowledgements

I would like to use this very last page to acknowledge the valuable support, which I received during the last years. First and foremost, I would like to devote very special thanks to Prof. Dr. Andreas Jankowiak who inspired my interest in the topic of accelerator physics, who gave me the opportunity to write my dissertation at Helmholtz-Zentrum Berlin, and who helped me to advance my scientific and professional skills. I would also like to express my gratitude to my supervisor Prof. Dr. Thorsten Kamps, who gave rise to the idea of developing a multi-objective optimization program, who supported me during this work and contributed many crucial ideas. Many thanks for proofreading my doctoral thesis and giving me useful advice.

My thanks also go to my reviewer Prof. Dr. Thomas Weis, who already accompanied my PhD thesis during its formation as a member of the dissertation committee at Helmholtz-Zentrum Berlin. Thank you for the helpful feedback and advice. Furthermore, I wish to thank Prof. Dr. Ursula van Rienen for her willingness to act as a second reviewer.

I am also grateful to the members of the FG-IA and FG-ISRF groups for their open doors and discussions, in particular Dr. Guido Klemz, Dr. Julius Kühn, Dr. Michael Abo-Bakr, Dr. Jeniffa Knedel and Dr. Markus Ries. Special thanks go to Bettina Kuske who allowed me to include her simulation results in my doctoral thesis and who was always available for scientific and private discussions. Furthermore, I would like to thank Dr. Axel Neumann for the input about SRF cavities and field flatness issues.

I would like to sincerely thank my colleagues from the SRF photoinjector group at Helmholtz-Zentrum Dresden-Rossendorf, in particular Dr. Jochen Teichert, Dr. Hannes Vennekate, Dr. Pengnan Lu and Dr. Rong Xian, for the opportunity to obtain operation and measurement experiences with their SRF photoinjector and for the open exchange concerning simulation strategies for SRF photoinjectors. Many thanks for all the support.

I wish to thank Claudia Bubke who proofread and edited my English text, even during her stay abroad.

My special thanks go to my colleagues and friends Martin Schmeisser, Sebastian Keckert, Dr. Julia Köszegi, Dr. Georgios Kourkafas and Dr. Stephanie Rädcl for their patience and their permanent willingness to listen and to discuss different topics related to this work. Most of all, I want to thank Dr. Jens Völker who shared his incredible knowledge in accelerator physics with me, who helped me with countless MATLAB challenges and who was always open for theoretical beam dynamic debates. Thank you all for your time and your endless support. Thank you for the unforget-

table moments at the institute, conferences all over the world, and in our free time throughout the last years.

Finally, a huge thank you to my family for their love, encouragement and endurance in those years. Thank you for being part of my life!



# Selbstständigkeitserklärung

Hiermit versichere ich, dass ich die vorliegende Arbeit selbstständig verfasst und keine anderen als die angegebenen Quellen und Hilfsmittel verwendet habe.